Kite Tether Force Control

Reducing Power Fluctuations for Utility-Scale Airborne Wind Energy Systems

Master of Science Thesis

Jesse Hummel

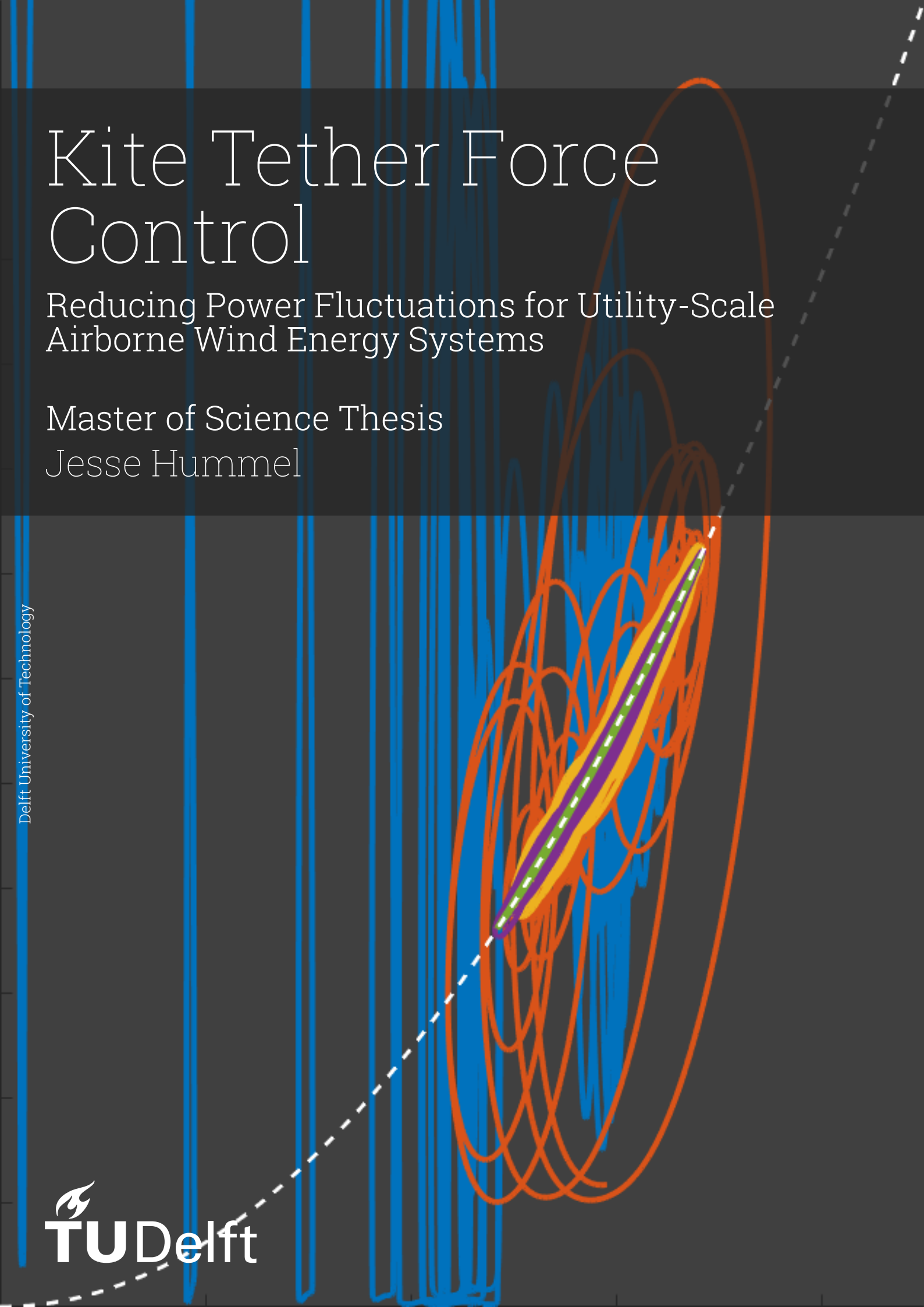

Delft University of Technology

TU Delft

Kite Tether Force Control

Reducing Power Fluctuations for Utility-Scale Airborne Wind Energy Systems

by

Jesse Hummel

to obtain the degree of Master of Science
at the Delft University of Technology,
to be defended publicly on Friday June 30, 2023 at 10:30.

Student number:	4497554	
Project duration:	May 1, 2022 – June 30, 2023	
Thesis committee:	Dr.ing. R. Schmehl,	TU Delft, chair and supervisor
	Dr.ir. E. van Kampen,	TU Delft, supervisor
	Ir. D. Eijkelhof,	TU Delft, supervisor
	Ir. T.S.C. Pollack,	TU Delft, supervisor
	Dr. S.J. Hulshoff,	TU Delft, external committee member

Cover:	Response on the winch control curve for system with different inertia's when using kite tether force control.
Style:	TU Delft Report Style, with modifications by Daan Zwaneveld.

An electronic version of this thesis is available at http://repository.tudelft.nl/.

TU Delft

Contents

Part I

Introduction

1 Introduction

Wind is a great resource of renewable energy. The exact amount that can be sustainably sourced from the wind is still a subject of scientific debate, ranging from 20 to 80 TW close to the surface level, and up to 1800 TW for high altitude winds (Bechtle, Schelbergen, Schmehl, Zillmann, & Watson, 2019). Wind energy is recognised for having one of the highest potentials for emission reduction of the energy sector (Shukla, Skea, Slade, Khourdajie, et al., 2022). This is due to its increasingly lower cost and effectiveness at large-scale (Shukla, Skea, Slade, Khourdajie, et al., 2022).

In 2020, 6% of electricity was produced by wind energy globally and was as high as 47% in Denmark (IRENA, 2022; Jørgensen, Holttinen, IEA Wind Operating Agents, & Charlotte Hede Lindev, 2021). With favourable policies from government this sector has seen a high growth and this is expected to continue as policy momentum is on its side (Jørgensen et al., 2021).

Most of the energy from the wind is captured using horizontal axis wind turbines. While the design concept has been constant for many years, the wind turbine design is continually evolving to increase performance mainly through higher turbines and longer blades (Jørgensen et al., 2021). Higher towers allow to capture generally stronger and more steady winds (C. Archer & Caldeira, 2009; C. L. Archer, 2013; Bechtle et al., 2019) and larger blades allow to sweep a larger area. This has led to an increase in capacity and capacity factor while reducing costs (Jørgensen et al., 2021). The capacity of a wind turbine is simply its rated power and the capacity factor is the fraction of how much electricity a wind turbine produces compared to its theoretical maximum if the wind was always optimal.

There are some challenges for future expansion for wind turbines. The capacity factor of wind turbines is now 27% onshore and 42% offshore, both with increasing trend, but with high variability between locations (Jørgensen et al., 2021). A low capacity factor makes grid integration harder because it can not be relied on as base load. This also causes "high rates" of wind farms to temporarily produce below their capacity to avoid overproduction (Jørgensen et al., 2021). Higher capacity factors can be reached offshore and in more windy areas onshore. But onshore land availability in those areas is one of the challenges for future expansion of wind energy (Jørgensen et al., 2021; Shukla, Skea, Slade, Al Khourdajie, et al., 2022).

Furthermore, access to finance and ecological regulations, such as related to visual and acoustic impacts, are challenges for further expansion (Shukla, Skea, Slade, Khourdajie, et al., 2022).

1.1. Airborne Wind Energy

Airborne Wind Energy (AWE) aims to tackle some of these challenges with a radical new design for harvesting energy from the wind. This technology was first envisioned by Loyd (1980) who calculated that large-scale kites could extract multi-megawatts of power from high altitude wind. Most of today's concepts are still based on his principle of crosswind flight where kites fly in circles or figures of eight and are attached to a ground station with a tether (Vermillion et al., 2021), see Figure 1.1 (Fagiano, Quack, Bauer, Carnel, & Oland, 2022).

There are two methods for energy extraction when flying in crosswind patterns: fly-gen and ground-gen. Fly-gen uses on-board propellers to generate electricity and sends this down through the tether that is attached to the ground station. In contrast, ground-gen operation uses a pumping cycle

that consists of two phases: the traction (energy generating) and retraction (energy consuming) phase. During the traction phase, the pull that the kite exerts on the tether is transformed into electricity by rotating a ground-based generator. When the maximum tether length is reached, the kite needs to be retracted. Since the kite can be put in an aerodynamically favourable position for the retraction phase, this takes only a fraction of the energy produced in the traction phase (Fagiano et al., 2022; Vermillion et al., 2021).

While many different concepts are possible, there are three system layouts that most of the airborne wind energy community has converged towards (Fagiano et al., 2022). All these systems utilize Loyd's principle of crosswind flight, either with fly-gen or ground-gen. For fly-gen, only fixed-wing kite concepts exist since the generators are heavy and need a rigid attachment point. However, for ground-gen systems, both soft kite and fixed-wing kite concepts exists. These three system layouts that are shown in Figure 1.1 (Fagiano et al., 2022). Sometimes soft kites are reinforced with a rigid support structure (Candade, Ranneberg, & Schmehl, 2020), which can be named hybrid kites.

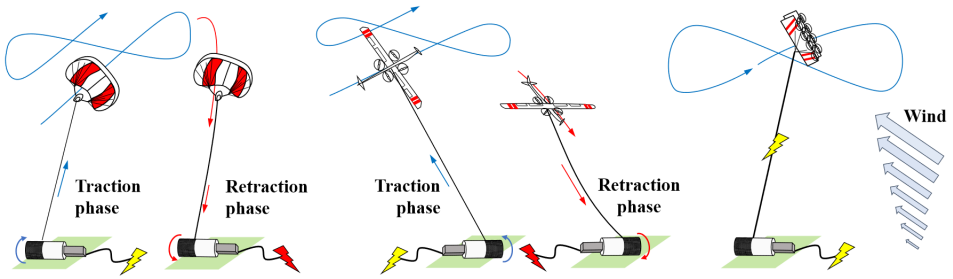

Figure 1.1: Visualization of the three most advanced operating concepts. From left to right: soft wing with ground-gen, fixed-wing with ground-gen, fixed-wing with fly-gen (Fagiano, Quack, Bauer, Carnel, & Oland, 2022).

1.1.1. Advantages

Airborne Wind Energy comes with some advantages over wind turbines. First of all, by using a tether instead of a tower, the operating altitude can leapfrog the current trend of increasing tower heights (Jørgensen et al., 2021; Vermillion et al., 2021). At higher altitudes, the winds are generally stronger and more consistent (C. Archer & Caldeira, 2009; C. L. Archer, 2013; Bechtle et al., 2019), potentially leading to more production, higher capacity factors, and "unlock" new locations where wind energy extraction could become economical (Bechtle et al., 2019; De Lellis, Mendonça, Saraiva, Trofino, & Lezana, 2016; Zillmann & Bechtle, 2018).

A high capacity factor is important for baseload applications as the intermittency of the power production is reduced. That would mean that airborne wind energy could reduce the reliance on energy storage as the grid transitions to renewable sources of energy (Zillmann & Bechtle, 2018). The advantages of reaching higher altitudes can be magnified by allowing the kite to adjust its altitude to the optimum altitude in real-time (Bechtle et al., 2019; Vermillion et al., 2021). Bechtle et al. (2019) investigated the potential wind resource that can be reached assuming a system that can optimally adjust its altitude. They found that in most of Europe the wind speed is above the cut-in wind speed 80% of the time, which is good for base load applications. In addition, the wind power density that is available 95% of the time is twice as much as the wind power density at a fixed 100 m hub height. Meaning that more energy can be extracted from the wind with less intermittency using airborne wind energy.

However, these advantages are derived from increased wind resource potentials and not potential energy extraction using an airborne wind energy system. So the actual performance increase is still up for debate. In a recent study, Malz, Hedenus, Göransson, Verendel, and Gros (2020) suggested that fly-gen systems might only outperform wind turbines in certain locations where wind shear is high and low altitude wind speeds are low.

A second advantage is that airborne wind energy uses less materials for the same capacity as a wind turbine. Using less materials itself could reduce costs and lifetime emissions and creates a snowball effect where (floating) foundations can also be smaller and thus come with a lower cost and environmental impact (Schmehl, 2018; United States Department of Energy, 2021; Vermillion et al., 2021; Zillmann & Bechtle, 2018). This could lead to an estimated overall reduction of global warming potential of 40% for

multi-MW systems (Van Hagen, 2021).

Finally, some other advantages could be that the visual and acoustic impact is smaller, which make intuitive sense because the kites fly at a higher operating altitude and are generally smaller than the rotors of a wind turbine of the same power. However, these claims lack scientific evidence (Schmidt, de Vries, Renes, & Schmehl, 2022b), but there are on-going studies that are investigating the social impact of airborne wind energy systems (Schmidt, de Vries, Renes, & Schmehl, 2022a).

Commercialisation

All these advantages have attracted academia and about a dozen startups to pursue airborne wind energy. Currently, SkySails Power GmbH is operating the only commercial system in the Republic of Mauritius (Wrage, 2022). It is a small, soft-wing, ground-gen system of 80 kW, but a start in commercialisation nonetheless. Small islands are one of the potential starting points for market entry because those remote locations often need to import diesel for their generators making energy expensive (Hussen et al., 2018; Weber et al., 2021).

In the long-term, bigger systems could be able to provide more utility-scale power. The biggest system flown to date is the M600 by Makani Power with a design power output of 600 kW. But after a challenging test campaign in the waters of Norway they had to file bankruptcy as the business case wasn't strong enough for investors (Echeverri, Fricke, Homsy, & Tucker, 2020). "MegAWES" is the first publicly available reference model and simulation framework multi-megawatt, ground-gen, fixed-wing AWE system (Eijkelhof, Rapp, Fasel, Gaunaa, & Schmehl, 2020; Eijkelhof & Schmehl, 2022). It's intended to be used for benchmarking and cross validation. An envisioned future by many technology developers has multiple multi-MW systems arranged in a wand farm layout (Fagiano et al., 2022).

It seems that in the short-term, airborne wind energy won't contribute significantly to the energy transition. However, it remains a very interesting concept because of its long-term benefits for renewable energy generation (United Nations, 2021).

1.1.2. Challenges

In this subsection both general challenges as well as challenges particular to systems with high mass will be discussed, where power flucutations are a particular challenge.

General challenges

As a developing technology, airborne wind energy also has challenges that need to be overcome on the path towards commercialisation. In an expert survey in 2012, the biggest challenges identified were reliability, regulation, and control systems (Near Zero, 2012). Those main challenges still are true today (Vermillion et al., 2021; Zillmann & Bechtle, 2018).

Airborne wind energy systems need to remain in flight to produce energy and thus have little time for maintenance or repair. Furthermore, they must be resilient to different weather conditions. This means that the different components, such as kite, tether, and generator, launching/landing systems, must have a high reliability and that the control system must be robust, as will be discussed as a separate point later.

These systems don't fit into a well-established regulatory framework. A framework has been built together with the FAA in the U.S., however experts have raised concerns about the resulting decrease in development speed and uncertainty about future regulations (Near Zero, 2012).

Control is an important part towards high reliability and has remained one of the main technical challenges (Salma, Friedl, & Schmehl, 2020; United States Department of Energy, 2021). Especially in non-ideal atmospheric conditions, robust control is still an "open challenge" (Vermillion et al., 2021).

Control of airborne wind energy systems is difficult because of the highly nonlinear dynamics (Li, Olinger, & Demetriou, 2018; Zanon, Gros, & Diehl, 2013), the strong coupling between the physically separated winch and kite, and the operating condition which is at high angles of attack and at large tether force (Rapp, Schmehl, Oland, & Haas, 2019).

Power fluctuations

Wind turbines usually operate in a steady-state. The rotation speed is constant and so is the power output. It only has to adapt to a change in wind speed, which happens at rather large timescales. Airborne wind energy has two aspects that make the power more oscillatory. First, ground-gen systems have a traction and retraction phase where power is produced in the traction phase and consumed

during the retraction phase. Second, systems with lots of mass experience gravity as a disturbance force that increases or decreases airspeed, depending on the position in the figure of eight. This results in higher and lower power extraction during the figure of eight or ellipse that is flown during the power generating phase.

The largest multi-MW simulation, MegAWES (Eijkelhof et al., 2020; Eijkelhof & Schmehl, 2022), currently uses an adapted control architecture from Rapp (2021), Rapp, Schmehl, Oland, and Haas (2019), and Rapp, Schmehl, Oland, Smidt, et al. (2019). The control philosophy behind that architecture is to keep the tether force constant for a given wind speed. This leads to smaller changes in the dynamics thus enabling more robust control. Since the MegAWES kite has significant mass, its pull on the tether is reduced when flying upwards. To keep the same tether force, the winch has to reel-in, thus consuming power momentarily. Furthermore, when the kite is flying downwards, gravity is "helping" and the winch needs to reel-out faster to keep the tether force constant. This leads to power fluctuations between 20.0 MW and −4.7 MW during the traction phase, at a wind speed of 22 m/s when using the 3DOF simulation.

Power fluctuations are undesired because they increase system cost since they require more power smoothing, which is a necessary step before power can be transmitted to the energy grid (Joshi, von Terzi, Kruijff, & Schmehl, 2022). For example, when using an electrical drivetrain, the generator and battery will need to be oversized to handle high peak loads. Furthermore, negative power must come from an energy storage device, leading to power conversion losses. There are ideas to momentarily overload the drivetrain (Bauer, Petzold, Kennel, Campagnolo, & Schmehl, 2019). But even then, lower overloading can soften system requirements.

1.2. Control of airborne wind energy systems

The objective of airborne wind energy is to produce power, which cannot be directly controlled so there are two strategies: First, flying as close as possible to power-optimal flight paths. Second, not fighting the disturbances too much and "go with the flow". A lot of work has gone into optimizing flight paths for maximum power extraction using the first strategy. In those architectures, cascaded control architectures must be used where path planning and path following are two distinct parts. In both strategies, path following is needed, but the definition of the path is more strict in the first strategy. Since this work focusses on path following, it can be applicable to both.

The three main concepts, shown in Figure 1.1, all require different control strategies for path following. For soft kites, an analytical expression related to the turn rate of the kite and the pull on the steering lines can be derived, named the "turn-rate-law" (Erhard & Strauch, 2015, 2018; Fagiano, Zgraggen, Morari, & Khammash, 2014; Fechner, van der Vlugt, Schreuder, & Schmehl, 2015). This makes the inner flight control loop for soft-kites a "well-understood" problem (Fagiano, Nguyen-Van, Rager, Schnez, & Ohler, 2018). So the focus of this work will be on fixed-wing systems. Bauer et al. (2019) presented a control architecture for fly-gen systems that it being used and further developed by KiteKRAFT (Fagiano et al., 2022). However, while a lot of literature exists for ground-gen, fixed-wing control, companies are still using controllers that were proposed in early literature on airborne wind energy control. One of the reasons could be that the literature focuses extensively on optimal control (Vermillion et al., 2021), which, while the best choice for studies towards the theoretical performance of airborne wind energy, are heavily reliant on models and have a high computational complexity. So they could lead to a higher power output and more robust flight if these challenges are overcome. In this work, the focus will be to bridge the gap between optimal control and the controllers currently used in industry by designing a nonlinear controller that has a relatively low model dependency and has low computational complexity, while having a high performance on the nonlinear dynamics of ground-gen, fixed-wing systems.

The focus will be on two control strategies in particular: winch control and angle of attack control. As discussed previously, MegAWES uses a winch control strategy that keeps the tether force constant for a given wind speed. However, other strategies use a variable tether force reference based on a measurable quantities like reel-out speed (Todeschini, Fagiano, Micheli, & Cattano, 2021; Zgraggen, Fagiano, & Morari, 2016) or airspeed (Erhard & Strauch, 2015). By simply setting the torque of the winch equal to the reference tether force using a feedforward controller, the system is driven on the defined curve. It will be investigated if this is a better winch control strategy for MegAWES, particularly relating to lowering power fluctuations.

Angle of attack control is needed when the system is at its power limit and power extraction from the wind must be curtailed in order to not go over system limits. There are many optimal control studies that compute a dynamic angle of attack reference (De Schutter, Leuthold, Bronnenmeyer, Paelinck, & Diehl, 2019; Licitra et al., 2019), or flight controllers that follow a precomputed angle of attack reference (Echeverri et al., 2020; Li, Olinger, & Demetriou, 2015a; Zanon et al., 2013). However, the goal of these studies is to analyze system performance or optimize trajectories and are not suitable for implementation outside of simulation due to model uncertainties. Currently, MegAWES does not have a power limit. It will be investigated if a power limit can be implemented with a feedback controller with less model dependencies that current optimal control approaches.

One potential control structure to tackle these challenges is incremental nonlinear dynamic inversion (INDI). INDI is a feedback linearisation control technique and was developed as alternative to Nonlinear Dynamic Inversion (NDI). NDI aims to invert the system dynamics over the entire flight envelope. This linearises a nonlinear system, which greatly simplifies outer loop controller design, since gain scheduling is no longer required (Chai et al., 2021). While NDI has been successfully applied to aerospace systems (Grondman, Looye, Kuchar, Chu, & Van Kampen, 2018; Kawaguchi, Ninomiya, & Miyazawa, 2011; Moncayo, Perhinschi, Wilburn, Wilburn, & Karas, 2012), its main drawback is a lack of robustness because exact inversion is impossible due to model uncertainties (Chai et al., 2021).

Around 2000, alternatives to NDI called "simplified NDI" (Smith, 1998) and "modified NDI" (Bacon & Ostroff, 2000) were developed that were less dependent on a model in both the qualitative and quantitative sense and used acceleration estimates in their controllers. This technique was further developed and renamed to "incremental NDI (INDI)" by S. Sieberling, Chu, and Mulder (2010)[1], and this technique still goes by that name today. Its ability to linearise nonlinear systems, high performance, lower model dependency, and good disturbance rejection mean that could be a very good candidate for airborne wind energy control.

1.3. Research Objective and Questions

This thesis consists of a broad literature study after which a more narrow scope was redefined for the experimental work. The literature study, in Part III, was used to explore how INDI could be used on fixed-wing, ground-gen systems to improve robust control without the drawbacks of high model complexity and computational complexity.

With that, the research objective for the literature study can be formulated as follows.

Research objective of the literature study

Improve the reliability of fixed-wing, ground-gen airborne wind energy systems in a turbulent and gusty wind field by investigating the nominal and robust performance of INDI controllers on the MegAWES simulation framework.

To achieve this objective, the following questions will have to be answered:

1. How to design an INDI controller for an airborne wind energy system?
   - (a) What is the state-of-the-art of airborne wind energy control design? chapter 2
   - (b) What is the state-of-the-art of INDI controller design? chapter 3
   - (c) How could INDI be applied in airborne wind energy control design? chapter 4
2. How to measure the nominal and robust performance of an airborne wind energy system controller? chapter 5
3. What is the nominal performance of INDI in a preliminary experiment on the MegAWES simulation framework? chapter 6

All these questions will be answered in the literature study, in Part III. From Question 1c, it will become apparent that INDI can be used in different ways to improve the performance of fixed-wing, ground-gen airborne wind energy systems. However, not all those ideas can be explored during

[1]This name might also be familiar to the airborne wind energy community from his work at Ampyx Power (Ruiterkamp & Sieberling, 2013).

the thesis. The most rudimentary idea, to use INDI as inner loop rate control, will be explored in a preliminary experiment, discussed in chapter 6. This idea can be extended with kite tether force control, which will be extensively discussed first in chapter 4, and then in chapter 7, where a plan is presented on how to develop a kite tether force control control architecture which reduces power fluctuations. This will include control requirements and scope and implementation considerations that need to be taken. This will lead to a new set of research questions will be answered in the rest of this thesis:

Research objective of the experimental work

Reduce the power fluctuations of utility-scale airborne wind energy systems by implementing a power limit in the 3DOF MegAWES simulation framework using a feedforward winch controller and kite tether force control.

To achieve this objective, the following research questions will have to be answered:

4. What is the effect of the radius and inertia of the winch on the system dynamics? chapter 9
   (a) What are the equations of motion of the winch?
   (b) How does the pole location change based on the radius and inertia?
   (c) What is a desirable pole location for MegAWES?
   (d) What is the effect of good and bad design of the winch radius and inertia.
5. How to adapt the existing feedforward winch controllers that are derived for massless kites for kites with mass? chapter 10
   (a) How does the optimal reel-out factor change for kites with mass?
   (b) Is there a minimum required tether force to keep the kite in the air when it is overcoming the force of gravity?
   (c) How can the optimal winch control strategy take this into account?
   (d) Is the generated power higher when using the adapted winch controller?
6. What is the performance of the kite tether force controller? chapter 11
   (a) How to design a 3DOF kite tether force controller?
   (b) What is the peak power when using kite tether force control?
   (c) How much does the mean power reduce when implementing a power limit with kite tether force control?

The development of kite tether force control will be done in Part IV. It starts with resizing the winch parameters in chapter 9, since the current winch parameters of MegAWES are too small, leading to too fast dynamics. The current winch controller will be exchanged for a feedforward winch controller, which can adapt the tether force based on the reel-out speed. In chapter 10, it will be explored how the feedforward winch control law can be adapted for kites with significant mass. It is shown that this increases the minimum power during the traction phase from negative to positive in the 3DOF simulation. In chapter 11, the kite tether force controller will be designed. This "shaves off" the power peaks so decreasing the maximum power by about 50% while minimally affecting mean power production. This thesis will finally be concluded in Part V.

Part II

Paper

Kite Tether Force Control for Power Fluctuation Reduction in the MegAWES Simulation Framework

J.I.S. Hummel*,
Faculty of Aerospace Engineering, Delft University of Technology, 2629HS Delft, the Netherlands

Power output during flight operation of multi-megawatt airborne wind energy systems is substantially affected by the mass of the airborne subsystem, resulting in power fluctuations. In this paper, an approach to control the tether force using the airborne subsystem is presented that improves the quality of the power output. This kite tether force control concept is implemented on the 3DOF dynamic simulation of the MegAWES reference model. First, the winch of MegAWES is resized because an analysis of winch inertia and radius shows its effect on power output and tether force overshoot. Second, the power consuming sections during the traction phase are eliminated by using a feedforward winch controller. Finally, the peak power is substantially reduced by implementing the kite tether force controller which uses a measurement of the tether force, angle of attack, and airspeed to keep the tether force constant when the system is at its power limit. This reduces the range between minimum and maximum power output by 75%.

I. Introduction

Wind is a great resource of renewable energy. Horizontal axis wind turbines are the most prominent way of harvesting this wind energy. While the design concept has been constant for many years, the wind turbine design is continually evolving to increase performance mainly through higher turbines and longer blades [1]. Higher towers reach generally stronger and more steady winds [2, 3] and larger blades allow to sweep a larger area. This has led to an increase in capacity and capacity factor while reducing costs [1]. Airborne wind energy aims to leapfrog this trend with a radical new design for harvesting energy from the wind. This technology was first envisioned by Loyd [4] who calculated that large-scale flying devices could extract multi-megawatts of power from higher altitude winds. Most of today's concepts are still based on Loyd's principle of crosswind flight where kites fly in circles or figures of eight and are attached to a ground station with a tether [5, 6].

One of the popular system layouts are the ground-gen, fixed-wing systems. Ground-gen operation uses a pumping cycle that consists of two phases: the traction (energy generating) and retraction (energy consuming) phase. Fixed-wing refers to the rigid materials used for the kite.

Systems currently in development have a rated power from 1 kW to 500 kW [7]. However, to achieve large scale power production, this technology will need to be scaled up to several MW's per unit [6]. "MegAWES" is the first publicly available reference model and simulation framework multi-megawatt, ground-gen, fixed-wing AWE system [8, 9]. It's intended to be used for benchmarking and cross validation.

MegAWES uses an adapted control architecture from [10–12]. The control philosophy behind that architecture is to keep the tether force constant for a given wind speed. While not optimal for power production, using the winch to control the tether force leads to less overshoot above the tether force limit. This was one of the focus points of that work [12].

Since the MegAWES kite has significant mass, its pull on the tether is reduced when flying upwards. To keep the same tether force, the winch has to reel-in, thus consuming power momentarily. Furthermore, when the kite is flying downwards, gravity is helping and the winch needs to reel-out faster to keep the tether force constant. This leads to power fluctuations between 20.0 MW and -4.7 MW, at a wind speed of 22 m/s when using the 3DOF simulation.

Power fluctuations are undesired because they increase system cost since they require more power smoothing, which is a necessary step before power can be transmitted to the energy grid [13]. For example, when using an electrical drivetrain, the generator and battery will need to be oversized to handle high peak loads. Furthermore, negative power must be provided from an energy storage device, leading to power conversion losses. Besides a rise in financial cost, increasing the size of the ground systems also increases the environmental costs [14]. Instead of increasing the size of the drivetrain, there are ideas to momentarily overload the system [15]. But even then, lower overloading can soften system requirements.

Instead of keeping a constant tether force, most winch control architectures aim to reel-out the kite at the optimal reel-out speed for power production. Loyd derived that for massless kites in quasi-steady flight, the optimal reel-out speed is one third of the wind speed, and defined this as the optimal reel-out factor [4]. When considering the mean

*MSc student, Control & Simulation division, Faculty of Aerospace Engineering, Kluyverweg 1

power over the traction and retraction phase, the optimum reel-out factor is slightly smaller [16]. After selecting a reel-out factor, an ideal winch control curve can be found that prescribes the ideal tether force based on measurable quantities such as reel-out speed [17, 18] or airspeed [19]. Instead of using a model to predict the optimal winch control curve, it can also be estimated empirically, as shown in simulation by [20]. This winch control curve can be used by a feedforward controller that ensures the system stays on that winch control curve as the wind speed changes. The feedforward controller calculates the ideal tether force for the given reel-out speed (or other quantity used), and sets its torque to balance that ideal tether force. The advantage of this approach is that it ensures that the tether force is always in balance with the available lift force of the kite. So switching from a winch controller that keeps the tether force constant to a feedforward controller could potentially avoid the negative power during the traction phase. It can furthermore result in more quiet and stable system behavior, as hypothesized by [9].

Besides increasing the minimum power, the peak power should be reduced. This can be done by implementing a power limit. At the tether force limit, the winch can reel-out faster if the wind speed is increasing further. However, once the power limit is reached, increasing the reel-out speed further would exceed the power limit. So the aerodynamic performance of the kite needs to be lowered, similar to pitch control of wind turbines blades when operating at rated power [21]. The system design where the tether force limit is reached before the power limit is called the 3-phase strategy [22]. If the tether force limit and power limit coincide on the winch control curve and are thus reached at the same reel-out speed, this is called the 2-phase strategy [16]. Lowering the aerodynamic performance can be done by lowering the angle of attack. There are many optimal control studies that compute a dynamic angle of attack reference [23, 24], or flight controllers that follow a precomputed angle of attack reference [25, 26]. However, the goal of these studies is to analyze system performance or optimize trajectories and are not suitable for implementation outside of simulation due to unaccounted model uncertainties. So a different controller has to be designed that can dynamically adapt the angle of attack once the power limit is reached.

Besides looking at power fluctuations, this paper also focuses on winch sizing. The size of the winch plays an important role in the dynamics of the overall system. Even though this has been hypothesized in literature [19], to the best of the author's knowledge, no publications have been made on sizing the winch. Especially for large scale systems, of which no real-life prototypes exist, selecting appropriate values is difficult. According to [8, 9], the winch sizing for MegAWES requires additional analysis. Its current value is based on a smaller system [10] and thus requires upscaling.

The main contributions of this paper are threefold and together achieve a reduction in power output fluctuations when tested in the MegAWES simulation framework. First, a new approach to size the winch of the system is developed. Instead of estimating the winch inertia and radius from a mechanical design, an upper bound for the inertia and corresponding lower bound for the radius is obtained based on performance requirements for power and tether force overshoot. This is achieved using a frequency domain analysis of winch dynamics. New values for the radius and inertia of the winch will be proposed that lead to slower dynamics of the winch but are still sufficiently fast for power production and tether force tracking. Second, using a feedforward winch control law increases the minimum power during the traction phase. Because it allows a lower tether forces when the kite has to use a larger portion of its lift force to fight gravity when flying upwards. For the simulation presented it eliminates the negative power such that the winch no longer needs to put energy into the system to keep the tether force constant.

Third, a power limit will be added. Instead of using optimal control, the kite tether force control concept will be presented. It uses a measurement of the tether force, angle of attack, and airspeed to keep the tether force constant when the system is at its power limit. The 2-phase strategy is used where the tether force limit and power limit coincide.

This paper is structured as follows: In Section II a model description of the MegAWES simulation framework is given, including the control architecture as described by [8, 9]. In Section III, the frequency domain analysis related to the sizing of the winch is presented. In Section IV, the novel kite tether force control concept will be described. In Section V, first, new parameters for the winch will be proposed and then two control concepts will be compared to the controller proposed by [8, 9]. First, the winch inertia and radius will be updated with the values proposed in this work together with a feedforward winch control law to increase the minimum power output. Second, the kite tether force controller will be added to reduce the maximum power output. This article is concluded in Section VI with the main conclusions and discussion thereof.

II. Model Description

In this section, an overview of the MegAWES reference design, 3DOF dynamics, and control architecture is given based on [8, 9]. The GitHub repository for MegAWES can be found at [27], where the code for this paper can be found on the branch `DevTetherForceControl`*.

*`https://github.com/awegroup/MegAWES/tree/DevTetherForceControl`

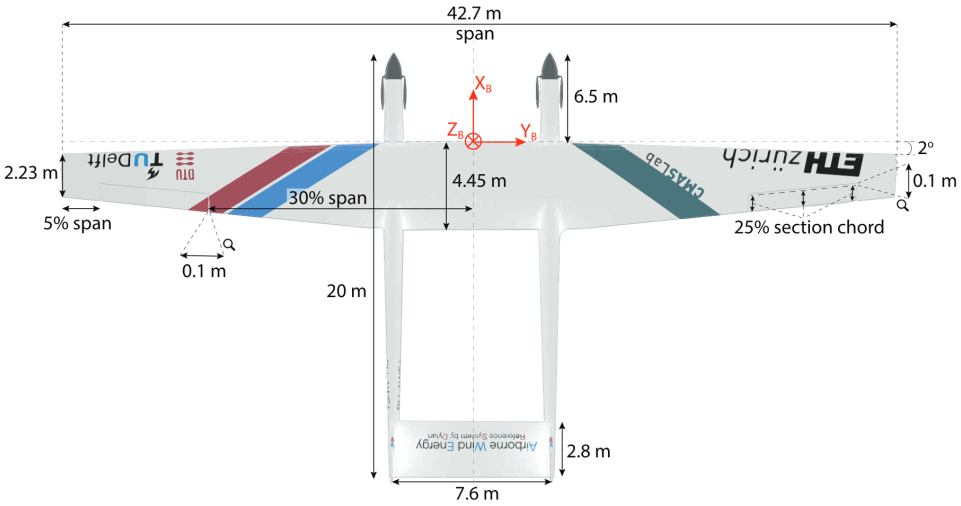

Fig. 1 Top view of the wing planform of MegAWES [8].

A. Reference Design

The design of the kite is shown in Fig. 1 [8]. Its starting point was the planform of the AP-3 of Ampyx Power scaled up to their intended wing area for the AP-4. It features a twin-fuselage design with a propeller at the front of each fuselage to assist during take-off. There is a single tether, attached to the center of gravity. The main wing has a surface area of 150 m^2. It has a mass of approximately 6885 kg. Because of the twin-fuselage design, it has two rudders but a single elevator. In addition, it has two ailerons, one on each side of the main wing.

B. 3DOF dynamics

The MegAWES simulation offers both 3DOF and 6DOF dynamics. In this work, the 3DOF dynamics are used. The angle of attack can then be directly changed, in contrast to commanding the elevators in the 6DOF dynamics. This allows a focus on the core of the kite tether force control concept: an angle of attack reference controller, discussed in Section IV.

The 3DOF dynamics can be described as a vector with $\left[V_a, \chi_a, \gamma_a\right]^T$ and is shown in Eq. (1) [8]. V_a denotes the airspeed, χ_a the course angle, γ_a the path angle, F_{tot} the sum of the aerodynamic, gravity, and tether force, m_a the mass of the kite, and v_w the wind speed. This is then expressed in the aerodynamics frame, denoted by $\bar{A}$.

$$\begin{pmatrix} \dot{V}_a \\ \dot{\chi}_a \\ \dot{\gamma}_a \end{pmatrix}_{\bar{A}} = \begin{pmatrix} 1 & 0 & 0 \\ 0 & \frac{1}{V_a \cos\gamma_a} & 0 \\ 0 & 0 & \frac{-1}{V_a} \end{pmatrix}_{\bar{A}} \left[\frac{(\mathbf{F}_{tot})_{\bar{A}}}{m_a} - \begin{pmatrix} \dot{v}_{w,x} \\ \dot{v}_{w,y} \\ \dot{v}_{w,z} \end{pmatrix}_{\bar{A}} \right] \tag{1}$$

The aerodynamic force is calculated from pre-computed static aerodynamic coefficients that were calculated using a fluid structure interaction algorithm. The coefficients were calculated for angles of attack from −15 deg to 4.2 deg

The tether force is calculated using the quasi-static model from [28]. This allows the tether to be modeled with mass, drag, and its full stiffness while allowing a reasonable time step. However, it does neglect elastic vibrations.

The winch is modeled as a single rotating body and has an inertia (J), radius (r), and viscous friction (μ_ω). This is the same model as used in [10]. To ensure that the winch acceleration and velocity remain within bounds, a saturation is applied on the dynamics. The maximum reel-out speed is ±20 m/s^2 and the maximum acceleration is ±5 m/s^2.

The only available airspeed in the 3DOF dynamics is 22 m/s.

C. Control Architecture

The block diagram with the kite controller, winch controller and dynamics is given in Fig. 2, including an indication of the parts that will be changed in this work. As mentioned in Section I, this cascaded control architecture is based on [10–12] and adapted for the MegAWES system. The main adaptation is a simplification of the winch controller [9]. In Section V, this control architecture will be used as a "baseline" to compare the newly obtained results to.

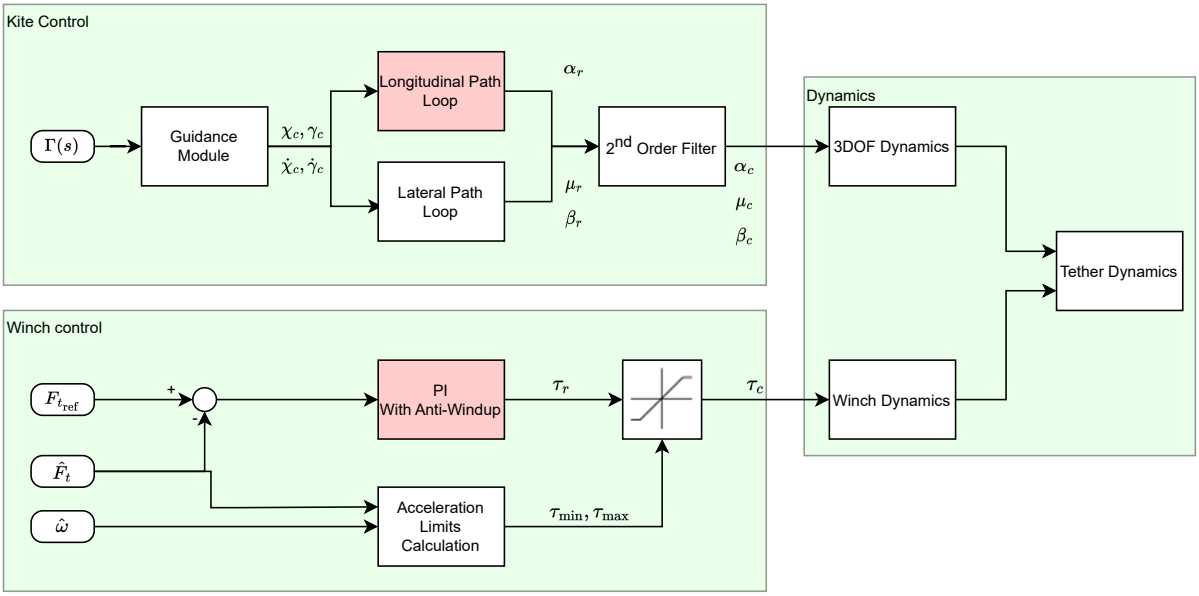

Fig. 2 Block diagram of the traction phase controller for the 3DOF dynamics as proposed by [8, 9] based on [10–12] and will be referred to as "baseline" in Section V. The PI with anti-windup and longitudinal path loop blocks, indicated in red, will be replaced in this work by a feedforward winch controller (discussed in Section III) and the kite tether force controller (developed in Section IV).

The path is described as a continuous figure of eight, by $\Gamma(s)$, with $s \in (0, 2\pi)$ denoting the position in the figure of eight. Based on the current position and velocity of the kite and the position and 'velocity' of the path, the desired course and path angle rates, $\dot{\chi}_{k,c}$ and $\dot{\gamma}_{k,c}$, are calculated.

In the Path Loop, the kite controller assumes that the winch can accurately keep the tether force at the reference value. Since the gravity force is known, the controller solves for the required aerodynamic force. This force can be obtained with a certain bank angle and angle of attack. In the block diagram this is shown as two separate blocks, one for the longitudinal path and one for the lateral path but in the current architecture these two are integrated. In this work, they are separated because only the Longitudinal Path Loop will be changed with the kite tether force controller.

In the 3DOF dynamics, the commanded angle of attack and bank angle are delayed using a second order reference filter. This delay mimics the response delay that would be present in a 6DOF simulation where the inner loop controller uses the control deflectors to follow these commanded values.

The current winch controller uses a tether force reference that is constant for a certain wind speed. A PI controller is used to track the commanded tether force. To ensure that the resulting acceleration is not out of bounds, a dynamic saturation on the winch torque is used. In this work, this winch controller will be changed to a feedforward controller as described in Section III.

The current controllers were tuned using the covariance matrix adaptation evolution strategy (CMA-ES) optimization method. The cost function includes the mean power production and several penalties for unsafe flying behavior.

III. Winch Sizing

In this section, it will be shown that the size of the winch has a substantial effect on the dynamics of the system and its ability to extract power from the wind and avoid a tether force overshoot. The analysis is very general and thus applies to many different system architectures. It can be used to find suitable winch parameters, but does not present an actual mechanical design with these system characteristics.

A. Winch Dynamics and the Winch Control Curve

The winch consists of a drum on which the tether spools and an energy conversion system. The winch is modeled as a single rotating body and has an inertia (J), radius (r), and viscous friction (μ_ω). This is the same winch model as used in [10] and makes the analysis general and applicable for winches using electrical, hydraulic, or mechanical drivetrains, as long as they can be described by these three parameters. Therefore, inertia refers to the inertia of the entire drivetrain. Furthermore, the radius of the winch is assumed to remain constant despite the

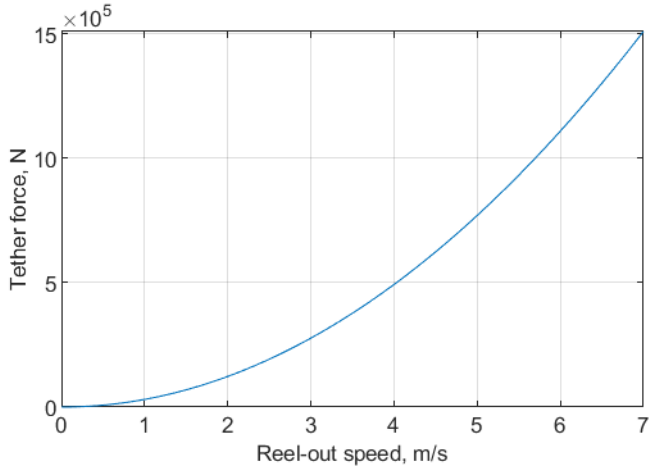

Fig. 3 Winch control curve, showing the optimal (quasi-steady) tether force as a function of reel-out speed for a reel-out factor of 1/3.

spooling of the tether.

There are three moments acting on the winch: the tether force (F_t) multiplied by the radius of the winch, the winch control torque (τ), and the torque resulting from friction.

The tether force is calculated using the quasi-steady model shown in Eq. (2) which was described by [29], and using the convention from [17] for the constant $\mathscr{C}$, which is related to the performance of the kite. ρ denotes the air density, v_w the wind speed, S the reference wing area, C_R the resultant force coefficient, L/D the lift-to-drag ratio, f the reel-out factor, v_r the reel-out speed. A quasi-steady model is assumed to isolate the dynamics of the winch without considering the dynamics of a flying kite. This assumption will be lifted during verification using a 3DOF simulation in Section V.

The winch control torque is used to keep the system at its optimal reel-out factor. A desired reel-out factor of 1/3 is selected, which is the optimal for an infinite traction phase [4]. When considering the reel-out and reel-in phases together, the optimal reel-out factor for the highest mean cycle power is lower than 1/3 [16]. But it then depends on the specifics of the system and would not change the conclusions from this analysis. For a reel-out factor of 1/3, the optimal tether force as a function of reel-out speed can be calculated using Eq. (2) and is shown in Fig. 3. When the winch is keeping the kite in equilibrium at this optimum, the winch control law described by Eq. (3) can be used. This winch control strategy is well established [17, 18]. For a more detailed derivation of this winch control law, the reader is referred to [17].

The friction moment is modeled as a linear function of rotation speed, as is common in literature [10, 18, 30]. The block diagram for this system is shown in Figure 4.

$$\begin{aligned} F_t &= \frac{1}{2}\rho v_w^2 S C_R \left[1 + \left(\frac{L}{D}\right)^2\right](1-f)^2 \\ &= \mathscr{C}(v_w - v_r)^2 \end{aligned} \tag{2}$$

where

$$\mathscr{C} = \frac{1}{2}\rho S C_R \left[1 + \left(\frac{L}{D}\right)^2\right]$$

$$\tau = 4\mathscr{C} v_r^2 r \tag{3}$$

In Eq. (4), the closed-loop equations of motion for the winch are derived that include the tether force, the winch control law, and dynamic friction. ω denotes the rotational speed. The only input to this system is the wind speed.

$$\begin{aligned} \dot{\omega} &= \frac{\sum M}{J} \\ \frac{\dot{v}_r}{r} &= \frac{F_t r - \tau - \mu_\omega \omega}{J} \\ \dot{v}_r &= \frac{\mathscr{C}(v_w - v_r)^2 r^2 - 4\mathscr{C} v_r^2 r^2 - \mu_\omega \omega r}{J} \end{aligned} \tag{4}$$

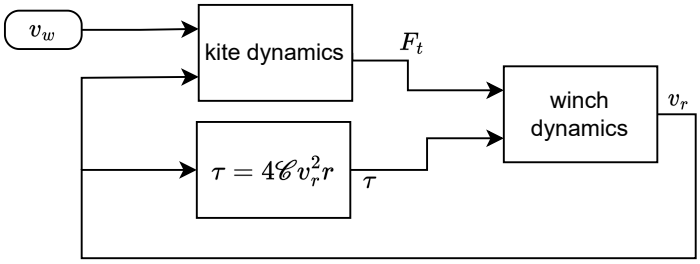

Fig. 4 Block diagram used for the winch sizing analysis.

By using a Taylor series expansion, these closed loop equations of motion are linearized around a trim point where the winch control torque and tether force are in equilibrium. The Laplace transform of these linearised equations is taken, resulting in Eq. (5). The pole location of this system is described by $s = -1/J \cdot (12\mathscr{C}r^2 v_{r_0} + \mu_\omega)$. So the control law described by Eq. (3) results in asymptotic stability of the system for positive values of J, $\mathscr{C}$, r, v_{r_0}, and μ_w, as mentioned in [17]. This also demonstrates the robustness of this control law to parametric uncertainties. Furthermore, it can be seen that an increase in inertia makes the system slower and an increase in radius makes the system faster. Furthermore, the pole location is highly dependent on the trim reel-out speed.

$$\frac{V_r(s)}{V_w(s)} = \frac{4\mathscr{C}r^2 v_{r_0}}{Js + 12\mathscr{C}r^2 v_{r_0} + \mu_\omega} \tag{5}$$

B. Effect on Power Production and Tether Force Overshoot

Besides stability, the bandwidth of the dynamics is important because it influences power production and the tether force overshoot. By multiplying the winch rotational speed by the winch control torque, the power production is calculated. By first linearising the power production, the transfer function from wind speed to power output is derived, as shown in Eq. (6), where P denotes the mechanical output power. Similarly, by linearising the quasi-steady model, a linear equation for tether force can be derived. By substituting the transfer function derived previously (Eq. (5)), the transfer function from wind speed to tether force can be derived and is shown in Eq. (7). This transfer function has a zero at $s = -1/J \cdot (8\mathscr{C}r^2 v_{r_0} + \mu_\omega)$, which is always closer to the origin than the pole (which is at the same location as for $V_r(s)/V_w(s)$). This means that an increase in tether force overshoot is unavoidable above certain input frequencies. This is because the wind has a feedthrough effect on the tether force in this model.

$$\begin{aligned} \frac{P(s)}{V_w(s)} &= 12\mathscr{C}v_{r_0}^2 \frac{V_r(s)}{V_w(s)} \\ &= \frac{48\mathscr{C}^2 r^2 v_{r_0}^3}{Js + 12\mathscr{C}r^2 v_{r_0} + \mu_\omega} \end{aligned} \tag{6}$$

$$\begin{aligned} \frac{F_t(s)}{V_w(s)} &= 2\mathscr{C}(v_{w_0} - v_{r_0})(1 - \frac{V_r(s)}{V_w(s)}) \\ &= \frac{Js + 8\mathscr{C}r^2 v_{r_0} + \mu_\omega}{Js + 12\mathscr{C}r^2 v_{r_0} + \mu_\omega} \end{aligned} \tag{7}$$

Both Eq. (6) and (7) are normalized using the final value theorem. The Bode plot is shown in Fig. 5. The numerical values for the radius (0.4 m) and inertia (32 kgm^2), as proposed by [8, 9] are used and a typical (trim) reel-out speed of 5 m/s (with a corresponding trim windspeed of 15 m/s). From the bode plot it can be seen that at low input frequency (slow changes in windspeed), the magnitude of the normalized tether force and power output are 0 dB. So the tether force is at the ideal tether force and the power is maximized. However, as the change in windspeed increases in frequency, the winch starts to lag, which has two consequences. First, the tether force exceeds the ideal tether force, up to 3.52 dB (50 % overshoot). This makes sense because the winch does not adapt its reel-out speed sufficiently quickly to avoid a sudden increase in tether force due to the feedthrough component. This increases the probability of tether rupture and is thus undesired. However, as discussed before, because the pole is always located closer to the origin than the zero this behavior is unavoidable. Second, the power output drops due to a lag between reel-out speed and tether force. An increase in tether force does not sufficiently quickly result

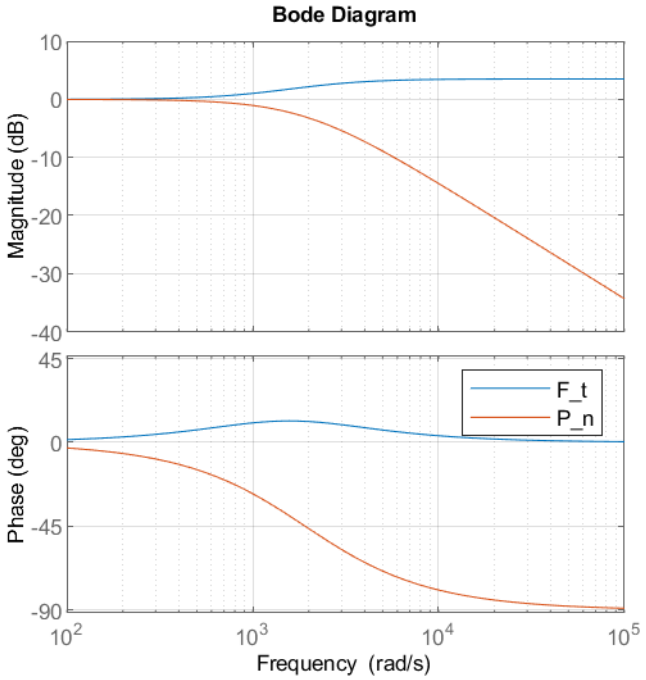

Fig. 5 Bode plot of the normalized tether force and power output.

in a change in reel-out speed. This makes the system unable to stay at the optimum reel-out factor. When operating at suboptimal reel-out factors, less power is produced. Because the pole locations are dependent on the winch parameters, this Bode plot can be shifted left or right depending on system requirements for tether force overshoot and power production at certain frequencies. Since desired power production and low tether force overshoot is achieved at low frequencies, an upper bound on inertia and a lower bound on radius can be selected.

The bandwidth of this winch is 1.92×10^3 rad/s, which is very high. As indicated by [8], the winch parameters had not been scaled up when designing the MegAWES simulation. The reference design for a different 5 MW system by [14] has a radius of 2.0 m and the generator for a wind turbine of similar power has an inertia around the low speed axis of approximately 1×10^7 kgm^2 [31]. So a higher radius and higher inertia would be more realistic and furthermore is less disturbed by noise, resulting in more gentle system dynamics.

C. Winch Sizing Method

Small scale airborne wind energy systems (where the effect of gravity is negligible) and wind turbines need sufficient bandwidth to react to a change in wind speed. Since the wind changes slowly, a high inertia is allowed. However, for ground-gen airborne wind energy systems with mass, the apparent wind speed changes as the kite is flying its figure of eight, due to the effect of gravity. So the bandwidth requirement is higher, meaning that the winch must have a smaller inertia or larger radius.

To find suitable values for the radius and inertia, the magnitude of the transfer function of the normalized tether force and power output at a certain frequency is analyzed. The MegAWES system completes a figure-of-eight roughly once every 40 seconds, so it experiences a change in apparent wind speed every 20 seconds, or at a frequency of 0.05 Hz. A safety factor of 10 is chosen to account for uncertainties such as arising from linearisation and using simplified models. So the tether force increase and power loss at a wind speed input frequency of 0.5 Hz is analyzed. As shown by Eq. (6) and (7), the response is dependent on inertia, radius, friction coefficient, and reel-out trim speed. By neglecting the friction, the inertia and radius can be factored together in a winch sizing constant, defined as $K_w = \frac{J}{r^2}$. The winch sizing constant can be physically interpreted as being equal to the mass of a thin-walled cylinder with radius r and inertia J. By neglecting friction, the pole locations move to the origin thus shifting the Bode plot to the left. This lowers the power output and increases the tether force overshoot at the apparent wind speed frequency. So neglecting friction makes the analysis more conservative. The magnitude of the transfer functions at the apparent wind speed frequency is given by Eq. (8) and (9) for the normalized power output and tether force respectively. Using these equations an upper bound for the winch sizing constant can be selected based on requirements on maximum power loss and maximum tether force overshoot at a certain frequency.

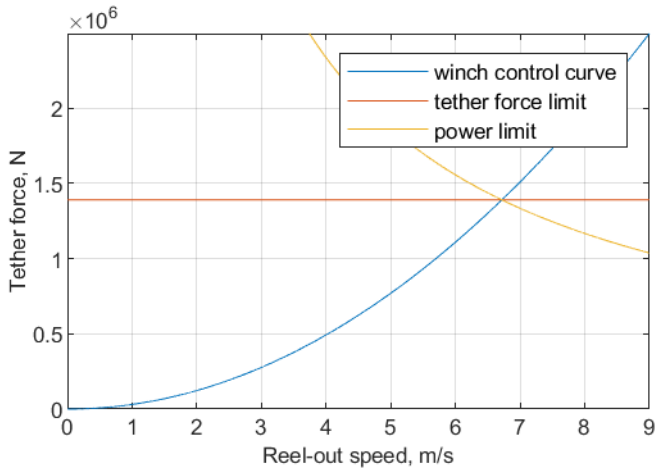

Fig. 6 Winch control curve with a tether force (1.39×10^6 N) and power limit (9.3 MW). It uses the 2-phase strategy [16] because both limits intersect the winch control curve in the same point.

The upper bound on winch sizing constant thus defines a maximum inertia for a given radius or minimum radius for a given inertia and thus leads to a certain minimum bandwidth for the winch. So upscaling of the winch, as recommended by [8], can be achieved with this method where the winch is scaled up to the given upper bound. This will be done in Section V.A.

$$\left|\frac{P_{\text{normalized}}(jw)}{V_w(jw)}\right| = \left|\frac{12\mathscr{C}v_{r_0}}{K_w jw + 12\mathscr{C}v_{r_0}}\right| \tag{8}$$

$$\left|\frac{F_{t_{\text{normalized}}}(jw)}{V_w(jw)}\right| = \left|\frac{3K_w jw + 32\mathscr{C}v_{r_0}}{2K_w jw + 24\mathscr{C}v_{r_0}}\right| \tag{9}$$

IV. Kite Tether Force Control

In this section, the kite tether force control concept will be presented. It is designed to be used in conjunction with the 2-phase strategy [16], but could be adapted by any control architecture that requires the kite to control the tether force. In this work it is designed for the 3DOF dynamics of MegAWES. In the 3DOF dynamics, the angle of attack can be directly changed, in contrast to commanding the elevators in a more realistic scenario. This allows a focus on the core of this architecture, an angle of attack reference controller, but does neglect the details of inner loop design.

A. 2-phase strategy

The optimal winch control curve without limits was previously shown in Fig. 3. The 2-phase strategy defines that the tether force limit and power limit coincide on the winch control curve. For a tether force limit of 1.39×10^6 N, the power limit can be calculated by Eq. (10) and is equal to 9.3 MW. Since some overshoot is expected this is the 'design' power limit. Both are shown together with the winch control curve in Fig. 6. So once the system reaches the point on the winch control curve where both limits are reached, it should stay at that point if the wind speed increases. When using the 2-phase strategy, the kite's control system can infer when the power limit is reached by only measuring the tether force. This assumes that the winch is able to keep the system on the winch control curve and does not deviate from it. So when the kite ensures that the maximum tether force is not exceeded, the system stays at the power limit.

$$P_{\max} = F_{t_{\max}} v_{r_{F_{t_{\max}}}} = F_{t_{\max}} \sqrt{\frac{F_{t_{\max}}}{4\mathscr{C}}} \tag{10}$$

B. Controller design

The objectives of a kite angle of attack controller are threefold. First, when operating below the tether force limit, the kite shall fly at the optimum angle of attack, resulting in an optimal lift-to-drag ratio, resulting in maximum power extraction from the wind. For tethered kites, this is usually the angle of attack close to $C_{L_{\max}}$ because drag

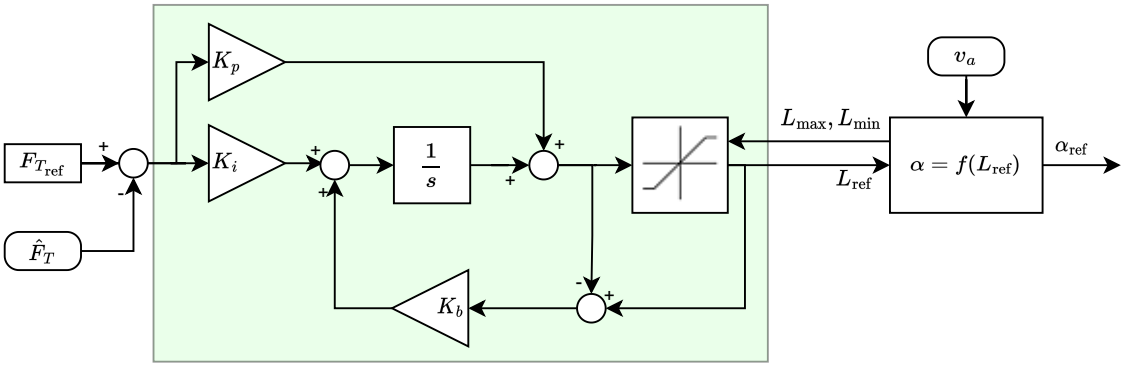

Fig. 7 Block diagram of the kite tether force controller. The part that represents a PI controller with back-calculation is enclosed in mint.

is influenced by the tether drag [32]. Doing this successfully will result in a high mean power. Second, when operating above the tether force limit, the kite must lower its angle of attack such that the system stays at the tether force limit. This shall be achieved with little overshoot above the reference tether force limit. Third, the peak power shall be reduced. This will be achieved as a result from having little tether force overshoot. To achieve this, a kite tether force control concept is designed that uses a PI controller with back-calculation and dynamic inversion to calculate the angle of attack reference. The block diagram for this architecture is shown in Fig. 7.

The first part of the controller outputs a reference lift force for the kite. While for massless kites in quasi-steady flight, the lift force is always in equilibrium with the tether force, heavy systems such as MegAWES must also use part of the lift force to compensate gravity. While extensions to the quasi-steady model exist that incorporate the effect of gravity [29], they still don't capture the effect of inertial forces and require knowledge on the reel-out speed to calculate the ideal lift force. So instead of using a model-based controller that requires measurements which are hard to obtain, a PI controller is used, which is furthermore widely present in industry. The input is the difference between the reference and measured tether force and it outputs a reference lift force that drives the system to the reference tether force. The integrator compensates for effects such as gravity and inertial forces.

In the second part of the controller, the reference lift force is used to calculate the reference angle of attack. This is done using a linear lift curve, shown in Eq. (11).

$$\alpha_{\text{ref}} = \frac{\frac{L_{\text{ref}}}{\frac{1}{2}\rho v_a^2 S} - C_{L_0}}{C_{L_\alpha}} \tag{11}$$

The PI controller uses a constant tether force reference, which is a little below the tether force limit. It needs to be a little below the tether force limit to allow some margin for overshoot. When the system is above this reference, the PI controller will output a lower lift force reference, lowering the angle of attack reference.

But when the system is operating below the tether force limit, the PI controller will increase the lift force reference to drive the angle of attack reference up to its maximum value, as desired. To avoid integrator wind-up and unsafe angle of attack references, back-calculation is used. Back-calculation limits the error going into the integrator, thus limiting the integral control action. It multiplies the difference between the saturated and unsaturated control signal (reference lift force in this case) by the back-calculation coefficient and subtracts it from the signal going into the integrator. By setting $K_b = 1$, the integrator is effectively limited such that the output of the controller always remains within the saturation bounds, thus avoiding integrator wind-up.

The dynamic saturation comes from the minimum and maximum possible lift force that the system can provide, based on (fixed) minimum and maximum allowable angle of attack and the measured airspeed. This could also make the controller robust to wind gust disturbances because a gust would lead to a increase in measured airspeed which immediately lowers the angle of attack reference according to Eq. (11).

This control concept thus only uses a measurement of the tether force and airspeed, which can be obtained using a load sensor and pitot tube in the kite. Furthermore it's only model dependency is the lift curve, which is often known.

C. Tuning

The two gains of the PI controller are tuned by sweeping through a grid of possible values and evaluating the three control objectives for different values in the 3DOF simulation. Both gains are swept from 0 to 2.5 with a

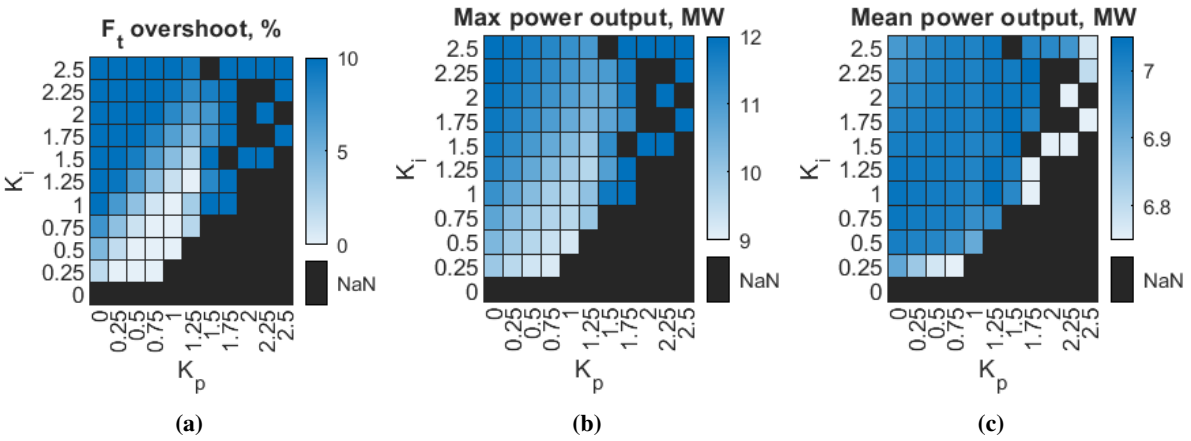

Fig. 8 Tether force overshoot (a), maximum power (b), and mean power (c) during the traction phase for different values of K_p and K_i.

stepsize of 0.25 and the resulting tether force overshoot, maximum power output, and mean power are analyzed. These results are shown in Fig. 8.

Some combinations of gains lead to failures in the 3DOF simulation. These mostly occur during the transition to the traction phase. Since this work does not focus on the retraction phase or transitions between phases, these failed simulations were simply disregarded. In the successful simulations, enough satisfactory responses were found.

In Fig. 8a, the tether force overshoot for both gains is shown. There is a region shown in white and light blue where the tether force overshoot is a couple of percent. This means that the reference tether force can be set closer to the tether force rupture limit, allowing for a higher power extraction.

A low tether force overshoot always coincides with a low peak power, as shown in Fig. 8b. This makes sense because most power is produced at the peak tether force, assuming the winch keeps the system on the winch control curve, which is the case here.

Finally, in Fig. 8c, the mean mechanical output power during the traction phase is shown. Apart from some outliers, most combinations of gains lead to a mean power output of around 7.0 MW. The few outliers are not able to sufficiently quickly increase the angle of attack again when the tether force is low, which results in suboptimal power production.

Doing a qualitative analysis of Fig. 8, gains of 0.75 and 1.0 were selected for K_p and K_i respectively. This combination is not close to a combination that leads to failure, has a lower tether force overshoot, low maximum power, and high mean power, and thus fulfils all control objectives.

V. Results

In this section, the results of the three main contributions of this paper are presented by applying them to the MegAWES simulation framework. In Subsection V.A, new winch parameters are selected. These new parameters allow the use of a feedforward winch controller. Using the feedforward controller combined with the new winch sizing results in a higher minimum power during the traction phase. In Subsection V.B, this architecture is extended with the kite tether force controller which allows the system to limit its peak power output. An overview of the results is given in Subsection V.C.

A. Winch Sizing and Feedforward Winch Control

In this subsection, new winch parameters are proposed for the MegAWES system. This allows the use of a feedforward winch control law, which is implemented based on Eq. (3). This increases the minimum power output and is compared to the baseline, the implementation proposed by [8, 9]. Finally, the effect of a larger winch sizing on the dynamics is shown by selecting a winch sizing constant above the proposed upper bound.

1. Selecting new winch parameters

The normalized power output from Eq. (8), as a fraction from 0 to 1 instead of in dB, for different trim-reel-out speeds and winch sizing constant (J/r^2) is given in Fig. 9a at a frequency of 0.5 Hz. It shows that if the winch sizing constant goes up, the normalized power output goes down, due to the increased lag between reel-out speed and tether force. Furthermore, the normalized power output is better at higher trim reel-out speeds since the system has

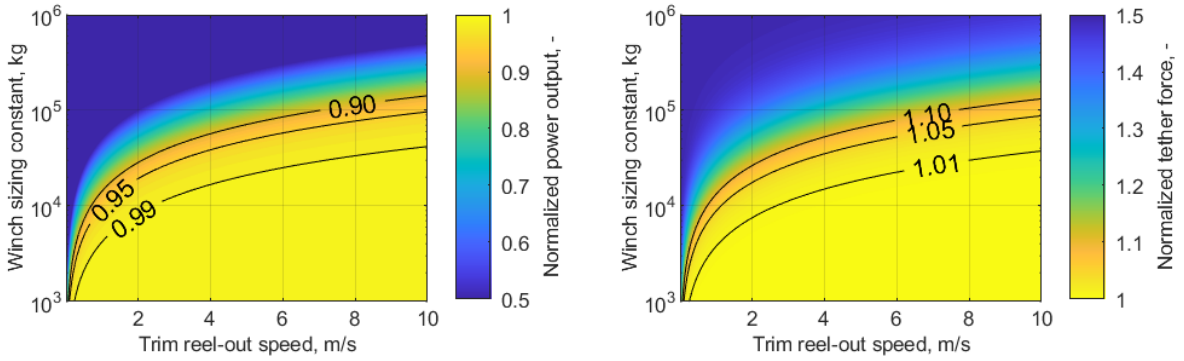

(a) Normalized power output. **(b) Normalized tether force.**

Fig. 9 Normalized system outputs as a function of trim reel-out speed and winch sizing constant ($\frac{J}{r^2}$) when the linearized system is excited at 0.5 Hz.

a higher bandwidth there. That is because the winch control curve (Fig. 3) is steeper at higher reel-out speeds.

Secondly, the normalized tether force from Eq. (9) is shown in Fig. 9b, again for different trim reel-out speeds, winch sizing constants and at a frequency of 0.5 Hz. It shows the overshoot with respect to the ideal steady-state tether force as a fraction. It has a very similar shape as the normalized power output and low trim reel-out speeds or high winch sizing constants lead to a system that is too slow, resulting in tether force overshoot of up to 50 %.

The requirements on power and tether force are set fairly conservative such that the winch can be sized at to the calculated upper bound of the winch sizing constant. The two requirements are: harvest 99 % of the ideal power at a reel-out speed of 1.0 m/s and have a maximum tether force overshoot of 1.0 % at a reel-out speed of 1.0 m/s. For these requirements, the upper bound for winch sizing constant is roughly 4.5×10^3 kg. This can be achieved with a radius of 1.5 m and an inertia of 1.0×10^4 kgm^2. This choice thus results in a system with dynamics that are sufficiently fast to be close to optimal power and have little tether force overshoot.

2. Feedforward Winch Control

The winch controller proposed by [8, 9], based on the work of [10], aims to keep the tether force constant for a given wind speed. So this does not allow the tether force to change as the kite is flying its figure of eight in contrast to the feedforward winch control law described by Eq. (3) and shown in Fig 4. After resizing the winch, this feedforward winch control law is implemented.

The angle of attack of the kite is kept constant at its optimum value, and no power limit is added in this scenario. When there is no power limit, the winch needs to keep the system at the maximum tether force by reeling out faster, in this case above a tether force of 1.390×10^6 N. This reference tether force allows a little bit of overshoot until the same tether force peak as the baseline is reached. When above this tether force, the torque of the winch is constant so if the pull of the kite increases it will start reeling out faster and find an equilibrium again at the specified tether force. The feedforward winch control as shown by Fig 4 is thus adapted as shown in Eq. (12). This method of bounding the torque to avoid tether force overload is also used by [17].

$$\tau = \min(4\mathscr{C} v_r^2 r, 1.390 \times 10^6 \cdot r) \tag{12}$$

All subsequent simulations are performed in the 3DOF simulation of MegAWES at a wind speed of 22 m/s. In Fig. 10a, the mechanical power output during the traction phase using the feedforward winch controller in conjunction with the new winch parameters is compared to a baseline: the winch controller and parameters proposed by [8, 9]. It is shown that the lowest power during the traction phase is no longer negative and went from −4.7 MW to 3.3 MW. This means that when using the feedforward winch control law and new winch parameters the controller does not have to put energy into the system each time the kite is flying upwards (and fighting gravity). The negative peak power in the baseline controller is similar to what was found by the previous 3DOF study of MegAWES [8]. Furthermore, the peak power is slightly higher when the winch has to reel out fast to keep the tether force at its maximum value. Finally, because of the higher winch sizing constant, the power has less high-frequency components and is in general smoother.

This higher minimum power is achieved by the feedforward winch controller by driving the system towards a lower tether force when the reel-out speed is lower. This happens when the kite is flying upwards when it must use more of its lift force to fight gravity instead of pulling on the tether. The tether force over time is shown in Fig. 10b.

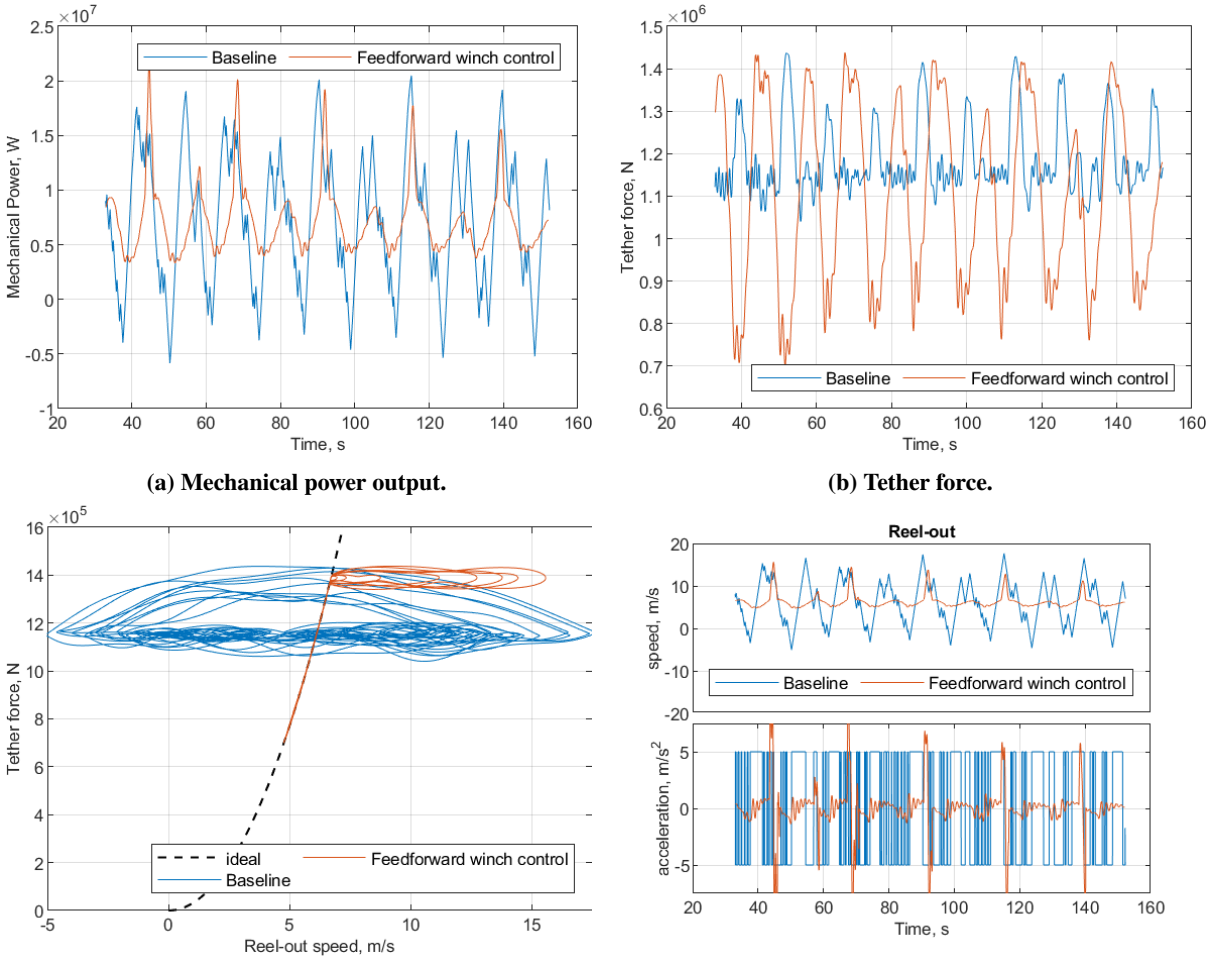

(a) Mechanical power output.

(b) Tether force.

(c) Response on the winch control curve during.

(d) Reel-out speed and acceleration.

Fig. 10 Comparing "Baseline" ([8, 9]) against "Feedforward winch control" (Eq. (12) with $J = 1.0 \times 10^4\,\mathrm{kgm}^2$, $r = 1.5\,\mathrm{m}$) during the traction phase.

It is shown that the tether force peaks are similar at 1.4×10^6 N, meaning both systems stay similarly far away from tether rupture. However, the feedforward winch controller also allows lower tether forces.

How the winch changes the tether force can be observed even better when plotting the response of tether force and reel-out speed on top of the winch control curve, shown in Fig. 10c. Here, the control strategy for the baseline is clearly seen: it aims to keep the tether force constant, as revealed by the horizontal lines. While the feedforward winch controller moves up and down the prescribed curve without much error, it only deviates from it around the maximum allowable tether force.

To keep the tether force constant around its limit, the reel-out speed increases quite a lot as shown in Fig. 10c. To achieve this in a short time period of time, the acceleration of the winch is high. In Fig. 10d, the reel-out speed and reel-out acceleration over time are shown. The baseline acceleration is saturated at $\pm 5\,\mathrm{m/s}^2$, as discussed in Section II and due to the low winch sizing constant, it saturates often which thus results in a reel-out speed with a lot of high-frequency changes, as could be observed in [8, 9]. The feedforward winch controller has a higher maximum acceleration when it is limiting the peak tether force by reeling out faster. Apart from that, the winch acceleration is lower due to the higher winch sizing constant.

3. Larger Winch Size

As predicted by the linear analysis in Section III, the system is able to stay on the winch control curve without lag. To show the effect of lag, the winch inertia is increased by a factor of 100 to $1 \times 10^6\,\mathrm{kgm}^2$. The response on the winch control curve for that is shown in Fig. 11. The response follows the prescribed curve poorly. More importantly, since the winch is not able to sufficiently quickly adapt the reel-out speed, the tether force peaks are a lot higher, which could result in tether rupture. In this scenario, it would also be more difficult to employ the 2-phase strategy and have the kite lower its angle of attack once the tether force limit is reached as the transitions

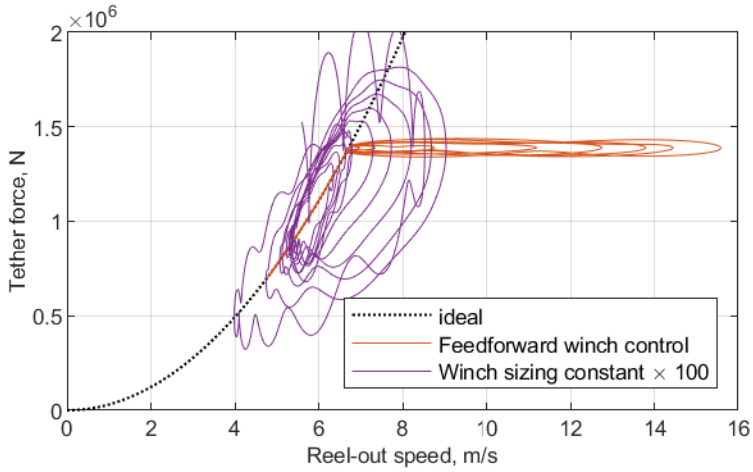

Fig. 11 Response on the winch control curve during the traction phase. Comparing "Feedforward winch control" (Eq. (12) with $J = 1.0 \times 10^4$ kgm^2, $r = 1.5$ m) against "Winch sizing constant $\times$ 100" (Eq. (12) with $J = 1.0 \times 10^6$ kgm^2, $r = 1.5$ m).

are not smooth. Furthermore, since the system deviates from the prescribed winch control curve, it is not operating at the prescribed reel-out factor, thus lowering power production.

B. Kite Tether Force Control

As mentioned in Section IV, once a power limit is reached, the aerodynamic force of the kite must be limited. The kite tether force controller described in Section IV is added to the simulation with a tether force reference of 1.380×10^6 N. This reference tether force allows a little bit of overshoot so that the same actual tether force peak as the baseline is reached. The kite tether force controller always works in conjunction with the feedforward winch controller.

In Fig. 12a, the mechanical power output during the traction phase using the feedforward winch controller is compared to the same winch controller but combined with the kite tether force controller. It is clear that the power peaks have been reduced from about 21.7 MW to 9.8 MW. This is achieved by lowering the angle of attack when the tether force limit is reached. The lowest power is slightly increased from 3.3 MW to 3.5 MW, but most importantly still positive during the entire traction phase.

Since the kite tether force controller is used in conjunction with the feedforward winch control, the tether force follows a similar pattern over time, as shown in Fig. 12b.

It is clear how the kite tether force controller works by looking at the response on the winch control curve, shown in Fig. 12c. While the feedforward winch controller needs to increase the reel-out speed to keep the tether force constant at the tether force limit, the architecture combining the feedforward winch controller with a kite tether force controller only ever operates on the ideal winch control curve. It simply stops progressing further up the line by lowering its angle of attack when the tether force gets too high.

Since the kite keeps the tether force at its limit, the winch does not reel-out faster as previously seen in Fig. 12c and simply keeps the system on the ideal winch control curve. Compared to only using the feedforward winch controller, the kite tether force controller combined with a feedforward winch controller has a lower peak winch acceleration and a smoother reel-out speed as a result, as shown in Fig. 12d.

The angle of attack is shown in Fig. 13. When using only the feedforward winch controller, the angle of attack is always constant at its maximum value. The kite tether force controller also clips at this value, but rather smoothly lowers its angle of attack when needed. It is clear that it lowers its angle of attack twice per figure of eight: each time that it is flying downwards and the tether force gets too high due to the increase in apparent wind speed. Furthermore there are two more observations: there is an asymmetry in the angle of attack when it is flying down in the figure of eight from the right or the left, this correlates with an asymmetry in airspeed and tracking error, which is also present in the baseline. Furthermore the minimum value of the angle of attack goes up over time. This is explained by the fact that the tether drag increases as the kite is reeled out so that a similar tether force is achieved at a higher angle of attack due to the decrease in airspeed. This shows that the kite tether force controller is able to compensate for these changes that would be difficult to precisely model.

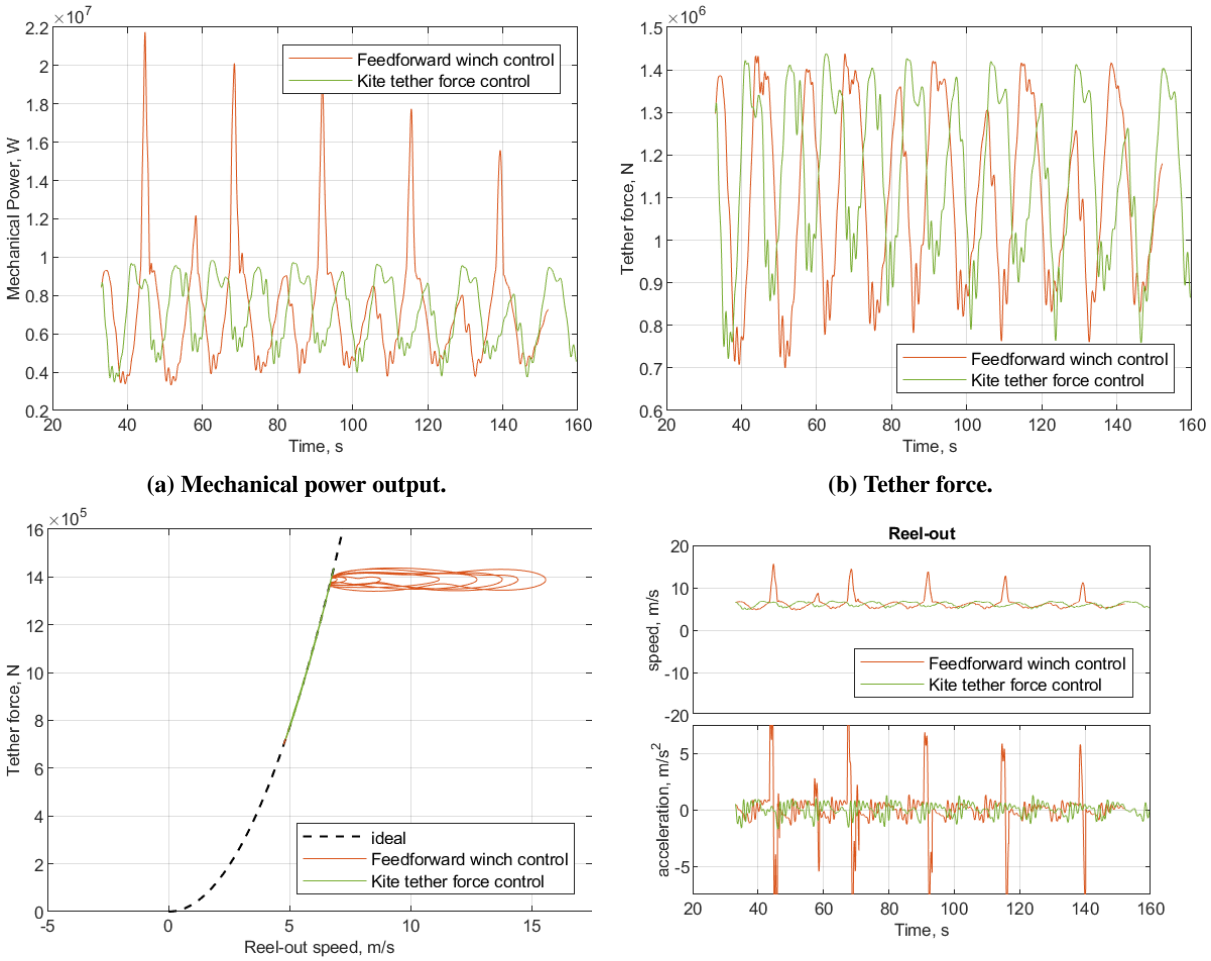

(a) Mechanical power output.

(b) Tether force.

(c) Response on the winch control curve during.

(d) Reel-out speed and acceleration.

Fig. 12 Comparing "Feedforward winch control" (Eq. (12) with $J = 1.0 \times 10^4\,\mathrm{kgm}^2$, $r = 1.5\,\mathrm{m}$) against "Kite tether force control" (with feedforward winch control) during the traction phase.

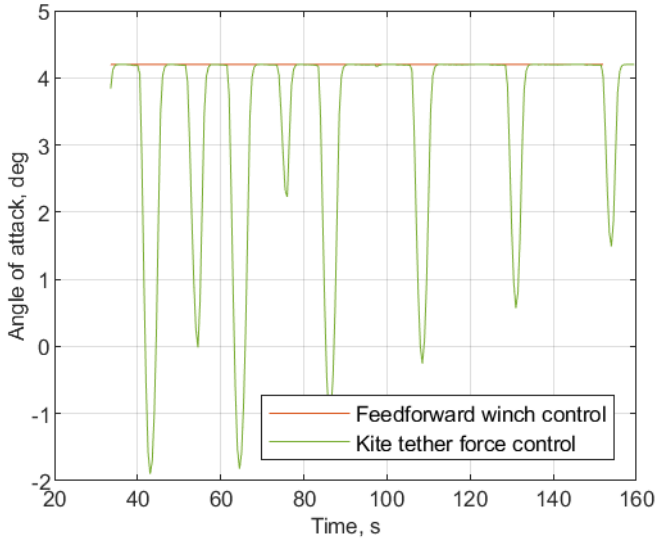

Fig. 13 Angle of attack during the traction phase. Comparing "Feedforward winch control" (Eq. (12) with $J = 1.0 \times 10^4\,\mathrm{kgm}^2$, $r = 1.5\,\mathrm{m}$) against "Kite tether force control" (with feedforward winch control).

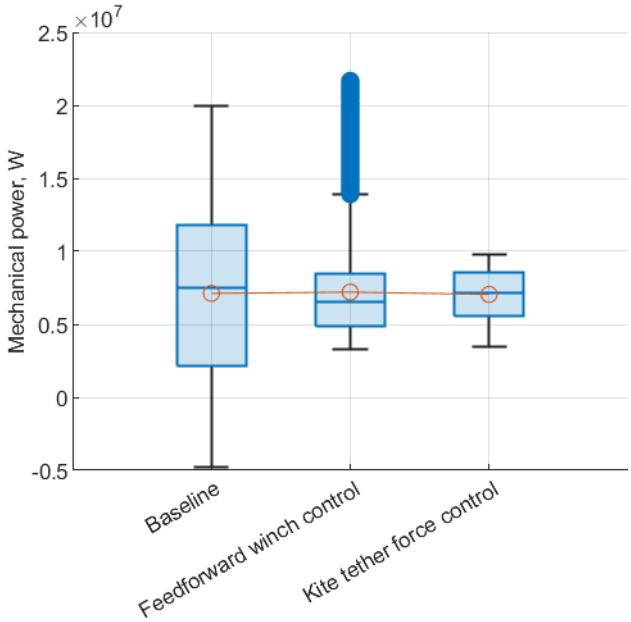

Fig. 14 Power distribution as boxplots during the traction phase. Comparing "Baseline" ([8, 9]), "Feedforward winch control" (Eq. (12) with $J = 1.0 \times 10^4$ kgm^2, $r = 1.5$ m) and "Kite tether force control" (with feedforward winch control). The mean power during the traction phase is shown in red.

C. Overview of results

The distribution of mechanical power output during the traction phase is given in Fig. 14. It shows that the mean power is almost identical for all three strategies: 7.1 MW, 7.2 MW, and 7.0 MW. The feedforward winch control is able to increase the minimum power from −4.7 MW to 3.3 MW. To reduce the peak power, the novel kite tether force controller is used in conjunction with the feedforward winch controller, lowering the peak power from 20.0 MW to 9.8 MW.

VI. Conclusion and Discussion

In this paper, a feedforward winch controller together with a kite tether force control concept are implemented in the MegAWES simulation framework to reduce the power fluctuations during the traction phase. Furthermore, the winch is upscaled to more realistic values for a system of this scale.

The results are obtained from a 3DOF simulation at a wind speed of 22 m/s at a height of 250 m. The feedforward winch controller reduces the minimum power during the traction phase from −4.7 MW to 3.3 MW because it lowers the tether force when the kite is flying upwards. When combining the feedforward winch controller with the kite tether force controller, the the angle of attack is lowered when the power limit is reached. This reduces the power peak from 20.0 MW to 9.8 MW and increases the minimum power slightly to 3.5 MW. Even though the peak power is reduced, the mean power is only reduced by 0.1 MW to 7.0 MW.

There are three major conclusions: First, the winch radius and inertia have a substantial effect on the dynamics of the system and should thus be carefully selected. While the effect of winch sizing on the system dynamics has been hypothesized, to the best of the author's knowledge, this is the first paper explicitly addressing it. Using a frequency domain analysis of the winch dynamics, an upper bound on the winch sizing constant (defined as $\frac{J}{r^2}$) based on power output and tether force overshoot requirements can be set. It is shown that for large airborne wind energy systems, the bandwidth of the winch needs to be sufficiently fast to respond to a change in apparent wind speed due to gravity. If the inertia of the generator is too large or radius too small, the power production is reduced due to lag between reel-out speed and tether force. Furthermore, it leads to a tether force overshoot, potentially resulting in tether rupture. The frequency domain analysis is used to upscale the winch of MegAWES since its parameters were still based on a design of a smaller ground-station. When analyzing the bandwidth at a frequency 10 times higher than the airspeed frequency (due to the patterns flown), and setting a requirement of 99 % of ideal power production and 1 % tether force overshoot, an inertia of 1.0×10^4 kgm^2 and a radius of 1.5 m are selected. Instead of accepting the potential lag between tether force and reeling speed due to the winch sizing, an additional controller to compensate this lag could be added. However, this would come at the expense of additional control effort which increases the power fluctuations. A reference wind turbine with a rated power of 5.0 MW has a

generator inertia around the low speed axis of roughly 1×10^7 kgm^2 [31]. If the same generator is to be used on the MegAWES system, it would require a radius of 47 m to have the same bandwidth as the winch designed in this paper. The requirements of this paper could likely be relaxed as a power fraction of 99 % and tether force overshoot of 1 % at 10 times the tether force frequency of the system is quite stringent. The increase in winch inertia was not compatible with the existing transition-to-traction controller. To study the system over multiple cycles, the winch controller for outside the traction phase will have to be redesigned.

Second, a feedforward winch control law is better suited for large scale systems than a winch control law that keeps the tether force constant. The feedforward winch control law allows a lower tether force when the kite is flying upwards thus not needing to spend energy during the traction phase to keep the tether force constant. This work assumes a winch control curve that is ideal for massless systems with a reel-out factor of $\frac{1}{3}$. However, since large systems need to use some of their lift force to compensate gravity the ideal winch control curve is likely different. So further power optimization in this direction could be done. [33] showed for fly-gen systems how kites with significant mass can trade between kinetic energy and energy extraction to optimally extract power over their entire cycle. An analysis like that has not been performed yet for ground-gen systems. Furthermore, at low wind speeds the feedforward winch control strategy might not work for kites with significant mass because they require the winch to put in a bit of energy to help them overcome gravity when flying upwards. This could be implemented with a minimum tether force, as proposed by [17]. An empirical study towards the optimal feedforward winch control manifold with minimum tether force for fixed-wing systems, like [20] did for soft-wing kites, is an interesting research opportunity. The figures-of-eight flown by the MegAWES kite are outside-up, meaning that the system has to fight gravity when it is also experiencing cosine losses due to the increased azimuth [34]. It should be investigated whether flying outside-down figure of eights could also reduce the power fluctuations.

Third, the kite tether force control concept reduces the peak power at little cost to the mean power. It ensures that the system stays below a certain power limit and thus reduces the requirements on the drivetrain without many drawbacks. Furthermore, the winch reel-out acceleration is smoother and has lower peaks. Compared to optimal control based approaches that dynamically change the angle of attack, this controller uses a measurement of the tether force, airspeed, and angle of attack and an estimate of the lift curve and is thus simpler to implement and doesn't have as much model dependency. In this study, no model and sensor uncertainties or disturbances were considered. Furthermore, even though there was a second order reference model that followed the commanded angle of attack, this strategy should be verified in a 6DOF simulation and at multiple wind speeds. The kite likely needs good control authority on the angle of attack to follow the reference. Alternatively, direct lift surfaces, like flaps, could be used to increase the control authority and bandwidth of the controller that follows the lift reference, like in [35]. At lower wind speeds the kite tether force controller would likely be less active because the system reaches the power limit less often, but might require retuning. Furthermore, the kite tether force controller was used in conjunction with the 2-phase strategy but could also be employed with the 3-phase strategy [22] in the future. In the 3-phase strategy there would need to be a communication between the ground station and the kite since the tether force limit and power limit do not coincide anymore so the kite shall remain at the maximum angle of attack when the tether force limit is reached but not yet the power limit.

VII. Acknowledgments

I would like to thank Nikolaus Vertovec, PhD candidate at Oxford University, for our frequent discussions around our research. Furthermore, I would also like to thank, Sebastian Rapp, control engineer at MBDA Deutschland, for helping me better understand his PhD thesis on robust control for airborne wind energy, Duda Dominic, PhD researcher assistant at RWTH Aachen, for discussing my research ideas, Nicola Rossi, MSc student at University of Trento, for discussing our work on the MegAWES simulation framework, and the Prof v.d. Maas fund of Delft University of Technology for funding me to gather inspiration for my work at the Airborne Wind Energy Conference 2022 in Milan.

References

[1] Jørgensen, B. H., Holttinen, H., IEA Wind Operating Agents, and Charlotte Hede Lindev, *Annual Report 2020*, IEA Wind TCP, 2021.

[2] Archer, C., and Caldeira, K., "Global Assessment of High-Altitude Wind Power," *Energies*, Vol. 2, No. 2, 2009, pp. 307–319. https://doi.org/10.3390/en20200307.

[3] Archer, C. L., "An Introduction to Meteorology for Airborne Wind Energy," *Airborne Wind Energy*, edited by U. Ahrens, M. Diehl, and R. Schmehl, Green Energy and Technology, Springer Berlin Heidelberg, Berlin, Heidelberg, 2013, pp. 81–94. https://doi.org/10.1007/978-3-642-39965-7.

[4] Loyd, M. L., "Crosswind Kite Power (for Large-Scale Wind Power Production)," *Journal of Energy*, Vol. 4, No. 3, 1980, pp. 106–111. https://doi.org/10.2514/3.48021.

[5] Vermillion, C., Cobb, M., Fagiano, L., Leuthold, R., Diehl, M., Smith, R. S., Wood, T. A., Rapp, S., Schmehl, R., Olinger, D., and Demetriou, M., "Electricity in the Air: Insights from Two Decades of Advanced Control Research and Experimental Flight Testing of Airborne Wind Energy Systems," *Annual Reviews in Control*, Vol. 52, 2021, pp. 330–357. https://doi.org/10.1016/j.arcontrol.2021.03.002.

[6] Fagiano, L., Quack, M., Bauer, F., Carnel, L., and Oland, E., "Autonomous Airborne Wind Energy Systems: Accomplishments and Challenges," *Annual Review of Control, Robotics, and Autonomous Systems*, Vol. 5, No. 1, 2022, pp. 603–631. https://doi.org/10.1146/annurev-control-042820-124658.

[7] Schmidt, H., de Vries, G., Renes, R. J., and Schmehl, R., "The Social Acceptance of Airborne Wind Energy: A Literature Review," *Energies*, Vol. 15, No. 4, 2022, p. 1384. https://doi.org/10.3390/en15041384.

[8] Eijkelhof, D., Rapp, S., Fasel, U., Gaunaa, M., and Schmehl, R., "Reference Design and Simulation Framework of a Multi-Megawatt Airborne Wind Energy System," *Journal of Physics: Conference Series*, Vol. 1618, No. 3, 2020. https://doi.org/10.1088/1742-6596/1618/3/032020.

[9] Eijkelhof, D., and Schmehl, R., "Six-Degrees-of-Freedom Simulation Model for Future Multi-Megawatt Airborne Wind Energy Systems," *Renewable Energy*, Vol. 196, 2022, pp. 137–150. https://doi.org/10.1016/j.renene.2022.06.094.

[10] Rapp, S., Schmehl, R., Oland, E., and Haas, T., "Cascaded Pumping Cycle Control for Rigid Wing Airborne Wind Energy Systems," *Journal of Guidance, Control, and Dynamics*, Vol. 42, No. 11, 2019, pp. 2456–2473. https://doi.org/10.2514/1.G004246.

[11] Rapp, S., Schmehl, R., Oland, E., Smidt, S., Haas, T., and Meyers, J., "A Modular Control Architecture for Airborne Wind Energy Systems," *AIAA Scitech 2019 Forum*, American Institute of Aeronautics and Astronautics, San Diego, California, 2019. https://doi.org/10.2514/6.2019-1419.

[12] Rapp, S., "Robust Automatic Pumping Cycle Operation of Airborne Wind Energy Systems," Ph.D. thesis, Delft University of Technology, 2021. https://doi.org/10.4233/UUID:AB2ADF33-EF5D-413C-B403-2CFB4F9B6BAE.

[13] Joshi, R., von Terzi, D., Kruijff, M., and Schmehl, R., "Techno-Economic Analysis of Power Smoothing Solutions for Pumping Airborne Wind Energy Systems," *Journal of Physics: Conference Series*, Vol. 2265, No. 4, 2022, p. 042069. https://doi.org/10.1088/1742-6596/2265/4/042069.

[14] Hagen, L. V., Petrick, K., Wilhelm, S., and Schmehl, R., "Life-Cycle Assessment of a Multi-Megawatt Airborne Wind Energy System," *Energies*, Vol. 16, No. 4, 2023, p. 1750. https://doi.org/10.3390/en16041750.

[15] Bauer, F., Petzold, D., Kennel, R. M., Campagnolo, F., and Schmehl, R., "Control of a Drag Power Kite over the Entire Wind Speed Range," *Journal of Guidance, Control, and Dynamics*, Vol. 42, No. 10, 2019, pp. 2167–2182. https://doi.org/10.2514/1.G004207.

[16] Luchsinger, R. H., "Pumping Cycle Kite Power," *Airborne Wind Energy*, edited by U. Ahrens, M. Diehl, and R. Schmehl, Springer Berlin Heidelberg, Berlin, Heidelberg, 2013, pp. 47–64. https://doi.org/10.1007/978-3-642-39965-7_3.

[17] Zgraggen, A. U., Fagiano, L., and Morari, M., "Automatic Retraction and Full-Cycle Operation for a Class of Airborne Wind Energy Generators," *IEEE Transactions on Control Systems Technology*, Vol. 24, No. 2, 2016, pp. 594–608. https://doi.org/10.1109/TCST.2015.2452230.

[18] Todeschini, D., Fagiano, L., Micheli, C., and Cattano, A., "Control of a Rigid Wing Pumping Airborne Wind Energy System in All Operational Phases," *Control Engineering Practice*, Vol. 111, 2021. https://doi.org/10.1016/j.conengprac.2021.104794.

[19] Erhard, M., and Strauch, H., "Flight Control of Tethered Kites in Autonomous Pumping Cycles for Airborne Wind Energy," *Control Engineering Practice*, Vol. 40, 2015, pp. 13–26. https://doi.org/10.1016/j.conengprac.2015.03.001.

[20] Berra, A., and Fagiano, L., "An Optimal Reeling Control Strategy for Pumping Airborne Wind Energy Systems without Wind Speed Feedback," *2021 European Control Conference (ECC)*, IEEE, Delft, Netherlands, 2021, pp. 1199–1204. https://doi.org/10.23919/ECC54610.2021.9655018.

[21] Njiri, J. G., and Söffker, D., "State-of-the-Art in Wind Turbine Control: Trends and Challenges," *Renewable and Sustainable Energy Reviews*, Vol. 60, 2016, pp. 377–393. https://doi.org/10.1016/j.rser.2016.01.110.

[22] Fechner, U., and Schmehl, R., "Model-Based Efficiency Analysis of Wind Power Conversion by a Pumping Kite Power System," *Airborne Wind Energy*, edited by U. Ahrens, M. Diehl, and R. Schmehl, Springer Berlin Heidelberg, Berlin, Heidelberg, 2013, pp. 249–269. https://doi.org/10.1007/978-3-642-39965-7_14.

[23] Licitra, G., Koenemann, J., Bürger, A., Williams, P., Ruiterkamp, R., and Diehl, M., "Performance Assessment of a Rigid Wing Airborne Wind Energy Pumping System," *Energy*, Vol. 173, 2019, pp. 569–585. https://doi.org/10.1016/j.energy.2019.02.064.

[24] De Schutter, J., Leuthold, R., Bronnenmeyer, T., Paelinck, R., and Diehl, M., "Optimal Control of Stacked Multi-Kite Systems for Utility-Scale Airborne Wind Energy," *2019 IEEE 58th Conference on Decision and Control (CDC)*, IEEE, Nice, France, 2019, pp. 4865–4870. https://doi.org/10.1109/CDC40024.2019.9030026.

[25] Zanon, M., Gros, S., and Diehl, M., "Model Predictive Control of Rigid-Airfoil Airborne Wind Energy Systems," *Airborne Wind Energy*, edited by U. Ahrens, M. Diehl, and R. Schmehl, Green Energy and Technology, Springer Berlin Heidelberg, Berlin, Heidelberg, 2013, pp. 219–234. https://doi.org/10.1007/978-3-642-39965-7.

[26] Li, H., Olinger, D. J., and Demetriou, M. A., "Attitude Tracking Control of an Airborne Wind Energy System," *2015 European Control Conference (ECC)*, IEEE, Linz, Austria, 2015, pp. 1510–1515. https://doi.org/10.1109/ECC.2015.7330752.

[27] Eijkelhof, D., Fasel, U., and Rapp, S., "MegAWES (3DoF & 6DoF Kite Dynamics)," https://github.com/awegroup/MegAWES, 2021.

[28] Williams, P., "Cable Modeling Approximations for Rapid Simulation," *Journal of Guidance, Control, and Dynamics*, Vol. 40, No. 7, 2017, pp. 1779–1788. https://doi.org/10.2514/1.G002354.

[29] van der Vlugt, R., Bley, A., Noom, M., and Schmehl, R., "Quasi-Steady Model of a Pumping Kite Power System," *Renewable Energy*, Vol. 131, 2019, pp. 83–99. https://doi.org/10.1016/j.renene.2018.07.023.

[30] Fechner, U., van der Vlugt, R., Schreuder, E., and Schmehl, R., "Dynamic Model of a Pumping Kite Power System," *Renewable Energy*, Vol. 83, 2015, pp. 705–716. https://doi.org/10.1016/j.renene.2015.04.028.

[31] Elkodama, A., Ismaiel, A., Abdellatif, A., and Shaaban, S., "Modelling and Simulation of an Asynchronous Generator for a 5 MW Wind Turbine," *International Review of Automatic Control (IREACO)*, Vol. 15, No. 5, 2022, p. 233. https://doi.org/10.15866/ireaco.v15i5.22922.

[32] Ruiterkamp, R., and Sieberling, S., "Description and Preliminary Test Results of a Six Degrees of Freedom Rigid Wing Pumping System," *Airborne Wind Energy*, edited by U. Ahrens, M. Diehl, and R. Schmehl, Springer Berlin Heidelberg, Berlin, Heidelberg, 2013, pp. 443–458. https://doi.org/10.1007/978-3-642-39965-7_26.

[33] Trevisi, F., Castro-Fernández, I., Pasquinelli, G., Riboldi, C. E. D., and Croce, A., "Flight Trajectory Optimization of Fly-Gen Airborne Wind Energy Systems through a Harmonic Balance Method," *Wind Energy Science*, Vol. 7, No. 5, 2022, pp. 2039–2058. https://doi.org/10.5194/wes-7-2039-2022.

[34] Diehl, M., "Airborne Wind Energy: Basic Concepts and Physical Foundations," *Airborne Wind Energy*, edited by U. Ahrens, M. Diehl, and R. Schmehl, Green Energy and Technology, Springer Berlin Heidelberg, Berlin, Heidelberg, 2013, pp. 3–22. https://doi.org/10.1007/978-3-642-39965-7.

[35] Lombaerts, T., and Looye, G., "Design and Flight Testing of Nonlinear Autoflight Control Laws Incorporating Direct Lift Control," *Advances in Aerospace Guidance, Navigation and Control*, edited by Q. Chu, B. Mulder, D. Choukroun, E.-J. van Kampen, C. de Visser, and G. Looye, Springer Berlin Heidelberg, Berlin, Heidelberg, 2013. https://doi.org/10.1007/978-3-642-38253-6.

Part III

Literature study

This part has been previously graded under AE4020 (Literature Study).

2

State-of-the-art of airborne wind energy control

The first sub-question for the literature study is:

Research question 1A

What is the state-of-the-art of airborne wind energy control design?

To answer this question the theory of power curves will be discussed in section 2.1. Then, an overview will be given of the general control architecture of airborne wind energy systems in section 2.2. The focus of this work will be flight and winch control systems of which the state-of-the-art will be presented in section 2.3. The chapter is concluded and discussed in section 2.4.

2.1. Power curve

The power produced at a given wind speed is analysed with a power curve. Ideally, a system can convert all wind energy into electric energy. However, it is impossible for any system to extract all kinetic energy from the wind, because wind cannot become stationary after it has passed through the system. For wind turbines, this is called the Betz limit (Betz & Randall, 1966). Furthermore, all systems have physical limitations. For wind turbines this is normally the power rating of the generator. This yields a power curve with two phases: one of maximum power extraction from the wind, and one for suboptimal power extraction to stay at the rated power of the generator. There are two distinct control strategies for these two phases: partial load control and full load control (Njiri & Söffker, 2016).

Using the same two-phase strategy, Luchsinger (2013) made a theoretical power curve for ground-gen airborne wind energy systems, shown in Figure 2.1. In contrast to wind turbines, pumping cycle airborne wind energy systems don't operate in steady-state. Instead, it switches between a power generating (traction) and power consuming (retraction) phase. In addition, the mass of the kite also causes transients in the power output as it makes the kite accelerate and decelerate as it flies loops during the traction phase. So the power curve for airborne wind energy systems describes the average power output for a given wind speed. Luchsinger (2013) analyses the average power output for different fractions of the traction force (F_{out}) and the retraction force (F_{in}), to define the aerodynamic efficiency. In the extreme case, where the force during retraction is infinitely smaller than the generated force during the traction phase, the average power output stays at rated power above the rated wind speed (10 m/s in Figure 2.1). However, if $\frac{F_{\text{out}}}{F_{\text{in}}} < \infty$, the effort to pull the kite back during the retraction phase increases with wind speed and the average power output reduces as the wind speed increases. As shown in Figure 2.1, this effect becomes more negative for lower fractions of $\frac{F_{\text{out}}}{F_{\text{in}}}$.

Note that the power could stay constant above rated wind speed if the tether force was allowed to increase so that the reel-out speed could decrease, making the traction phase longer. However, Luchsinger (2013) assumed that the tether would reach its maximum force at the same time as the system would reach rated power.

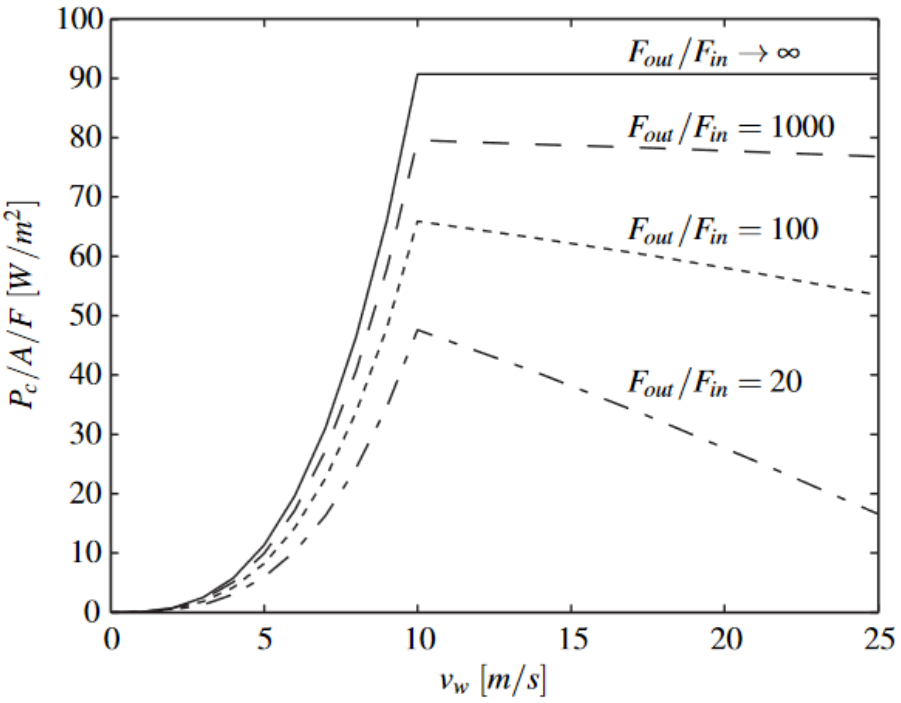

Figure 2.1: The power curve for a power limited airborne wind energy system using the 2-phase strategy with different reel-in reel-out efficiencies (Luchsinger, 2013).

Instead of having the tether force limit coincide with the power limit, for different system designs it could be that the tether force limit and reeling speed limit are reached earlier. Fechner and Schmehl (2013) makes a three-phase strategy for the power curve where the three phases are operated as follows and shown in Figure 2.2:

Region I Maximum energy extraction from the wind.

Region II The tether force limit is reached. To keep it constant at its maximum value the tether must be reeled out faster, which still increases the generated power.

Region III In addition to the tether force limit, the reeling out speed limit is reached.

In the first phase of the 2-phase strategy and the first two phases of the 3-phase strategy the kite is flying in the best aerodynamic configurations at its best lift-to-drag ratio to extract as much energy from the wind as possible. However, in the last phase, the energy extraction must be limited to avoid going over system limits. Fechner and Schmehl (2013) do this by (theoretically) flying the kite at a higher elevation angle (as shown in Figure 2.2), such that the wind speed goes down in the tether-radial direction. A different strategy could be to fly the kite at lower lift-to-drag ratio's by adjusting the angle of attack. There are a lot of publications that optimise the reference angle of attack as a path parameter in offline fashion (Canale, Fagiano, & Milanese, 2010; De Schutter et al., 2019; Echeverri et al., 2020; Licitra et al., 2019; Malz et al., 2020). However, these approaches are sub-optimal when faced with model uncertainties and wind speed measurement uncertainties.

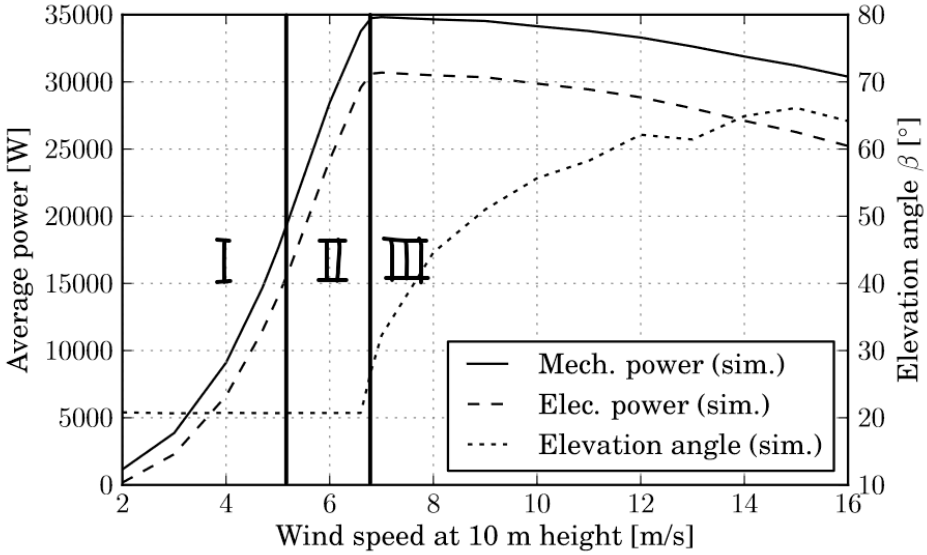

Figure 2.2: The power curve for a tether force and reeling speed limited airborne wind energy system using the 3-phase strategy (Fechner & Schmehl, 2013).

2.2. General control architecture

Autonomous systems typically use hierarchical control architectures with multiple layers that go from a top layer that is responsible for high-level and slow decisions to the lowest layer that executes commands by means of manipulating hardware and senses the environment (Antsaklis, Passino, & Wang, 1991). Such an hierarchical control architecture also applies to airborne wind energy systems (Vermillion et al., 2021). A generic control architecture for fixed-wing, ground-gen airborne wind energy systems is shown in Figure 2.3. This overview and the coming sections focus on the power production phase and thus doesn't include information on for example launching and landing. This block diagram is the author's own work but inspired by different sources (Echeverri et al., 2020; Fagiano et al., 2014; Li et al., 2018; Rapp, Schmehl, Oland, & Haas, 2019; Todeschini et al., 2021). In the following sections, each of these blocks will be elaborated upon. The names of each block correspond as much as possible with existing literature. However, they might differ from certain papers as these names are not used consistently throughout the literature.

Different control architectures than the one shown in Figure 2.3 are possible but the philosophy of optimizing flight paths for power generation and then following those paths is widespread throughout the airborne wind energy community. In section 2.4, alternative control architectures are briefly discussed.

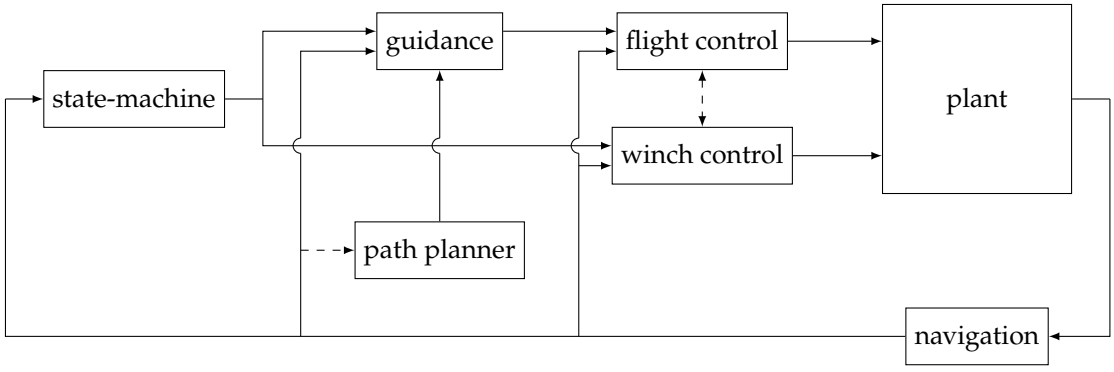

Figure 2.3: Generic control architecture for fixed-wing, ground-gen airborne wind energy systems. Arrows indicate the flow of information and a dotted arrow indicates that this flow only exists in some specific architectures.

2.2.1. State-machine

The state machine, or sometimes called supervisory controller, is responsible for deciding when the system should change its operational phase, based on system and environment state, e.g. wind conditions. For example, it needs to decide when to launch, land, hover, or transition in or our of power production (Ruiterkamp & Sieberling, 2013). This high-level decision is not fully automated yet in most practical settings (Fagiano et al., 2022).

It can also be responsible for switching between the traction and retraction phase, including the transition phases between the two (Rapp, Schmehl, Oland, & Haas, 2019; Todeschini, Fagiano, Micheli, & Cattano, 2019). When a transition occurs can for example be defined based on tether length, the longitude, and the latitude of the system with respect to the ground station (Rapp, Schmehl, Oland, & Haas, 2019).

2.2.2. Path planner

The goal of an airborne wind energy system is to harvest energy but because of the transient flying behaviour it is difficult to directly control for power production. That's why most systems are controlled to follow a certain path and power production comes as a by-product from doing this successfully.

Ground-gen systems require a path for both the traction and retraction phase. The path for the retraction phase is usually just a straight line (Vermillion et al., 2021). But this can get more complex when the feasibility of the retraction path is taken into account (Rapp, Schmehl, Oland, & Haas, 2019).

For the traction phase there are more trade-offs to be made in designing the path and doing this has been a major topic in the airborne wind energy community (Vermillion et al., 2021). There are two different options for path shape: ellipses (sometimes circles specifically) or figures of eight. When flying an ellipse, the kite is always turning in the same direction so the aerodynamics can be optimized to turn a specific direction, the path can also span a smaller azimuth range, thus catching more direct wind, and it is the simplest option. However, this does twist the cable going from the ground station to the kite so it needs a special "detwisting" mechanism (Echeverri et al., 2020), or change the rotation direction in subsequent traction phases. Alternatively, figure of eights can be flown. The outside of the eight can either be taken while going down or when going up, both options are still explored as some think outside-down is better (Erhard & Strauch, 2015) while others think outside-up is better (Bauer et al., 2019). At the moment both ellipses and figures of eight are still pursued by the airborne wind energy community.

In addition to path shape, other variables such as the size, elevation, the altitude of the path, and the angle of attack over the path can also be varied which can have an effect on mean power output, total energy generation, robustness and safety, or other targets (Vermillion et al., 2021).

The easiest way to make a path is by using switching logic. This way a figure of eight can be flown in an effective manner without the need for a mathematical model of the system and it has few tuning parameters (Fagiano et al., 2014). It works with two target points, one of which is active at a given time and will be used as a target for the kite to fly towards. By switching between those two points at appropriate times, a figure of eight will be flown. Though Fagiano et al. (2014) originally developed this for soft wing kites, an extension of this path planner is used for fixed-wing kites by Bauer et al. (2019).

Another option is to use offline optimal control to find an optimal trajectory. Licitra et al. (2019) formulated an optimal control problem with full fixed-wing kite dynamics of the Ampyx Power AP-2 prototype that finds a feasible trajectory that maximizes the average power output of the system. The optimization problem computes the best inputs that lead to an optimal trajectory for power extraction. The final trajectory was then stored in the path planner of a closed loop simulation of the AP-2 prototype which then achieved 90% of the average power of the theoretical optimum. Similar strategies of offline optimization of the trajectory is widely used in literature (Canale et al., 2010; De Schutter et al., 2019; Echeverri et al., 2020; Licitra et al., 2019; Malz et al., 2020).

The last option for path planning is online path optimisation. Offline optimal control problems are heavily dependent on system models. One way around this is to measure the performance of the system in real-time and iterate to a better path over time. M. Cobb, Barton, Fathy, and Vermillion (2019) and M. K. Cobb, Barton, Fathy, and Vermillion (2020) proposes an 'economic' form of iterative learning control that can adjust the path shape for optimal performance. After each loop, the path shape is adjusted to achieve a better power output. This is shown to work well in simulation as it achieves a 35% higher average power output than the initial path. For online path optimisation, the path planner is connected to the navigation block, indicated with a dashed line in Figure 2.3.

2.2.3. Navigation

The navigation module is responsible for estimating the state of the system. For airborne wind energy systems this is quite difficult because of the "nonlinear dynamics, wide speed range, large accelerations, and fast changes of direction" that these systems experience (Fagiano, Huynh, Bamieh, & Khammash, 2013).

Fagiano et al. (2013) tried sensor fusion of GPS measurements with IMU measurements with an extended Kalman filter, which is a common setup for aircraft vehicles. However, this led to poor performance since the GPS has a relatively low accuracy close to the ground and has a low update rate, which were insufficient for the fast dynamics. The other algorithm they tried, using a line angle sensor worked better and has also been used by Polzin, Wood, Hesse, and Smith (2017).

This technique however, uses a straight tether approximation, which is valid for small systems (Fagiano et al., 2013). However, for bigger systems this assumption might be violated, leading to deterioration of the state estimation. However, they expect that since the dynamics of larger systems with higher inertia is lower, GPS could work better again since bigger systems fly farther away from the ground and have slower dynamics.

Other sensors can also be used. Polzin et al. (2017) used a camera that also takes measurements of the kite's position.

2.2.4. Guidance

The guidance module is responsible for guiding the system from its current state, measured by the navigation block, to the desired state as prescribed by the path planner. In this work path planning and guidance are defined as separate blocks but some other authors define the path planning as a part of guidance. Since there an infinite ways to return to a path once the systems has deviated from it, the guidance module must be designed with a trade-off between going back quickly to the path and the control effort required to do so.

When using target points to prescribe the path, Fagiano et al. (2014) proposes to calculate the velocity angle that points towards the new target point and filter this with a 2^{nd}-order Butterworth filter to provide a smooth reference to the inner loop controller.

However, this method does not actively control the angle of attack and angle of sideslip, which can deteriorate the power output of the system. Li et al. (2015a) propose two types of attitude tracking that calculate the required attitude of the kite based on a desired angle of attack and sideslip using knowledge of the wind field which dramatically increases the power output of the system. Their first work focussed on fly-gen systems, but they have extended it to ground-gen systems in Li, Olinger, and Demetriou (2016).

When the path is specified as a continuous line, trajectory tracking or path following can be used. These two methods are very similar but trajectory tracking also specifies an instantaneous point on the path where the system should be at a certain point in time. Path following does not care about the time aspect of the path and rather tries to just stay as close to the path as possible (Aguiar, Hespanha, & Kokotovic, 2005). Most (if not all) airborne wind energy systems utilize path following rather than trajectory tracking.

L1 path following is a popular nonlinear path following guidance logic that calculates the desired centripetal acceleration to move back towards the path based on a certain reference point that is upstream on the path (Park, Deyst, & How, 2004). Fernandes, Vinha, Paiva, and Fontes (2022) simplified its implementation to "L0 guidance" which can be shown to be asymptotically stable. The desired centripetal acceleration can then be used to calculate a reference roll angle for an airborne wind energy system using its mass and lift force.

Makani used a simple model predictive controller to find the desired centripetal acceleration, which was then converted to a roll angle reference. The other attitude degrees of freedom are solved for using a kinematic inversion that uses an estimate of the wind vector and the angle of attack and angle of sideslip commands from the path planner (Echeverri et al., 2020).

In the cascaded control architecture of Rapp, Schmehl, Oland, and Haas (2019), they use PID control on the error between the specified path and current state of the system. They then invert the nonlinear dynamics of a point-mass kite model, using a straight tether approximation, to get the required attitude to follow the pseudo control inputs that come out of the PID controller. Note that Rapp, Schmehl, Oland, and Haas (2019) call this block in their controller the path loop and uses guidance to refer to the module that specifies the ideal path.

2.2.5. Flight control

Once the desired state to get back to the desired path is calculated, the flight control module is responsible for getting the system to the desired state by manipulating the on-board actuators. For fixed-wing, ground-gen systems this usually means manipulating the aileron, elevator, and rudder.

The flight control block is the part of the control architecture where INDI will be applied in this thesis, so specific implementations for the flight control block will be reviewed in much more detail than the other blocks in section 2.3.

2.2.6. Winch control

Winch control is required to control the tether as the kite is launching, landing, or hovering. In addition, ground-gen systems require active winch control during power generation, because that is where the power is generated. It should be robust against disturbances and avoid high tether loads, which could lead to tether rupture, which is one of the worst failure modes for airborne wind energy systems that can occur when the tether force becomes too high (Rapp, Schmehl, Oland, & Haas, 2019; Salma et al., 2020).

Loyd (1980) calculated the reel-out speed that is optimal for power generation to be $\frac{1}{3}$ of the wind speed perpendicular to the kite, when reeling out with an infinite tether. It is a bit lower when considering a full reel-out reel-in cycle (Erhard & Strauch, 2018).

However, since the wind speed is time and space-varying and cannot be accurately measured it cannot be used as feedback signal for the system (Berra & Fagiano, 2021; Erhard & Strauch, 2015; Zgraggen et al., 2016). That's why most power optimal winch control strategies exploit a model to find a link between signals that can be easily measured, such as winch torque or tether force and reel-out speed.

In Zgraggen et al. (2016), the power optimal winch torque is a function of reel-out speed. This is analogous to partial load control (power is below rated power) for wind turbines where the generator torque reference is a function of rotor angular speed (Njiri & Söffker, 2016). The downside of their approach is that it only optimizes power output during the traction phase, which is suboptimal for a complete cycle that includes the retraction phase. That's why Berra and Fagiano (2021) includes both reel-out and reel-in in their optimization and finds optimal reel-out and reel-in speeds based on the tether force for all wind speeds. However, these optimal reeling strategies are all made for soft wing kites, though Berra and Fagiano (2021) plan to extend this strategy for rigid wing kites in the future. Furthermore, extending the analogy to wind turbines, they are optimal for partial load control and thus don't take system limits such as the rated power into account.

In some papers, optimal power production is not the goal, such as in Eijkelhof and Schmehl (2022), Rapp, Schmehl, Oland, and Haas (2019), and Ruiterkamp and Sieberling (2013) where they just want to show robust flying control. So a constant tether force set point is tracked. This strategy is simpler and generally leads to a lower probability for tether rupture and can be preferred when working towards reliability and optimal power production is not the goal.

Since the winch and flying kite are spatially separated, their control is usually done independently of each other, otherwise a safety critical communication link between the two would be necessary (Fagiano et al., 2018; Rapp, Schmehl, Oland, & Haas, 2019; Ruiterkamp & Sieberling, 2013). In these cases each controller assumes the output of the other controller as a disturbance. This can lead to the two controllers fighting against each other so careful control design is required. Aternatively, some simulation implementations combine flight and winch control in the same controller to increase performance (Zanon et al., 2013). This is indicated by a dashed line in Figure 2.3.

A more detailed discussion on flight and winch control implementations can be found in the following sections.

2.3. Detailed flight and winch control overview

In this section different flight and winch controllers from literature will be discussed in detail. They have been grouped into five categories: linear control, model predictive control, nonlinear dynamic inversion, reinforcement learning, and safety augmentations.

2.3.1. Linear controllers

Since linear controllers are extensively used in industry, the linear flight controllers from Makani (Echeverri et al., 2020) and Ampyx Power (Ruiterkamp & Sieberling, 2013; Sören Sieberling, 2013) will be

discussed in detail.

Makani
After Makani's bankruptcy in 2020, they published a three-part report sharing all their knowledge. This includes a detailed account of how their flight controller worked in Echeverri et al. (2020). This flight controller controlled the M600, a 600 kW fixed-wing, fly-gen kite. Even though it is a fly-gen system it is still relevant for ground-gen systems because Makani separated the attitude control from the airspeed (power generating) control.

Control design Makani follows the control philosophy of separating path planning and path following with power generation as a side-effect. A lot of work went into the flight controller because: "After all, precision flying is directly connected to our bottom line—any power lost to drag is power that we can't sell" (Echeverri et al., 2020).

After the guidance block (which Makani refers to as "kinematics"), the error of the angle of attack (α_e), pitch rate (q_e), angle of sideslip (β_e), tether roll angle(φ_{t_e}), yaw rate (r_e), roll rate (p_e) and airspeed (v_{a_e}) together with the gravity and path curvature acceleration are given to the flight controller. It outputs the deflections (relative to the trim condition) of the aileron (δ_a), elevator (δ_e), and rudder (δ_r) and the desired speed of each of the eight motors (Ω_i). An overview of the flight controller is given in Figure 2.4.

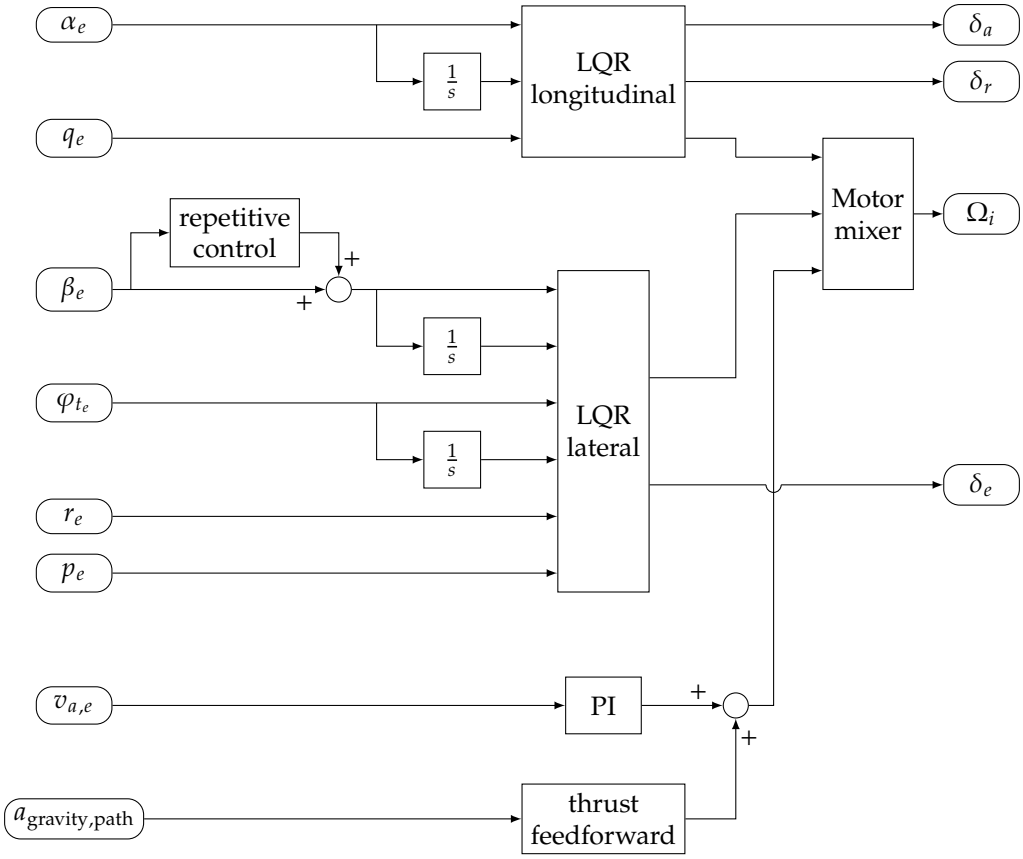

Figure 2.4: Block diagram of Makani's flight controller.

Makani used linear control design so the plant must first be trimmed and linearized. The plant includes a full kite model with aileron, elevator, and rudder, and net motor torques in roll and pitch direction, making the system over-actuated. Actuator dynamics are omitted. Since a kite in crosswind motion is never in steady-state, an artificial trim condition is designed. For this trim condition the kite flying circles in the horizontal plane, with upward wind, and no gravity. This mimics crosswind flight, assuming gravity is a small perturbation. This condition is then solved for three different wind speeds: 5, 10, and 15 m/s, assuming an angle of attack of 8° and a loop radius of 150. For each of these wind

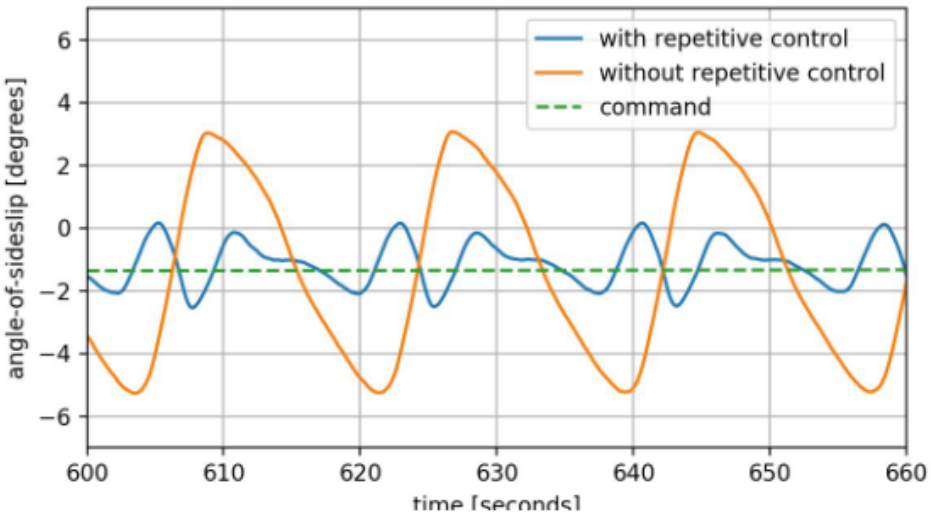

Figure 2.5: Makani's sideslip errors with and without the repetitive controller, in simulation without turbulence (Echeverri, Fricke, Homsy, & Tucker, 2020).

speeds, controller gains are calculated. During the flight, these gains are interpolated using a gain scheduling scheme.

The resulting linear models can be block-diagonalized. Meaning, some of the terms are set to zero to separate longitudinal, lateral, and airspeed dynamics, so that three separate controllers can be used.

For the longitudinal and lateral dynamics, LQR controllers are designed and the airspeed is controlled with a PI controller.

The LQR controllers compute the deflection of aileron, elevator, and rudder, and give an net motor pitch and roll moment in Nm. The net motor commands are then calculated with a control allocation algorithm (referred to as the motor mixer).

Although this flight control architecture achieved stable crosswind flight, the tracking performance was not satisfactory. The errors were very periodic in nature, meaning that each loop the system would have more or less the same errors. This was solved using repetitive control. By adding a sine and cosine wave to the reference sideslip angle with an empirically determined phase offset, the periodic sideslip error could be corrected. As shown in Figure 2.5, this helped eliminate the once-per-loop errors, but not the higher harmonics since they only focussed on the fundamental frequency errors.

Discussion While this controller must have an honourable mention for flying the largest airborne wind energy system to date, it did have its flaws. The power output was lower than expected and the system suffered a few crashes, three out of four were due to loss-of-control. So the team wanted a better path following controller.

The way forward to tighter path following that they saw was a better path and guidance module that proves feasible paths and doesn't just use the commanded path, but also the desired derivatives of said path (like the path planner of Rapp, Schmehl, Oland, and Haas (2019) discussed in section 2.2). The derivatives of the path could then help the flight controller to know where it is going, rather than requiring accumulating error before starting to turn. Another improvement that would lower error accumulation is the use of feedforward control. By using an approximate inverse plant, the controller can reduce the tracking errors.

The airspeed controller was generally satisfactory but couldn't cope well with motor saturation. Similarly to the LQR controllers, it was deemed that a feasible path (airspeed command as function of the loop angle in this case) and better feedforward control were thought to be a way forward from this.

Ampyx Power

While the latest flight controller of Ampyx Power is not public, an earlier version from 2013 was presented in Ruiterkamp and Sieberling (2013) and Sören Sieberling (2013). Based on the time of publishing, it has likely been used to control their fixed-wing, ground-gen AP1 and possibly AP2 prototype. Since

their system was ground-gen, both traction and retraction phase and transitions in between need to be controlled. Since linear controllers are used, these phases all have different trim points and require separate control design.

Control design Ampyx used discrete target points on a figure of eight to specify the path. The guidance module then used a look-ahead-point from the closest position of the path to steer towards with a certain bank angle. Only this reference bank angle was then given to the flight controller. An overview of the controller is given in Figure 2.6. While the dynamics of a kite are quite aggressive and

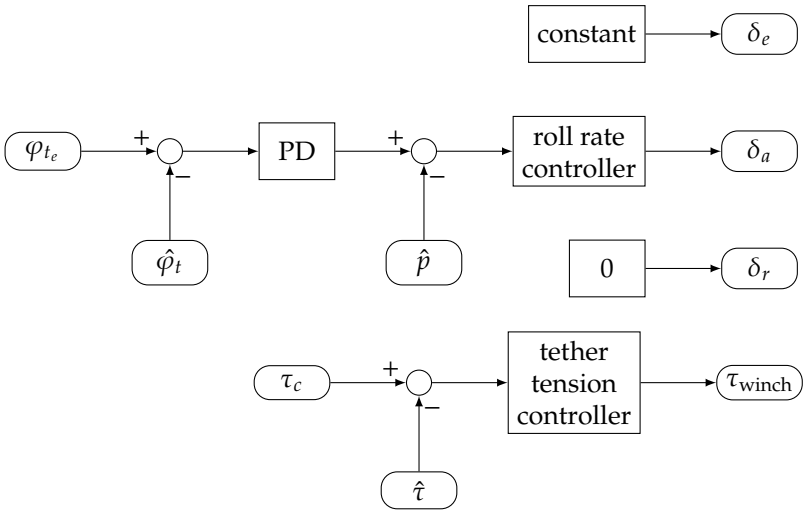

Figure 2.6: Block diagram of Ampyx Power's flight controller during the traction phase.

nonlinear, they become a lot more mild when looking from a coordinate system attached to the tether. Ampyx Power used this to separate the longitudinal and lateral dynamics during control design.

The control objective for the longitudinal dynamics is to fly at a high lift-to-drag ratio to generate maximum power. For a free flying aircraft this would be at a certain angle of attack. However, as shown in Figure 2.7 when the tether drag is taken into account, the highest lift-to-drag ratio is practically achieved at the highest angle of attack of the kite. The challenge is that angle of attack can be controlled

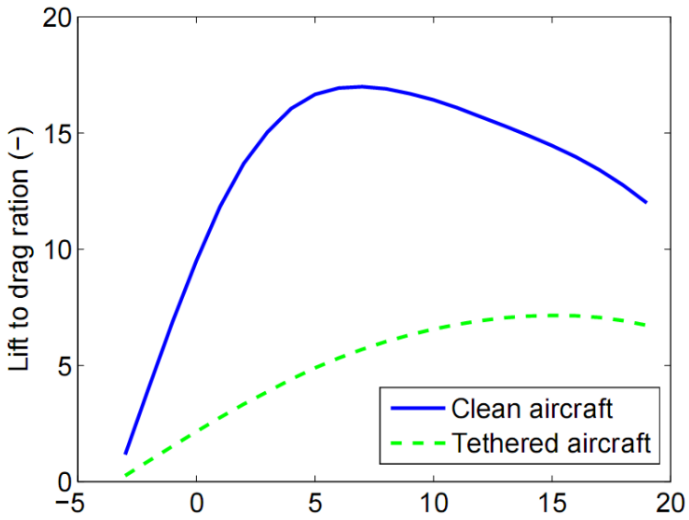

Figure 2.7: The lift to drag ratio (y-axis [-]) per angle of attack (x-axis [°]) of a clean free flying aircraft or tethered aircraft (Sören Sieberling, 2013).

by both the elevators and the reel-out speed, whose actuators are physically separated, making combined control difficult due to the communication delay. That's why Ampyx Power chose to set the elevators to

a fixed value, giving the system a fixed aerodynamic performance and controlling the angle of attack with the reel-out speed of the winch. Since the angle of attack is correlated with the tether force, this was chosen as control variable for the winch control.

Lateral control was done by two simple linear controllers: A PD-controller to set the reference roll rate from a tether roll angle error and a different linear control (the type of which was not specified) to turn the roll rate error into an aileron deflection. The rudder was not used for lateral control and simply set to zero.

At the end of the traction phase there is a short transition to retraction with a fast pitch down manoeuvre of the kite which lowers the tether force. Afterwards the winch will start reeling in the tether at its maximum reeling speed. This will ensure that the retraction phase is as short as possible. A new retraction controller on the kite is activated that follows a certain flight path angle. The transition from retraction to traction is a delicate manoeuvre since the tether force will have to rise in about an order of magnitude without snapping or creating high shock loads. Switching to the traction controller directly is not an option since the transition lies too far from its trim condition. So instead, the control system commands a fixed elevator position and the winch controller controls the winch speed as the tether force rises up to the desired tether force.

Discussion The flight controller was working satisfactory when tuned properly. The angle of attack showed a high correlation to oscillations in reel-out speed and was desired to be more constant.

Because the guidance module uses a look-ahead-point, the kite always steers towards a point in the future of the path, which makes the curves smaller than specified. So even when the path following performance is very consistent, it always cuts the corners. This phenomenon is shown in Figure 2.8.

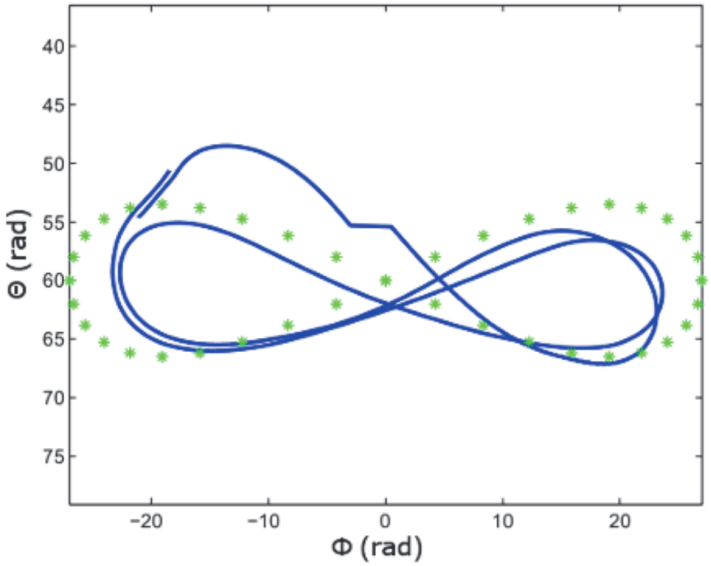

Figure 2.8: Path following performance during a test flight with a wind speed of 7 m/s (Ruiterkamp & Sieberling, 2013).

As previously discussed in subsection 2.2.6, there is a certain optimal reel-out speed optimal for power generation. But since this flight control architecture uses the reel-out speed for longitudinal control, it cannot be used at the same time to set the reel-out speed to its optimum value. So, it should be possible to increase the performance of this controller when the winch controller is allowed to follow the optimum reel-out speed. In addition, if the winch reel-out speed is saturated, the elevators won't be used to reduce the tether force, potentially leading to a tether rupture (Rapp, 2021).

Since Ampyx Power used linear controllers, they required different inner loop controllers for all phases of the flight.

2.3.2. Nonlinear model predictive control

In the airborne wind energy literature, optimal control is often used for performance prediction for studies investigating the potential of this technology (Vermillion et al., 2021). These control strategies

are supposed to be used offline and are not suited for real-time implementation. Examples are Canale et al. (2010), De Schutter et al. (2019), Licitra et al. (2019), and Malz et al. (2020).

A nonlinear optimal control technique that can be used online is nonlinear model predictive control (NMPC). Its use on soft wing kites has been extensively researched (Canale, Fagiano, Ippolito, & Milanese, 2006; Canale et al., 2010; Ilzhöfer, Houska, & Diehl, 2007; Karg & Lucia, 2019) and to a lesser extend on rigid wing kites (Gros, Zanon, & Diehl, 2012; Zanon et al., 2013). A more detailed discussion on one of the implementations of NMPC of rigid wing kites can be found in the following section.

Zanon et al. (2013)
In short, NMPC finds a certain input over time ($u(t)$) that optimises a cost function (J) related to the performance of the vehicle during a certain time horizon (T_C) subject to certain constraints. It effectively simulates the entire system for T_c time and finds the input $u(t)$ that optimizes J while satisfying constraints. This operation is performed at each time step of the system, after which the first input ($u(0)$) is used. While computationally expensive and heavily relying on models, it has been shown to effectively deal with highly nonlinear, constrained, unstable, and fast systems.

In Zanon et al. (2013), the cost function is defined as Equation 2.1, where the pre-computed reference x is defined by the position, velocity, attitude, attitude rate, tether length, reel-out speed, and static deflection of control surfaces, P_c, Q_c, and R_c are weighting matrices and constraints as Equation 2.2. The inputs that the system can control are the control deflections and the tether acceleration ($u = [\frac{\mathrm{d}\delta_a}{\mathrm{d}t}, \frac{\mathrm{d}\delta_e}{\mathrm{d}t}, \frac{\mathrm{d}\delta_r}{\mathrm{d}t}, \ddot{l}]$). This controller thus does not separate the ground station and the flight controls.

$$J = \|x(T_c) - x^r(T_c)\|^2_{P_c} + \int_0^{T_c} \|x(t) - x^r(t)\|^2_{Q_c} + \|u(t) - u^r(t)\|^2_{R_c} \,\mathrm{d}t \tag{2.1}$$

$$\begin{aligned} \dot{x}(t) &= f(x(t), z(t), u(t)) \\ 0 &= g(x(t), z(t), u(t)) \\ q(x(t), z(t), u(t)) &\leq 0, \quad t \in [0, T_c] \\ x(T_c) &\in \mathcal{X}_{t_c} \\ x(0) &= \hat{x}(0) \end{aligned} \tag{2.2}$$

For real-world implementation there are two main hurdles addressed by Zanon et al. (2013): model dependency and computational complexity. NMPC is highly dependent on accurate models of the system (f and g in Equation 2.2) because it needs to simulate the system T_c time into the future (almost 10 s in their case). To obtain an accurate model, an online parameter estimation algorithm was used. They used moving horizon estimation that is also based on optimization. For NMPC to be feasible in a real-time application, efficient optimization solvers need to be used. They use a combination of direct multiple shooting, real-time iteration, and code generation to make it feasible in real-time.

The tracking performance in a turbulent wind field is good as shown in Figure 2.9.

Discussion The controller works well since the moving horizon estimator is able to estimate the model with high accuracy. While realistic standard deviations of the measurements have been used, sensor dynamics (such as lags) have not been taken into account. But in a combined ground station and flight control scheme lags will be inevitable and could be detrimental for performance.

The nonlinear nature of NMPC allows the use of a single inner loop controller for all flight phases. This means that as the guidance module switches between traction and retraction the same NMPC controller can be used.

The real-time performance of this controller was achieved on a 2.8 GHz processor, which still puts high requirements on computational complexity. This requirement for MPC is one of the barriers why it has only been implemented on simplified real-world airborne wind energy setups (Vermillion et al., 2021).

Besides path-following flight control, MPC can also be used to optimize some other metric, such as power production. This could lead to very interesting results for airborne wind energy as real-time power optimization could break the philosophy of first making optimal paths and then flying them. This is already often done (Canale et al., 2010; De Schutter et al., 2019; Licitra et al., 2019; Malz et al., 2020) but is currently unfeasible in real-time.

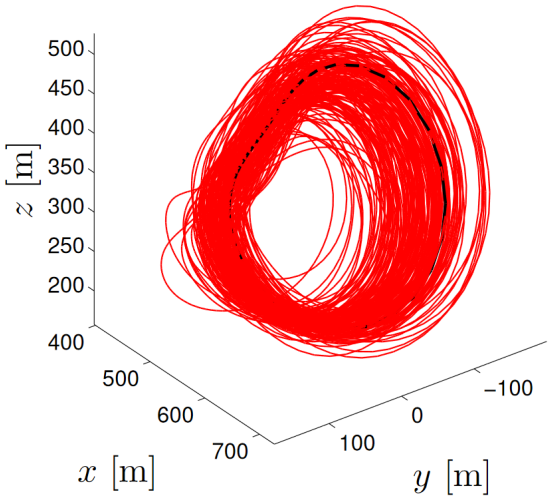

Figure 2.9: Pumping cycle trajectory of a rigid wing airborne wind energy system controlled by an NMPC controller (Zanon, Gros, & Diehl, 2013).

2.3.3. Nonlinear dynamic inversion

Nonlinear Dynamic Inversion (NDI) inverts the system dynamics so that complex, coupled, and nonlinear dynamics become simple n^{th}-order linear dynamics. It has been used for aircraft control (Grondman et al., 2018; Kawaguchi et al., 2011; Moncayo et al., 2012) and has been applied to airborne wind energy as well. Li et al. (2015a, 2016, 2018) use it for attitude control, mainly to verify their attitude tracking theorem that calculates a reference attitude from a target angle of attack and angle of sideslip. However, they don't make use of an aircraft model and instead directly control the external moment on the kite. Rapp, Schmehl, Oland, and Haas (2019) uses an NDI controller in their cascaded control architecture for airborne wind energy systems, which will now be discussed in more detail.

Rapp, Schmehl, Oland, and Haas (2019)

In their cascaded control architecture, the previous cascade calculates a target attitude rate (ω) and attitude acceleration (v_ω). Using Euler's rotation equations, the required moment to achieve that attitude acceleration is shown in Equation 2.3.

$$M = Jv_\omega + \omega \times (J\omega) \tag{2.3}$$

The resulting moment (M) should then be achieved through the aerodynamic moment (M_a) and control moment (M_c). This means that this method required an accurate estimation of the aerodynamic moment.

Through a model of the control effectiveness, the control moment can then be allocated to the control surfaces. Since the control effectiveness is nonlinear and not globally invertible, they actually use an incremental form of the NDI formulation. Note that this is the model-based incremental NDI and not the sensor-based incremental NDI (which will be the subject of chapter 3).

Though it is difficult to say which performance comes from the NDI controller and which one from the upper cascades, their controller works well. The tracking performance in a turbulent wind field is very consistent as shown in Figure 2.10.

The winch controller in this work tracks a reference tether force, which is set to a constant reference value, well below the structural limit of the tether. However, this is not optimal for power generation, as mentioned in subsection 2.2.6, because the tether force should be adapted to the reel-out speed to keep the kite at the optimum reel-out factor. However, it was used in this work since tether force control is better for robustness and avoidance of tether rupture.

Discussion NDI controllers are heavily dependent on good model information since they use both the control effectiveness and the system model to invert the dynamics. The assumption that the aerodynamic moment that is acting on the system is known should be verified with a state estimation algorithm, and the system should be tested to robustness to sensor uncertainties and estimation lags.

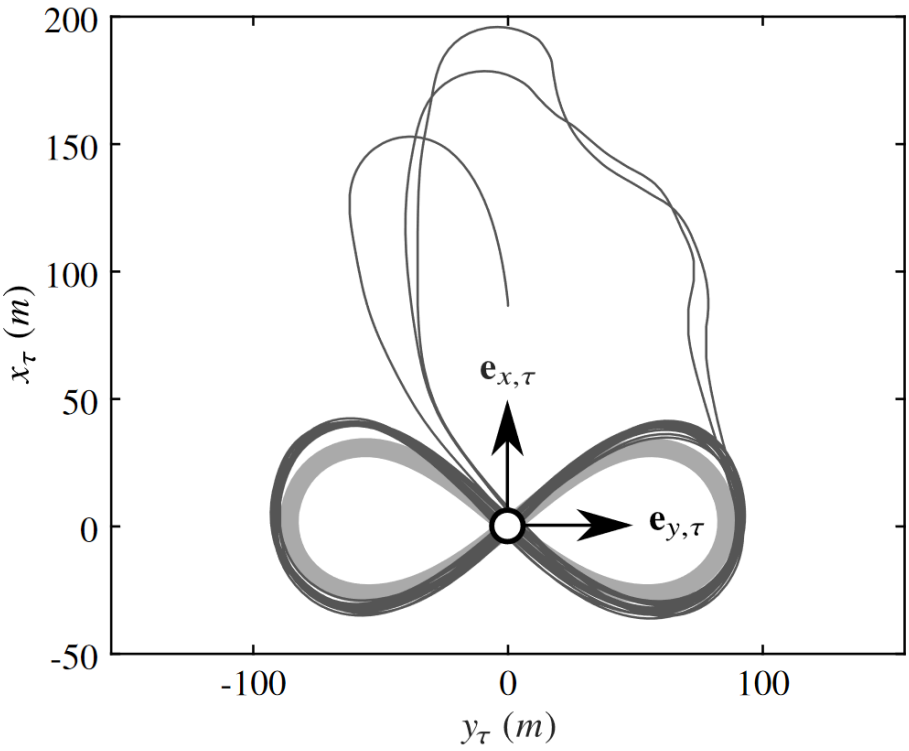

Figure 2.10: Tracking performance in a turbulent wind field projected on the tangential plane using an NDI controller (Rapp, Schmehl, Oland, & Haas, 2019).

Furthermore, it would be good to test this flight control strategy with a power optimal winch control strategy and see how it works in that operating regime.

2.3.4. Reinforcement learning

Reinforcement Learning is one of three basic areas of machine learning besides supervised and unsupervised learning. Compared to supervised learning, where an agent learns based on human-labelled input/output pairs, reinforcement learning trains an agent by giving it rewards for good outcomes rather than good actions. This is a subtle but essential difference that allows the designer to be unaware of what a good action is and only specify what a good outcome is.

This is interesting for airborne wind energy because a reinforcement agent could learn how to get the outcome of power production without the explicit definition by the designer of how the kite should fly.

One published contribution has been made in the airborne wind energy field (Han & Chen, 2022).

Han and Chen (2022)

Their reinforcement learning agent can directly control the roll angle of a soft wing kite. Only the traction phase is considered. It is unclear how the ground station control is performed.

The reward function consists of three parts that aim to maximize produced energy, pull the tether at a steady speed, and prevent the kite from hitting the ground.

Two different reinforcement algorithms were used: Deep Deterministic Policy Gradient (DDPG) and a Proximal Policy Optimization (PPO). Both are model-free (and thus don't require a model of the system to be used by the controller) and make use of the actor-critic framework.

After 5000 episodes of training, both agents had converged their policies and could capture more energy than an MPC controller on the same tasks. The (many) tried flight trajectories together with the average reward over time is shown in Figure 2.11 (Han & Chen, 2022).

Discussion Though the used model is simplified and only the traction phase was considered the application of reinforcement learning to airborne wind energy is interesting because it can also break

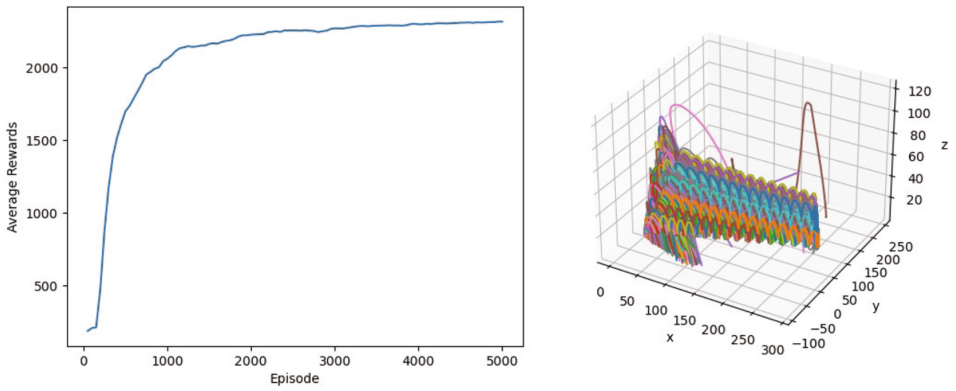

Figure 2.11: Average reward over subsequent training episodes (left) and flight trajectories (right, in (x,y,z) meters from the ground station) of the PPO agent (Han & Chen, 2022).

the philosophy of separating optimal path planning and path following and only focus on optimizing power generation - the ultimate goal of airborne wind energy.

However, the dependency on long training, uncertainty in effectiveness of the agent's simulation training translating to the real-world, and the low amount of reinforcement learning applications to airborne wind energy will be challenges.

2.3.5. Safety augmentations

Sometimes a system might go outside of its safe boundaries. Then, it is important to have a safety net to avoid a system failure, such as tether rupture. One can design special controllers or control modes as a safety net. This is interesting for airborne wind energy because while most controllers focus on performance, the system is unstable and safety augmentations can help improve the safety and reliability of a system.

Fernandes, Silva, Paiva, and Fontes (2018) presents a "gust mode" during which the controller will put the kite in a safe equilibrium position, pointing upwards, and temporarily stopping reel-out and reel-in. This gust mode is activated whenever the wind speed reaches a certain threshold above which it is known that the tether force might exceed limits.

Rapp and Schmehl (2021) present a whole framework for upset condition generation, prediction, and avoidance and applies this to tether rupture due to gusts. Using subset simulation (further discussed in subsection 5.2.2) many situations where tether rupture occurs are generated in simulation. This simulation data is fed into a machine learning algorithm, a support vector machine in this case, that can predict the upset condition. Once the prediction model has been trained, it can be used to trigger an avoidance manoeuvre. In their work, they lower the tether force target as avoidance manoeuvre against tether rupture. Using this technique the operation can continue by simply resetting the force target when the upset condition has passed.

Instead of additional manoeuvres, Vertovec, Ober-Blöbaum, and Margellos (2022) presents a hybrid control law that uses two controllers: an arbitrary performance-based controller and a safety critical controller that is only activated when the system approaches the boundary of where the performance-based controller can safely fly. This both lowers the probability of system failure and allows the performance-based controller to make no concessions in performance that lead to safer control since there is always a backup.

2.4. Conclusion and discussion

From this state-of-the-art review of airborne wind energy control, a few points will be explicitly discussed and concluded upon. Namely: power-optimal control, alternative control architectures, combined flight and winch control, and flight control complexity.

Power-optimal control

Most power-optimal control schemes are heavily model-dependent and solve complex optimization problems and are thus not suited for real-time application. In contrast, simpler control architectures

that use fixed elevators and/or use a winch controller that tracks the tether force are not power optimal.

Simpler control architectures usually neglect the fact that in the last part of the power curve the lift-to-drag ratio of the kite should be suboptimal to stay at system limits. Instead, they reel-out faster, which is a robust and safe strategy but not optimal for power generation.

Alternative control architectures

All control architectures implemented on real systems follow the philosophy of path following an optimized path. Because of disturbances and uncertainties, a precomputed path is no longer optimal, so some research has gone into online optimization of the path. These online optimization algorithms adjust the path once per loop. So still, if a disturbance occurs, such as a gust, that makes the kite deviate from the path, the kite will spent control effort on getting back to the path. It is unclear whether this is the best strategy instead of "riding through" the gust.

Economic MPC or reinforcement learning omits paths altogether and allows the kite to instantly reevaluate the optimal trajectory in case of a disturbance. This is what Makani refers to as "soft" path control and while they didn't experiment with it, it is something they had been thinking about. It allows the kite to not spent unnecessary control effort on following a path that might not be optimal considering the current disturbance on the system.

Combined flight and winch control

Combining flight and winch control can lead to performance and reliability increases. For example, the optimum reel-out speed can only be achieved if the elevators are also used for angle of attack tracking.

However, time lags and connectivity reliability concerns make this integration difficult. So many control architectures separate flight and winch control. This can be done in two ways. First, the control authority over a shared control variable can be artificially set to zero for one of the two controllers. For example, by fixing the elevators. Secondly, the two controllers can both track a certain target and consider the effect of the other controller as a disturbance.

Flight control complexity

For performance analysis complex offline optimal control strategies are used. This is in stark contrast with the linear controllers that were used by Makani and Ampyx Power. It is clear that a performance gain can be realised by using more sophisticated controllers. However, there are some barriers. High model dependency or dependency on complex online model identification can be a significant barrier, especially for small companies. This makes NMPC or NDI difficult to practically use. NMPC furthermore has a high computational requirement. Lastly, reinforcement learning is too undeveloped as flight control method.

Incremental nonlinear dynamic inversion (INDI) could be a good candidate with high performance but a smaller model dependency and computational complexity. The state-of-the-art of INDI will be the topic of chapter 3 and its potential uses for airborne wind energy will be discussed in chapter 4.

3

State-of-the-art of INDI

The second sub-question for the literature study is:

Research question 1B

What is the state-of-the-art of INDI controller design?

To answer this question, the control law is derived for first-order systems and general systems separately after which the implications of the assumptions and results of the derivation are discussed in section 3.1. To analyse the robustness qualities of INDI control, the derivation is extended with regular perturbations (model uncertainties) and singular perturbations (unmodelled dynamics, such as actuator dynamics) in section 3.2. From this, the robustness properties of INDI can be seen. Some design implications (such as synchronization) and further augmentations of INDI to improve its robustness properties are also discussed there. There are also some novel INDI augmentations that aim to broaden its applicability (for example to under or over-actuated systems). These augmentations will be discussed in section 3.3.

3.1. Control law derivation and implications

Around 2000, alternatives to nonlinear dynamic inversion (NDI) called "simplified NDI" (Smith, 1998) and "modified NDI" (Bacon & Ostroff, 2000) were developed that were less dependent on a model in both the qualitative and quantitative sense and used acceleration estimates in their controllers. This technique was further developed and renamed to "incremental NDI (INDI)" by S. Sieberling et al. (2010), and this technique still goes by that name today.

3.1.1. Derivation for first-order systems

Before a more general derivation is shown, a more simple case is derived, inspired from S. Sieberling et al. (2010). This must be seen as an derivation of an INDI control law for first-order systems where the control variables are equal to the state variables ($y = x$). A first-order nonlinear control-affine system is then given by Equation 3.1.

$$\dot{x} = f(x) + G(x)u \tag{3.1}$$

An NDI control law for this system can be designed by inverting Equation 3.3 which yields Equation 3.2. Which linearizes this system to $\dot{x} = \nu$.

$$u = G(x)^{-1}\left(\nu - f(x)\right) \tag{3.2}$$

To instead get to the incremental NDI control law, the first step is to take the first-order Taylor series expansion of Equation 3.1, which yields Equation 3.3. By ignoring the Δx term, a very simple relation could be found. The idea behind this is that $\Delta x \ll \Delta u$ since the state changes much less than the input during a single timestep, assuming that the sampling frequency is high and that the dynamics related

to x are (much) slower than the dynamics related to u. This is referred to as time-scale separation in some literature.

$$\begin{aligned}\dot{x} &\approx \dot{x}_0 + \left.\frac{\partial [f(x) + G(x)u]}{\partial x}\right|_{(x_0,u_0)} \Delta x + \left.\frac{\partial [f(x) + G(x)u]}{\partial u}\right|_{(x_0,u_0)} \Delta u \\ &\approx \dot{x}_0 + G(x_0)\Delta u\end{aligned} \tag{3.3}$$

Inverting Equation 3.3, yields the INDI control law, given by Equation 3.4.

$$\Delta u = G^{-1}(x_0)\,(\nu - \dot{x}_0) \tag{3.4}$$

The final control input to the system is then given by $u = u_0 + \Delta u$. Plugging the control law back into the simplified Taylor series expansion it is clear that under these simplifications the system has been full-state linearized to $\dot{x} = \nu$. This (most) simple linear system can then be controlled with a new linear controller that sets the ν to drive the system to a reference x_r.

Comparing the NDI control law in Equation 3.2 with the INDI control law Equation 3.4, it is clear that INDI does not require an estimate of $f(x)$ and replaces it with an estimate of $\dot{x}_0$. Furthermore, the sampling frequency must be high to fulfil the time-scale separation assumption. Under these conditions the system can be feedback linearized.

3.1.2. General derivation

This derivation follows the work by Xuerui Wang, van Kampen, Chu, and Lu (2019) and will work towards a feedback-linearized system. It is more mathematically rigorous than the derivation presented in the previous section. Furthermore, it will be shown that the feedback-linearization case can be easily extended to output tracking.

Feedback linearization

Using Assumption 1, a multi-input, multi-output system is given by Equation 3.5. It is possible to drop this assumption and design an INDI controller for a non control-affine system (Matamoros & de Visser, 2018). However, a mathematically rigorous derivation was not found in the literature. In section 3.3 a control allocation method for non control-affine systems will be discussed.

Assumption 1 *Assume the system is control-affine.*

$$\begin{aligned}\dot{x} &= f(x) + G(x)u \\ y &= h(x)\end{aligned} \tag{3.5}$$

Where Assumption 2 and Assumption 3 hold. For over-actuated and under-actuated systems, INDI can still be used with some adaptations as will be discussed later in section 3.3.

Assumption 2 *f: $\mathbb{R}^n \to \mathbb{R}^n$ and h: $\mathbb{R}^n \to \mathbb{R}^p$ are smooth vector fields and G: $\mathbb{R}^n \to \mathbb{R}^{n\times m}$ is smooth function mapping, whose columns are smooth vector fields.*

Assumption 3 *$p = m$, meaning the system is not under-actuated nor over-actuated.*

Then, sequential derivatives of the output equation in Equation 3.5 must be taken, until the input u shows up in the equation. The first iteration is shown in Equation 3.6. In the last step, the notation is simplified by using Lie derivatives.

$$\begin{aligned}\dot{y} &= \frac{\mathrm{d}}{\mathrm{d}t}h(x) \\ &= \frac{\partial}{\partial x}h(x)\frac{\mathrm{d}x}{\mathrm{d}t} \\ &= \frac{\partial}{\partial x}h(x)\,(f(x) + G(x)u) \\ &= \frac{\partial}{\partial x}h(x)f(x) + \frac{\partial}{\partial x}h(x)G(x)u \\ &= \mathcal{L}_f h(x) + \mathcal{L}_g h(x)u\end{aligned} \tag{3.6}$$

It seems as if u has already appeared in this equation, but $\mathcal{L}_g h(x)$ is only nonzero for systems with a relative degree of 1. The number of differentiations before a nonzero product with u appears is defined as the relative degree ρ_i of each output element. The vector relative degree then consists of m elements whose sum is defined as the system's relative degree ρ.

Using Assumption 4, the derivation from now on can be greatly simplified. A derivation that splits the state equation into internal and external dynamics is possible, but doesn't result in a different control law and is thus mainly interesting for a stability and robustness analysis for systems with internal dynamics, as done by Xuerui Wang, van Kampen, et al. (2019). In reality, all systems have some form of internal dynamics (e.g. flexible structures) and these must be stable because they can not be directly controlled by INDI. An extension to INDI exists that also stabilizes the internal dynamics. This augmentation will be discussed in section 3.3.

Assumption 4 *$n = \rho$, meaning there are no internal dynamics.*

After taking the derivative of y ρ times (denoted by $y^{(\rho)}$), the system can be rewritten into Equation 3.7. Where $\mathcal{L}^k$ is used to denote Lie derivatives of the k^{th} order.

$$\begin{aligned} y^{(\rho)} &= \alpha(x) + \mathcal{B}(x)u \\ &\text{Where} \\ \alpha(x) &= \mathcal{L}_f^{\rho} h(x) \\ \mathcal{B}(x) &= \mathcal{L}_g \mathcal{L}_f^{\rho} h(x) \end{aligned} \tag{3.7}$$

Equation 3.7 shows a direct relation between the output y and the input u. This equation can be inverted to arrive at an NDI formulation shown in Equation 3.8, where ν is the virtual input of the system. Using this as a control law, the system has been feedback linearized with NDI to $y^{(\rho)} = \nu$.

$$u = \mathcal{B}(x)^{-1}\left(\nu - \alpha(x)\right) \tag{3.8}$$

To instead arrive at the INDI control law, a first-order Taylor series expansion of Equation 3.7 is taken, as shown in Equation 3.9.

$$\begin{aligned} y^{(\rho)} &= \alpha(x) + \mathcal{B}(x)u \\ &= y_0^{(\rho)} + \left.\frac{\partial\left[\alpha(x) + \mathcal{B}(x)u\right]}{\partial x}\right|_{(x_0,u_0)} \Delta x + \left.\frac{\partial\left[\alpha(x) + \mathcal{B}(x)u\right]}{\partial u}\right|_{(x_0,u_0)} \Delta u + O(\Delta x^2, \Delta u^2, \Delta x \Delta u) \end{aligned} \tag{3.9}$$

By realizing that $O(\Delta u^2, \Delta x \Delta u) = 0$ since the system is control-affine and lumping the second and last term together in δ, the equation can be rewritten to Equation 3.10.

$$\begin{aligned} y^{(\rho)} &= y_0^{(\rho)} + \mathcal{B}(x_0)\Delta u + \delta(z, \Delta t) \\ &\text{Where} \\ \delta(z, \Delta t) &= \left[\left.\frac{\partial\left[\alpha(x)\mathcal{B}(x)u\right]}{\partial x}\right|_{(x_0,u_0)} \Delta x + O(\Delta x^2)\right]\Bigg|_{x=T^{-1}(z)} \end{aligned} \tag{3.10}$$

Using Assumption 5, the final INDI control law can be derived from Equation 3.10 and is shown in Equation 3.11. In the case that Assumption 5 does not hold and $\mathcal{B}(x_0)$ is not invertible, augmentations exist that will be discussed in section 3.3. With the control law shown in Equation 3.11, the system simplifies to $y^{(\rho)} = \nu + \delta(z, \Delta t)$. So the INDI controller doesn't quite linearize the system, but the remainder $\delta(z, \Delta t)$ can be made arbitrarily small by increasing sampling frequency of the controller.

Assumption 5 *$\mathcal{B}(x_0)$ is invertible.*

$$\Delta u = \mathcal{B}^{-1}(x_0)(\nu - y_0^{(\rho)}) \tag{3.11}$$

Output tracking

If the goal of the controller is not just to feedback linearize the system, but to track a reference signal r with y, the INDI control law can be slightly adjusted for output tracking as shown by Xuerui Wang, van Kampen, et al. (2019). In that case the control law is given by Equation 3.12.

$$\Delta u = \mathcal{B}^{-1}(x_0)(\nu - y_0^{(\rho)} + r^{(\rho)}) \tag{3.12}$$

Block diagram

Since the system has been feedback linearized to approximately $y^{(\rho)} = \nu + r^{(\rho)}$ a linear controller (LC) can be easily designed to set ν to drive the system to y_{ref}, for example using pole placement, LQR, or other PID tuning methods. A block diagram with the INDI control law, a linear controller and a feedforward signal is shown in Figure 3.1.

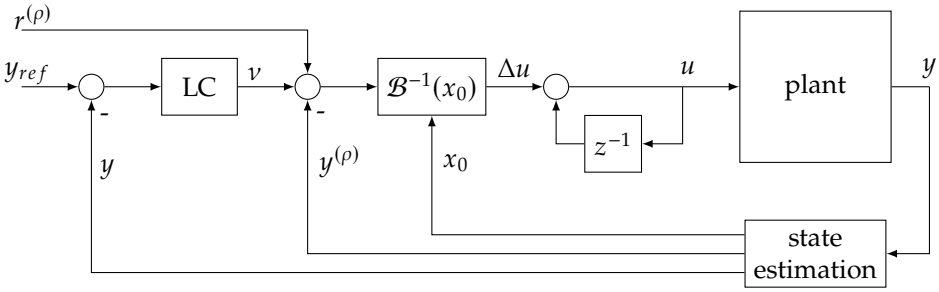

Figure 3.1: A simple INDI block diagram with linear controller controlling ν.

3.1.3. Implications from the derivation

The conclusions from this derivation are the same as for the first one, albeit that given its mathematical rigour, the result is more complete. The INDI controller can approximate feedback linearization when using a high sampling frequency and no longer requires a model of $\alpha(x)$ but instead needs an estimate of $y_0^{(\rho)}$.

Feedback linearization

Nonlinear feedback linearization controllers are useful because they are an alternative to the time-consuming divide-and-conquer approach. With divide-and-conquer, a nonlinear system is split up around different trim points for which linear controllers are designed. The gains of these linear controllers are then interpolated to act on the current operating point of a system using gain-scheduling. Using feedback linearization, a controller is designed that linearizes the system around an entire nonlinear operating regime. Single linear outer-loop controllers can then be designed to control the system.

Since INDI tries to increment the actuators at each timestep with Δu to compensate the error in $y_0^{(\rho)}$, the controller is quite aggressive. This makes it a high-performance controller but the high frequency signals to the actuators can also cause extra wear (Grondman et al., 2018).

Sampling frequency

When Grondman et al. (2018) flew a Cessna Citation II with an INDI controller, they used $f_s = 100$ Hz, which was enough. However, applications with faster dynamics will require a higher sampling frequency to achieve the same ultimate error bounds (Xuerui Wang, van Kampen, et al., 2019). So when X. Wang, Van Kampen, Chu, and De Breuker (2019), used an augmentation of INDI to explicitly control the structural vibrations of a flexible aircraft wing for gust load alleviation, they used $f_s = 1000$ Hz, this augmentation will be further discussed in section 3.3. Lower sampling frequencies are also possible as shown by Acquatella, Van Kampen, and Chu (2022), who used an INDI controller running as low as 1 Hz for spacecraft attitude control. This was possible due to their new sampled-data reformulation of INDI that is useful at low sampling rate applications.

Lower model dependency

Since $\alpha(x)$ is the largest part of the aerodynamic model, a large part of the model dependence of this controller has disappeared (S. Sieberling et al., 2010). This means that inevitable uncertainties in such a model can no longer affect the controller.

Estimation of $y_0^{(\rho)}$

INDI is a sensor-based controller and thus relies heavily on good state estimation. There are three options to get an estimate of $y_0^{(\rho)}$: direct measurements, numerical derivatives, and models.

Direct measurement of the output derivatives ($y_0^{(\rho)}$) is possible when such a sensor exists. For attitude rate control with INDI, this means measuring the angular acceleration. Cakiroglu, Van Kampen, and Chu (2018) used a novel angular acceleration sensor to measure the output derivative directly and feed it back to the INDI controller. However, angular accelerometers are not yet widely used.

Instead, gyroscopes are widely used to measure angular velocity. This can then be numerically differentiated to obtain the angular acceleration. Numerical differentiation greatly amplifies noise in the signal so filtering of the differentiated signal is required. This technique is most widely used, for example by Grondman et al. (2018), S. Sieberling et al. (2010), and van 't Veld, Van Kampen, and Chu (2018).

A final option is to reintroduce model information to estimate the output derivatives. When one solely relies on a model, it is basically the same as NDI. But Kumtepe, Pollack, and Van Kampen (2022) showed that sensor information and model information can be fused using a complementary filter to get an estimate of the output derivatives, this augmentation will be further discussed in section 3.2.

3.2. Robust performance analysis

INDI has excellent robustness properties. To show this, a derivation with regular and singular perturbations in the system equations will be presented. Regular perturbations are model uncertainties. This is indicated by substituting $\alpha(x) = \hat{\alpha}(x) + \xi$ and $\mathcal{B} = \hat{\mathcal{B}} + \Xi$, following the convention of Pollack and van Kampen (2022). These additional terms indicate that there are parts of the dynamics ($\xi(x)$ and $\Xi(x)$) that are unknown to the controller. They are, for example, slight deviations in aerodynamic coefficients. By definition, regular perturbations do not change the order of the system (Pollack & van Kampen, 2022). Singular perturbations are perturbations that increase the order of the system (Xuerui Wang, van Kampen, et al., 2019), such as actuator dynamics or signal lags. In the following derivation, singular perturbations on u_0 and $y_0^{(\rho)}$ are explicitly taken into account. This is indicated with $u_0 = (I + \Delta_1)u$ and $y_0^{(\rho)} = (I + \Delta_2)y^{(\rho)}$, with Δ_i representing smooth, causal mappings, again following the convention of Pollack and van Kampen (2022). This choice is made as these particular singular perturbations are known to cause issues with INDI controller design because of the synchronization effect (Pollack & van Kampen, 2022), which will be explained after the derivation.

3.2.1. Derivation with regular and singular perturbations

This derivation towards an explicit equation for the closed-loop dynamics follows the work of Pollack and van Kampen (2022).

With explicit regular perturbations, the system described by Equation 3.7 can be rewritten into Equation 3.13.

$$y^{(\rho)} = [\hat{\alpha}(x) + \xi(x)] + \left[\hat{\mathcal{B}} + \Xi(x)\right] u \tag{3.13}$$

Furthermore, introducing the singular perturbations (Δ_1 and Δ_2) on u_0 and $y_0^{(\rho)}$, to reflect imperfect and/or delayed measurements, the INDI control law is shown in Equation 3.14. Equation 3.13 can be rewritten to Equation 3.15 and substituted in Equation 3.14, this can then be simplified to arrive at the closed loop system dynamics. This derivation is shown in Equation 3.16, where in the last step of the derivation $\nu = \nu - \mathcal{D}(x, \Delta_1)\nu + \mathcal{D}(x, \Delta_1)\nu - \Delta_2\nu + \Delta_2\nu$ is used.

$$u = (I + \Delta_1)u + \hat{\mathcal{B}}^{-1}(x)\left[\nu - (I + \Delta_2)y^{(\rho)}\right] \tag{3.14}$$

$$u = \left(\hat{\mathcal{B}} + \Xi(x)\right)^{-1}\left(y^{(\rho)} - [\hat{\alpha}(x) + \xi(x)]\right) \tag{3.15}$$

3.2.2. Implications from the derivation

$\epsilon_{INDI} = 0$ if the regular perturbations and singular perturbations are set to zero and the sampling rate is infinitely high. Which is expected as then perfect feedback linearization occurs, as was first shown in subsection 3.1.2.

Furthermore, the robustness to model uncertainties and an analysis of the synchronization effect can now be directly seen from Equation 3.16. Another robustness quality of INDI is disturbance rejection which will also be discussed.

$$
\begin{aligned}
\left(\hat{\mathcal{B}}(x)+\Xi(x)\right)^{-1}\left(y^{(\rho)}-[\hat{\alpha}(x)+\xi(x)]\right) &= (I+\Delta_1)\left(\hat{\mathcal{B}}(x)+\Xi(x)\right)^{-1} \\
&\quad\cdot\left(y^{(\rho)}-[\hat{\alpha}(x)+\xi(x)]\right) \\
&\quad+\hat{\mathcal{B}}^{-1}(x)\left[\nu-(I+\Delta_2)y^{(\rho)}\right] \\
\left[-\Delta_1\left(\hat{\mathcal{B}}(x)+\Xi(x)\right)^{-1}+\hat{\mathcal{B}}(x)\left(1+\Delta_2\right)\right]y^{(\rho)} &= \hat{\mathcal{B}}^{-1}(x)\nu-\Delta_1\left(\hat{\mathcal{B}}(x)+\Xi(x)\right)^{-1}[\hat{\alpha}(x)+\xi(x)] \\
\left[I-\hat{\mathcal{B}}(x)\Delta_1\left(\hat{\mathcal{B}}(x)+\Xi(x)\right)^{-1}+\Delta_2\right]y^{(\rho)} &= \nu-\hat{\mathcal{B}}(x)\Delta_1\left(\hat{\mathcal{B}}(x)+\Xi(x)\right)^{-1}[\hat{\alpha}(x)+\xi(x)] \\
[I-\mathcal{D}(x,\Delta_1)+\Delta_2]\,y^{(\rho)} &= \nu-\mathcal{D}(x,\Delta_1)\,[\hat{\alpha}(x)+\xi(x)] \\
\text{where}: \quad \mathcal{D}(x,\Delta_1) &= \hat{\mathcal{B}}(x)\Delta_1\left(\hat{\mathcal{B}}(x)+\Xi(x)\right)^{-1} \\
y^{(\rho)} &= [I-\mathcal{D}(x,\Delta_1)+\Delta_2]^{-1} \\
&\quad\cdot[\nu-\mathcal{D}(x,\Delta_1)\,[\hat{\alpha}(x)+\xi(x)]] \\
y^{(\rho)} &= \nu+\epsilon_{INDI} \\
\text{where}: \quad \epsilon_{INDI} &= [I-\mathcal{D}(x,\Delta_1)+\Delta_2]^{-1} \\
&\quad\cdot[\mathcal{D}(x,\Delta_1)\,(\nu-[\hat{\alpha}(x)+\xi(x)])-\Delta_2\nu]
\end{aligned}
\tag{3.16}
$$

Model uncertainties

If no singular perturbations are present so that Δ_1 and Δ_2 are zero, $\epsilon_{INDI}=0$, even in the presence of model uncertainties on the control effectiveness ($\Xi(x)$) (Pollack & van Kampen, 2022; Xuerui Wang, van Kampen, et al., 2019). However, this is unobtainable in reality as this requires ideal measurements, infinite actuator bandwidth, and an infinite control rate. Furthermore, for control reversal (when the elements in $\hat{\mathcal{B}}(x)$ have the wrong sign), the system can become unstable (Chang, De Breuker, & Wang, 2022) even if all those conditions are met.

When a discrete-system is considered, ϵ_{INDI} remains bounded if $\left\|I-\mathcal{B}\hat{\mathcal{B}}^{-1}(x)\right\|<1$ (Chang, De Breuker, & Wang, 2022; X. Wang, Van Kampen, Chu, & Lu, 2019). So INDI is highly robust to model uncertainties in theory.

This was confirmed in simulation by for example Xuerui Wang, van Kampen, et al. (2019) when comparing the effect of model uncertainties between INDI and NDI on tracking performance. For both the INDI and NDI controller the control effectiveness was overestimated by 30% ($\hat{\mathcal{B}}(x)=1.3\mathcal{B}(x)$). Both INDI and NDI then used perfect sensor measurements and NDI in addition a perfect model of $\alpha(x)$. With that setup, the tracking performance using the INDI controller was superior to that of the NDI controller.

Grondman et al. (2018) also simulated an engine failure during a real test-flight with an INDI controller on a Cessna Citation II. The INDI controller was able to compensate for the asymmetric trust and track its reference without any knowledge of the failure.

However, while stability is guaranteed for model uncertainties that don't cause control reversal (Chang, De Breuker, & Wang, 2022), large model uncertainties can lead to inferior performance and handling qualities. In that case INDI can be made adaptive with an online system identification algorithm that estimates the control effectiveness ($\mathcal{B}(x)$) (Chang, Guo, De Breuker, & Wang, 2022; Smeur, Chu, & de Croon, 2016; Smit, Pollack, & Kampen, 2022). Using adaptive techniques, the controller also becomes even more robust against system faults (Chang, Guo, et al., 2022).

The synchronization effect

The synchronization effect can be investigated by looking at the perturbations Δ_1 on u and Δ_2 on $y^{(\rho)}$. From Equation 3.16 it can be seen that ϵ_{INDI} can become unbounded, and cause the system to become unstable when $[I-\mathcal{D}(x,\Delta_1)+\Delta_2]$ is non-singular. This means that Δ_1 and Δ_2 must be carefully designed, within system constraints. This is in contrast with NDI, which inversion residual will remain

bounded under these same assumptions (Pollack & van Kampen, 2022).

With perfect and instant sensing, these lags could both be zero. This has shown to work best in simulation (S. Sieberling et al., 2010). However, in practice, as $y^{(\rho)}$ often requires numerical differentiation and filtering, this signal has a certain lag. As shown in theory by Pollack and van Kampen (2022), a possible design solution is to set $\mathcal{D}(x, \delta_1) = \Delta_2$, called the "matching strategy". If both $\hat{\mathcal{B}}(x)$ and Δ_1 are diagonal, and $\Xi(x) = 0$, which is often approximately the case, this simplifies to $\Delta_1 = \Delta_2$. So an artificial lag needs to be added to u to synchronize it with the filtered $y^{(\rho)}$. This strategy has been used since early works (Bacon & Ostroff, 2000) and is common practice (Grondman et al., 2018; Smeur, Chu, & de Croon, 2016) because it greatly improves the performance (van 't Veld et al., 2018). An INDI controller with perturbations and a synchronization block (H_{sync}) is shown in Figure 3.2.

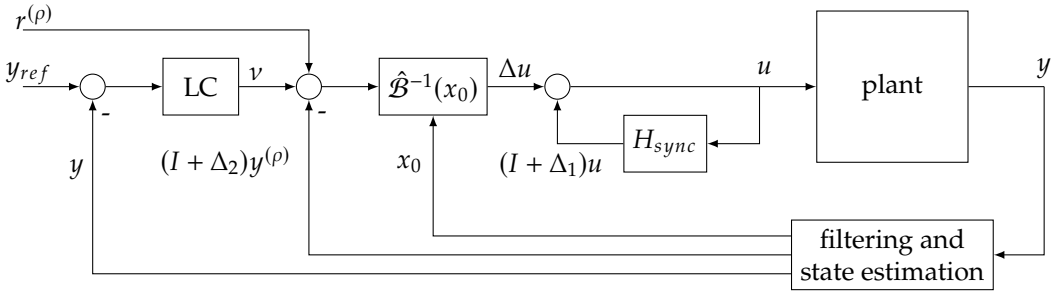

Figure 3.2: INDI architecture with regular and singular perturbations.

In order to employ the matching strategy, the high-order dynamics such as time delays should be known. If the uncertainty of the relative time delay is too high, a real-time time delay identification method may be used (van 't Veld et al., 2018). This time delay identification method aims to calculate the current time lags of the u and $y^{(\rho)}$ signals and then synchronize them by artificially delaying one of the signals. This method only uses existing signals and doesn't introduce additional model dependency.

Even if the lags are synchronized but are non-zero, a linearization error remains. In addition, there will always be unsynchronized delays due to model uncertainties. The synchronization effect can further be lowered by reducing the amount of lag. This is possible by using models to estimate the (most) current u and $y^{(\rho)}$. S. Sieberling et al. (2010) used a predictive filter to estimate $y^{(\rho)}$ and Kumtepe et al. (2022) generalized this idea and formalized "hybrid-INDI". Hybrid-INDI fuses the model-based NDI and sensor-based INDI using a complementary filter to use models to estimate $y^{(\rho)}$ with a high bandwidth and correct these estimates with filtered sensor data which has a lower bandwidth. Hybrid-INDI has shown to be robust to unexpected measurement delays, which is something the matching strategy cannot account for (Kumtepe et al., 2022). In addition, Pollack and van Kampen (2022) showed that hybrid-INDI can increase the performance in systems where the time-scale separation assumption is violated when the feedback signals have too much lag.

Disturbance rejection

Disturbance rejection is the controllers ability to track a certain reference under the influence of outside disturbances, such as wind gusts. This is shown in practice by Smeur, De Croon, and Chu (2016) who flew an INDI controller on a small quadrotor in and out of a fan's wake. The performance was much better than for linear controllers. This is because disturbances are measured as they influence the output derivative ($y^{(\rho)}$), where changes are thus much faster detected compared to just measuring the output (y) (Xuerui Wang, van Kampen, et al., 2019).

Fast disturbance rejection can lead to higher loads in the structure. Kier, Müller, and Looye (2020) showed that INDI causes higher torsion loads on the vertical tail plane when correcting for a sideways gust compared to NDI and traditional yaw dampers. This issue must be addressed with careful estimation and filtering of $y^{(\rho)}$. These higher loads were not seen in normal tracking tasks.

3.3. Other augmentations

The bare INDI control law shown in Equation 3.11 cannot explicitly account for actuator dynamics and over or under-actuated systems. However, some augmentations have been developed to expand its use to these cases.

3.3.1. Actuator dynamics

Control deflectors have certain maximum rates at which they can be moved, limiting the bandwidth at which the system can be controlled. This can be quite restricting and is thus important to take into account during control design. Furthermore, the deflectors can have nonlinear physical limitations such as minimum and maximum values for their angle.

Since the control bandwidth of INDI is high, there might be too little bandwidth separation between the controller and the actuator dynamics meaning the INDI controller commands faster changes than the actuators can give. This can lead to wind-up of the control input u. To avoid performance and stability issues due to this phenomenon, pseudo-control hedging may be used (Grondman et al., 2018; Simplício, Pavel, van Kampen, & Chu, 2013; van 't Veld et al., 2018). In addition, it can help avoid integrator wind-up of the linear controller that commands ν to the INDI controller (van 't Veld et al., 2018).

Pseudo-control hedging (PCH) was pioneered by Johnson and Calise (2001) and first applied on an INDI controller by Simplício et al. (2013). The idea is to limit (in other words: hedge) the reference that the controller is trying to follow such that it perfectly stays within the limitations of the actuators. This way the controller never "sees" the actuator dynamics. However, the commands of the outer loop or pilot are being hedged and cannot thus be completely obtained as desired since they lie outside of systems bounds. The system input that was unobtainable for the system due to actuator dynamics (called the hedge signal ν_h) is easy to calculate using a system model. It is simply the difference between the commanded input ν_c based on the commanded input u_c to the reached input ν_{reached} based on the realized input $\hat{u}$. The derivation is shown in Equation 3.17. Just like the INDI control law, the PCH signal only depends on the control effectiveness, as other terms cancel out. This does introduce an additional dependency on model uncertainties in the system, but not on additional models.

$$\begin{aligned} \nu_h &= \nu_{\text{commanded}} - \nu_{\text{reached}} \\ &= \alpha(x_0) + \mathcal{B}(x_0)u_c - [\alpha(x_0) + \mathcal{B}(x_0)\hat{u}] \\ &= \mathcal{B}(x_0)\,(u_c - \hat{u}) \end{aligned} \tag{3.17}$$

This hedge signal is then used by a reference model to limit the reference y. In the literature where PCH is used, a first-order reference model is always used since they also control a first-order system with the INDI controller (Grondman et al., 2018; Simplício et al., 2013; van 't Veld et al., 2018). The unhedged feed-forward ν_{rm} is calculated by $\nu_{rm} = K_{rm}(y_{ref} - y_{rm})$, where K_{rm} is a diagonal matrix which makes this a low pass filter with bandwidth K_{rm_i} for the i-th element of y. ν_{rm} is the ideal input to the system and is thus used as feed-forward term. The reference model output is then updated by integrating the difference between the ideal and the reached ν, so $y_{rm} = \frac{1}{s}(\nu_{rm} - \nu_h)$. This last step uses the hedge signal and outputs an obtainable y_{rm} for the system. A block diagram with this PCH implementation is shown in Figure 3.3.

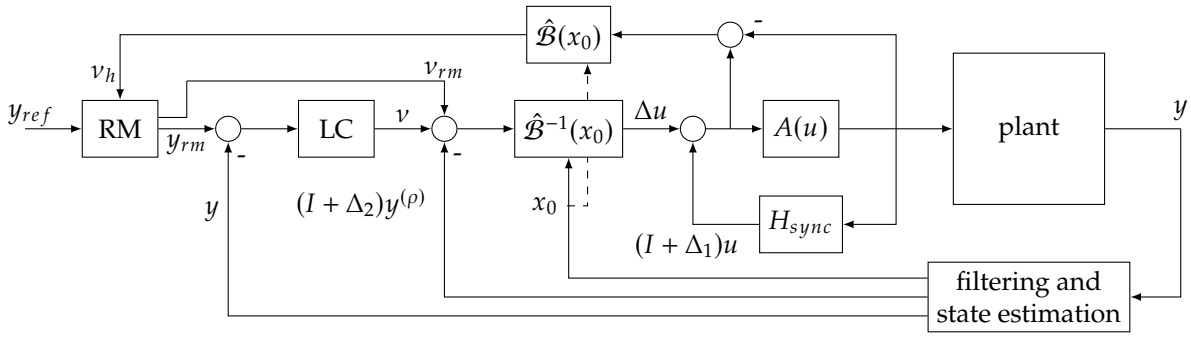

Figure 3.3: INDI architecture with synchronisation and PCH.

The actual control deflection can be estimated by measuring it or modelling the actuator dynamics. In Figure 3.3, $\hat{u}$ is obtained by measuring the actuators. This method was also done by Grondman et al. (2018) and van 't Veld et al. (2018) who found that this method could lead to steady-state errors because of the bias in the actuator measurement. Because of this steady-state error van 't Veld et al. (2018) added an integrator term in the reference signal that cancels out the bias of the measurement. On the other

hand, Grondman et al. (2018) recommends to only activate PCH when reaching actuator saturation and/or using a model for the actuator dynamics (even though this adds a new uncertainty term in the controller) based on their findings after the test flight. When using a model of the actuator dynamics the block diagram can be easily adapted by replacing $A(u)$ with $\hat{A}(u)$ and moving the actuator dynamics block into the plant.

3.3.2. Over and under-actuated systems

For airborne wind energy applications, both over, under, and fully-actuated systems exist. If the kite attitude controller can use ailerons, an elevator, and a rudder it is fully-actuated. Some system designs are over-actuated, for example the Ampyx AP-3 which has 9 control surfaces in total (a flap, flaperons, and aileron on each wing, two rudders, and an elevator) (Ampyx Power, n.d.). If in addition to the attitude, the kite needs to balance the loads in its wings, this adds additional control variables and the system could become under-actuated.

Formally, Assumption 3 does not hold, the system is either over or under-actuated. Assume that the row rank of $\mathcal{B}$ is p (meaning that there are p linearly independent outputs that need to be controlled). The system is then over-actuated if the column rank of $\mathcal{B}$ is larger than p (Xuerui Wang, Mkhoyan, Mkhoyan, & De Breuker, 2021). In other words (and slightly simplified), if there are more inputs than outputs, the system is over-actuated. Conversely, if the column rank of $\mathcal{B}$ is lower than p, the system is under-actuated.

This is analogous to overdetermined (under-actuated) and underdetermined (over-actuated) systems of equations and this relation can easily be seen when rewriting the INDI control law in $Ax = b$ form, shown in Equation 3.18.

$$\mathcal{B}(x_0)\Delta u = \nu - y_0^{(\rho)} \tag{3.18}$$

Over-actuated systems

For over-actuated systems, there are an infinite amount of solutions for Equation 3.18, so control allocation must be used. Based on a secondary objective, a single optimal solution can be selected.

Many linear control allocation algorithms exist. Some don't take the actuator constraints into account, such as the (weighted) pseudoinverse. Other algorithms do, such as daisy chaining, redistributed weighted pseudoinverse, direct allocation, and numerical optimization (e.g. linear or quadratic programming) (Matamoros & de Visser, 2018). For control-affine systems (which have been the focus so far), where a linear relationship exists between the control effectiveness $\mathcal{B}(x)$ and the input u, these linear control allocation methods can be readily used.

For non control-affine systems, this linear relationship does not exist. Nonlinear control allocation algorithms do exist but are not real-time applicable as they rely on nonlinear optimization. Matamoros and de Visser (2018) used the incremental form of the dynamics to linearize the nonlinear control allocation problem around the current operating point and make linear control allocation algorithms feasible for non control-affine systems and called this incremental nonlinear control allocation (INCA).

All these techniques will now be discussed in more detail.

Linear control allocation without actuator constraints Analogous to least-square solutions for underdetermined systems, the norm of Δu can be minimized as secondary objective for control allocation, leading to the least-squares solution $\Delta u = \mathcal{B}^+(x_0)(\nu - y_0^{(\rho)})$, where $(\cdot)^+$ is the Moore-Penrose inverse. If $\mathcal{B}$ is full rank (which is the case for over-actuated systems), the pseudoinverse can be calculated by $\mathcal{B}^+ = (\mathcal{B}^T\mathcal{B})^{-1}\mathcal{B}^T$.

The primary objective of tracking ν will always be met and the secondary objective ensures that this is done with minimal changes to the control inputs. This was shown by Smeur, Chu, and de Croon (2016) who used it to fly a small quadrotor.

If some changes to inputs must be weighted more than others, the weighted pseudoinverse can be calculated. This method for control allocation is analogous to solving a weighted least-squares problem.

Linear control allocation with actuator constraints While many linear control allocation algorithms with actuator constraints exist, the two that will be discussed here are the redistributed weighted pseudoinverse and quadratic programming method as they have been used in the INDI literature.

The (weighted) pseudoinverse does not account for actuator constraints (Matamoros & de Visser, 2018; Xuerui Wang et al., 2021), so these constraints can be added in the form of rate and angle constraints. Matamoros and de Visser (2018) defines a cost function that penalizes control deflections away from their nominal position and uses the redistributed weighted pseudoinverse (RWPI) method to iterate through pseudoinverse solutions until all actuator constraints are met.

It is possible that no solution exist because of the added constraints, so alternatively Matamoros and de Visser (2018) proposes a quadratic programming (QP) method that minimizes the control allocation error, which was later called INDI-QP by Xuerui Wang et al. (2021). This means that Equation 3.18 is no longer an equality constraint of the optimization, but $\left\| \mathcal{B}(x_0)\Delta u - \left(\nu - y_0^{(\rho)}\right) \right\|$ will be minimized. This ensures that a feasible solution is always found and allows for explicit actuator constraints in the QP formulation.

The cost function then consists of two parts: the first part minimizes the control allocation error and the second part minimizes the control deflection away from their nominal position. It is important to weigh the second term sufficiently small to prioritize the minimization of the allocation error.

An extension to this called INDI-QP-V was made by Xuerui Wang et al. (2021) to add smoothness constraints to the control deflections of a morphing wing. It does this by adding a term to the cost function.

Incremental nonlinear control allocation (INCA) Non control-affine systems have some nonlinear mapping from control deflections to control moments. Following the convention of Matamoros and de Visser (2018), this mapping is indicated by $\Psi(x, \delta)$. A non control-affine system with this mapping is shown in Equation 3.19.

$$\dot{x} = F(x) + g(x)\Psi(x, \delta) \tag{3.19}$$

It is assumed that this is a first-order system where the state needs to be controlled ($y = x$). Using the incremental form of Equation 3.19, the INDI control law shown in Equation 3.20 can be derived.

$$\Delta\delta = \left[\left. \frac{\partial \Psi(x, \delta)}{\partial u} \right|_{(x_0, u_0, \delta_0)} \right]^{-1} g(x)^{-1} (\nu - x_0) \tag{3.20}$$

Defining $d_c = g(x)^{-1}(\nu - x_0)$, the system that needs to be solved for control allocation is shown in Equation 3.21. Because of the incremental form, this system is linear and can be solved using simple linear control allocation algorithms.

$$\left. \frac{\partial \Psi(x, \delta)}{\partial u} \right|_{(x_0, u_0, \delta_0)} \Delta\delta = d_c \tag{3.21}$$

This way of using the incremental form to be able to use linear control allocation methods on nonlinear non control-affine systems was developed by Matamoros and de Visser (2018). In their work, they successfully use INCA together with RWPI and QP for control allocation for the innovative control effectors aircraft that has 13 highly nonlinear, interacting and axis-coupled control effectors.

Under-actuated systems

Some linear controllers such as LQR controllers can control some under-actuated systems just fine. Think of an LQR controller controlling the position of a cart by pushing/pulling on it while it balances a stick on top of the cart. INDI cannot decouple the cart's and the stick's dynamics and can thus only control the angle of the stick or the cart's position. If the stick had its own actuator, this would of course be no problem, but without, the INDI controller suffers from the internal dynamics of the stick that are "hidden" from the controller when it tries to control the cart's position and the angle of the stick simultaneously. In formal terms, the relative degree is smaller than the order of the system: $\rho < n$.

In the INDI literature there have been two augmentations to control internal dynamics: virtual input design and reintroducing model information. Systems can be under-actuated when there are multiple, conflicting references for the control variables and the controller needs to find an optimum. Other under-actuated systems are under-actuated because there are control variables with different relative degrees. When controlling these systems with NDI or INDI controllers, the control variables with higher relative degree are "hidden". In the literature only INDI adaptations that focus on the latter under-actuated systems were found and will be discussed in the coming section.

Virtual control input design Usually, the virtual control input ν is calculated by a simple linear controller that drives y to y_{ref}. However, this controller could also take additional states into account that it is trying to control. The INDI controller is then used to partially linearize a system which hides some of the nonlinear dynamics to the outer loop controller which can then focus on controlling the internal dynamics by calculating an appropriate ν.

One controller that can be used to calculate ν is sliding mode control (SMC). Xuerui Wang (2019) pioneered this idea which was applied in Mooij and Wang (2021) to control a launcher including the slosh dynamics of the propellants. The INDI controller was used to partially linearize the dynamics of a rocket launcher such that $\ddot{\theta} = \nu$ (in other words: linearize the rigid body dynamics). The sliding mode controller then calculates a virtual control ν that controls the pitch angle of the launcher to follow a θ_{ref} and damp the slosh dynamics. This architecture was named I-SMC and besides on launchers with sloshing dynamics has been used for (real-world) quadrotor attitude control (Xuerui Wang, Sun, van Kampen, & Chu, 2019), attitude control an F-16 (Chang, De Breuker, & Wang, 2022), and in a flight path loop for gust load alleviation (Xuerui Wang, Mkhoyan, & De Breuker, 2022).

Reintroducing model information For over-actuated systems, the pseudoinverse of the control effectiveness matrix can do control allocation. For under-actuated systems this is also possible. However, since $\mathcal{B}(x)$ is not full-rank for under-actuated systems, the closed-loop dynamics are not linearized anymore because $\mathcal{B}(x_0)\mathcal{B}^+(x_0) \neq I$ if $\mathcal{B}(x_0)$ is not full rank. For some systems this might still work, such as shown by X. Wang, van Kampen, and Chu (2017), but stability is not guaranteed.

To guarantee stability, model information can be reintroduced into the control law. This is particularly interesting if high frequency dynamics need to be damped, such as for flexible aircraft and generally interesting for systems where the time-scale separation principle does not hold ($\Delta x \not\ll \Delta u$). For high frequency dynamics the Δx-term in the Taylor series expansion in the derivation of the INDI control law (Equation 3.9) cannot be neglected. X. Wang, Van Kampen, et al. (2019) included some Δx terms in the INDI control law and combined it with a weighted pseudoinverse for control allocation to control the attitude and the gust loads of a flexible aircraft.

3.4. Discussion and conclusion

INDI is a feedback linearization technique that has a lower model dependency and increased robustness compared to NDI. With feedback linearization the controller works over the entire (nonlinear) dynamic domain so gain scheduling is not required in theory. A single, simple, linear outer loop controller can be used together with INDI to control a system. Disturbance rejection of INDI is excellent and remains good under model uncertainties of the control effectiveness.

To ensure a proper functioning of an INDI controller a high sampling frequency and a good estimate of the output derivative is needed. Because the output derivative is often obtained through filtering, the matching strategy can be utilized to mitigate the issues arising from the synchronization effect.

Because the controller and actuator bandwidth might overlap, PCH can ensure that the INDI bandwidth stays below the actuator bandwidth to avoid issues. Furthermore, augmentations exist to use INDI on over and under-actuated systems.

Especially its reduced model dependency and disturbance rejection properties, while feedback linearizing a nonlinear system, make it an interesting controller for airborne wind energy. In the next chapter (chapter 4), multiple ideas how INDI could be used for control of airborne wind energy will be presented.

4

Using INDI for airborne wind energy control

The third sub-question for the literature study is:

Research question 1C

How could INDI be applied in airborne wind energy control design?

In this chapter, a novel kite control architecture using tether force control will be presented. The motivation behind it and its architecture will be shown in section 4.1. This architecture can be realised with different controller types, of which INDI is one promising option. The chapter is concluded in section 4.2.

4.1. Kite tether force control

As the wind speed increases, the pull that the kite can exert on the tether increases, this can increase the tether force and/or the reel-out speed. Since power output is tether force multiplied by reel-out speed, a stronger pull of the kite results in more power. As discussed in subsection 2.2.6, the goal of winch control is to keep the kite flying at an optimal reel-out factor that balances an increase in wind speed between an increase in tether force and an increase in reel-out speed that results in the highest increase in power. As discussed in section 2.1, as the wind speed increases, eventually system limits are reached. Once the system reaches the tether force limit and power limit, the system cannot physically convert more energy from the wind. So the kite should lower its aerodynamic performance such that the produced power stays constant Fechner and Schmehl (2013) and Luchsinger (2013).

In section 2.1, it was discussed that adjusting the path, by flying at higher elevation angles, can lower the aerodynamic performance of the kite, as the wind vector becomes more misaligned with the tether. But this strategy does not work for MW-scale systems. For large-scale airborne wind energy systems, gravity has a significant effect, because the airspeed (and thus tether force) does not only vary as a function of wind speed but also as the kite is flying its figure of eight. So instead of flying at higher elevation angles, kites must fly at a lower angle of attack to lower the lift coefficient. This way, the pull that the kite exerts on the tether can remain constant as the airspeed of the kite changes. There are many publications that control the angle of attack of the kite to adjust its aerodynamic performance (Canale et al., 2010; De Schutter et al., 2019; Echeverri et al., 2020; Licitra et al., 2019; Malz et al., 2020). However, these studies use a pre-computed optimal angle of attack reference using optimal control strategies. This works well for performance analysis studies, but model-uncertainties and the inability to accurately measure the wind speed make these techniques difficult to implement outside of simulation environments.

4.1.1. Control architecture for kite tether force control using INDI

Instead of using a pre-computed angle of attack reference, kite tether force control aims to use the kite's measurement of the tether force to dynamically compute its optimal angle of attack. The optimal angle of attack changes at different bandwidths, from low to high: change in mean wind speed, change in airspeed (due to flying down/up in heavy systems), gusts. To achieve high-bandwidth control of the tether force, control surfaces that directly influence the lift such as flaps, flaperons, lift dumpers, or symmetric aileron deflections might be necessary, such as in (X. Wang, Van Kampen, et al., 2019; X. Wang et al., 2017). Furthermore, a high-bandwidth inner loop controller for the kite's attitude is required. It is hypothesised that combining an INDI inner loop controller together with direct lift control could achieve this required bandwidth. The architecture for this idea is shown in Figure 4.1. This architecture is similar to the control architecture by Lombaerts and Looye (2013) but for airborne wind energy instead of untethered aircraft. So there are a few important differences:

1. The lift reference is not calculated from the desired flight path angle and bank angle, but instead from the measured tether force. The L_{ref} controller is not trivial since, especially for large kites, the lift force and tether force are not in balance. Designing this controller will be one of the tasks of the thesis.
2. An INDI inner loop is used instead of an NDI inner loop because it has a lower model dependency in both the qualitative and quantitative sense, softening requirements on system identification.. This INDI controller will be designed and tested chapter 6.
3. An INCA control allocation loop is used to allocate a commanded change in lift coefficients over different control surfaces. This is explained in subsection 4.1.2.
4. Only the control architecture for the radial control is shown here. However, this architecture should work alongside an integrated or separate bank angle controller.

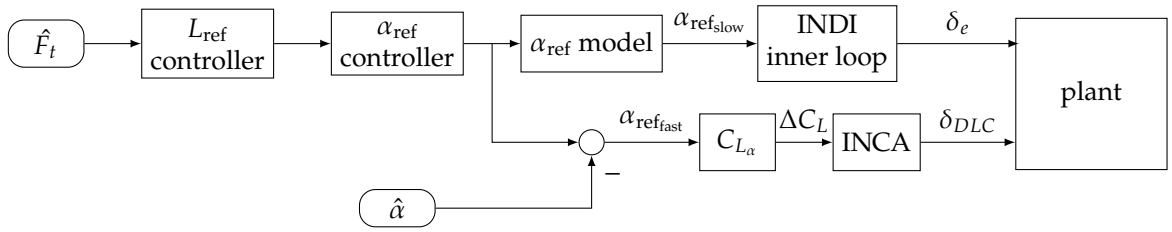

Figure 4.1: Block diagram for kite tether force control using INDI inner loop control and INCA.

4.1.2. Optimal control allocation

Some kites might be over-actuated and require control allocation between the elevators and (multiple) direct lift devices. For example, the Ampyx AP-3 has 9 control surfaces in total: a flap, flaperons, and aileron on each wing, two rudders, and an elevator (Ampyx Power, n.d.). Multi-element airfoils are also being investigated by the airborne wind energy community for their high lift coefficients, for example by Bauer et al. (2018). If the multi-element airfoils are adjustable, and for the example of Ampyx Power, these wing configurations will require control allocation algorithms. As stated in subsection 3.3.2, INCA can be used for nonlinear optimal control allocation.

4.1.3. Alternative strategies

Instead of keeping a strict power limit and strictly lowering the aerodynamic performance to stay at rated power, the generator might be temporarily overloaded to generate a peak power above its rated power. Bauer et al. (2019) utilise this strategy in their control architecture for a fly-gen airborne wind energy system and deems generator overloading a "system requirement" that enables a significantly higher mean power. But even with power overloading, the tether force cannot be overloaded and the generator overloading limits must still be taken into account, meaning a control strategy that can limit the tether force is also necessary in this case.

Oversizing the generator, such that the power limit is never reached is also an option that makes this control strategy less attractive. However, this of course increases the cost (Joshi et al., 2022) and environmental impact (Van Hagen, 2021) of the system. Especially for multi-MW scale systems this

is not an option. In the current implementation of MegAWES the generator requires a peak rating of almost 15 MW at a mean power of 3.6 MW at a wind speed of 22 m/s Eijkelhof and Schmehl (2022).

While only relying on the kite for tether force control at rated power is power-optimal, it could lead to an increase in the probability for tether rupture. It is hypothesised that the winch has more control authority for the tether force than kite tether force control using direct lift surfaces. However, using the winch would more easily go over power limits and thus require over-sizing of the generator. Which is why kite tether force control is a promising idea.

4.2. Discussion and conclusion

Once the power limit of an airborne wind energy system is reached, the kite must lower is aerodynamic performance in order for the system to stay at the power limit. Current approaches increase the elevation angle or use pre-computed angle of attack references. Raising the elevation does not work for large scale systems because the power limit is not only reached when the wind speed increases but potentially also when the kite is flying downward and is exchanging potential for kinetic energy. Pre-computing the angle of attack reference leads to sub-optimal solutions when there are model uncertainties and wind speed measurement uncertainties. Kite tether force control circumvents these issues by using only a measurement of the tether force to adjust its angle of attack reference.

For large scale systems, where the tether force changes as they fly up and down, this must be down with a high bandwidth. So INDI inner loop control coupled with direct lift control will be investigated in the rest of this thesis. The INDI inner loop controller will be developed in chapter 6 while the rest of the control architecture will be the focus of this thesis.

Besides controlling the tether force, the kite should also control its bank angle in order to remain on the prescribed path. This can be done in an integrated or separate controller. Furthermore, the winch controller can be integrated or separate. Separate controller have as advantage that they don't require a safety critical communication channel between the winch and kite.

The main idea behind kite tether force control is to improve the performance during the traction phase. However, it could also be benefitial for the retraction phase since lowering the tether force during retraction can improve the mean power production Luchsinger (2013). However, this is outside the scope of this thesis.

5

Nominal and robust performance metrics

The second research question for the literature study is:

Research question 2

How to measure the nominal and robust performance of an airborne wind energy system controller?

To answer this question, nominal performance metrics will be discussed in section 5.1 and robust performance metric will be discussed in section 5.2. The chapter is concluded in section 5.3

5.1. Nominal performance

The nominal performance of a controller is measured under ideal conditions. This performance is thus the upper-bound of what can be achieved with a given system in the real world.

The goal of an airborne wind energy system is to produce power and do so in a desired manner. However, usually the controller only has an indirect influence on this since power production comes as a side-product of following a power-optimal path in most control architectures as reviewed in chapter 2. Thus, besides evaluating the power output of the system, the path following performance becomes important. Finally, other metrics such as control effort are discussed.

5.1.1. Power output

One of the most important metrics when analysing an airborne wind energy system is the mean cycle output for a given wind speed at the height where the kite is flying. For pumping cycle systems, this consists of the energy produced during the traction phase minus the energy consumed during the retraction phase divided by the total cycle time. Controller architecture and performance can have a great influence on this mean power output. Li et al. (2018) found an increase of almost 500% when using an attitude controller that also follows the desired angle of attack, and not just a desired angle to stay on the path. This can be best captured by comparing the power curves, which were discussed in section 2.1.

Besides mean power output, the intermittency, variability, and correlation with other power sources are also important (Weber et al., 2021). These metrics are heavily system and site dependent. For example, the capacity factor of a system is highly correlated with the location at which it is placed. However, a controller can influence the capacity factor through its effect on the minimum and maximum allowable wind speed. Having a broader range between the two lowers intermittency which is good for baseload applications (Zillmann & Bechtle, 2018).

In general terms, intermittency of the system can be lowered if the flight envelope of the controller is expanded. This also has a positive effect on other power related metrics such as capacity factor. This topic is underrepresented in the airborne wind energy literature as discussed by Rapp and Schmehl (2021). They show that the flight envelope of the system can be expanded by predicting failure conditions

and starting an evasive manoeuvre that keeps the system operational under a condition that would normally be outside the flight envelope.

5.1.2. Reference tracking

To use the philosophy of path following with power as a side-product, a cascaded control architecture is used, like many autonomous systems, as discussed in chapter 2. To measure the tracking performance of such an architecture, the error of each cascade can be taken. For example, for Rapp, Schmehl, Oland, and Haas (2019) this would mean: the position, heading, and flight path angle error w.r.t. the ideal path, the attitude error w.r.t. the path loop reference, the rate error w.r.t. the attitude loop reference, and the control allocation error w.r.t. the rate loop reference. There are multiple attitude references within such a cascaded loop because the inner loop attitude reference is supposed to steer the system back on the ideal path, while the outer loop attitude reference is simply the attitude if the system were already on that path.

In general, the error of each cascaded loop can be used to evaluate the performance of the controller. While the outer loop error is the most important, the controller cannot function without good inner loop control.

5.1.3. Other metrics

Even if the references are perfectly tracked there are other metrics that are important to assess controller performance.

Control effort is a widely used term in control theory, however a precise definition is not widely shared. As shown by Bartyś and Hryniewicki (2019), it is sometimes used as the instantaneous control deflection, the force required by the actuator, or the power of a signal. Whatever the specific definition is used, the general idea is to measure how much effort it takes to follow that control signal. This effort can be somewhat measured abstractly in deflections or by making a heuristic for the actual power consumption of the actuators. In addition, a heuristic for actuator wear can be added by measuring the variability and high frequency components of the control signal.

Control saturation occurs when the controller commands cannot be physically met by the actuators. When this happens, it can be a sign that the controller is overly aggressive or that the actuators are not designed correctly. In both cases, it can lead to lower performance as experienced by Makani, for whom it was common to ran into saturation problems each loop of the flight (Echeverri et al., 2020).

Finally, the controller also influences the loads on the system. Aggressive controller might track the reference more closely but they might also lead to higher loads in the structure. As mentioned in subsection 3.2.2, INDI control leads to higher loads on the vertical tail plane than NDI control or traditional yaw dampers. Since airborne wind energy systems operate under an already high wing loading, it is important that the controller doesn't cause additional loads that can lead to failures or the need for structural reinforcements that negate the controller performance gain.

5.1.4. Discussion

An open question in the airborne wind energy community is whether using tight reference tracking to the optimal path is actually good for power or if it is better to "ride through" a disturbance that pushes the system off the path. So while reference tracking is a good metric to evaluate controller performance, the bigger picture together with power output should always be considered. Ideally, the control effort should be expressed in a consumption of power which could be compared to the increase in power output that that increase in control effort achieves. This way it can be evaluated whether it is worth it to use controllers that require a large control effort.

Taking this to the extreme, a cost-benefit analysis of INDI should also include the fact that INDI causes high frequency control signals that can lead to additional wear of the actuators (Grondman et al., 2018) and higher loads on the structure (Kier et al., 2020) requiring more material during manufacturing which makes the kite heavier.

5.2. Robust performance

Robust performance is the performance under non-ideal circumstances. Non-ideal circumstances are uncertainties and disturbances. The performance can then be assessed by analysing the performance loss with respect to the nominal case. In addition, there are some specific robustness metrics that only

apply to robust performance analysis. Finally, robustness can be assessed using a systematic robustness analysis.

5.2.1. Uncertainties and disturbances

Uncertainties are internal to the system and arise from (inevitable) imperfect knowledge of the system and environment. The ones discussed here are model uncertainties, sensor error, and time delays. Disturbances are external to the system. The two disturbances that will be discussed are turbulence and gusts. Both uncertainties and disturbances are crucial to take into account during controller design. Otherwise, the controller might not work satisfactory outside an idealised simulation.

Model uncertainties

Model uncertainty can manifest itself in two ways when using an INDI controller. Firstly, the model of the controller and the simulation can be two models with entirely different architectures. The controller then uses a simpler model than the simulation . An example would be if the simulation uses a neural network-based model while the controller uses a more conventional regression-based model or a simulation model that includes actuator dynamics that are neglected in the model of the controller. Secondly, if the model of the controller and the simulation have overlapping parts, the parameters in the overlapping part can be made different. For example, the aerodynamic coefficients of the controller can be varied w.r.t. the aerodynamic coefficients of the simulation. By introducing these two ways of model uncertainty, the robustness of the controller with respect to them can be assessed.

Having the actuator dynamics in the simulation model but not in the controller model is a widely used practice in literature for INDI (Grondman et al., 2018; Simplício et al., 2013; van 't Veld et al., 2018) and to a lesser extend for airborne wind energy (Rapp, Schmehl, Oland, & Haas, 2019). This is because most AWE model-based controllers use MPC with actuator dynamics (Canale et al., 2006; Canale et al., 2010; Gros et al., 2012; Ilzhöfer et al., 2007; Karg & Lucia, 2019; Zanon et al., 2013). However, it should be noted that these MPC controllers are used for performance prediction rather than flying outside of simulations, as mentioned in subsection 2.3.2. Other than added actuator dynamics, additional model architecture differences are not used.

Changing model parameters is the main way of assessing robustness in the literature. Any coefficient can be varied but typically uncertainty is introduced through aerodynamic coefficients, moment of inertia coefficients, and center of gravity locations (Kumtepe et al., 2022; Mooij & Wang, 2021; S. Sieberling et al., 2010; Xuerui Wang, van Kampen, et al., 2019), and specifically for airborne wind energy: tether attachment location (Rapp, 2021). Kumtepe et al. (2022) increases all aerodynamic coefficients by 50% and Rapp (2021) by ±20%. S. Sieberling et al. (2010) use a more sophisticated method to determine suitable uncertainty percentages in aerodynamic coefficients: They use three different system identification techniques and analyse the distribution of resulting aerodynamic coefficients to make a realistic estimate of the uncertainty.

Sensor error

Sensors have measurement error. This is typically represented in simulation with bias and noise, where the noise is usually normally distributed.

Sometimes there are redundant measurements and the bias can be estimated using for example a Kalman filters. But for non-redundant measurements (such as actuator position) this is not possible. That is why actuator sensor bias can have a significant effect on the performance of the controller (van 't Veld et al., 2018).

Sensor noise lowers the performance of the controller. S. Sieberling et al. (2010) directly feeds the noisy sensor data into the controller and observes a slight loss of performance. Instead of directly using the noisy sensor data, filters can be used to lower the noise (Grondman et al., 2018; van 't Veld et al., 2018). Filtering introduces delays, which degrade performance and need to be taken into account during the design of the INDI controller through synchronisation as discussed in section 3.2.

A complete integration of state-of-the-art state estimation (navigation, as discussed in subsection 2.2.3) in a simulation is lacking in literature but also not as relevant since its effects (bias and time delays) can be separately modelled.

Time delays

As discussed in the previous section time delays can arise from filtering. In addition, time delays occur since data transmission is not instant (sometimes called "transport delay"). In the INDI literature, delays

of the angular acceleration estimation have a significant effect on the INDI performance and need to be taken into account in both design and simulation, as discussed in section 3.2. In the airborne wind energy literature, Rapp (2021) adds time delays on flight and ground sensors and flight and ground actuation.

A realistic time delay for the system that is analysed can be estimated so that the performance for that time delay can be checked. S. Sieberling et al. (2010) adds a time delay of 10 ms and doesn't filter the noisy data and Kumtepe et al. (2022) adds a time delay of 50 ms, while also filtering the noisy sensor data.

In contrast, when no realistic time delay can be estimated, the highest allowable time delay can be estimated by running simulations with different magnitudes of time delays and checking the performance. van 't Veld et al. (2018) systematically runs simulations with up to 250 ms delay on the angular rate and actuator position. Rapp (2021) does a Monte-Carlo analysis with varying levels of flight and ground sensors and flight and ground actuation delays. They then show what the maximum allowable combinations of delays are.

Turbulence

Turbulence is local wind velocity variation on many different scales. These local differences in wind velocity can have translating (force) effect on the vehicle, but can also cause rotational (moment) effects since the wind velocity varies along the vehicle. This interaction can be simulated using CFD but due to its computational complexity this is often not feasible. So alternatively, a simpler turbulence model and its translational and rotational effects on the vehicle can be modelled.

There are two popular turbulence models in the flight dynamics literature: the Dryden (Liepmann, 1952) and von Kármán (Diederich, Drischler, & Aeronautics, 1957) turbulence models. Both these models define the power spectral density of the linear and angular wind velocity variations as a function of length scales (L) and intensities (σ) , which can be selected based on altitude and turbulence intensity according to guidelines defined by Department of Defence (1997). Based on the speed of the aircraft, the spatial frequency (Ω) can be calculated ($\Omega = \omega/V$), so that the power spectral densities are adapted to the speed of the aircraft. The equations for the power spectral densities for the Dryden and von Kármán model for the u-direction are shown in Equation 5.1 and Equation 5.2 (Beal, 1993). The spectral densities for the v and w direction are similar but slightly different.

$$\Psi_u(\Omega) = \sigma_u^2 \frac{2L_u}{\pi} \frac{1}{1 + (L_u\Omega)^2} \tag{5.1}$$

$$\Psi_u(\Omega) = \sigma_u^2 \frac{2L_u}{\pi} \frac{1}{\left[1 + (1.339L_u\Omega)^2\right]^{5/6}} \tag{5.2}$$

The difference in turbulence over the dimension of the aircraft causes angular effects. So the variation in upward turbulence along the span of the aircraft ($\frac{\partial w}{\partial y}$) can be used to calculate the angular turbulence velocity along the roll axis, as example shown in Equation 5.3, which is the same for the Dryden and von Kármán turbulence model (Beal, 1993).

$$\Psi_p(\Omega) = \frac{\sigma_w^2}{L_w} \frac{0.8\left(\frac{\pi L_w}{4b}\right)^{1/3}}{1 + (4b\Omega/\pi)^2} \tag{5.3}$$

Generally, the von Kármán is recommended as it is a better fit to observational data of gusts (Etkin, 2012) and is also used for structural analysis (Department of Defence, 1997). These power spectral densities can then be used to realize a turbulence field in the time or spatial domain. When defined in the time domain, the turbulence that the system is experiencing changes as a function of time, while when defined in the spatial domain, the turbulence field would be a static field in space through which something could move. Beal (1993) presented algorithms to implement both models in discrete-time simulations. However, the von Kármán model is slightly more complex to implement due to its irrational power spectral density. This problem is avoided when realizing a von Kármán turbulence field in the spatial domain, as done by X. Wang, Van Kampen, et al. (2019), X. Wang et al. (2017), and Xuerui Wang, van Kampen, et al. (2019). However, it is important for airborne wind energy simulations to have temporally defined turbulence since the kites stay in a similar location spatially. Spatially defining

the turbulence would generate a static turbulence field so the kite would fly through the exact same turbulence each cycle. So a Dryden turbulence model in the time domain is used by Rapp (2021) and von Kármán in the time domain by Zanon et al. (2013).

In wind turbine literature, other turbulence models are used, such as the Kaimal and Mann turbulence models (Burton, Jenkins, Sharpe, & Bossanyi, 2011). The Mann model (Mann, 1998) is thus also used in some airborne wind energy literature (Fechner & Schmehl, 2018).

To reduce complexity further one can realize that turbulence mainly affects the angle of attack and angle of sideslip. So instead of modelling turbulence, Mooij and Wang (2021) adds a disturbance on the angle of attack of the vehicle to assess the effect that turbulence would have.

Gusts

Gusts are larger atmospheric disturbance that cause a sudden and large change in windspeed, typically at scales that affect the entire vehicle. So it is reasonable to neglect the rotational effect that a gust can have and instead model it as a change in mean wind velocity. This method is used by Rapp, Schmehl, Oland, and Haas (2019). In contrast, X. Wang, Van Kampen, et al. (2019) defines the gust spatially and lets an aircraft fly through it. This could lead to some small rotational effects since the gusts won't have the same magnitude at any point of the aircraft. Just like for turbulence, airborne wind energy applications require temporally defined gusts since the kites stay in a similar location spatially.

Gusts can be modelled in different ways. Department of Defence (1997) uses a "1 - cosine" discrete gust model that can be used as a single gust or multiple simultaneous ones by superimposing them. This gust model is also used by X. Wang, Van Kampen, et al. (2019), though they mention that simpler models such as a ramp or step model also exists. In the (airborne) wind literature, the extreme operating gust or "Mexican hat gust" is used (Rapp, Schmehl, Oland, & Haas, 2019), which is used in wind turbine design requirements (International Electrotechnical Commission, 2005; Manwell, McGowan, & Rogers, 2009).

The magnitude of the gust can range from mild to severe and is also specified by Department of Defence (1997) for the 1-cos gust for piloted aircraft and by International Electrotechnical Commission (2005) for the extreme operating gust for wind turbines. No specifications exist yet that are specific for airborne wind turbines.

The worst-case gust is one that excites the natural frequency of the aircraft including its control system (Department of Defence, 1997). The length of the gust is the parameter that can be varied to excite the system at its natural frequency.

Just like for turbulence, the gusts itself can be neglected and only its effect on angle of attack and angle of sideslip can be modelled in a simulation. Mooij and Wang (2021) does this by modelling gusts as a disturbance on angle of attack.

5.2.2. Robustness metrics

The robust performance is analysed by both looking at the nominal performance metrics in non-ideal circumstances, such as when introducing model uncertainties, sensors errors, time delays, turbulence, and gusts. Different values can be used for these uncertainties and disturbances can be introduced by adjusting the parameters in the simulation. All possible combinations of these parameters is referred to as the parameter space. Furthermore, there are a few specialized robustness metrics.

The specialized robustness metrics are related to the safety and reliability of the system. The first published study about this topic was done by Salma et al. (2020) who defined the ultimate failure to be a crash outside the operational zone. This can be caused due to tether rupture and a loss of control. Even when tether rupture occurs, fixed wing systems should be able to fly back safely like a glider.

So a good robustness metric is to look at the probability of tether rupture or a crash without tether rupture. This metric was also used by Rapp and Schmehl (2021) and Rapp, Schmehl, Oland, and Haas (2019). The failure probability function is way to complex to derive analytically or even numerically. So typically, Monte-Carlo simulations are done to estimate the failure probability as a function of the parameters space. However, for systems with low failure probability, this may require too many Monte-Carlo simulation. Rapp and Schmehl (2021) used a technique called "subset simulations" (Au & Beck, 2001) that doesn't distribute the simulation parameters according to their probability distributions but aims to get a global estimation of the failure probability function by zooming in on regions in the parameter space that are likely to lead to failures. Using this technique, more failure scenario's can

be found leading to a better understanding of those failures and a better approximation of the failure probability function (especially for small failure probabilities).

Besides looking at failures or failure probability, robust performance can also be assessed by analysing the accuracy and variability of meeting the control objectives. For example, one could analyse the distribution of the tether force during nominal operation. Robust operation would accurately keep the tether force close the design tether force with low variability.

5.2.3. Systematic robustness analysis

Instead of analysing the nominal and robust performance of the system by analysing its response to challenging conditions, one can aso performs a systematic robustness analysis.

For example, the structured singular value (μ) framework can be used to assess the robustness of linear systems in the frequency domain (Pollack & van Kampen, 2022; Rapp, 2021). However, these techniques mostly exist for linear systems. Augmentations for nonlinear techniques exist but are outside of the scope of this project.

5.3. Conclusion and discussion

For piloted aircraft and wind turbines, formal requirements on nominal and robust performance have been made by the relevant government authorities. However, such requirements (or even guidelines) do not exist for airborne wind energy.

The objective of airborne wind energy systems is to produce renewable power. So power output in nominal conditions is one of the main metrics, which can be evaluated using power curves. Because of the cascaded control architecture, reference tracking performance becomes a good intermediate metric to see where in the control architecture changes need to be made.

It is important that the system is robust to uncertainties and disturbances. During the design the performance with respect to model uncertainties, sensor errors, and measurement delays must be taken into account. Furthermore, the performance during turbulence and gust disturbances must be assessed.

6

Preliminary experiment: INDI in the MegAWES simulation framework

The third research question for the literature study is:

Research question 3

What is the performance of INDI when applied in the MegAWES simulation framework in a preliminary experiment?

To answer this question, the NDI inner loop rate controller in the MegAWES simulation framework is changed with an INDI implementation. First, the MegAWES simulation framework is described in section 6.1. Then the INDI control design with PCH is discussed in section 6.2. Finally, results are discussed in section 6.3.

6.1. The MegAWES simulation framework

The MegAWES simulation framework was made and described by Eijkelhof et al. (2020) and Eijkelhof and Schmehl (2022) and is available on GitHub through Eijkelhof, Fasel, and Rapp (2021). The framework is made as an open-source reference system for multi-megawatt, fixed-wing, ground-gen airborne wind energy systems. The current model has a nominal power of 3 MW. The aircraft is based on a scaled up version of Ampyx Power's AP-3 but with a wing area of 150 m^2. A render is shown in Figure 6.1 (Eijkelhof & Schmehl, 2022).

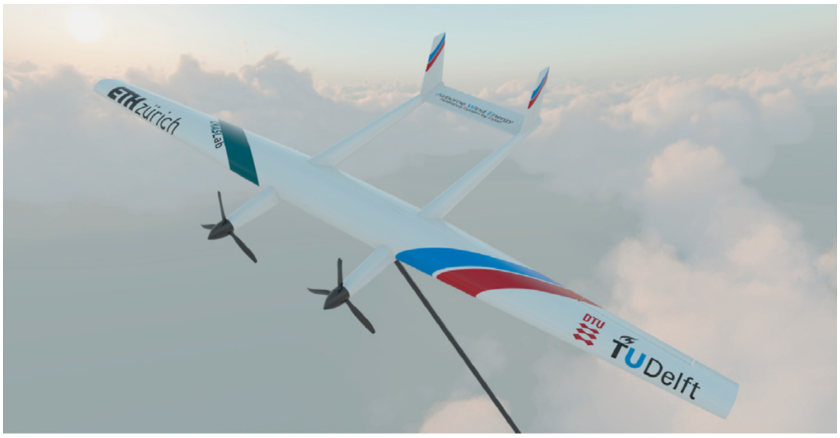

Figure 6.1: Render of the kite used by the MegAWES framework (Eijkelhof & Schmehl, 2022).

6.1.1. Modelling

The equations of motion are shown in Equation 6.1 and Equation 6.2 for translational and rotational dynamics respectively, where the superscript $\mathcal{B}$ refers to the body frame. Since this is a rotating frame the correction term with the cross product is needed. The Earth is assumed to be an inertial frame so the body rates can be used for this correction. For the rotational dynamics, the moment force of the tether is neglected as it is assumed that it is connected at the center of gravity of the kite.

$$\dot{v}_k^{\mathcal{B}} = \frac{1}{m}\left(F_{\text{aero}} + F_{\text{tether}} + F_{\text{g}} + F_{\text{prop,brake}}\right) - \omega \times v_k \tag{6.1}$$

$$\dot{\omega}^{\mathcal{B}} = J^{-1}\left[\left(M_{\text{aero}} + M_{\text{prop,brake}}\right) - \omega \times (J\omega)\right] \tag{6.2}$$

The aerodynamic properties of this kite are precomputed and used as lookup tables in the simulation. The aerodynamic coefficients as a function of angle of attack are obtained using a static fluid-structure interaction (FSI) algorithm for the main wing. The aerodynamic coefficients of the elevator and rudder are not determined using FSI but using RFoil (Van Rooij, 1996) and corrected for three-dimensional effects. Combining these gives the full system model including a model of the control moment coefficients as a function of angle of attack, shown in Equation 6.3. As can be seen from the matrix, some of the terms (for example $C_{n_{\delta_a}}$) were artificially set to zero. Furthermore, even though the pitching moment due to an aileron deflection ($C_{m_{\delta_a}}$) is usually set to zero, it has a nonzero value in this simulation. As the ailerons deflect they change the pitching moment of the wings asymmetrically for the left and right wing. Through the FSI simulation the effect was found to be significant enough to include in the simulation.

$$B_a = \begin{bmatrix} C_{l_{\delta_a}}(\alpha) & 0 & C_{l_{\delta_r}}(\alpha) \\ C_{m_{\delta_a}}(\alpha) & C_{m_{\delta_e}}(\alpha) & 0 \\ 0 & 0 & C_{n_{\delta_r}}(\alpha) \end{bmatrix} \tag{6.3}$$

A "quasi-steady lumped-mass tether model" is used, which neglects elastic vibrations but allows modelling the actual stiffness of the tether without using unreasonable small time steps. Tether modelling is quite important as its drag contribution to the overall system is significant and for large systems cannot be assumed to be straight or weightless.

The wind field consists of a non turbulent wind field with realistic wind shear taken from a reference offshore site - the IJmuiden offshore wind measurement tower. For the operating altitude of airborne wind energy this is more accurate than using the logarithmic wind speed profile, which is generally only valid up to an altitude of 200 m.

6.1.2. Control architecture

The control architecture is based on the work of Rapp, Schmehl, Oland, and Haas (2019) as discussed in subsection 2.3.3 The inner loop NDI controller has perfect information of the system model and measurements, which makes this controller suitable for investigating maximum performance.

The controller, flight path, and tether force setpoints are optimized using a Covariance Matrix Adaptive Evlotution Strategy (CMA-ES). The cost function is chosen so that the optimization maximises the mean pumping cycle power while penalising dangerous behaviour.

However, the winch controller tracks a tether force reference which is not optimal for power production, as discussed in subsection 2.2.6. So the power production could be optimized further by changing the winch control strategy.

6.2. INDI implementation

The inner loop rate controller makes use of the complete system model in two places: the NDI rate loop that calculates the control deflections and the hedging signal that limits the reference. The NDI loop will be replaced by an INDI loop and the hedge signal that uses the complete system model will be replaced by a PCH algorithm that only uses the control effectiveness.

6.2.1. INDI rate loop

The INDI controller will replace the NDI rate controller. So the starting point is to take the rotational equation of motion (Equation 6.2) and write it in the form of Equation 3.1, this simplified equation can

be used since the control variables are equal to the states of the system. This yields Equation 6.4, where $f(x)$ is left ambiguous since it is not needed for the control design.

$$\begin{aligned}\dot{\omega}^{\mathcal{B}} &= J^{-1}\left[M_{\text{total}} - \omega \times (J\omega)\right] \\ &= f(x) + G(x)u \\ &\text{Where} \\ G(x)u &= J^{-1}M_{\text{control}} \\ &= J^{-1} \cdot \frac{1}{2}\rho v_a^2 S \cdot \begin{bmatrix} bC_{l_{\delta_a}}(\alpha) & 0 & bC_{l_{\delta_r}}(\alpha) \\ bC_{m_{\delta_a}}(\alpha) & cC_{m_{\delta_e}}(\alpha) & 0 \\ 0 & 0 & bC_{n_{\delta_r}}(\alpha) \end{bmatrix} \begin{bmatrix} \delta_a \\ \delta_e \\ \delta_r \end{bmatrix}\end{aligned} \tag{6.4}$$

By substituting this expression for $G(x)$ into the INDI control law, as previously presented by Equation 3.4, the final INDI control law for rate control can be easily formulated and is shown in Equation 6.5. $\nu_{\dot{\omega}}$ is already calculated by a linear controller in the existing framework and was not adapted.

$$\Delta u = G^{-1}(x_0)(\nu_{\dot{\omega}} - \dot{\omega}) \tag{6.5}$$

6.2.2. PCH

Instead of the hedge signal that uses the complete system model, a hedge signal that only uses the control effectiveness, as discussed in subsection 3.3.1 was implemented. To do this, the difference between commanded and actual control deflection is used and the $G(x)$ term, as derived in Equation 6.4 to get the hedge signal $\nu_h = G(x)(u_c - \hat{u})$.

6.2.3. Control architecture

Combining these elements leads to the control architecture shown in Figure 6.2.

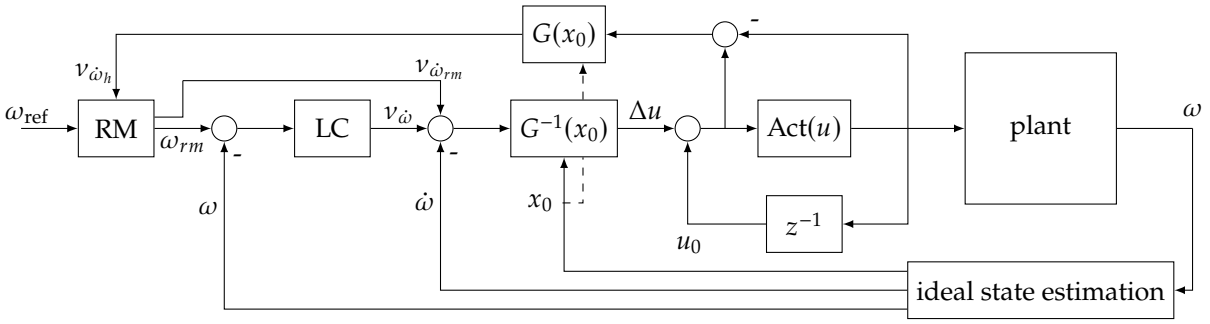

Figure 6.2: Block diagram of the inner loop attitude rate INDI controller used in the preliminary experiment.

6.2.4. Tuning

As discussed in section 3.1, INDI is a feedback linearization technique that results in perfect feedback linearization if there are no model uncertainties, sensing errors, and an infinitely high sampling rate is used. In this preliminary experiment the first two assumptions hold and the sampling rate is sufficiently high that INDI approximates perfect linearization, which the old NDI controller was also able to achieve (under the same assumptions). Grondman et al. (2018) noted that for their system, the outer loop gains could be tuned down since the INDI loop also acts as an integrator. But that was not needed in this experiment.

6.3. Results

A typical flight path together with the power output over time is shown in Figure 6.3 for one full cycle (traction and retraction). Since the MegAWES system is so heavy, it requires a positive power input

to keep the tether force in the upward motion of the figure of eight. This arises from the fact that the winch controller is commanded to keep a constant tether force. However, since the winch should aim to keep the kite at its optimal reel-out factor, the optimal tether force is not constant (Berra & Fagiano, 2021; Erhard & Strauch, 2015; Fechner & Schmehl, 2013; Luchsinger, 2013; Zgraggen et al., 2016). So changing the winch controller to reflect that could lead to an increase in power output.

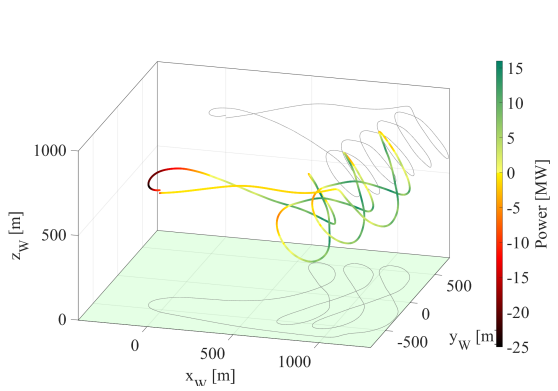

(a) Kite position over time including the power production at each point.

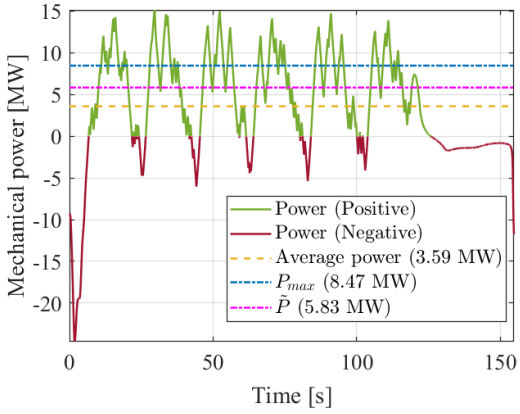

(b) The power production over time.

Figure 6.3: Kite performance with an INDI inner loop controller at a wind speed of 22 m/s.

As stated in the previous section, both NDI and INDI achieve perfect feedback linearization under the assumptions of this simulation. Thus, it is expected that the performance of the NDI and the INDI controller are almost identical. They are not exactly the same due to the step time of the simulation, which introduces a difference since the sampling time is not infinite. This can be observed when comparing the position in Figure 6.4 and attitude in Figure 6.5, which are almost exactly the same. This thus also leads to an equal power performance as shown in Figure 6.6

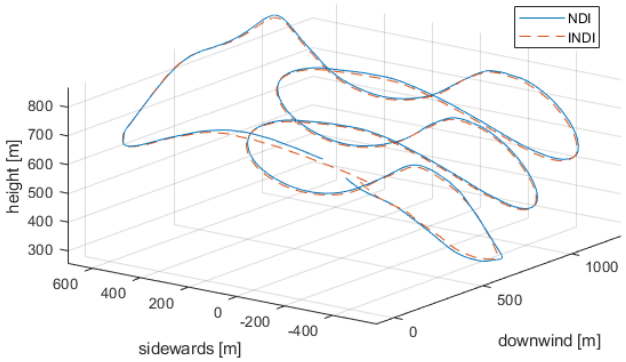

Figure 6.4: Comparing the position over time using NDI and INDI.

Lastly, the winch acceleration is clipping between its minimum and maximum desired value both when using the NDI and INDI kite controller as shown in Figure 6.7. This is because the winch controller uses a dynamic saturation to keep the acceleration a minimum and maximum value. It clips against these bounds 99.5% of the time. The reason is that the winch size is too small for the forces involved in this system. The radius of the winch is 0.4 m and its inertia 32 kgm^2, while the tether force is in the order of 1×10^6 N, leading to a winch system with extremely fast dynamics. Furthermore, the current radius and inertia are unrealistically small. So the winch must be resized to arrive at more realistic

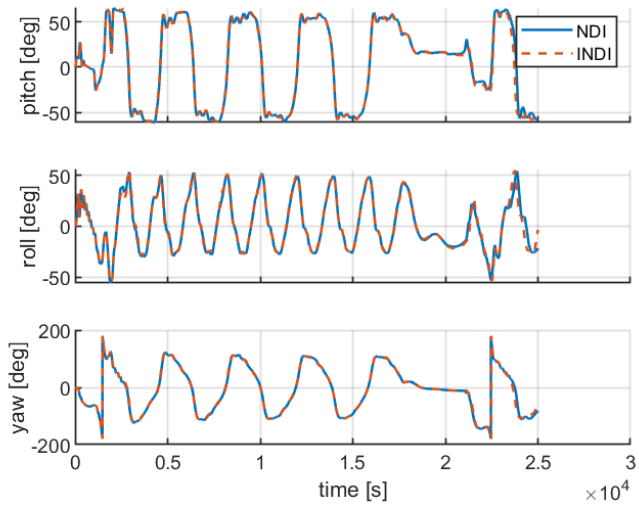

Figure 6.5: Comparing the attitude over time using NDI and INDI.

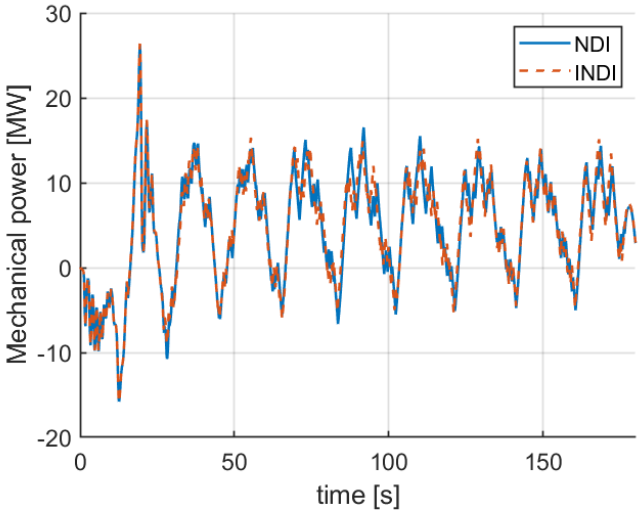

Figure 6.6: Comparing the power production over time using NDI and INDI.

values that lead to a more controllable system.

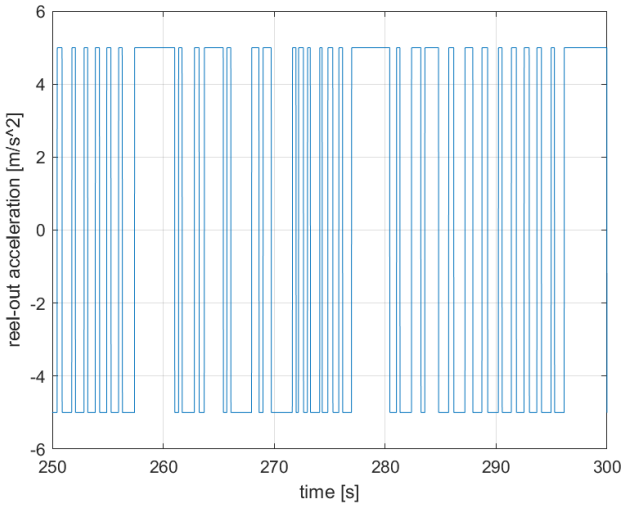

Figure 6.7: Winch reel-out acceleration during an arbitrary 50 second interval of the simulation.

6.4. Discussion and conclusion

MegAWES is the current state-of-the-art design and simulation framework for multi-MW scale airborne wind energy systems. A preliminary implementation of INDI as inner loop controller shows that it performs identical to the current NDI controller. Under the simulation's assumptions of no model uncertainty, perfect sensing, and a high sampling rate, this is expected.

The current control architecture keeps the tether force constant even though this is sub-optimal for power output. Furthermore, the winch is sized too small leading to extremely fast dynamics. A new power optimal winch controller and appropriately sized winch will be designed in this thesis.

7

Next steps towards kite tether force control

In chapter 4, a novel idea for kite control of airborne wind energy was presented: kite tether force control. When the system is at its power limit, the kite must lower its aerodynamic performance to stay at the power limit when the wind speed is increasing. Instead of using a precomputed reference angle of attack that is subobtimal in the face of model uncertainties and wind speed measurement uncertainties, kite tether force control allows the kite to adjust its angle of attack using the measured tether force. The platform on which this will be tested is the MegAWES simulation framework, which is a multi-MW scale airborne wind energy system simulation. In this work, a kite tether force controller in the point-mass simulation of MegAWES is developed. INDI is most useful for inner loop control, which is not required in 3DOF so will not be used in the rest of this thesis.

This will lower the peak power of MegAWES. Furthermore, the current winch controller will be changed to a feedforward winch controller. The current controller controls the tether force and would thus have the same objective as the kite controller. To separate the control authority, the winch controller will keep the kite on the ideal winch control curve while the kite controller will control the angle of attack.

7.1. Special considerations for kite tether force control on MegAWES

Some points of attention before implementing this novel control architecture in the MegAWES simulation are the kite mass, winch size, and winch control.

7.1.1. Kite mass

As the kite is flying figures of eight, gravity will have an accelerating and decelerating effect in the longitudinal direction. This increases and decreases the airspeed greatly, which in turn affects the lift, thus the tether force, and thus the produced power. This was clearly visible in Figure 6.3. This is analogous to a large amplitude sine-wave gust that constantly shifts the kite along the power curve. So not only should the kite adjust its angle of attack when the wind speed is increasing, it should also change the angle of attack when the airspeed is changing due to the effect of gravity.

That means that while the mean cycle power to wind speed will be the power curve for a given wind speed, as shown in Figure 2.1 and Figure 2.2, the instantaneous power will vary in time, at any constant wind speed. This is a subtle yet very important difference. Concretely, this means that the kite tether force control, which should be active above rated power, will not be activated above rated wind speed, but whenever the power exceeds rated power, which might be twice per figure of eight.

7.1.2. Winch mass

As discussed in chapter 6, the winch's size is currently too small. It's small radius (0.4 m) and its small inertia (32 kgm^2) combined with the high tether forces (about 1×10^6 N) create extremely fast dynamics which lead to unfavourable control qualities. With the current control architecture, this leads to the

winch acceleration clipping between its upper and lower bound more than 99% of the time.

This must be addressed by resizing the winch. A larger inertia makes the winch accelerate slower for a given difference between winch torque and tether force.

7.1.3. Winch control

As stated in chapter 6, the winch controller in the MegAWES framework controls the tether force. The reference tether force is only changed based on wind speed, which is in line with massless systems (Erhard & Strauch, 2015; Luchsinger, 2013; Zgraggen et al., 2016). However, this might not be a power optimal strategy because it does not keep the kite at its ideal reel-out factor. Since the airspeed changes as the kite is flying up and down, adjusting the tether force reference based on the airspeed (or a related measure) might be more optimal. It might be possible to reduce the tether force when the kite is flying upwards, meaning that the generator does not need to put energy in the systems (the red line in Figure 6.3). Furthermore, the peak power will be reduced by using kite tether force control. Lowering the spread between minimum and peak power is good for ground system sizing (Joshi et al., 2022).

For massless kites, the optimal winch controller is well-established (Todeschini et al., 2021; Zgraggen et al., 2016). However, for kite's with significant mass, such as the MegAWES kite, it needs to be investigated how to adjust this control law to be optimal for heavier systems. Optimal winch control for multi-MW scale systems has been performed for fly-gen systems (Trevisi, Castro-Fernández, Pasquinelli, Riboldi, & Croce, 2022) but not for ground-gen systems. The optimal strategy has a new layer of complexity due to the mass effect which makes the kite accelerate and decelerate over its figure of eight, meaning the power output during the traction phase cannot be constant. So an additional optimisation for during the loop should be done.

7.1.4. Actuators

Tether force control by the kite can be achieved using various direct lift actuators such as flaps, flaperons, lift dumpers, or flap deflections. The tether force can also be indirectly controlled using the elevators that can change the rotation rate, which has an effect on angle of attack. The latter has a lower bandwidth but is available in all systems. While using the flaps have a higher control bandwidth, they also don't have unlimited control authority so a control architecture like in Lombaerts and Looye (2013) could be adapted to let the flaps return to neutral positions by using the (slower) elevators to change the lift.

However, since a 3DOF simulation is used, the control inputs are the angle of attack and bank angle. So the controller does not need to use the elevators or direct-lift surfaces to achieve the desired angle of attack. To ensure that the angle of attack is not unrealistically used as input, there is a second order reference model that adds maximum rates and a delay between the actual and commanded angle of attack (Eijkelhof et al., 2020).

7.2. Control requirements

There are two areas for control requirements: optimum power output and safety. Unlike for piloted aircraft or wind turbine design, no official requirements are available since this is such an emerging technology that the regulatory framework is not there yet. So requirements are formulated based on existing requirements in literature, conversations with experts, and the author's own engineering experience.

1. The controller shall optimize the power curve (Li, Olinger, & Demetriou, 2015b).
   (a) In the MegAWES simulation framework, the controller shall be able to operate at or below the cut-in wind speed of 10 m/s at operating altitude (Eijkelhof & Schmehl, 2022).
   (b) In the MegAWES simulation framework, the controller shall be able to operate at or above the cut-out wind speed of 30 m/s at operating altitude (Eijkelhof & Schmehl, 2022).
   (c) When below system limits, the controller shall maximize power output by operating at the optimal reel-out speed[1] and optimal lift-to-drag ratio.
2. The controller shall respect system limits.

[1]As mentioned previously, this is currently not done in the MegAWES simulation framework as the winch controller controls the tether force to a maximum setpoint which is not power optimal.

   (a) When using a 2-phase strategy, the controller shall lower the lift-to-drag ratio of the kite in phase 2 (Luchsinger, 2013).
   (b) When using a 3-phase strategy, the controller shall stay at maximum tether force at the hightest lift-to-drag ratio in phase 2 (Fechner & Schmehl, 2013).
   (c) When using a 3-phase strategy, the controller shall lower the lift-to-drag ratio of the kite in phase 3.
   (d) With some designs, overloading of the generator is possible (Bauer et al., 2019), in that case, the controller shall take overloading limits into account.

3. The controller shall fly in a safe manner.

   (a) The controller shall have at least 90% of nominal power production and no significant increase in failure at turbulence of medium intensity as defined by Department of Defence (1997).
   (b) The controller shall not rupture the tether with wind gusts of at least 15 m/s as this is the state-of-the-art (Rapp & Schmehl, 2021).
   (c) The controller must be robust to design limitations such as model uncertainties up to 20% and time delays up to 200 ms, which are average in the studies literature.
   (d) The controller shall have a tether rupture probability below 2×10^{-7} if the design tether force is 2/3 of the maximum tension, which is the current state-of-the-art without avoidance manoeuvres (Rapp & Schmehl, 2021).
   (e) The controller shall keep the angle of attack below its stall limit, 18 deg for MegAWES (Eijkelhof & Schmehl, 2022).

4. The controller must be feasible to implement.

   (a) The computational complexity of the controller shall be appropriate for embedded systems to run in real-time.

7.3. Research objective and questions for the rest of this thesis

The research objective for the rest of the thesis is formulated as follows:

Research objective

Reduce the power fluctuations of utility-scale airborne wind energy systems by implementing a power limit in the 3DOF MegAWES simulation framework using a feedforward winch controller and kite tether force control.

To achieve this objective, the following research questions will have to be answered:

1. What is the effect of the radius and inertia of the winch on the system dynamics? chapter 9

   (a) What are the equations of motion of the winch?
   (b) How does the pole location change based on the radius and inertia?
   (c) What is a desirable pole location for MegAWES?
   (d) What is the effect of good and bad design of the winch radius and inertia.

2. How to adapt the existing feedforward winch controllers that are derived for massless kites for kites with mass? chapter 10

   (a) How does the optimal reel-out factor change for kites with mass?
   (b) Is there a minimum required tether force to keep the kite in the air when it is overcoming the force of gravity?
   (c) How can the optimal winch control strategy take this into account?
   (d) Is the generated power higher when using the adapted winch controller?

3. Does kite tether force control successfully limit the peak power? chapter 11

   (a) How to design a 3DOF kite tether force controller?
   (b) What is the peak power when using kite tether force control?
   (c) How much did the mean power reduce when implementing a power limit with kite tether force control?

7.4. Conclusion and discussion

To test the idea of kite tether force control a scope has been set. In the 3DOF MegAWES fixed-wing, ground-gen simulation framework, a power limit will be implemented using the 2-phase strategy. In the 3DOF simulation, kite tether force control can be achieved by directly changing the commanded angle of attack.

The research objective for the rest of the thesis is different than the one outlined for this literature study. Implementing a power limit in the MegAWES simulation framework will improve reliability of these systems in the future as operation close or over power limits can be dangerous. However, reliability won't be the main point of attention for the rest of the thesis. Rather it will be on improving the power output by reducing the peak power and eliminating the power-consuming parts during the traction phase.

8

Conclusion

Airborne wind energy is an emerging technology that could harvest high altitude winds which could lead to more energy extraction during a larger portion of the time. The fixed-wing, ground-gen concepts do this by letting a tethered kite pull on the tether to create power at the ground-based generator. One of the major challenges in further development is reliability, of which robust control is an important factor. INDI is a nonlinear control technique that could improve the nominal and robust performance of airborne wind energy systems. It has a lower model dependency than currently used MPC controllers and has good disturbance rejection capabilities. The goal of this literature study has been to improve the reliability of fixed-wing, ground-gen airborne wind energy systems in a turbulent and gusty wind field by investigating the nominal and robust performance of INDI controllers on the MegAWES simulation framework. To reach that goal, multiple research questions were answered, which led to a novel idea: kite tether force control.

Research question 1A

What is the state-of-the-art of airborne wind energy control design?

Control architectures for airborne wind energy usually consist of multiple cascades of which flight control is the most inner loop. An inner loop controller does not directly control the power output but rather aims to stay on a path that is precomputed to be power-optimal. The current state-of-the-art inner loop controllers are heavily model-dependent and have a high computational complexity, such as MPC and NDI. That's why sensor-based INDI could be a good inner loop control candidate as it has a lower model dependency but high performance.

Research question 1B

What is the state-of-the-art of INDI controller design?

INDI is a feedback linearization technique that has a lower model dependency and increased robustness compared to NDI. Disturbance rejection of INDI is excellent and remains good under model uncertainties of the control effectiveness. To ensure a proper functioning of an INDI controller a high sampling frequency and a good estimate of the output derivative is needed. Because the output derivative is often obtained through filtering, the matching strategy can be utilized to mitigate the issues arising from the synchronization effect. PCH can ensure that the INDI bandwidth stays below the actuator bandwidth to avoid performance losses. Furthermore, augmentations exist to use INDI on over and under-actuated systems.

Research question 1C

How could INDI be applied in airborne wind energy control design?

When the system is at its tether force limit and power limit, the kite controller should lower its angle of attack. For massless kites, this only happens as the wind speed increases beyond rated wind speed, but for kites with mass this can happen on a once-per-loop basis as the kite is flying up and down. Thus the angle of attack of the kite needs to be controlled. Current approaches use an offline optimised angle of attack reference but this is sub-optimal when taking model uncertainties and uncertain wind speed measurements into account. Furthermore, because of the fast interaction between the kite and the tether, a high bandwidth controller is desired to control the angle of attack based on the measured tether force. INDI is a good candidate for this control architecture because of its high bandwidth and low model dependency. It could use direct lift surfaces such as flaps, flaperons, lift dumpers, or symmetric aileron deflections to change the lift with a high bandwidth or use the elevators to change the angle of attack through a rotation. This is the main idea that will be further investigated in the thesis.

Research question 2

How to measure the nominal and robust performance of an airborne wind energy system controller?

While for piloted aircraft and wind turbines formal requirements on nominal and robust performance exist, they are not existent for airborne wind energy yet. However, from the objective of energy production for airborne wind energy system, nominal and robust performance metrics were chosen. The system should produce power optimally during nominal conditions and must lose less than 10% of its power output under model uncertainties, sensor noise, time delays, turbulence and gusts. Furthermore, the tether failure probability, the critical failure mode for airborne wind energy systems should have a probability below 2×10^{-7}, the current state-of-the-art.

Research question 3

What is the performance of INDI when applied on the MegAWES simulation framework in a preliminary experiment?

For the preliminary experiment an INDI inner loop controller was implemented in the MegAWES simulation framework. Under the simulation's assumptions of perfect sensing and no model uncertainties, it had the same performance as the existing NDI controller which is expected.

As mentioned before, the next steps in this project will further develop the kite tether force control architecture in the 3DOF simulation of MegAWES. This means that the research goal for the rest of the thesis can be formulated as "Reduce the power fluctuations of utility-scale airborne wind energy systems by implementing a power limit in the 3DOF MegAWES simulation framework using a feedforward winch controller and kite tether force control.". To achieve this, new research questions have been proposed which will be answered in the rest of the thesis.

Improving the quality of the generated power is not directly related to improving the reliability, so the research objective for the rest of this thesis deviates from this literature study. It will make control of utility-scale airborne wind energy systems more feasible as the current peak power of MegAWES would be difficult to work with as the generator needs to be heavily over-designed. To that end, it could be argued that it indirectly contributes to improving the reliability of utility-scale systems as the power output will be more gentile.

Part IV

Additional results

9

Winch parameter design

The fourth research question is:

Research question 4

What is the effect of the radius and inertia of the winch on the system dynamics?

The inertia and radius of the winch can have a large effect on the dynamics of an airborne wind energy system that has not yet been investigated in the literature. The current inertia and radius for the MegAWES system are unrealistically small compared to megawatt generators. In addition, this leads to dynamics that are too fast to be simulated without using stiff solvers or very small time steps or that lead to unrealistic results when this is not taken into account. Since no megawatt-scale airborne wind energy systems exist today, obtaining realistic estimates is difficult. Instead, this chapter aims to show what appropriate values for the winch sizing would be when the dynamics of the system are considered. In section 9.1 the equations of motion for the winch will be derived. These will be analysed in section 9.2, to arrive at appropriate values for the MegAWES system. The results will be verified in a quasi-steady simulation in section 9.3.

9.1. Equations of motion

The winch itself is a rotating drum with a tether rolled around it and can be connected with a gearbox to a generator. This whole system can be modelled when looking at detailed design of the generator, such as in Elkodama, Ismaiel, Abdellatif, and Shaaban (2022), that does this for a wind turbine. However, in this work, for simplicity, the system of winch and generator is modelled as a single rotating body that can be controlled by a torque.

The derivation of the equations of motion is given in Equation 9.1, where J denotes the winch inertia, ω the winch rotation speed, F_t the tether force, r the winch radius, τ the winch torque, d the winch rotational friction and v_r the reel-out speed. The output variable is the reel-out speed (v_r), rather than the winch rotational speed (ω) to be able to split the contributions of winch parameters and kite parameters later on.

$$
\begin{aligned}
\sum M(t) =& J\dot{\omega}(t) \\
&\text{where} \\
\sum M(t) =& F_t(t)r - \tau(t) - d\omega(t) \\
\omega(t) =& v_r(t)/r \\
&\text{so} \\
\dot{v}_r(t) =& \frac{F_t(t)r^2 - \tau(t)r - dv_r(t)}{J}
\end{aligned}
\tag{9.1}
$$

The tether force can be calculated by using a kite model. To keep the analysis independent of kite dynamics, a quasi-steady model is utilised. This model assumes that a kite instantly adjusts to a change in reel-out or wind speed. To keep the analysis general and solvable with analytic equations, the massless quasi-steady model from van der Vlugt, Bley, Noom, and Schmehl (2019) is used. The tether force as a function of reel-out and wind speed is shown in Equation 9.2, where the convention for $\mathscr{C}$ from Zgraggen et al. (2016) is used. Furthermore, ρ denotes air density, v_w denotes wind speed, S denotes wing reference area, L denotes lift, D denotes drag, β denotes elevation, φ denotes azimuth and f denotes reel-out factor.

$$\begin{aligned} F_t =& \frac{1}{2}\rho v_w^2 S C_R \left[1 + \left(\frac{L}{D}\right)^2\right](\cos\beta\cos\varphi - f)^2 \\ =& \frac{1}{2}\rho S C_R \left[1 + \left(\frac{L}{D}\right)^2\right](v_w\cos\beta\cos\varphi - v_r)^2 \\ =& \mathscr{C}(v_w\cos\beta\cos\varphi - v_r)^2 \end{aligned} \tag{9.2}$$

where

$$\mathscr{C} = \frac{1}{2}\rho S C_R \left[1 + \left(\frac{L}{D}\right)^2\right]$$

9.1.1. Winch control law

For the generator torque (τ) in Equation 9.1, a control law for this system must be derived to arrive at the closed loop dynamics. An ideal winch controller, drives the system such that the kite operates in its optimal state to extract the most amount of energy from the wind. Loyd (1980) already derived that for massless kites in an infinite traction phase where the wind is always perpendicular (no elevation or azimuth), the maximum power is obtained at a reel-out factor of $\frac{1}{3}$. More generally, the ideal reel-out factor is one third of the wind speed in tether direction, which was for example shown by van der Vlugt et al. (2019). This then occurs at a reel-out factor of $\frac{1}{3}\cos\beta\cos\varphi$. Since the reel-out factor is defined as $\frac{v_r}{v_w}$, this can be rewritten as $v_w = \frac{3}{\cos\beta\cos\varphi}v_r$ and substituted in Equation 9.2 to derive the ideal tether force as a function of only reel-out speed in Equation 9.3.

$$F_t^* = \mathscr{C}(3v_r - v_r)^2 = 4\mathscr{C}v_r^2 \tag{9.3}$$

A significant finding here is that the ideal tether force as a function of reel-out speed is independent of the kite's elevation and azimuth because the cosine terms cancel each other out. This means that without knowledge of wind speed or the kite's location, this equation can be used by the winch to derive the ideal tether force.

To drive the system to this ideal tether force a simple feedforward equation can be used. By multiplying the ideal force by the radius of the winch a torque is obtained which aims to be in equilibrium with the ideal tether force for a given reel-out speed. This control law is shown in Equation 9.4 as equation and Figure 9.1 and is used by Todeschini et al. (2021) and Zgraggen et al. (2016). If the wind speed would increase, causing an increase in tether force, the reel-out speed will increase, causing a deviation from this optimum. However, as the reel-out speed increases, the tether force will decrease. Furthermore, the torque of the winch will increase. The decreasing tether force and increasing torque will find a new equilibrium where the system is stable at a new tether force and reel-out speed but at the same ideal reel-out factor, leading to optimal power extraction.

$$\tau = 4\mathscr{C}v_r^2 r \tag{9.4}$$

Improvements to this control law exist that will be discussed in the next chapter are the effect of the kite's mass, tether length, the retraction phase, and the tether force and power limit.

9.1.2. Closed loop dynamics

The closed loop dynamics can be obtained by substituting the winch control law into the equations of motions and is shown in Equation 9.5. Next, the closed loop dynamics will be trimmed and linearise to

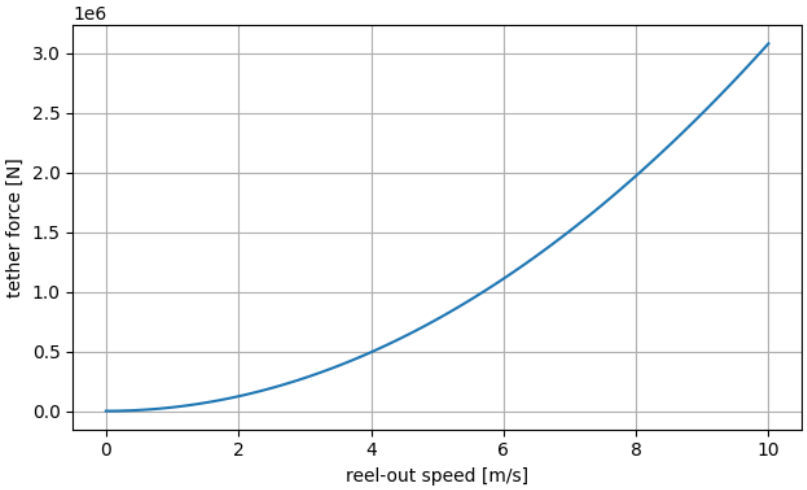

Figure 9.1: Optimal winch strategy for a massless system.

arrive at a transfer function for this system.

$$\begin{aligned}\dot{v}_r(t) =& \frac{\left[\mathscr{C}(v_w \cos\beta\cos\varphi - v_r)^2\right] r^2 - \left[4\mathscr{C}v_r^2 r\right] r - d v_r(t)}{J} \\ =& \frac{\mathscr{C}r^2\left[(v_w \cos\beta\cos\varphi - v_r)^2 - 4v_r^2\right] - d v_r(t)}{J}\end{aligned} \tag{9.5}$$

Trimming
The winch control law drives the system to equilibrium positions where the reel-out speed and wind speed are related through $v_{w_0} = \frac{3v_{r_0}}{\cos\beta\cos\varphi}$. So this defines the trim points.

Linearising
To do some frequency domain analysis, the closed loop dynamics are linearised to arrive at a system with the wind speed as input and reel-out speed as state. The elevation and azimuth are thus not used as inputs and are assumed to be constant. It is assumed that this linearisation is around a trim point such that $\dot{v}_{r_0} = 0$.

$$\begin{aligned}\dot{v}_r(t) \approx& \dot{v}_{r_0} + \frac{\partial \dot{v}_r(t)}{\partial v_r}_{v_{w_0}, v_{r_0}} \Delta v_r + \frac{\partial \dot{v}_r(t)}{\partial v_w}_{v_{w_0}, v_{r_0}} \Delta v_w \\ \approx& 0 + \left[-2\frac{\mathscr{C}r^2}{J}(v_{w_0}\cos\beta_0\cos\varphi_0 - v_{r_0}) - 8\frac{\mathscr{C}r^2}{J}v_{r_0} - d\right]\Delta v_r \\ &+ \frac{\mathscr{C}r^2}{J}\left[2(v_{w_0}\cos\beta_0\cos\varphi_0 - v_{r_0})(\cos\beta_0\cos\varphi_0)\right]\Delta v_w\end{aligned} \tag{9.6}$$

By omitting the Δ-notation and the approximation sign, and realising that the reel-out speed and wind speed are related through $v_{w_0} = \frac{3v_{r_0}}{\cos\beta\cos\varphi}$ at the trim points, the equation can be simplified to Equation 9.7.

$$\dot{v}_r(t)J = -\left[12\mathscr{C}r^2 v_{r_0} + d\right]v_r(t) + 4\mathscr{C}r^2 v_{r_0}\cos\beta_0\cos\varphi_0 v_w(t) \tag{9.7}$$

Laplace transform
Taking the Laplace transform allows a frequency domain analysis. The result of the Laplace transform of Equation 9.7 is shown in Equation 9.8 with a derivation to get it to transfer function form.

$$\begin{aligned} sV_r(s)J &= -\left[12\mathscr{C}r^2v_{r_0} + d\right]V_r(s) + 4\mathscr{C}r^2v_{r_0}\cos\beta_0\cos\varphi_0 V_w(s) \\ \frac{V_r(s)}{V_w(s)} &= \frac{4\mathscr{C}r^2v_{r_0}\cos\beta_0\cos\varphi_0}{Js + 12\mathscr{C}r^2v_{r_0} + d} \end{aligned} \tag{9.8}$$

9.2. Analysing the equations of motion

The transfer function shown in Equation 9.8 described the behaviour of the closed loop dynamics when using the popular feedforward winch control law derived in subsection 9.1.1. The pole location of this system is described by Equation 9.9. From this a couple of observations can be made, which can then be used to analyse the current winch parameters proposed for MegAWES and subsequently be used to select more appropriate ones.

$$s = -\frac{12\mathscr{C}r^2v_{r_0} + d}{J} \tag{9.9}$$

1. The pole is always in the left-hand plane. So using this control law (Equation 9.4) makes the system asymptotically stable, as also discussed by Zgraggen et al. (2016).
2. The pole location is highly dependent on the trim point v_{r_0}. This means that the system has a faster response around the trim point with a high reel-out speed and that the response is slower around trim points where the reel-out speed is low. It is important to realise that at a trim point the wind and reel-out speed are related through $v_{w_0} = \frac{3v_{r_0}}{\cos\beta\cos\varphi}$, so that trim points with a low reel-out speed correspond to low wind speeds. So the worst-case lag occurs at the lowest reel-out speed. This means that for the controller design, a certain minimum reel-out speed must be selected for which the system must behave well.
3. The two parameters of the winch (r and J) have an opposite effect on the pole location. Increasing r moves to pole to the left while increasing J moves the pole to the right.

9.2.1. Winch parameters for MegAWES

Using these observations about the closed loop dynamics, the specific system dynamics for the MegAWES parameters previously proposed in Eijkelhof et al. (2020) and Eijkelhof and Schmehl (2022) can be analysed. Using those winch parameters ($J = 32\,\mathrm{kgm^2}$, $r = 0.4\,\mathrm{m}$, at an typical reel-out speed of $v_r = 5\,\mathrm{m/s}$), the pole is located at $s = -2.3 \times 10^3$, meaning that the time constant of this system at this operating point is $4.3 \times 10^{-4}\,\mathrm{s}$, which is too small to realistically control or simulate the system. If the controller would run at 100 Hz, this would already lead to instabilities because of how much slower that is than the system. This also makes intuitive sense since the tether force is usually around 1 MN but it only has a winch inertia of $32\,\mathrm{kgm^2}$ to pull against. In addition, from a physical perspective, the winch inertia in MegAWES is currently unrealistically low. In contrast, Elkodama et al. (2022) analyses a 5 MW wind turbine which has a generator inertia of $5.3 \times 10^5\,\mathrm{kgm^2}$ about the high speed axis. With a gear ratio of 97 : 1, the inertia around the low speed axis, which is comparable to how it is modelled in the MegAWES framework, would be around $5.2 \times 10^7\,\mathrm{kgm^2}$. So a new set of winch parameters needs to be found that is more realistic and that has the correct time constant for the MegAWES system.

The required time constant for MegAWES is lower than the required time constant for wind turbines or small airborne wind energy systems. This is because the system must not only adapt to the change in wind speed (which has a large timescale) but also to the change in tether force as the kite is flying over the loop, due to the kite's mass. This has must faster dynamics than the wind itself. The frequency of halve a figure-of-eight (the fundamental frequency at which the tether force oscillates) is about 0.05 Hz or $\pi/10$ rad/s at a wind speed of 22 m/s, as can be seen from Figure 10.12. If the winch has a time constant higher than this, it will have a negative effect on power output because it won't be able to adapt its reel-out speed quickly enough to stay at the optimal reel-out factor. This can be analysed by looking at a bode plot of the power output over tether force frequency. For this, the transfer function for power output over tether force is derived in Equation 9.10, where P is the power output of the system.

$$
\begin{aligned}
P(t) =& \omega \cdot \tau = \frac{v_r(t)}{r} \cdot 4\mathscr{C} r v_r(t)^2 = 4\mathscr{C} v_r(t)^3 \\
&\text{linearise} \\
P(t) =& 12\mathscr{C} v_{r_0}^2 v_r(t) \\
&\text{Laplace transform} \\
P(s) =& 12\mathscr{C} v_{r_0}^2 V_r(s) \\
&\text{Substituting } \frac{V_r(s)}{V_w(s)} \\
\frac{P(s)}{V_w(s)} =& \frac{48\mathscr{C}^2 v_{r_0}^3 r^2 \cos\beta_0 \cos\varphi_0}{Js + 12\mathscr{C} r^2 v_{r_0} + d}
\end{aligned}
\tag{9.10}
$$

The power output and force are not on the same scale, which makes the bode plot not start at 0 dB. So the transfer function is divided by the steady-state power output for a given force. This can be calculated by the final value theorem as shown in Equation 9.11.

$$
\begin{aligned}
P_{\text{ideal}} &= \lim_{t\to\infty} P(t) = \lim_{s\to 0} sP(s) \\
&= \lim_{s\to 0} \frac{48\mathscr{C}^2 v_{r_0}^3 r^2 \cos\beta_0 \cos\varphi_0 s\frac{1}{s}}{Js + 12\mathscr{C} r^2 v_{r_0} + d} \\
&= \frac{48\mathscr{C}^2 v_{r_0}^3 r^2 \cos\beta_0 \cos\varphi_0}{12\mathscr{C} r^2 v_{r_0} + d}
\end{aligned}
\tag{9.11}
$$

The Bode plot of $\frac{P(s)/P_{\text{ideal}}}{V_w(s)}$ is shown in Figure 9.2 for different values of J and a v_{r_0} of 5 m/s. A vertical line is added at the frequency of halve a figure-of-eight of MegAWES. From this it is clear that the power output would be lowered dramatically for values of J higher than 1×10^5 kgm^2 when analysed at this reel-out speed.

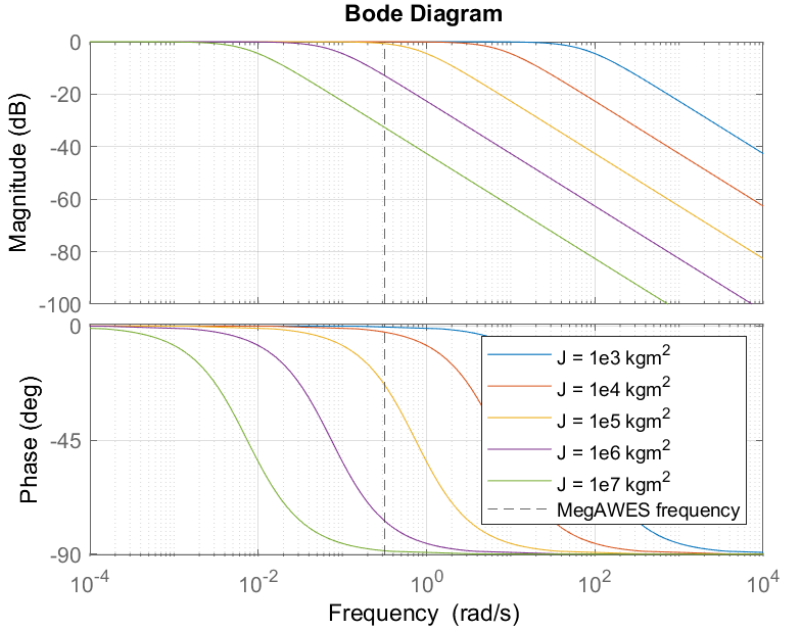

Figure 9.2: Bode plot of $\frac{P(s)/P_{\text{ideal}}}{V_w(s)}$ for different values of J and a v_{r_0} of 5 m/s.

There are a couple of options to solve this. First, the winch parameters (r and J) can be chosen differently. Since the current parameters are not realistic, this solution is used in this work. Two other

potential solutions are using a PI controller to track the tether force and push the winch when it is lagging behind. However, this would lead to additional power spent on rotating the winch rather than extracting power, as will be shown in the next chapter. Finally, the frequency of the figure-of-eight can be adjusted by flying a different flight path.

9.2.2. Selecting new winch parameters for MegAWES

To find suitable values for r and J over all reeling speeds, the magnitude of the bode plot (Figure 9.2) was calculated for different values of r, J, and v_{r_0}. The magnitude was taken at the tether force frequency of MegAWES multiplied by a factor of 10, so that the system can also adjust to slightly faster variations due to, for example, gusts. This creates a 3D volume from which different slices can be visualised. In Figure 9.3, J and r are plotted on the x and y axis while slices of the volume are made at distinct reel-out speeds and power fractions (pf), where the power fraction is the magnitude of the transfer function at 10-times the MegAWES frequency expressed as a fraction between 0 and 1, rather than in dB. For example, when following the solid red line, the required relationship between J and r can be read of to achieve a power fraction of 0.99 at $v_{r_0} = 0.1\,\mathrm{m/s}$. A few observation can be made:

1. For a given reel-out speed and desired power fraction, the radius must increase if the inertia of the winch increases.
2. For a given radius, the allowed maximum inertia to achieve a certain power fraction increases as the reel-out speed increases.
3. For a given inertia, the allowed minimum radius to achieve a certain power fraction decreases as the reel-out speed increases.
4. Moving to the left and up, yields a higher power fraction for a given reel-out speed or achieves the same power fraction at a lower reel-out speed.
5. To keep the same performance (same power fraction at the same reel-out speed, e.g. following one of the lines) the inertia must increase 4 times if the radius doubles. (This relation was previously explored with the fraction $\frac{Sr^2}{J}$.)

So a balance must be struck between a low inertia and high radius where the power fraction is high for all reel-out speeds and a high inertia and low radius which is more realistic and doesn't lead to simulation issues due to the low time constant.

Since the requirements become more stringent at lower reel-out speeds, the inertia and radius will be selected for the lowest reeling speed where the the feedforward control law should still apply. A minimum reel-out speed of 1 m/s is selected. So from Figure 9.3, the required inertia and radius for a reeling speed of 1 m/s are selected: $r = 1.5\,\mathrm{m}$ and $J = 1 \times 10^4\,\mathrm{kgm}^2$. The radius is similar to the 5.0 MW reference design used by Hagen, Petrick, Wilhelm, and Schmehl, 2023 that has a radius of 2.0 m. However, the inertia is smaller than the typical inertia of a generator of a wind turbine of similar power around the low speed axis of approximately $1 \times 10^7\,\mathrm{kgm}^2$ Elkodama et al., 2022. The chosen parameters serve more as a guideline to what would be desirable for such a system to operate without lags that lead to a loss of power without providing a realistic reference design. With these parameters, a zoomed in magnitude bode plot is shown in Figure 9.4. It is clear that at a reel-out speed of 1 m/s the loss of power is negligible at the MegAWES frequency ($\pi/10$ rad/s), reaches 0.99 (-0.0873 db) power fraction at 10 times the MegAWES frequency (π rad/s), and that the resulting bandwidth is 20.8 rad/s.

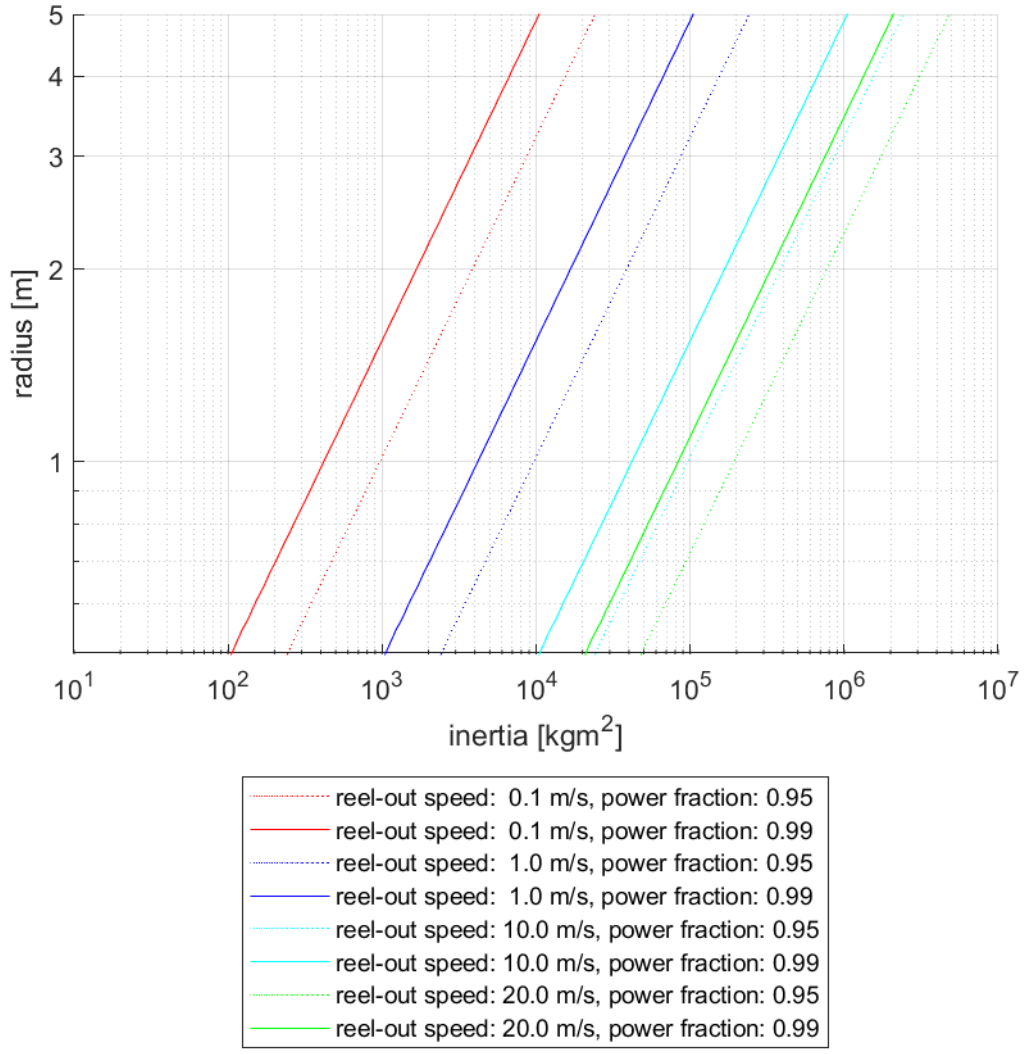

Figure 9.3: Inertia and radius for certain power fractions (pf) at distinct reel-out speed trim conditions at 10-times the MegAWES tether force frequency.

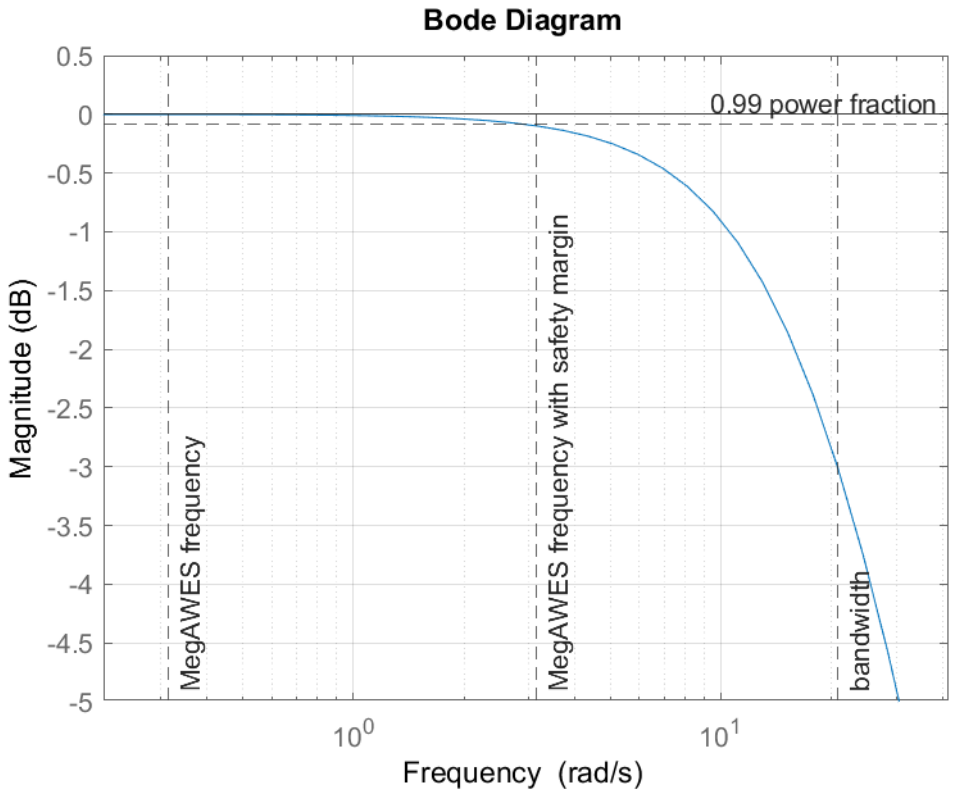

Figure 9.4: Magnitude bode plot of $\frac{P(s)/P_{\text{ideal}}}{V_w(s)}$ with the selected winch parameters of $I = 1 \times 10^4\,\text{kgm}^2$ and $r = 1.5\,\text{m}$ at a trim reel-out speed of $1\,\text{m/s}$.

9.3. Verification

To verify these results, a winch with different parameters was simulated in a nonlinear simulation. In addition to the winch model and controller, a massless kite model was added. This kite model uses the quasi-steady model from Loyd (1980) and maps a wind and reel-out speed to a tether force. The kite parameters of MegAWES are obtained from Eijkelhof and Schmehl (2022). A block diagram is shown in Figure 9.5.

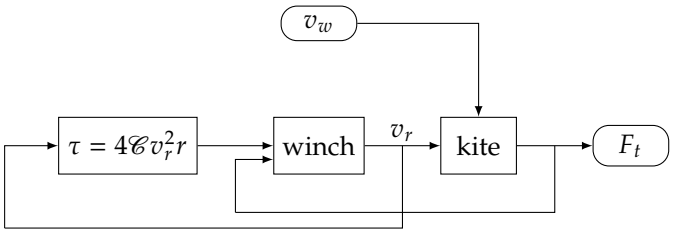

Figure 9.5: Block diagram for the winch parameter verification simulation

Using the feedforward control law (Equation 9.4) and a winch with an inertia of $1 \times 10^4\,\mathrm{kgm}^2$ and a radius of 1.5 m the response was simulated to a wind speed signal of $15 - 10\cos(\pi/10 \cdot t) + 2.5\sin(\pi \cdot t)$ where the kite was flying downwind of the ground station. This is much faster than how the wind would typically change, but it is designed to excite the system at the MegAWES tether force frequency of $\pi/10\mathrm{rad/s}$ together with a signal at 10 times that frequency. If the feedforward control law can keep the system at the optimal reel-out factor, the winch parameters are sized correctly. In Figure 9.6a, the reel-out speed, wind speed and reel-out factor are compared. The system is able to sufficiently quickly adapt its reel-out speed such that it is always around $\frac{1}{3}$ of the wind speed. At low reel-out speeds, the response is slightly slower, leading to small oscillations around the optimal reel-out factor. This is the desired response so will be the benchmark for comparing against higher and inertia and lower radius. The average power obtained in this benchmark is 6.59 MW, as show in Figure 9.6b. In that figure, both power in ($P_{\text{in}} = F_t \cdot v_r$) is shown as well as power out ($P_{\text{out}} = \tau \cdot \omega$). The power in is equal to the power that the kite puts into the system by pulling on the tether while the power out is equal to the power that is taken out of the system by using the winch torque. In this case, the power in and out are very close to each other over the time domain.

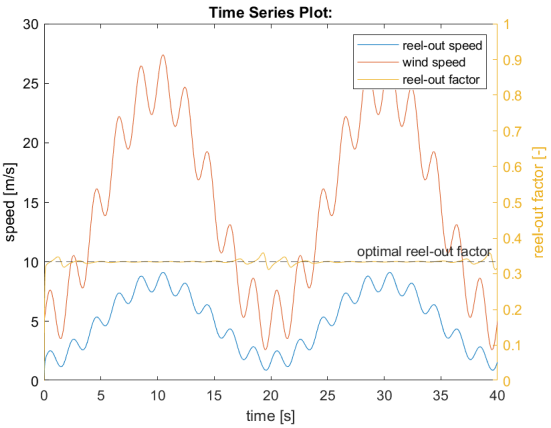

(a) Reel-out and wind speed (left axis) and reel-out factor (right axis).

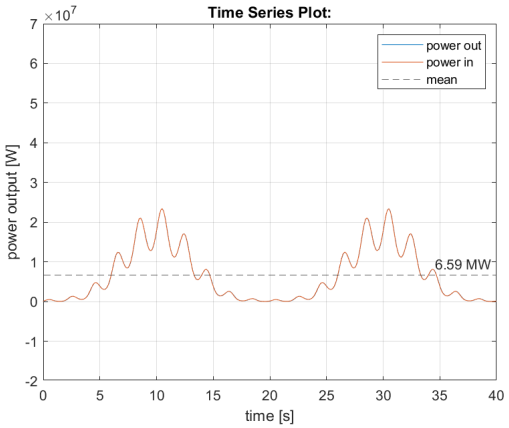

(b) Power input of the kite into the system and power output of generator.

Figure 9.6: Using the chosen winch parameters on a massless kite model.

The same scenario is repeated but with a winch with an inertia that is 200 times higher. From Figure 9.7a, it is clear that the reel-out speed does not respond as much to the higher frequency signal in the wind and that this effect is greater at lower reel-out speeds, just as predicted. The resulting reel-out factor is very oscillatory and deviates from the optimal value. Furthermore, at low wind speeds this even results in reel-out factors greater than 1. This means the tether is reeled out faster than the wind

speed, which can lead to a sagging tether and a snapping effect as the tether force is restored. This effect is neglected in this simulation but can lead to problems in reality. This also results in 5.5% less power output, as shown in Figure 9.7b. Furthermore, a side effect is that the power out is now lagging behind the power in.

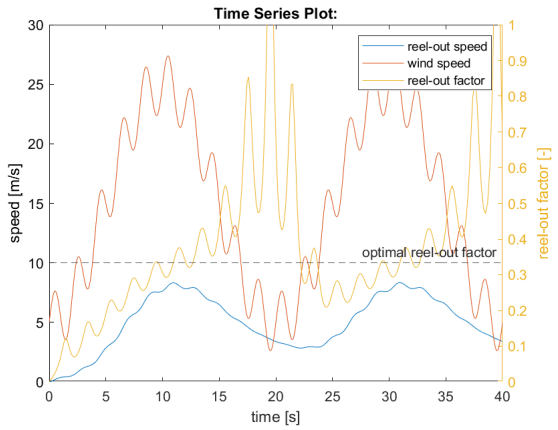

(a) Reel-out and wind speed (left axis) and reel-out factor (right axis).

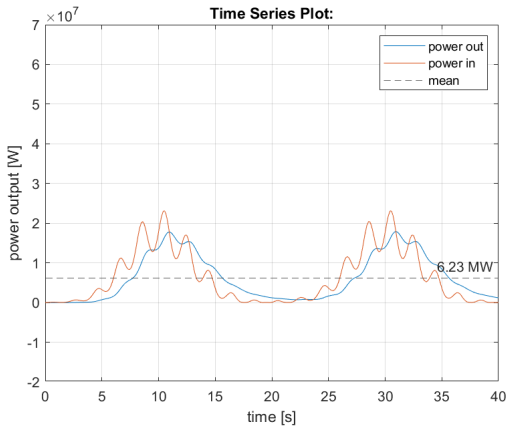

(b) Power input of the kite into the system and power output of generator.

Figure 9.7: Using a winch with an inertia 200x higher.

A similar result is obtained when resetting the winch inertia and using a radius that is 12.5 times smaller. From Figure 9.8a it is clear that the reel-out speed adapts too slow, leading to a sub-optimal reel-out factor and from Figure 9.8b it is clear that the average power output is lower.

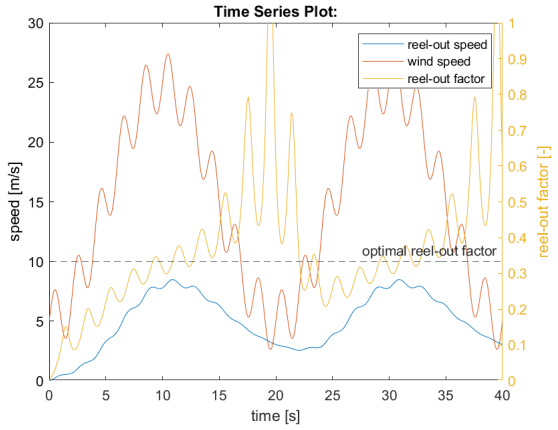

(a) Reel-out and wind speed (left axis) and reel-out factor (right axis).

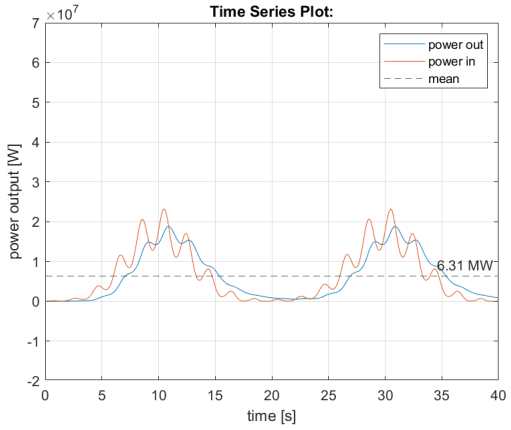

(b) Power input of the kite into the system and power output of generator.

Figure 9.8: Using a winch with a radius of 12.5x smaller.

9.4. Conclusion and discussion

The inertia and radius of the winch can have a large effect on the dynamics of an airborne wind energy system that has not yet been investigated in the literature. Since the inertia and radius of the winch of MegAWES are unrealistically small and no other megawatt-scale systems exist, an analysis was done to find values that lead to appropriate dynamics, rather than estimate these values based on scaling laws.

By using the widely used quasi-steady massless kite model and winch feedforward control law, the closed loop dynamics were analysed. It was found that a higher inertia and lower radius lead to lower responses which leads to a reduction of power.

The MegAWES system should react quickly enough to input signals with a frequency of $\pi/10$ rad/s, as this is the frequency at which the tether force oscillates as the kite is flying its figure of eight. To

emulate this effect in the massless model, the wind speed is changed at this frequency. Using this methodology with a safety factor of 10, an inertia of 1×10^4 kgm^2 and a radius of 1.5 m were found to only result in 1% loss of power w.r.t. the optimum.

This inertia is much lower than that of a similar wind turbine, whose generator has an inertia of about 1×10^7 kgm^2 around the drum axis. To get similar system dynamics with this inertia, a radius of 47 m would be required, which is very unrealistic. Without adaptations the system would produce less power and be likely uncontrollable since the reel-out factor will oscillate to values above 1. So future work should investigate this potential problem in the future. Solutions could come from less stringent power fraction requirements, different winch controller designs, or different flights paths (that lead to a slower tether force oscillation).

To verify the selected winch parameters, the different winch parameters were used in a nonlinear simulation with a massless kite and a feedforward winch controller. The selected winch parameters resulted in a desired behaviour where the reel-out factor always stays close to its optimum value. As predicted, the power output reduces if the inertia is further increased or if the radius is decreased. The power losses in this example were modest at 5% but more significant losses can be expected if the inertia were further increased or the radius further decreased. Besides a lower power output, the reel-out factor was sometimes higher than 1 which could lead to dangerous tether snaps which are avoided with the selected winch parameters.

The optimal reel-out factor that was used for verification was 1/3, and since the kite was downwind of the ground station, this is the reel-out factor for optimal instantaneous power output. In the next chapter the effect of mass on the optimal reel-out factor will be investigated to construct a new winch control law that is more optimal for kites with mass.

10

Winch control design

The fifth research question is:

Research question 5

How to adapt the existing feedforward winch controllers that are derived for massless kites for kites with mass?

In subsection 9.1.1 the widely used feedforward winch control law was described. It was then shown in section 9.3 that such a feedforward control keeps the system on the ideal reel-out factor irrespective of wind speed, under the conditions that the winch parameters are designed appropriately. The analysis to arrive at that feedforward winch control law is derived from a quasi-steady model of a massless kite. However, for MegAWES, the effect of its mass is significant. This was taken into account for the parameter design by selecting a higher wind speed oscillation at which the system dynamics should be sufficiently fast. However, the optimal reel-out factor was not adjusted.

In the current MegAWES implementation, the tether force is kept constant and is varied with wind speed (Eijkelhof & Schmehl, 2022). This ensures that the kite cannot stall as it is flying upwards but it also means that it might not adjust the reel-out factor to its optimum as the kite is flying the figure of eight. In addition, this strategy requires the winch to have an estimate of the wind speed to set its tether force reference. Finally, the winch does not have a power limit, while the power highly fluctuates in order to keep the tether force constant.

In this chapter, the effect of the mass of the kite on the optimal reel-out factor will be investigated to arrive at a new winch control law that is more optimal for kites with mass. It will also include a power limit and does not require a measurement of the wind speed.

10.1. Effect of the kite's mass

A good starting point for investigating the effect of the kite's mass on the optimal winch control law is looking at the optimal instantaneous power that can be produced in a given state, which is discussed in subsection 10.1.1. However, a greedy strategy of always maximum instantaneous power extraction is not optimal over the average of a pumping cycle so adaptations will be discussed in subsection 10.1.2.

In this analysis, wind shear is neglected. In reality, wind shear leads to higher winds at higher altitudes. Which favours high elevation angles and long tethers. However, this effect is neglected for simplicity since it is more relevant for path planning than power extraction on an existing path.

10.1.1. Optimal instantaneous power

In subsection 9.1.1, the widely used feedforward winch control law was described. To find what adjustments are needed to incorporate the effect of mass, first, the optimal states that lead to the original control law will be further investigated so that it is clear what the effect of mass is on the optimal states. This is done by solving the model provided by van der Vlugt et al. (2019) for different values of wind speed, elevation and azimuth, tether lengths, and mass.

Massless kites with elevation and azimuth

Elevation and azimuth cause the incoming wind to be no longer perpendicular to the kite, lowering the amount of energy that can be converted. The optimal reel-out factor is then $1/3 \cos\beta \cos\varphi$ (van der Vlugt et al., 2019) and is constant for all wind speeds, as shown in the left plot in Figure 10.1 for different elevations and azimuths. The optimal tether force at these different reel-out factors increases with wind speed, but is lower for kites that fly at a higher elevation or azimuth, as shown in the middle plot in Figure 10.1. Finally, since both the optimal reel-out speed and the optimal tether force are lower for a given wind speed as the elevation and azimuth go up, the maximal power extraction is also lower, as shown on the right in Figure 10.1.

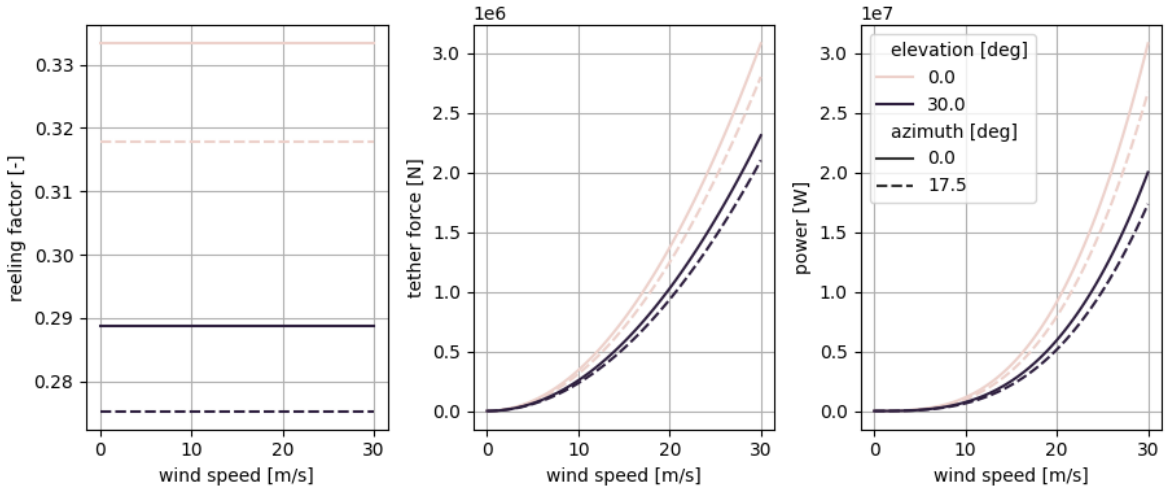

Figure 10.1: Optimal instantaneous reeling factor, tether force, and power output as a function of wind speed and for different elevation and azimuth angles for a massless system.

When combining the figure of optimal tether force and reel-out factor, the optimal winch control law can be made and is plotted in Figure 10.2. It can be seen that the curves for the different elevation and azimuth angles overlap each other, as was previously discussed in subsection 9.1.1. This means that a change in elevation or azimuth is equivalent to a change in wind speed. The equation that describes this curve was derived there (Equation 9.4).

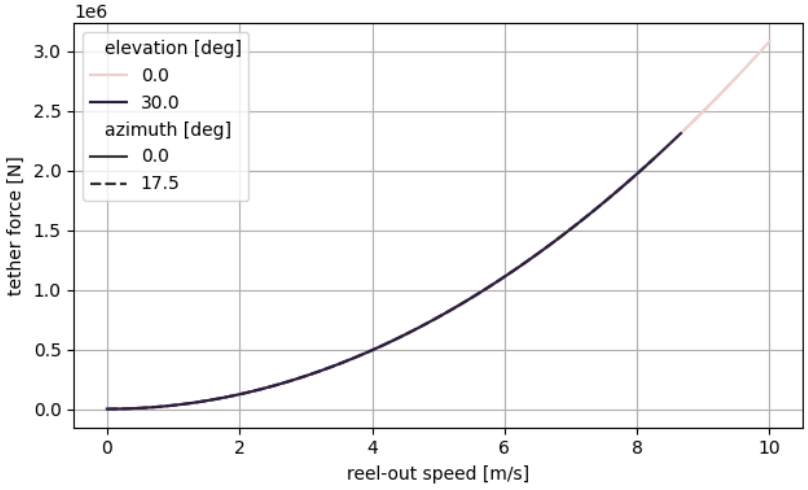

Figure 10.2: Optimal winch strategy for different elevation and azimuth angles for a massless system.

Effect of tether length

In the previous analysis, and in the popular feedforward winch control law, the effect of tether length is neglected. The tether has two effects, as described by van der Vlugt et al. (2019): First, its drag adds to the system drag, which is now a combination of kite and tether drag and is described as effective drag by Equation 10.1, where $C_{D_{\text{eff}}}$ is the effective drag coefficient of the system, $C_{D_{\text{kite}}}$ is the drag coefficient of the kite, d_{tether} is the diameter of the tether, L_{tether} is the length of the tether, and $C_{d_{\text{tether}}}$ is the drag coefficient of the tether. This means that as the tether length increases the system drag increases while the lift stays constant, resulting in a lower ideal tether force and power output, as shown by Figure 10.3. The second effect of the tether is its mass, which is neglected here but will be included later.

$$C_{D_{\text{eff}}} = C_{D_{\text{kite}}} + \frac{d_{\text{tether}} L_{\text{tether}}}{4S} C_{d_{\text{tether}}} \tag{10.1}$$

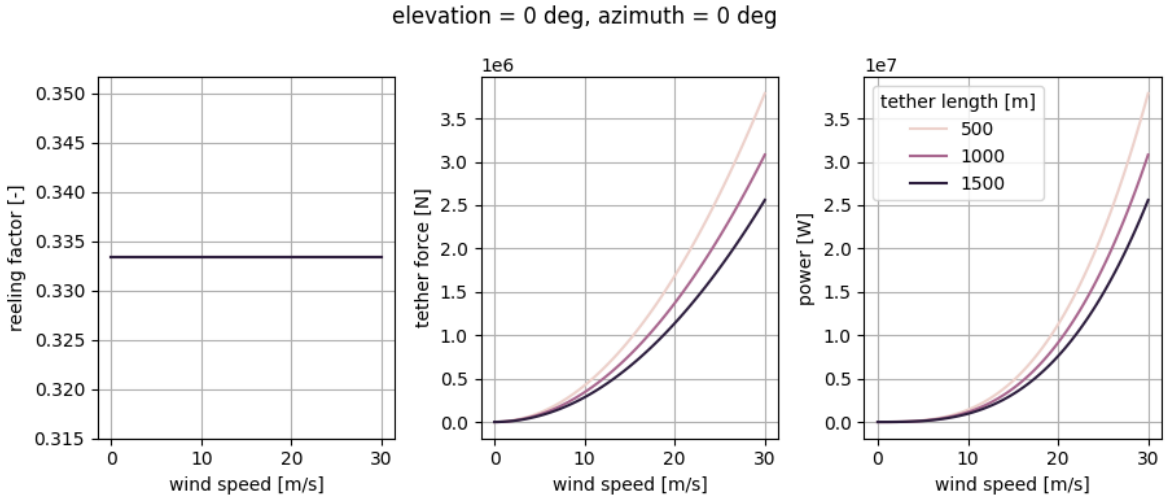

Figure 10.3: Optimal instantaneous reeling factor, tether force, and power output for different tether lengths for a massless system.

The ideal tether force and reel-out speed for each wind speed can again be plotted for different tether lengths. This is shown in Figure 10.4. Unfortunately, there are three distinct curves now on which optimal power extraction takes place, depending on the tether length. This means that the winch needs to switch between these curves to extract the most amount of power from the wind. Fortunately, the tether length is available to the winch as it can measure the amount of rotations of the drum.

Effect of mass

The effect of elevation and azimuth has been thoroughly explored in the literature but the preceding analysis on the effect of tether length is an addition to the literature. To expand this further, a similar analysis but for kites with mass is performed. van der Vlugt et al. (2019) presents a numerical iterative scheme to find operating points for kites and tethers with mass, since an analytic formula does not exist. This process starts by setting the initial guess for kinematic ratio equal to the lift-to-drag ratio, which is true for kites without mass. Using this guess, the equations can be solved with result in a certain lift-to-drag ratio of the system. Since the lift-to-drag ratio should be constant, the deviation of the lift-to-drag ratio from its target value can be used to update the kinematic ratio for the next iteration. This update step is shown in Equation 10.2, where G^* is the target lift-to-drag ratio and G_i the lift-to-drag ratio from the previous iteration. Once the G_i is sufficiently close to G^* the algorithm is done.

$$\kappa_{i+1} = \kappa_i \sqrt{\frac{G^*}{G_i}} \tag{10.2}$$

This model was implemented in Python and published on GitHub (Schelbergen & Schmehl, n.d.). One additional parameter that matters now is the course angle (χ), which is the angle the kite velocity has in the tangential plane, shown in Figure 10.5. When mass is introduced, it starts to matter whether

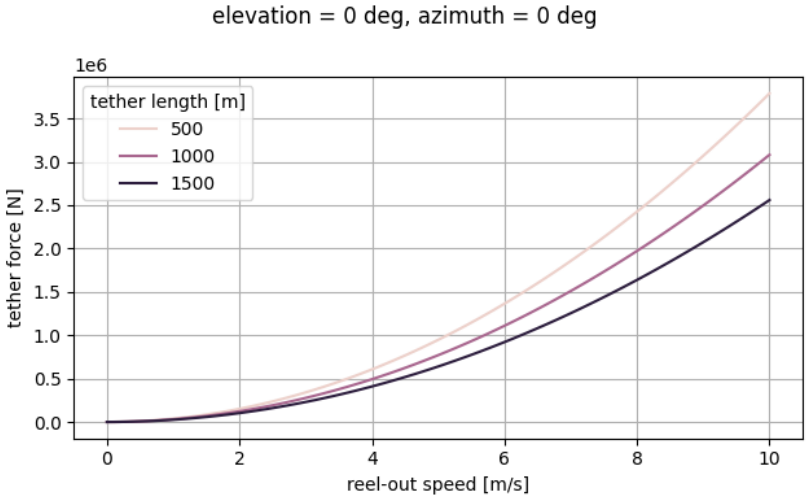

Figure 10.4: Optimal winch strategy for different tether lengths for a massless system.

the kite is flying upward or downward because of gravitational acceleration. This effect is quite severe for heavy kites.

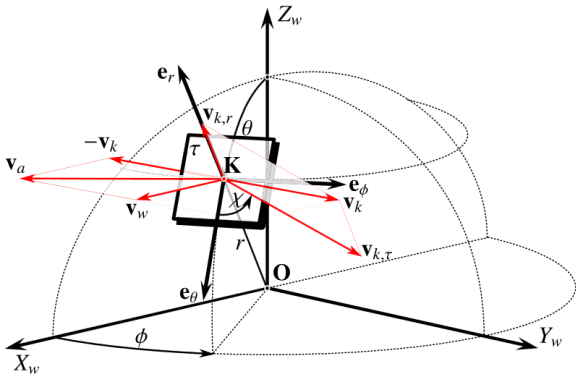

Figure 10.5: Coordinate system used by the quasi-steady model. Note that van der Vlugt, Bley, Noom, and Schmehl (2019) uses θ for 90° minus the elevation while in this work, β is used directly for the elevation.

Since the model is no longer analytical, the optimal reeling speed and tether force must be calculated by numerical optimisation. Since non-optimal operating points are also of interest, 3 120 000 operating points were generated using different wind speeds, tether lengths, elevation, azimuth, and course angles, and desired tether forces together with the parameters from MegAWES (Eijkelhof & Schmehl, 2022). The numerical model would then find a steady state of the kite in those operating points.

Using this approach, an unexpected behaviour of the model was found. In Figure 10.6 the tether force as a function of reel-out speed for a certain operating condition is shown. On the blue part of the curve, the behaviour is as expected: as the reel-out speed increases the tether force drops. Since power output is given by the tether force multiplied by reel-out speed, there's an optimum, which in this case is close to 3 m/s (though this is difficult to observe from this figure). However, as the tether force gets lower, it reaches a point where the reeling speed decreases when the tether force decreases. As shown by Figure 10.7, the kinematic ratio tends towards zero here. As noted by van der Vlugt et al. (2019), this means that the kite does not have sufficient tether force to counter the force of gravity. This causes the system to be unable to end up in a quasi-steady state, thus the algorithm fails to identify a physical solution. Thus, these data points are accordingly deleted, as shown in Figure 10.6. Furthermore, for this work, close to this area is not of interest anyway because the power output is suboptimal in these regions.

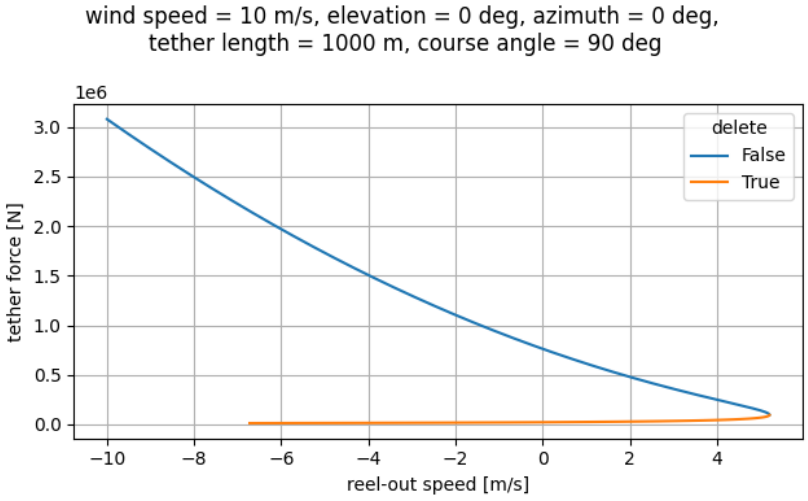

Figure 10.6: Relation between reel-out speed and tether force for a certain operating condition.

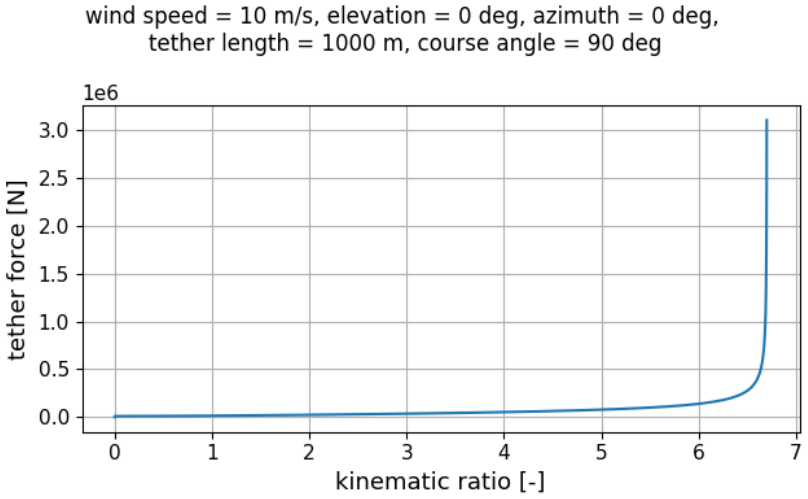

Figure 10.7: Relation between kinematic ratio and tether force for a certain operating condition showing that the kinematic ratio tends towards zero at low tether forces, making the results invalid.

With the resulting data, the optimal reeling factor, tether force, and power output can be found for a given elevation, azimuth, and tether length as shown in Figure 10.8. The main finding is that the optimal reeling factor is no longer constant over all wind speeds: When the kite is flying horizontally or upwards ($90 < \chi < 270°$) the optimal reeling factor at low wind speeds is negative, meaning that the winch needs to put energy into the system in order for the kite to remain airborne. While for high wind speeds it asymptotically approaches the massless optimal reeling factor.

For kites flying downwards ($\chi < 90$ or $\chi > 270$), the reeling factor at low wind speeds is higher than the massless case. This makes sense as the heavy kite is gaining kinetic energy as it loses potential energy. The winch can now extract more energy from the system than in the massless case. An additionally interesting thing to note is that there is a little bump in the optimal reeling factor at low wind speeds. This arises from the trade-off between lower reeling factors to keep the kite airborne which are more prominent at low wind speeds and additional power extraction which is more prominent at medium wind speeds. At the highest wind speeds the optimal reeling factor again asymptotically approaches the massless optimal reeling factor, since the gravitational force becomes proportionally smaller compared to the tether force.

For the tether force it can be observed that when the kite is flying upwards, the curve is not smooth: There is a certain minimum tether force that keeps the kite airborne at low wind speeds. This will

become important later, when a control law will be designed that can always keep the kites airborne.

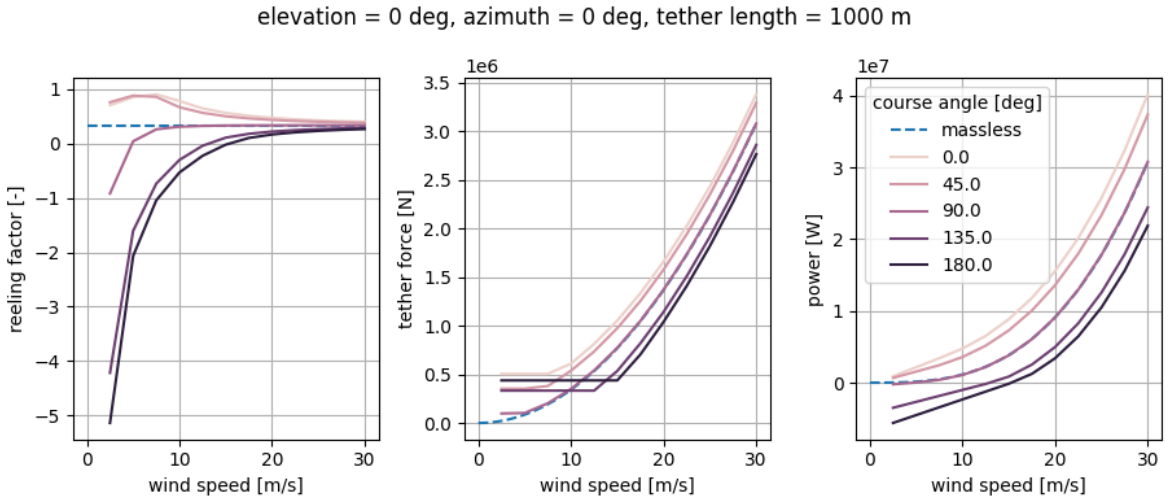

Figure 10.8: Optimal instantaneous reeling factor, tether force, and power output for different course angles for a system with mass, compared to a massless system.

The optimal reeling speed and tether force curve for kites with mass and different course angles is shown in Figure 10.9. For horizontal flight ($\chi = 90°$) the curve is quite close to the massless case, except for low reeling speeds. However, there is a big difference between optimal power extraction depending on the course angle, as the curve shifts left and right. This means that a change in course angle is not equivalent to a change in wind speed (as was the case for elevation and azimuth).

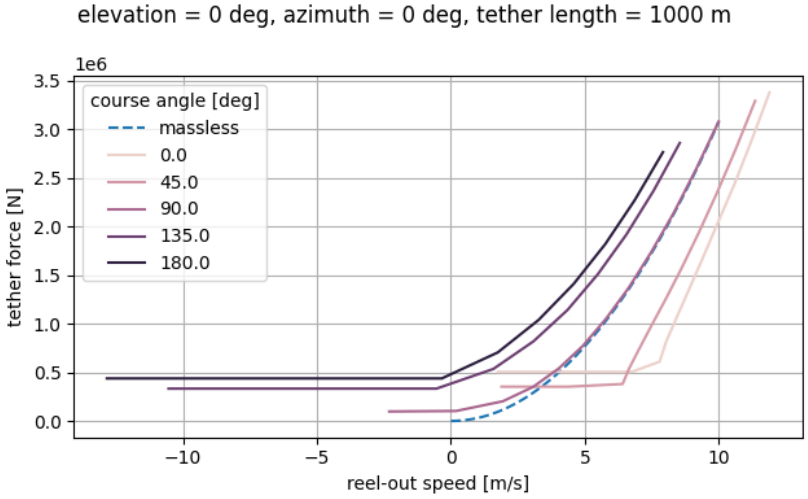

Figure 10.9: Optimal winch strategy for different course angles for a system with mass, compared to a massless system.

Effect of elevation and azimuth on kites with mass For the massless case a change in elevation and azimuth did not change the optimal winch control strategy (the (v_r, F_t)-curve). However, for kites with mass, this does have an effect. When comparing horizontal flight with mass and the massless model at different elevations and azimuth angles, the resulting (v_r, F_t)-curves are shown in Figure 10.10. It is clear that the curve shifts to the left when adding some elevation. Additionally, there is no effect when adding some azimuth. This means that a change in azimuth is still equivalent to a change in wind speed. However, a change in elevation also changes the direction of the gravity vector with respect to the tether. Since gravity now has a component in the tether force direction it works against the tether

force. This means that a change in elevation with non-massless kites is not equivalent to a change in wind speed, resulting in a shift in the (v_r, F_t)-curve.

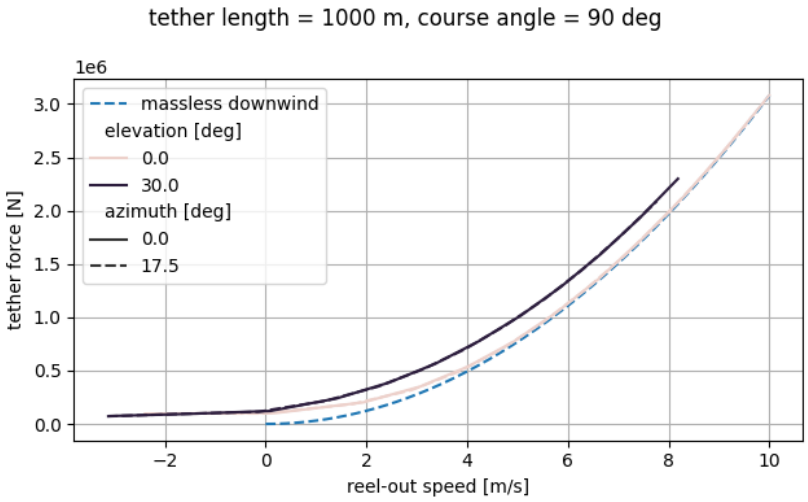

Figure 10.10: Optimal winch strategy for a system with mass and a massless system with an certain offset in elevation and azimuth.

10.1.2. Optimal mean cycle power

Until now, optimal instantaneous power extraction has been considered. However, when optimising for mean cycle power, always aiming for maximum instantaneous power extraction might not be optimal. There are two areas to consider here:

First, over a single figure-of-eight it might be better to spend more time flying downward and minimise the time spent in the upwards phase where less energy can be generated, even pulling up the kite when not strictly necessary. On the other hand, pulling the kite up leads to additional power losses as conversion between an energy storage device, electrical, hydraulic, or mechanical, back to mechanical power comes with losses Joshi et al. (2022). Trevisi et al. (2022) performed this optimisation for fly-gen systems and showed that under their energy conversion assumptions the optimal strategy was to never use energy to keep system in the air. Additionally, it should not extract the optimal instantaneous power but rather sometimes extract less in order to build up kinetic energy to make it up the loop again.

Secondly, ground-gen systems also have a retraction phase. It has been established for a while that when optimising mean cycle power the power extraction during the traction phase should be lower than maximally possible to achieve a higher mean cycle power (Erhard & Strauch, 2015). Luchsinger (2013) presents a formula to calculate the optimal reel-out and reel-in factor as a function of maximum tether force during the reel-out and reel-in phases. Berra and Fagiano (2021) used a regression algorithm on 6DOF simulation data to find the optimal operating points. However, both methods apply mainly to soft wing systems and cannot account for systems with mass that need to be pulled up sometimes at low wind conditions.

Additionally, any real system will have a tether force and generator power limit. This requires a different control strategy for once this limit has been reached.

10.2. Winch control strategy

In the previous section it has been shown that the operating points of maximum instantaneous power extraction do not lie on a single (v_r, F_t)-curve for kites with mass, in contrast to massless kites. Furthermore, actually always travelling through the instantaneous optimal points does not lead to the optimal mean cycle power and does not yet take tether force and power limits into account. Several options have been conceived to arrive a viable winch control strategy:

1. An average line on the (v_r, F_t)-curve can be selected. This ensures that the operating condition is always close to the optimal instantaneous operating condition. However, this does not take

optimisation over figure of eight or the retraction phase into account. Choosing an average operating condition allows the use of the 2-phase strategy, which ensures that tether force and power limits are handled (Luchsinger, 2013). During the first phase, the kite is operating at its optimal angle of attack for maximum power extraction. The line in the (v_r, F_t)-curve then coincides with the tether force and power limit such that once that point is reached the kite lowers its angle of attack in order to stay at that operating condition. To make this strategy work for kites with mass, a minimum tether force must be added in order to keep the kite in the air.

2. A similar strategy is possible but instead of using the 2-phase strategy using the 3-phase strategy (Fechner & Schmehl, 2013). Using the 3-phase strategy, the first phase is the same. But the second phase is at the tether force limit, but not yet the power limit. In this phase, the kite remains flying at its optimal angle of attack while the winch just reels out faster in order to extract more power while keeping the system at the tether force limit. In the third phase, the power limit is reached and the kite should lower its angle of attack in order to stay at the limit. In this case the kite and winch must communicate when the third phase starts and ends.
3. Another idea is to not take an average operating point but to let the winch operate in a (v_r, F_t)-plane. The instantaneous ideal point on the plane would be selected with information about the kite's current position and the tether length. This way the winch would always extract the instantaneous optimal amount of energy, but needs reliable and high-bandwidth information about the kite's position, putting higher requirements on that communication connection, or a separate ground measurement of the kite's position.
4. An alternative is to divide the plane up into a grid, one where one set of lines correspond to a the change in wind speed and another set of lines that correspond to a change in course angle at a constant wind speed, since these two variables have the greatest effect. This is shown in Figure 10.11. Since it can be assumed that a change in course angle has a higher frequency than the change in wind speed, a change in tether force can be interpreted as a change in course angle, thus moving on the constant wind speed lines (constant colour). When reaching the end of a line while the measured reel-out speed is still changing, the winch will interpret this as a change in wind speed and move along the constant course angle lines (constant line style). This makes it possible to adjust the operating points both along a line and between lines where the two motions are split between low and high frequency changes in reel-out speed.
5. The approaches above can be adjusted to optimise mean cycle power rather than instantaneous power. By assuming a single operating point for the traction phase, and measuring the energy loss of the retraction phase, an operating point can be chosen that optimises Equation 10.3, where $E_{\text{out/in}}$ is the energy generated during the traction/retraction phase, and L is the distance between the start and end of the traction phase. This is done by selecting appropriate values for P_{out} and v_{out}, rather than only optimising P_{out}. This also requires information about the retraction phase. Alternatively, this could also optimise the power during the traction phase. An alternative formulation of this optimisation uses tether forces rather than power consumption and is shown by Luchsinger (2013). However, these approaches have not been utilised on fixed wing kites that have a radically different retraction phase than soft kites since they can more actively glide back towards the ground station.
6. All approaches above neglect the optimisation over the figure of eight. Optimal control techniques, such as used by Trevisi et al. (2022) for fly-gen systems can be used to optimise this.
7. Finally, learning control algorithms can be used to adapt their strategy over time, also taking effects into account that this model cannot. This can use reinforcement learning or iterative learning control that can both adjust a control strategy based on feedback.

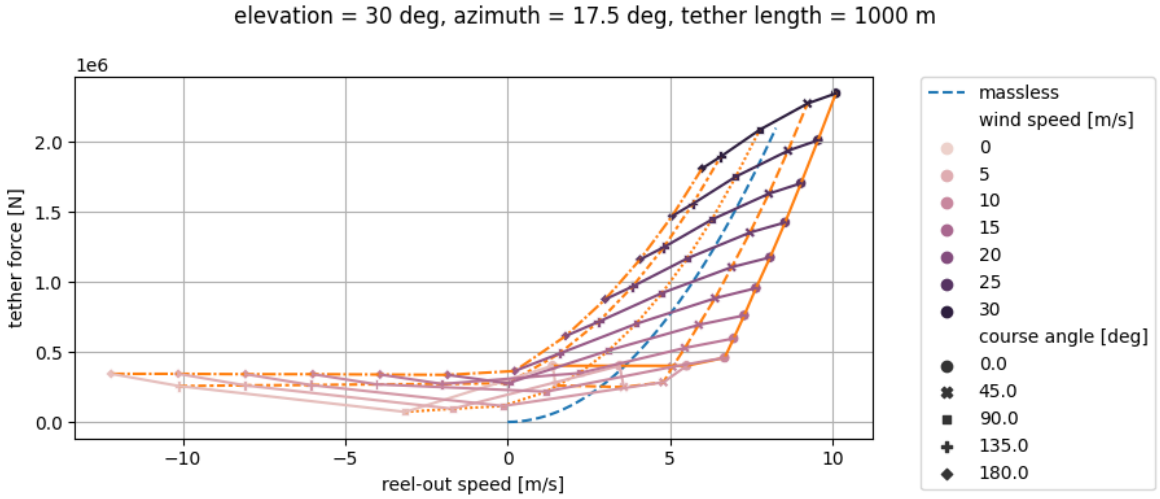

Figure 10.11: Similar to Figure 10.9, but with different lines for different wind speeds which makes a grid together with variations of course angle.

$$
\begin{aligned}
P_{\text{mean}} &= \frac{E_{\text{out}} + E_{\text{in}}}{t} \\
&= \frac{P_{\text{out}} t_{\text{out}} + P_{\text{in}} t_{\text{in}}}{t} \\
&= \frac{P_{\text{out}} \frac{L}{v_{r_{\text{out}}}} + P_{\text{in}} \frac{L}{v_{r_{\text{in}}}}}{\frac{L}{v_{r_{\text{out}}}} + \frac{L}{v_{r_{\text{in}}}}} \\
&= \frac{P_{\text{out}} v_{r_{\text{in}}} + P_{\text{in}} v_{r_{\text{out}}}}{v_{r_{\text{out}}} + v_{r_{\text{in}}}}
\end{aligned}
\tag{10.3}
$$

None of these methods have been tried out in the literature explicitly for ground-gen airborne wind energy systems with mass. Especially the final two idea's could really lead to optimum power extraction for systems with mass while the first four idea's are more analytic and simpler to implement.

10.2.1. Design of the winch control curve

The first idea was selected for implementation. It is not the most optimal but rather a first step in a winch control strategy that's suitable for systems with high mass. It is crucial that in the second phase the kite lowers its angle of attack. One might think that alternatively, the winch could reel out faster. However, the winch would have to reel-out so fast that the tether force drops to stay at the power limit (at a higher reel-out speed). Since this produces the same power but with a faster reel-out speed, it leads to a lower mean cycle power and thus it is better when the kite lowers its angle of attack.

Phase 1

For the first phase, an average operating condition must be chosen to get a single line on the (v_r, F_t)-curve. The average operating condition that was chosen is shown in Table 10.1. The elevation and azimuth are chosen as average from Figure 10.12. The absolute value for the azimuth was used since its effect is symmetric around the $\varphi = 0$ axis. A tether length of 1000 m is used as it is the average tether length during the reel-out phase (Eijkelhof & Schmehl, 2022). The course angle is cycling between flying upwards and downwards, so as "average", horizontal flight was selected.

This yields the (v_r, F_t)-curve shown in Figure 10.13. The shape is very similar to the massless case but it is slightly shifted to the left due to the elevation.

Phase 2

The second phase starts when the system hits the tether force limit. The tether force limit for MegAWES is 1.66×10^6 N (Eijkelhof & Schmehl, 2022). Using a safety margin, the maximum tether force set-point is

Table 10.1: Average operating condition used for the 2-phase strategy.

state	value
elevation	30 °
azimuth	17.5 °
tether length	1000 m
course angle	90 °

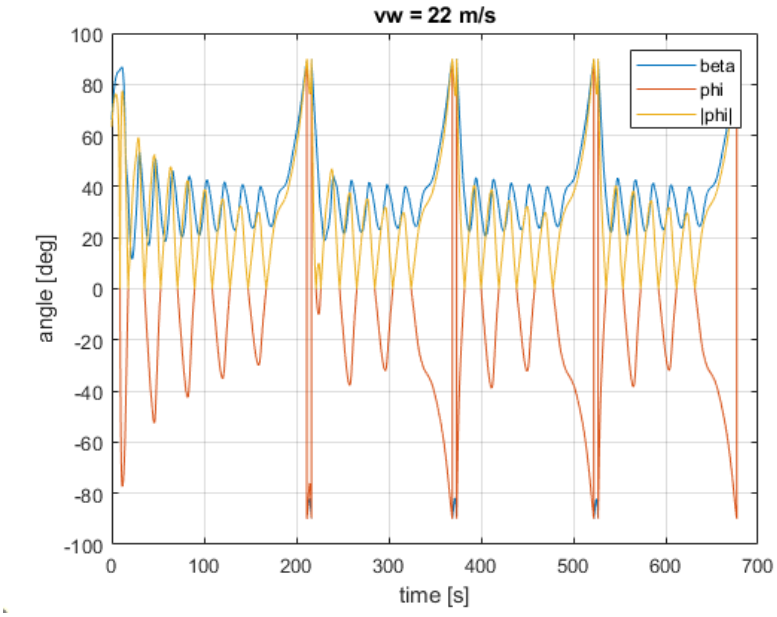

Figure 10.12: Elevation and azimuth angle of MegAWES over a couple of pumping cycles.

selected to be 1.0×10^6 N, which is the same as the original implementation, ensuring a fair comparison. This horizontal line intersects the (v_r, F_t)-curve (Figure 10.13) at 5.0 m/s. By multiplying the reel-out speed and tether force, the power at this point can be obtained. This is 5.0 MW, which thus defines the power limit of the system, and is shown in Figure 10.14.

When the system is at this point, the tether force and power limits coincide and the kite will start to do tether force control and make sure the kite keeps operating in that point. That's why the winch strategy does not change at the force limit, and simply assumes that the kite will control it. The controller design for the kite will be the main focus of chapter 11.

Minimum tether force

By assuming an average operating point in the 2-phase strategy, it is not guaranteed that the kite makes it up the figure of eight. So a minimum tether force is needed. When the tether force gets below this, the winch must put energy into the system to ensure the minimum tether force. From Figure 10.9 a minimum tether force of 0.5×10^6 N seems to be the minimum tether force on which the model still converges with the least amount of input power for course angles of 180°. Adding this minimum tether force leads to a "winch control with pull-up" strategy, shown in Figure 10.15.

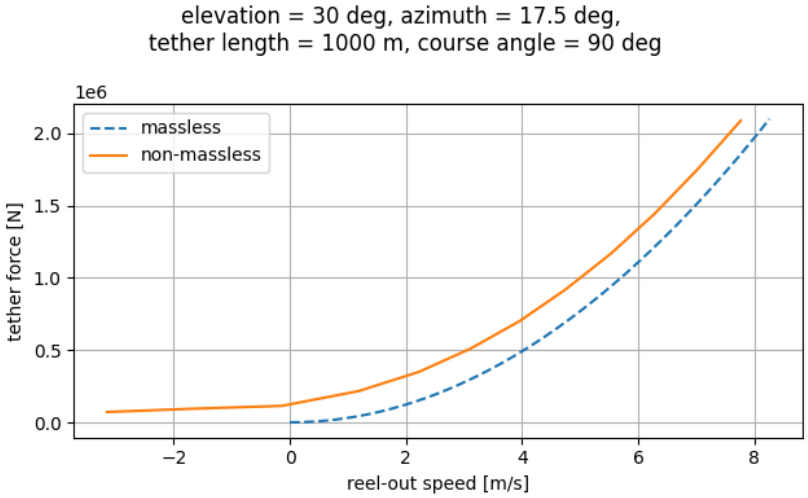

Figure 10.13: (v_r, F_t)-curve for the average operating condition.

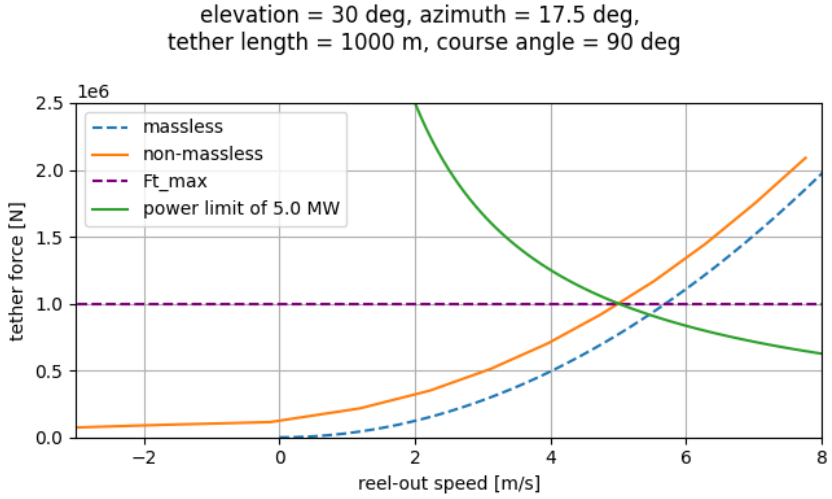

Figure 10.14: (v_r, F_t)-curve for the average operating condition with tether force and power limits.

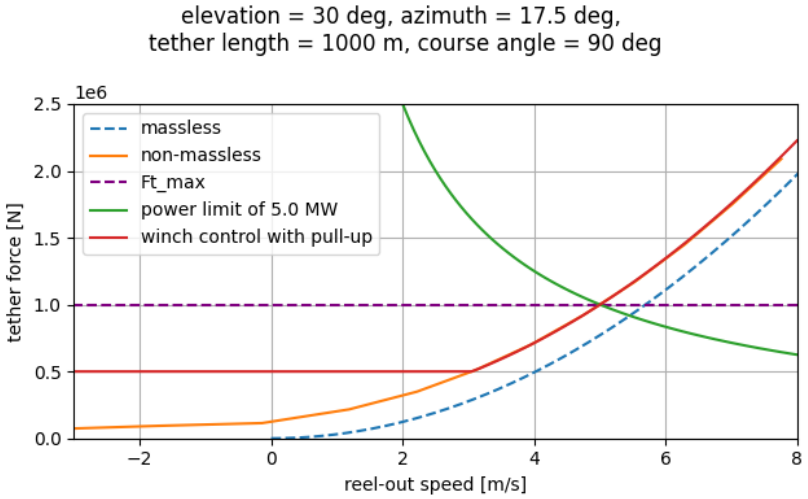

Figure 10.15: (v_r, F_t)-curve for the average operating condition with tether force, power limits, and a minimum tether force. The resulting winch control strategy is shown as "winch control with pull-up".

10.3. Winch controller design

The 2-phase strategy with a pull-up phase to keep the kite airborne prescribes a reference tether force as a function of reel-out speed, shown previously in Figure 10.15. The winch controller must thus drive the system to a reference tether force given a certain reel-out speed. Since the reference tether force consists of two distinct regions, a minimum tether force and tether force as quadratic function of reel-out speed, two controllers will be designed. By starting at the minimum tether force controller, it will be clear later that the second controller can be easily integrated into this.

10.3.1. Minimum tether force

Like the current winch controller (Eijkelhof et al., 2020), a PI controller will be designed to keep the tether force constant. A torque can be exerted on the winch in order to change the reel-out speed. The winch must thus know how a change in its reel-out speed changes the tether tension. The model with mass from van der Vlugt et al. (2019) that was used before (subsection 10.1.1) is not suitable for this because it requires an iterative procedure to solve it. Instead, system identification on the results from that model is used to get an analytic kite model that still incorporates the effect of mass. This model can then be used to design a PI controller that stabilises the system when there is a disturbance in tether force.

System identification

The quasi-steady model will be linearised around an operating point where it is most likely to reach the minimum tether force. This is when the kite is flying upwards, at the outer edge of the figure-of-eight. The controller will then be designed for this worst-case scenario. When analysing the elevation and azimuth of a typical MegAWES flight in Figure 10.12, the point where the kite is flying upwards, on the outer part of the figure-of-eight, has an elevation of about 30 ° and an azimuth of about 35 °. The course angle for flying upwards is 180 ° and the worst-case tether length is 1500 m, causing the most amount of tether drag.

In Figure 10.16, each line corresponds to the solutions for a different wind speed at this worst-case operating point. The optimum is also drawn and clearly goes through the point of optimum power production per wind speed. When only looking at tether force around the minimum tether force, it can be estimated using a simple linear model of the form $F_t = \theta_0 + \theta_1 v_r + \theta_2 v_w$. Doing this results in Equation 10.4 and is shown in Figure 10.17. It is the same curve as Figure 10.16, but coloured according to the wind speed, instead of power output. The dashed lines are produced using the linear model. The fit is only good around a tether force of 0.5×10^6 N, which is exactly the regime that this model will be used for when designing the PI controller.

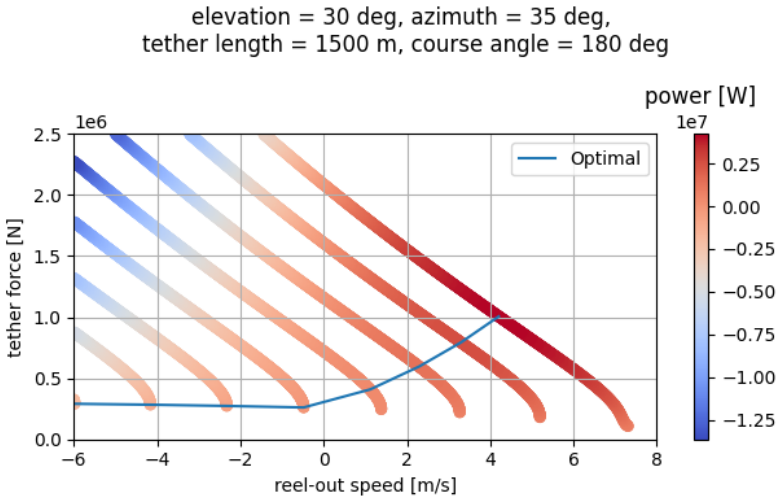

Figure 10.16: All solutions of the quasi-steady model for the average operating condition, including the optimal solutions.

$$
\begin{aligned}
F_t =& \theta_0 + \theta_1 v_r + \theta_2 v_w \\
&\text{where} \\
\theta =& \begin{bmatrix} -3991522.9 & -290436.9 & 210452.0 \end{bmatrix}^T
\end{aligned} \tag{10.4}
$$

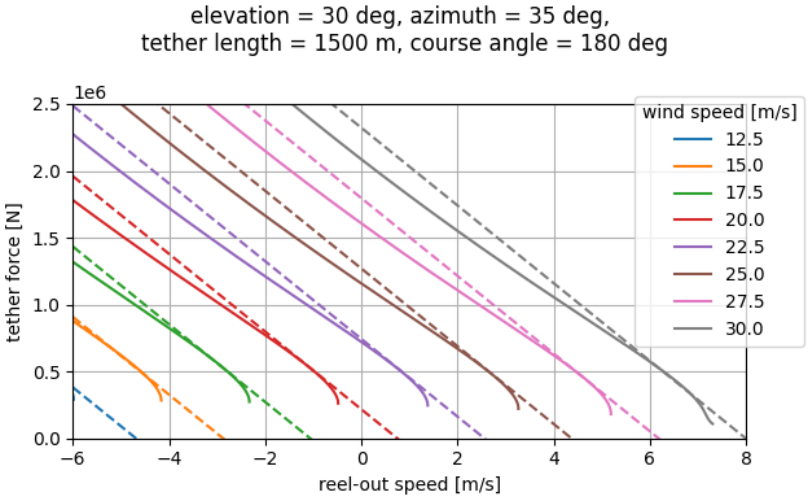

Figure 10.17: Linear fit of the tether force for different reeling and wind speeds.

PI controller design

Substituting the model for the tether force (Equation 10.4) into the equations of motion for the winch (Equation 9.1), Equation 10.5 can be derived. The trim condition is at $F_t = 0.5 \times 10^6$ N, so can be described by Equation 10.6 for a certain reel-out or wind speed. At the trim condition, the equations of motion can be rewritten into state-space form, with states v_r and $\int F_t dt$, input τ, disturbance v_w , and outputs F_{t_e} and $\int F_{t_e} dt$, shown in Equation 10.7. The integrals of the tether force error are required for the PI controller. The block diagram for this system is shown in Figure 10.18.

$$
\dot{v}_r(t) = \frac{\Big(\theta_0 + \theta_1 v_r + \theta_2 v_w\Big) r^2 - \tau(t) r - d v_r(t)}{J} \tag{10.5}
$$

$$
\begin{aligned}
\tau_{\text{trim}}(v_r) =& \frac{0.5 \times 10^6 r^2 - d v_r}{r} \\
\tau_{\text{trim}}(v_w) =& \frac{0.5 \times 10^6 r^2 - d \frac{0.5 \times 10^6 - \theta_0 - \theta_2 v_w}{\theta_1}}{r}
\end{aligned} \tag{10.6}
$$

The open-loop response to a step input on wind speed is shown in Figure 10.19. Since the wind has a feedforward effect on the tether force (D_{v_w}), the transient response starts at a nonzero value. However, the system does stabilise itself close to zero tether force error. Because of the scale of the figure it is difficult to see, but the tether force settles at a slightly higher value, due to the increase in friction. If friction is neglected the system would stabilises exactly to zero tether force error because then the tether force and torque are in equilibrium again. The bode plot of the open-loop response is shown in Figure 10.20 and shows that all low wind speed frequencies are better damped with respect to the higher frequencies. The main goal of adding the PI controller is to dampen the effect of a change in wind more, so to further improve disturbance rejection of the system.

Since F_{t_e} is not part of the state, an output-feedback controller of the form $\tau = -Ky$ is assumed. Since $y = \begin{bmatrix} F_{t_e} \\ \int F_{t_e} dt \end{bmatrix}$ and $K = \begin{bmatrix} K_p & K_i \end{bmatrix}$ this feedback law is equivalent to a PI controller on F_{t_e}. This

$$
\begin{aligned}
\dot{x} =& Ax + B_\tau \tau + B_{v_w} v_w \\
y =& Cx + D_\tau \tau + D_{v_w} v_w \\
\text{where} & \\
x =& \begin{bmatrix} v_r \\ \int F_{t_e} dt \end{bmatrix} \\
y =& \begin{bmatrix} F_{t_e} \\ \int F_{t_e} dt \end{bmatrix} \\
\text{and} & \\
A =& \begin{bmatrix} \frac{\theta_1 r^2 - d}{J} & 0 \\ -\theta_1 & 0 \end{bmatrix} \\
B_\tau =& \begin{bmatrix} \frac{-r}{J} \\ 0 \end{bmatrix} \\
B_{v_w} =& \begin{bmatrix} \frac{\theta_2 r^2}{J} \\ -\theta_2 \end{bmatrix} \\
C =& \begin{bmatrix} -\theta_1 & 0 \\ 0 & 1 \end{bmatrix} \\
D_\tau =& \begin{bmatrix} 0 \\ 0 \end{bmatrix} \\
D_{v_w} =& \begin{bmatrix} -\theta_2 \\ 0 \end{bmatrix}
\end{aligned}
\tag{10.7}
$$

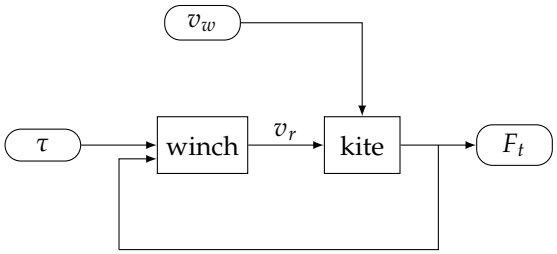

Figure 10.18: Block diagram of the system

results in a block diagram shown in Figure 10.21. The control objective is to drive the system to zero tether force error for a disturbance in the wind speed. To achieve this, the feedback controller will first be designed to stabilise the system from τ to F_{t_e}. Using Matlab, the transfer function from τ to F_{t_e} can be extracted from the state-space model and a PI controller can be designed using Matlab's PID tuner. A bandwidth and phase margin can then be selected. A bandwidth of 30 rad/s ($\approx$ 5 Hz) was assumed because it aligns with the bandwidth of the open loop response. Generator controllers are generally high-bandwidth and it was assumed that tether force sensors low noise at this bandwidth exist. A high phase margin of 80 ° was chosen to make the response less oscillatory to a step input to a tether force reference. During the minimum tether force the tether force input will of course be constant, but in the next section it will will become important why this is important. With that, a PI controller with gains of $K_p = 0.418$ and $K_i = 47.9$ was designed. The closed loop system is thus defined by Equation 10.8.

$$
\begin{aligned}
\dot{x} =& \Big(A - B_\tau K C\Big) x + \big(B_{v_w} - B_\tau K D_{v_w}\big) v_w \\
y =& Cx + D_{v_w} v_w
\end{aligned}
\tag{10.8}
$$

The closed-loop response to a step input in wind is shown in Figure 10.22. The response is now under-damped, but the rise time is faster. A more complete picture is drawn when looking at the Bode

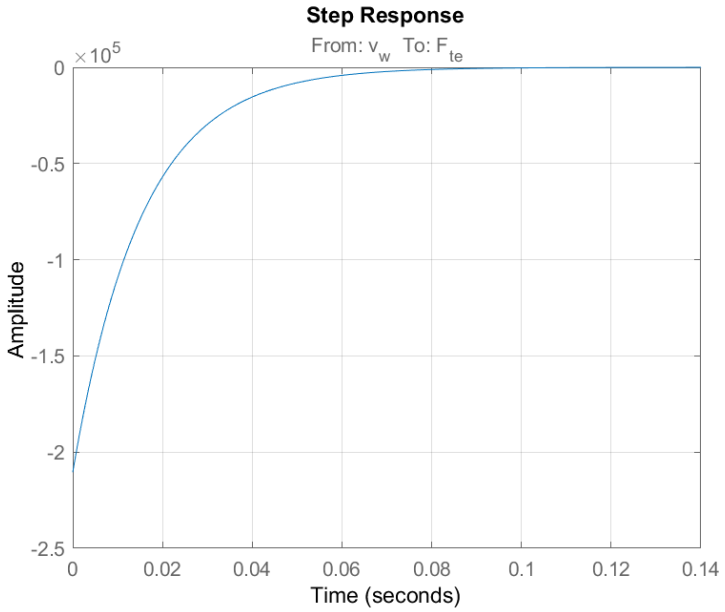

Figure 10.19: Tether force response of the open-loop system to a step in wind speed.

plot comparing the open and closed loop response in Figure 10.23. The controller is able to dampen the effect of the wind much more than the open-loop system, especially at lower frequencies. One frequency of particular interest is $\pi/10$ rad/s, which is the tether force frequency that MegAWES experiences, as discussed in chapter 9. With the wind speed at this frequency the closed loop response is much better than the open loop response as can be seen in Figure 10.24.

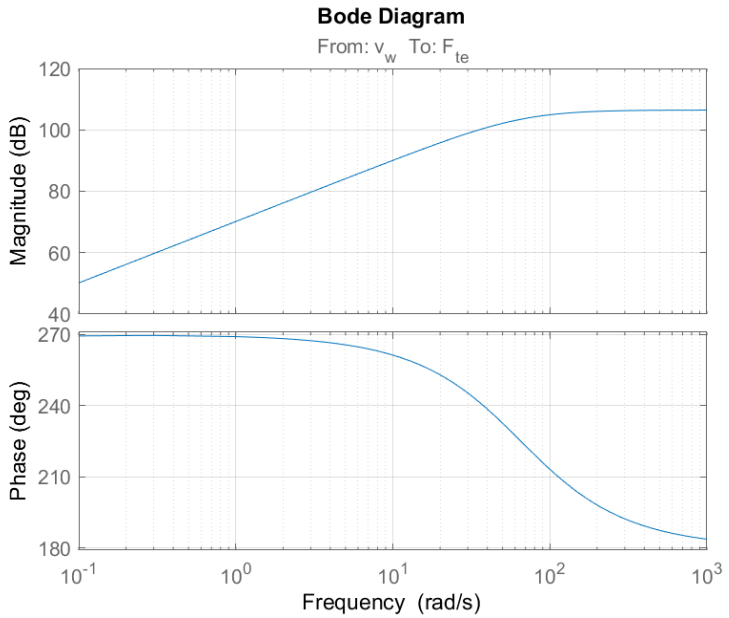

Figure 10.20: Bode plot of tether force of the open-loop system to a step in wind speed.

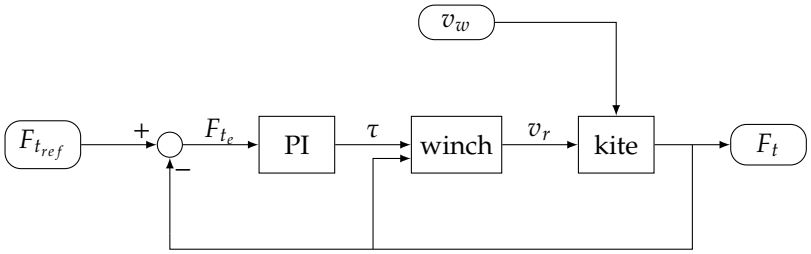

Figure 10.21: Block diagram of the system with PI feedback controller

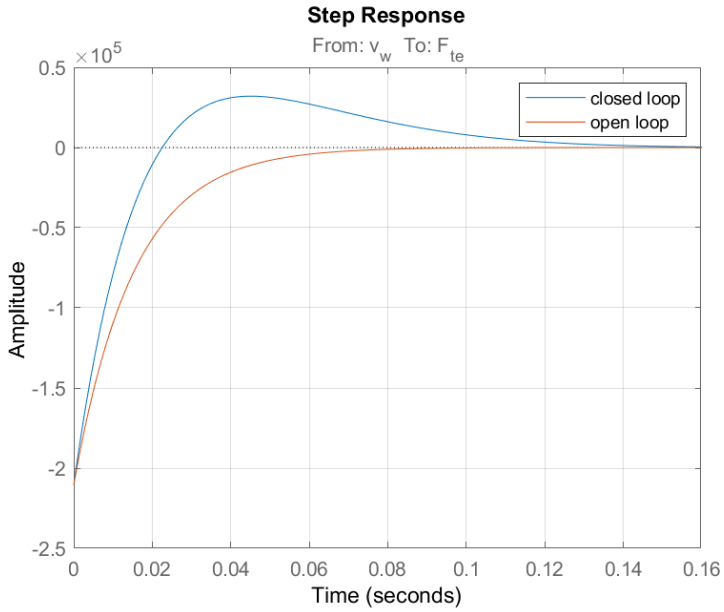

Figure 10.22: Tether force response of the closed-loop system to a step in wind speed.

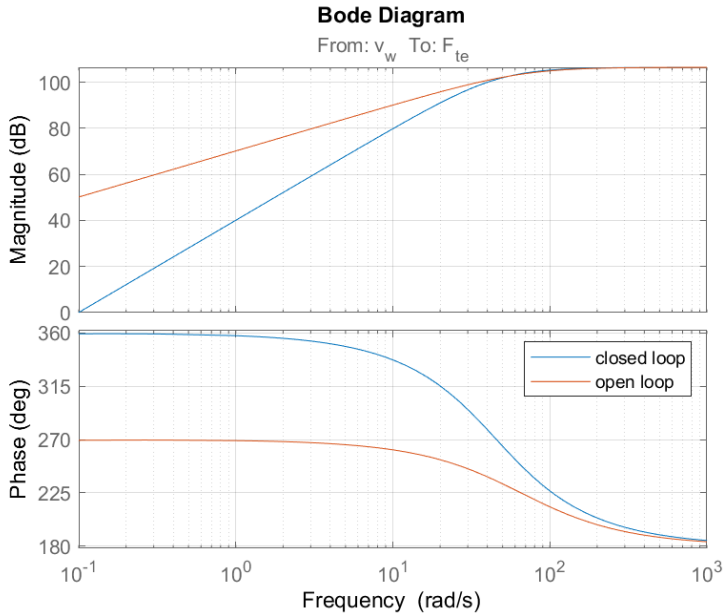

Figure 10.23: Bode plot of tether force of the closed-loop system to a step in wind speed.

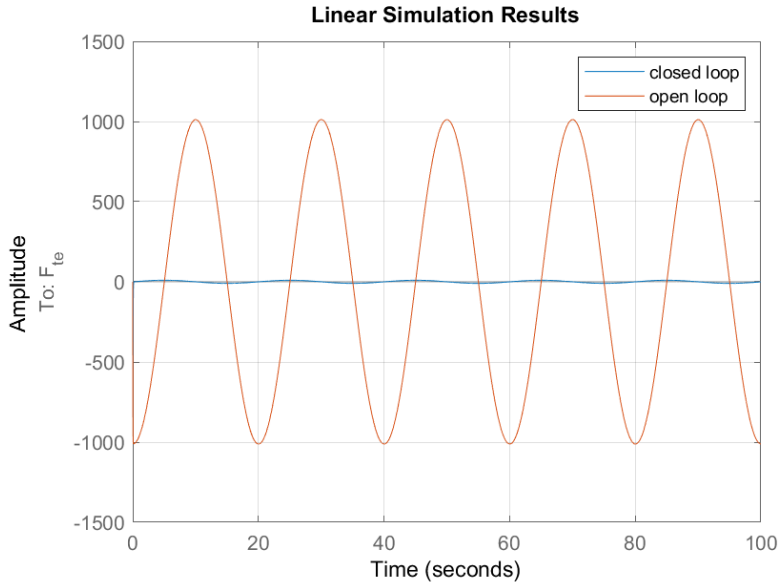

Figure 10.24: Simulated response to a wind speed changing at the tether force frequency of MegAWES (to simulate a change in course angle).

10.3.2. Phase 1

Now that the PI controller can keep the system at the minimum tether force when needed, the controller that keeps the system on the desired tether force as function of the reel-out speed can be designed. The (v_r, F_t)-curve between the minimum and maximum tether force can either be stored in the controller as lookup table (of the data of Figure 10.15) or as polynomial formula that fits to this data. The latter is simpler to implement and requires only a simple linear regression of the optimal (v_r, F_t)-curve of Figure 10.15, between the minimum and maximum tether force. The form of the model is chosen as $F_t^* = \theta_a + \theta_b v_r + \theta_c v_r^2$ and this results in Equation 10.9.

$$\begin{aligned} F_t^* =& \theta_a + \theta_b v_r + \theta_c v_r^2 \\ \text{where} & \\ \theta =& \begin{bmatrix} 146429.5 & 28806.3 & 28242.9 \end{bmatrix}^T \end{aligned} \tag{10.9}$$

Like in chapter 9 (Equation 9.4), a feed-forward controller can be used. However, this creates issues at the boundary between the feedback and feedforward one when switching between them occurs. So instead, the feedback controller is reused by feeding it the reference tether force using Equation 10.9 and extending it with a feedforward controller, which simply multiplies the reference force by the winch radius. This is shown in a block diagram in Figure 10.25.

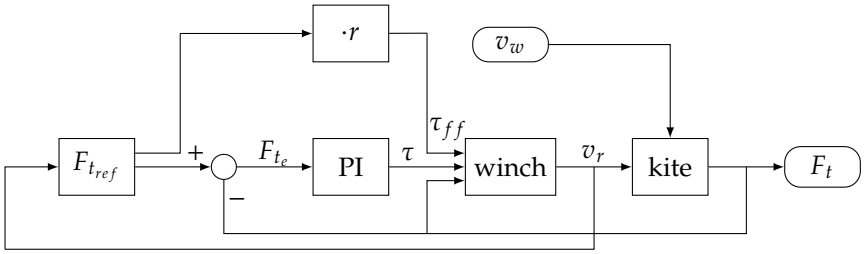

Figure 10.25: Block diagram of the system with PI feedback controller and feedforward controller.

The winch parameters have been sized such that with only a feedforward control law there is enough bandwidth to follow the change in tether force as the kite follows a figure-of-eight. So the PI controller will likely not be very active when the tether force is above the minimum tether force. So the gains did not need to be changed. Furthermore, in Figure 10.26, the response of the open and closed loop system to a step response in tether force reference is shown. It is clear that with the current gains the response is fast and has little overshoot. This controller was only designed around the minimum tether force so it be verified along the entire operating regime in section 10.4.

10.3.3. Phase 2

The PI and feedforward controller ensure that the kite stays on the desired (v_r, F_t)-curve. However, it does not have a tether force limit and power limit built in. The winch controller should not change its behaviour once the tether force and power limit are reached. This is the phase where the kite control, discussed in chapter 11 will take over.

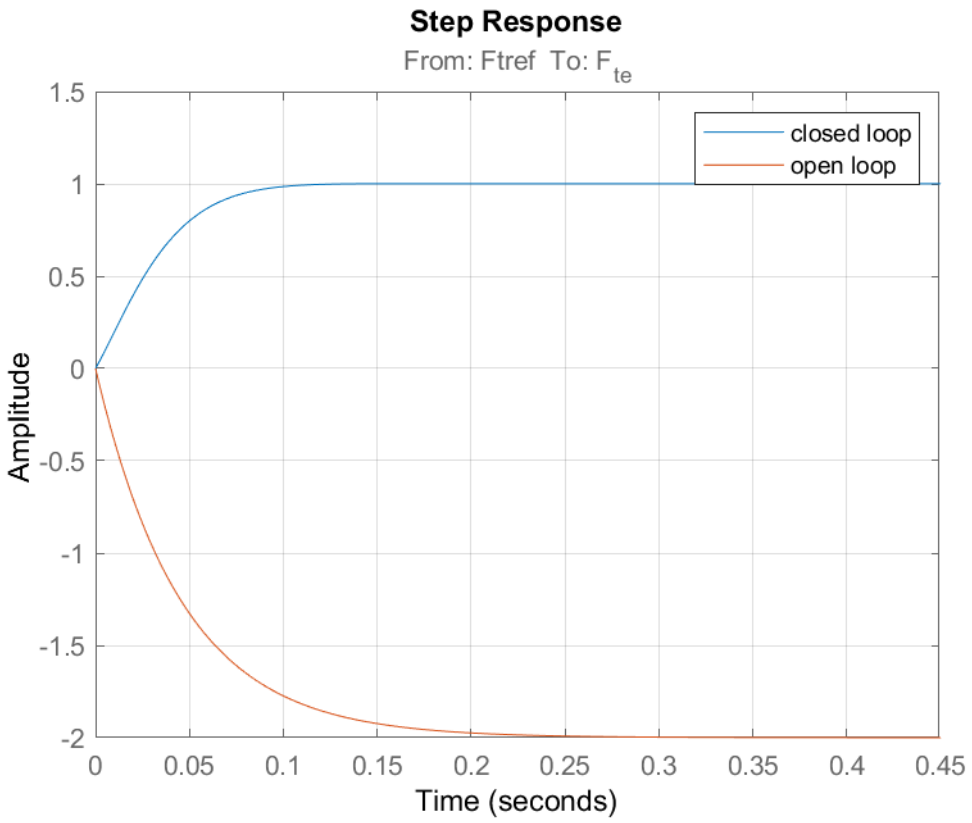

Figure 10.26: Response of the open and closed loop system to a step in tether force reference.

10.4. Verification

The winch controller will be verified in two different simulations. The 3DOF MegAWES simulation is the most relevant for this work but works only for 22 m/s wind speed, where the minimum tether force is not reached. To do an analysis at all wind speeds, the quasi-steady model with mass from van der Vlugt et al. (2019) will be used again to verify the design of the winch controller, similar to in section 9.3. The control architecture from Figure 10.25 has been implemented in Simulink together with a kite model that can call the quasi-steady model from Python. A couple of things need to be verified:

1. The goal of the winch controller is to stay on the (v_r, F_t)-curve as described by the red line in Figure 10.15. It should be verified that it can successfully do so while the wind speed, elevation, azimuth, course angle, and tether length (as the integral of reeling speed) are changing.
    - Tracking should be excellent for the tether force frequency of MegAWES. For higher frequency, which can be caused by gusts, the tracking is allowed to be worse.
    - The control effort when the tether force is above the minimum tether force should mainly come from the feedforward controller and not the PI-controller.
    - The transition between varying tether force and the minimum tether force should not be too oscillatory.
2. The winch controller uses the (v_r, F_t)-curve around an average operating condition for the quasi-steady model with mass. It should be verified that this strategy is better that using the (v_r, F_t)-curve from the massless quasi-steady model.
3. If the winch inertia is increased or the radius decreased, the PI controller can ensure that the system stays on the ideal reel-out factor (contrary to section 9.3). But that this comes with additional, unfavourable control effort and output power.

10.4.1. Quasi-steady simulation

All three objectives will be verified using the quasi-steady simulation.

Scenario 1: Staying on the winch control curve
To see how well the winch controller can drive the system to stay on the (v_r, F_t)-curve, three sub-scenarios were tested. The first one looking at a more realistic scenario where the wind is constant and the kite is flying a figure-of-eight. A second one where the wind is changing. And a third one with high frequency disturbances.

Scenario 1A: Constant wind, changing path The path is reconstructed from Figure 10.12 and shown in Figure 10.27. This path is parameterised with respect to time and the kite is forced to follow it at a constant speed. In reality, the kite of course changes speed as it flies over the figure-of-eight. This is internally reflected in the quasi-steady model, but not fed back to the path generation to simplify the implementation.

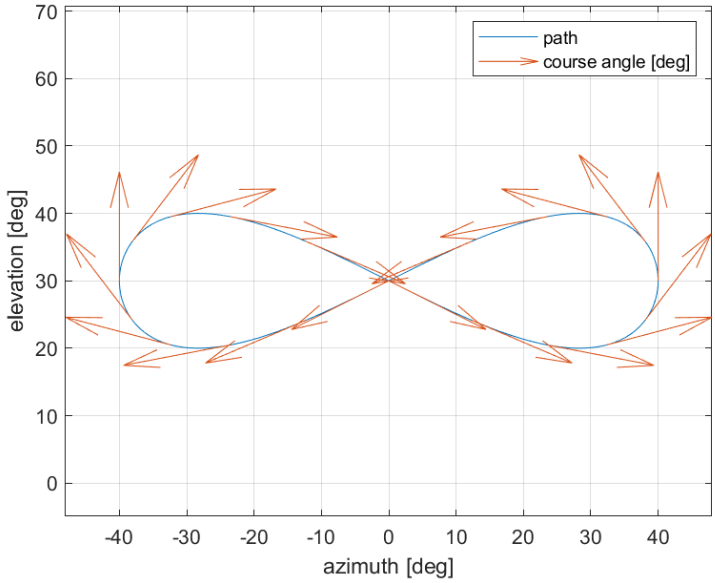

Figure 10.27: Path flown for scenario 1A.

With a constant wind speed of 17.5 m/s, the tether force over time and winch torque are shown in Figure 10.28. It is clear that the tether force is very accurately tracked as the error is always close to zero. Furthermore, this is achieved with almost only the feedforward controller, as the feedback contribution is almost always zero. This shows that the winch parameters have been sized appropriately to allow a sufficiently fast response to the feedforward controller and that the PI controller indeed doesn't have a big influence when the tether force is above the minimum tether force.

The (v_r, F_t)-curve, shown in Figure 10.29 also shows that the winch is able to keep the system on its ideal operating point very well. The part where the actual state is off the ideal line is upon initialisation and this is quickly resolved with little overshoot.

Scenario 1B: Changing wind To isolate the effect of wind, the position of the kite is fixed at horizontal flight at zero azimuth and elevation. The wind speed is meanwhile varying between 0 and 30, with a frequency equal to the tether force frequency of MegAWES. Furthermore, a sinusoidal signal with an amplitude of 5 m/s and a frequency of 10 times the tether force frequency of MegAWES is added. This is not a realistic scenario, but shows the robustness of the winch controller to slow and fast oscillations while also sometimes reaching the minimum tether force. This input is shown in Figure 10.30.

The resulting tether force and winch torque are shown in Figure 10.31. The tether force is very accurately tracked. There are some small tracking errors around the minimum tether force as the change in wind speed is fast there and there's a feedforward component of the wind to the tether force. However, the PI controller is always able drive those errors back to zero. When looking at the winch torque is it clear that the feedforward part is still dominant and that the PI controller is most active around the minimum tether force.

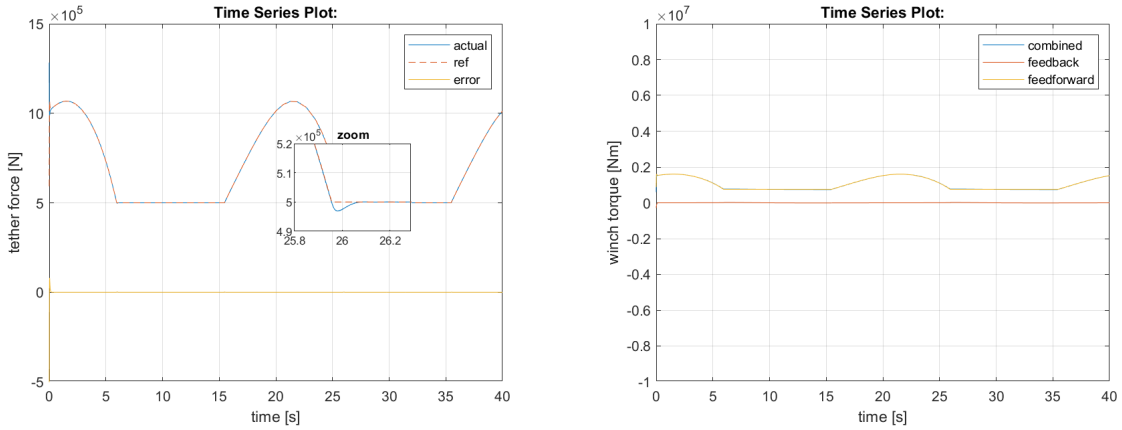

Figure 10.28: Tether force (left) and winch torque (right) for scenario 1A.

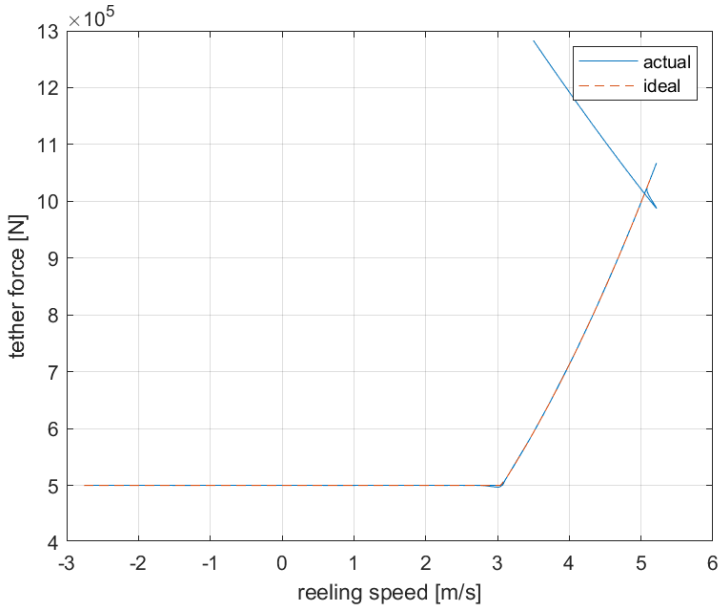

Figure 10.29: (v_r, F_t)-curve response for scenario 1A.

The (v_r, F_t)-curve is shown in Figure 10.32. It is clear that even under faster tether force variations, the winch is able to keep the system on its prescribed curve.

Scenario 1C: High frequency disturbances When adding an additional 2 m/s disturbance signal on the wind speed with a frequency 50 times the MegAWES frequency, the tether force tracking starts to deteriorate, especially around the minimum tether force, shown on the left in Figure 10.33. This is also reflected in the response on the (v_r, F_t)-curve as shown in Figure 10.34.

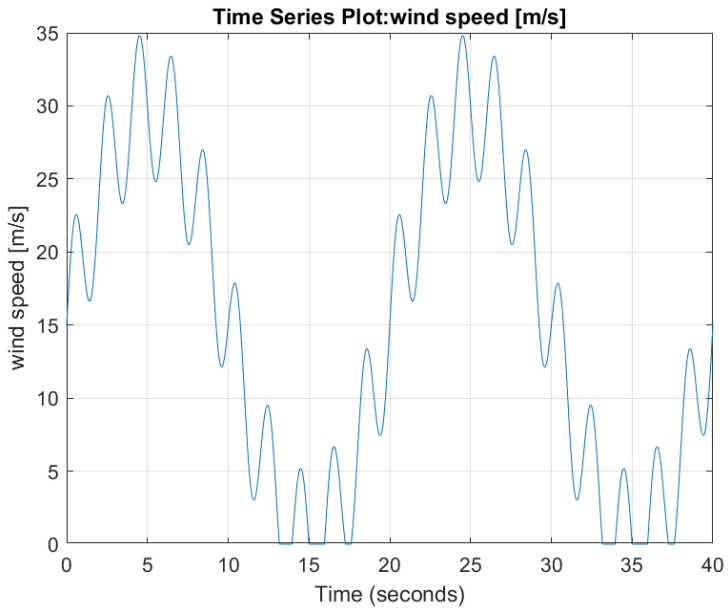

Figure 10.30: Wind speed input for scenario 1B.

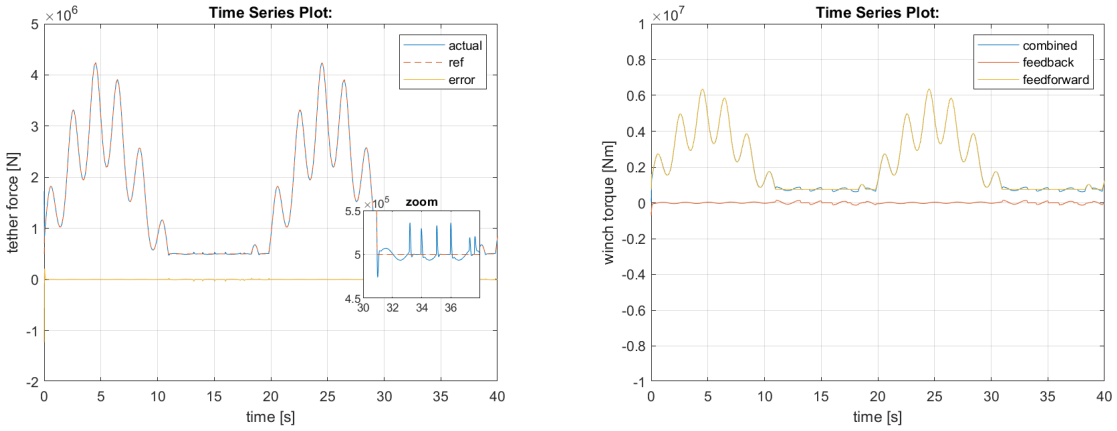

Figure 10.31: Tether force (left) and winch torque (right) for scenario 1B.

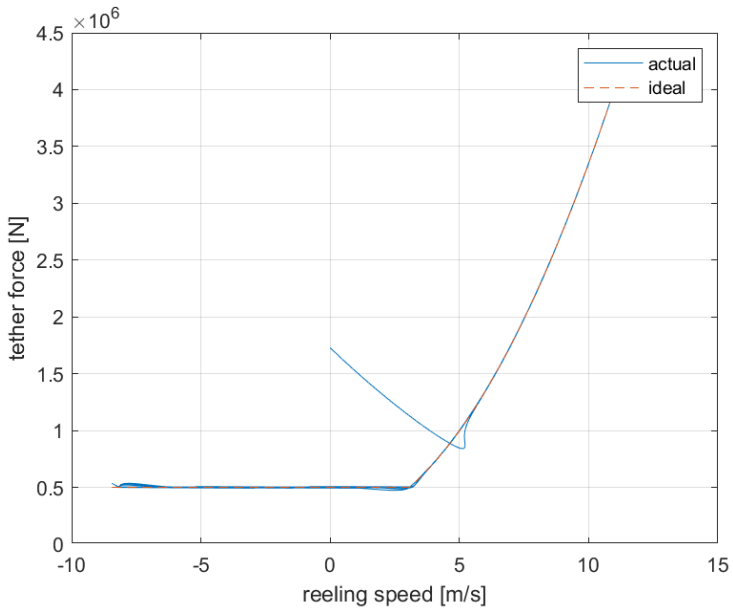

Figure 10.32: (v_r, F_t)-curve response for scenario 1B.

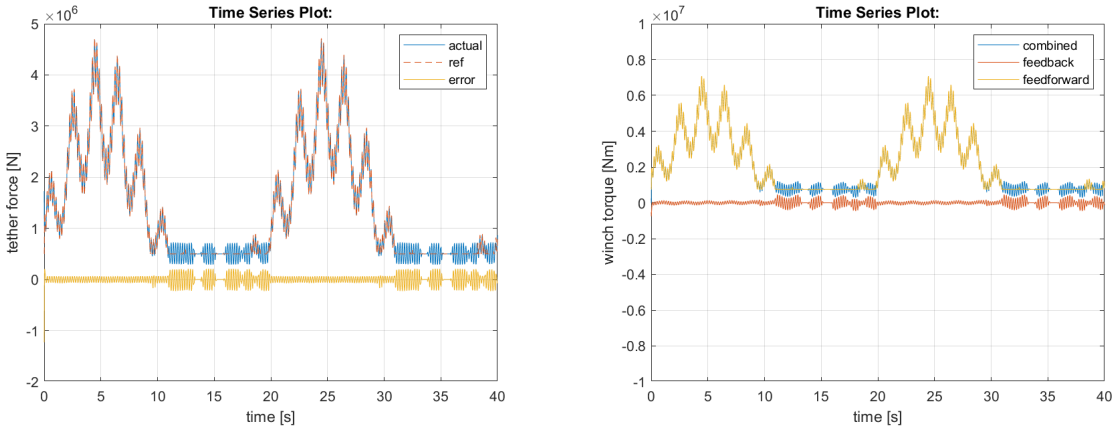

Figure 10.33: Tether force (left) and winch torque (right) for scenario 1C.

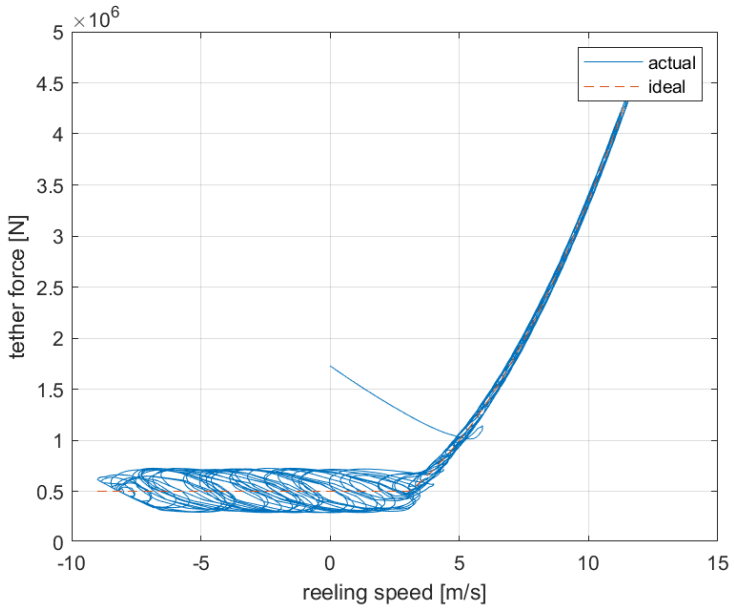

Figure 10.34: (v_r, F_t)-curve response for scenario 1C.

Scenario 2: Power output

In this chapter a winch controller has been designed that keeps the kite on an ideal (v_r, F_t)-curve for a certain average operating point using the quasi-steady model with mass. Then a PI controller has been tuned with a linearisation of this model. An alternative, and much simpler design strategy would be to design the winch control law and tune the PI controller based on a massless model of the kite. The resulting ideal (v_r, F_t)-curve was shown in Equation 9.4 and is used by Todeschini et al. (2021) and Zgraggen et al. (2016). The only addition is a minimum tether force to keep the kite airborne, the same minimum tether force of 0.5×10^6 N is used.

The state-space for the linear model is derived similarly to Equation 10.7 and shown in Equation 10.10. When trimmed around a tether force of 0.5×10^6 N and using again and PI bandwidth of 30 rad/s and a phase margin of 80 °, the resulting gains are: $K_p = 1.48$ and $K_i = 53.5$, which are similar to the gains calculated in subsection 10.3.1.

$$
\begin{aligned}
\dot{x} =& Ax + B_\tau \tau + B_{v_w} v_w \\
y =& Cx + D_\tau \tau + D_{v_w} v_w \\
\text{where} & \\
x =& \begin{bmatrix} v_r \\ \int F_{t_e} dt \end{bmatrix} \\
y =& \begin{bmatrix} F_{t_e} \\ \int F_{t_e} dt \end{bmatrix} \\
\text{and} & \\
A =& \begin{bmatrix} \frac{\mathscr{D} r^2 - d}{J} & 0 \\ -\mathscr{D} & 0 \end{bmatrix} \\
B_\tau =& \begin{bmatrix} \frac{-r}{J} \\ 0 \end{bmatrix} \\
B_{v_w} =& \begin{bmatrix} \frac{-\mathscr{D} \cos(\beta_0) \cos(\varphi_0) r^2}{J} \\ \mathscr{D} \cos(\beta_0) \cos(\varphi_0) \end{bmatrix} \\
C =& \begin{bmatrix} -\mathscr{D} & 0 \\ 0 & 1 \end{bmatrix} \\
D_\tau =& \begin{bmatrix} 0 \\ 0 \end{bmatrix} \\
D_{v_w} =& \begin{bmatrix} +\mathscr{D} \cos(\beta_0) \cos(\varphi_0) \\ 0 \end{bmatrix} \\
\text{Where} & \\
\mathscr{D} =& -2\mathscr{C}(v_{w_0} \cos(\beta_0) \cos(\varphi_0) - v_{r_0})
\end{aligned}
\tag{10.10}
$$

To compare the power output the kite flies in figures-of-eight for about 50 loops, while the wind speed is increasing from 10 m/s to 30 m/s. This simulation run is then repeated for a winch controller that assumes a massless kite together with a PI controller that was tuned on the massless linear model. The difference between the two winch strategies is apparent when looking at the (v_r, F_t)-curves on which the kites fly, shown in Figure 10.35.

Even though the two strategies are clearly different, the resulting power output is very similar. The power output over time and its moving average is shown in Figure 10.36. The different is difficult to see because both curves almost overlap. The strategy developed in this chapter (the "heavy" strategy) produces only 0.13% more power than the strategy that was designed based on a massless model.

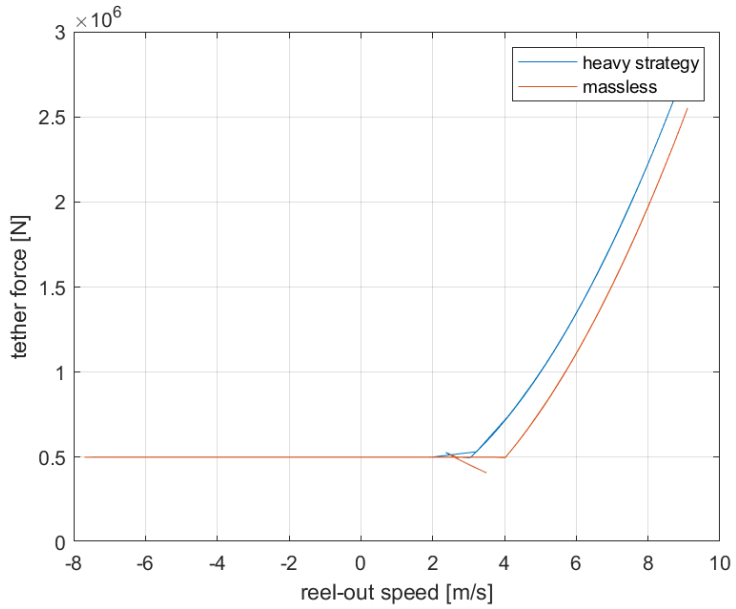

Figure 10.35: (v_r, F_t)-curves for two simulations: one using the optimal curve and PI gains from the analysis in this chapter (heavy strategy) and one using massless equations.

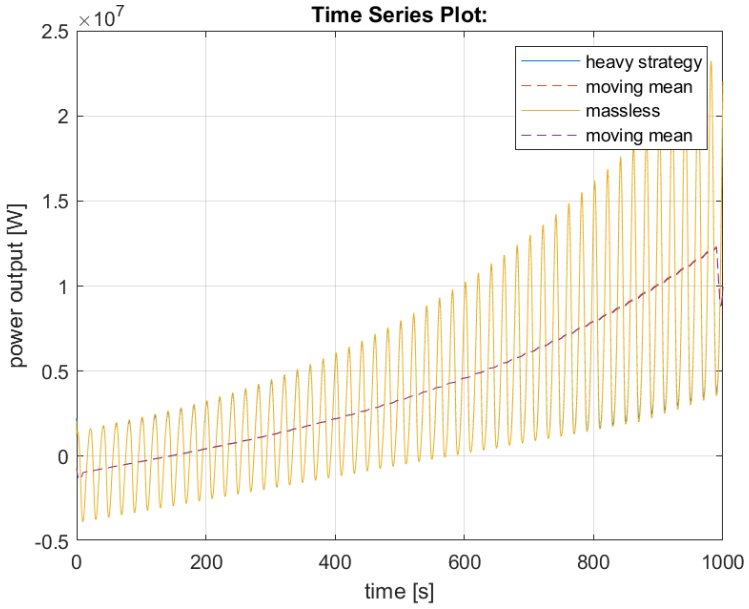

Figure 10.36: Power output for using the heavy strategy vs the massless strategy. The difference is so small that the lines are almost right on top of each other.

Scenario 3: Winch parameters

The winch inertia is increased by a factor of 100 in order to make the winch system react slower. The PI controller designed in this chapter was redesigned with this higher inertia to arrive at new gains: $K_p = 67$ and $K_i = 403$. Other than the increase in inertia and re-tuned PI controller, the scenario is the same as Scenario 1B.

Unlike in section 9.3, the slower dynamics of the winch are compensated by the PI controller, so the winch does not lag behind as shown in Figure 10.37 (compare this to Figure 9.7, where the reel-out speed lags because of the increase in winch inertia). Since the optimal-reel out factor is no longer constant it is not shown in this plot and instead the response on the (v_r, F_t)-curve is shown in Figure 10.38. It is clear that the PI controller is able to compensate for the lag of the higher inertia and keep the system around the prescribed winch control strategy.

This also means that the mean power output is the same as for scenario 1B. In Figure 10.39 the power in and output of the two scenario's are shown. The power in is the power that is put into the system by the kite while the power out is the power that is extracted using the winch controller. Even though the mean power output is equal in both scenario's, the quality of the power output is much worse when the winch inertia is increased. This is because the winch controller is having to push and pull the winch, sometimes in the same direction as the rotation in order to keep it on the (v_r, F_t)-curve. This means that the power output by the winch (power out) is much more oscillatory and much more frequently goes negative (meaning the winch is putting energy into the system). Even though the mean power output is good, this behaviour is very undesirable.

Similar behaviour is expected when lowering the winch radius instead of increasing the inertia.

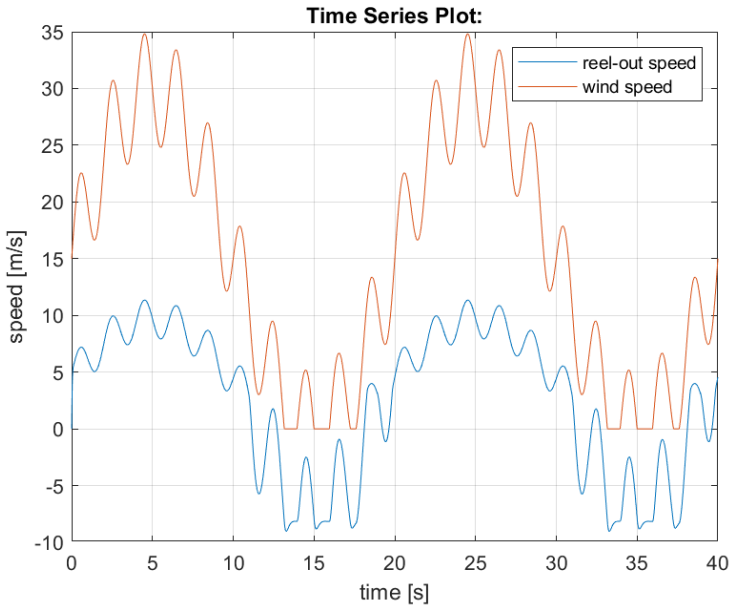

Figure 10.37: Wind and reel-out speed for a system with higher inertia.

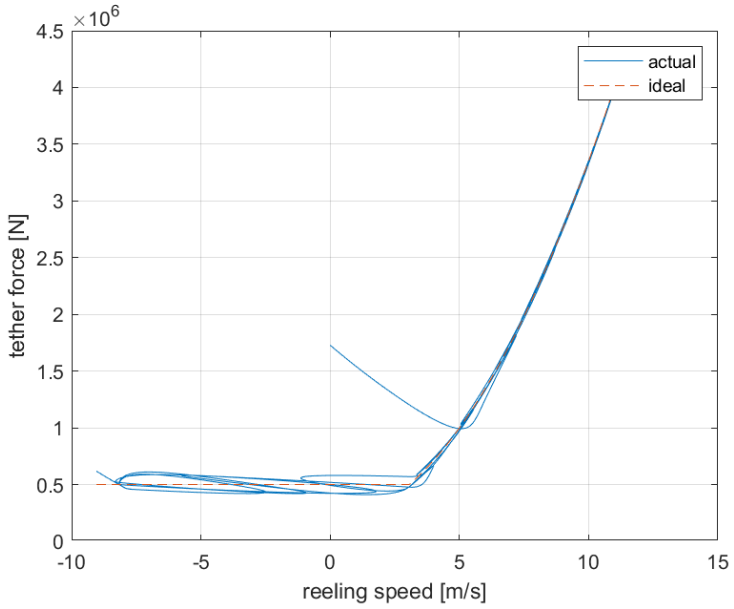

Figure 10.38: (v_r, F_t)-curve response for a system with higher inertia.

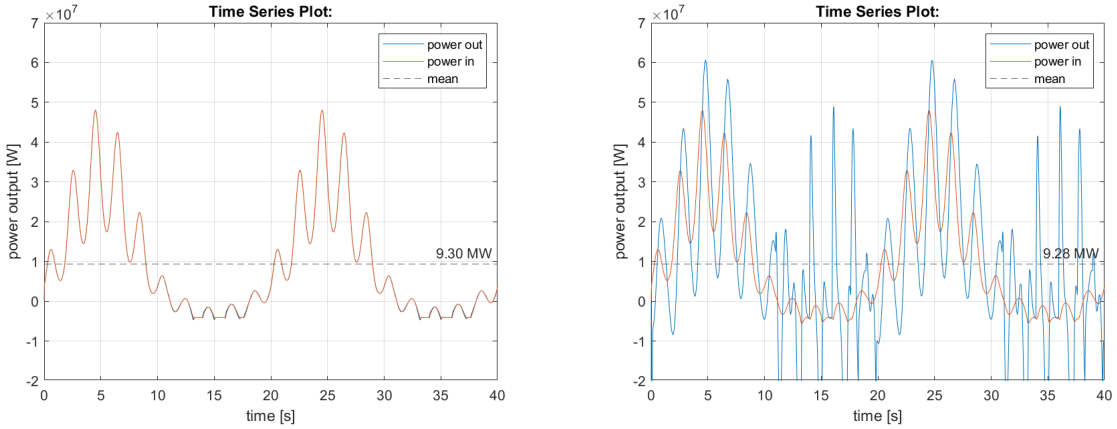

Figure 10.39: Power in and output for scenario 1B (left) and 3 (right).

10.4.2. 3DOF MegAWES simulation

The MegAWES simulation framework has a 6DOF (Eijkelhof & Schmehl, 2022) and a 3DOF simulation (Eijkelhof et al., 2020). To test this new winch feedforward control curve, the 3DOF simulation is used because it will also be used in chapter 11 to add kite tether force control. The 3DOF MegAWES simulation can only be ran at a wind speed of 22 m/s. At this wind speed the wind has enough power such that the kite does not reach the minimum tether force. The PI controller is thus not needed and only the feedforward controller is used. The only other change that was made was that the winch acceleration and velocity saturation on the dynamics were removed. With those dynamic constraints, the winch control curve does not work, but it does lead to high winch acceleration as will be shown later in this subsection. However, these high accelerations will disappear again later in chapter 11 when adding kite tether force control.

Again, the three objectives will be analysed. Since the MegAWES simulation is used, the new strategy using a feedforward winch controller is also compared to the current implementation, denoted by 'baseline'.

Scenario 1: Staying on the winch control curve
In Figure 10.40, the response on the winch control curve can be seen for both the baseline and the new feedforward winch controller. The feedforward winch controller indeed perfectly stays on the prescribed curve. At the maximum tether force, the winch reels out faster to keep the tether force at the limit.

The wind speed in the 3DOF simulation can only be 22 m/s. At this wind speed, the kite does not reach the minimum tether force.

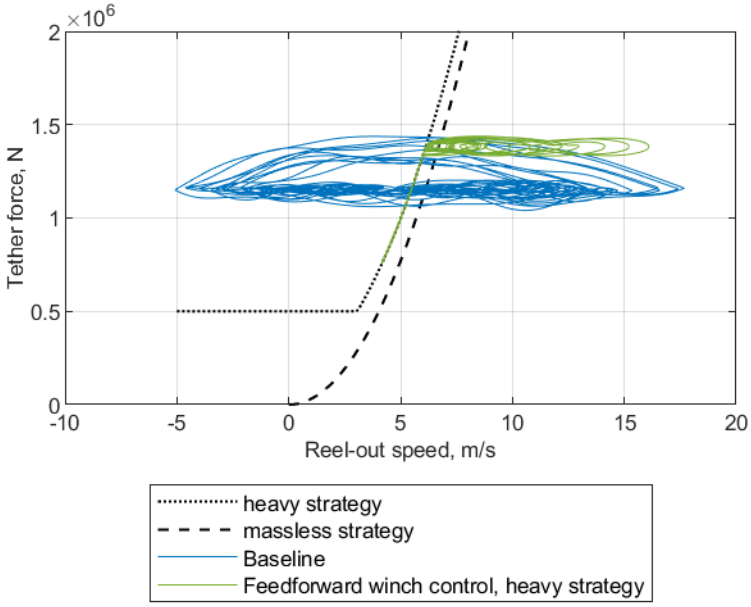

Figure 10.40: Winch control curve response for the baseline and the feedforward winch controller developed in this chapter.

The power output of these two winch control laws is compared in Figure 10.41. Since the baseline keeps a constant tether force, the winch has to put energy into the system when the kite is flying upwards. On the other hand, the feedforward winch controller lowers the reference tether force when the reel-out speed lowers. Thus allowing the kite to fly upwards at a lower tether force and thus not needing to spent power. The minimum power during the traction phase has been increased from −4.7 MW to 3.1 MW.

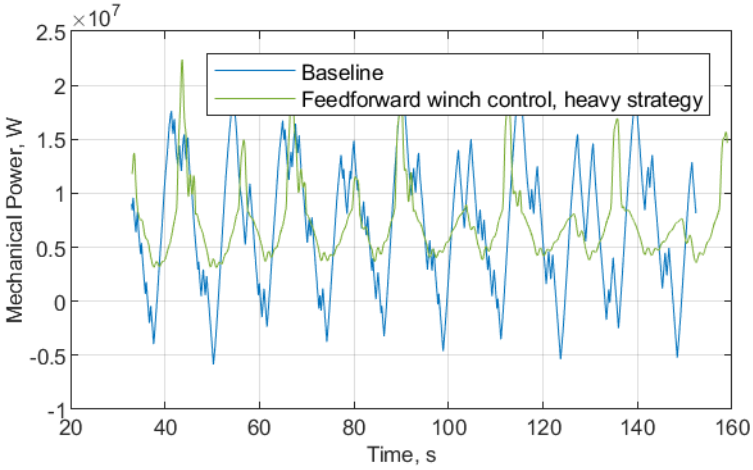

Figure 10.41: Power output for the baseline and the feedforward winch controller developed in this chapter.

In Figure 10.42, the reel-out speed and acceleration is shown. As mentioned in chapter 6, the current winch controller clips at the winch acceleration bounds more than 99% of the time. The feedforward winch controller combined with the new winch parameters has much more gentile acceleration. So the

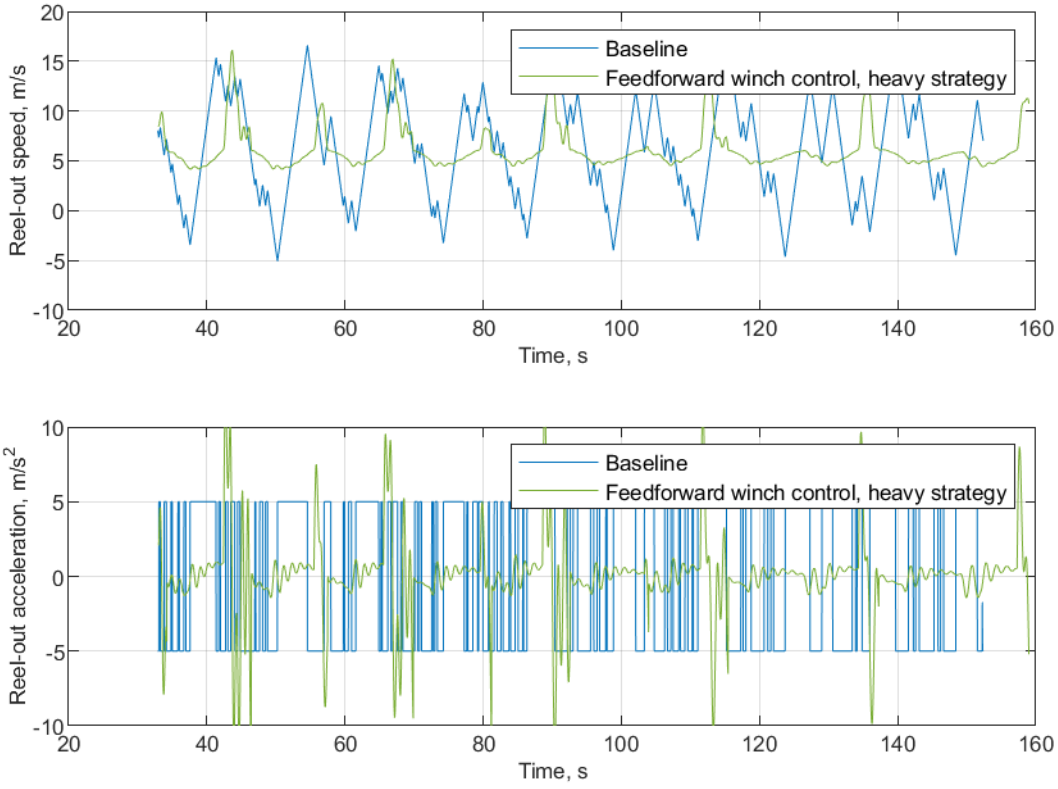

Figure 10.42: Winch reel-out speed and acceleration for the baseline and the feedforward controller developed in this chapter.

reel-out speed is also smoother. However, because the saturation bounds on winch acceleration and speed were removed, the it does sometimes have an acceleration that is higher than desired.

Scenario 2: Power output

The same scenario is repeated but a second feedforward winch controller is implemented. It uses the feedforward winch control law as derived in Equation 9.4. The response on the winch control curve is shown in Figure 10.43. The difference between the two strategies is clear since indeed the feedforward control curve developed in this chapter is shifted a little to the left.

In verification using the quasi-steady model, using the massless curve produced the same amount of power. The power output using the 3DOF model for both the massless and 'heavy' winch control curve is shown in Figure 10.44. The average for the new curve is 7.3 MW while the average for the massless curve is 7.2 MW, so a very small difference. It should be noted that since the new curve keeps a lower reel-out speed on average, the traction phase is longer. This would result in a slightly higher mean cycle power. However, as mentioned in subsection 10.1.2, this effect was neglected when constructing the new winch control curve. However, this does show the importance of taking that into account in future studies.

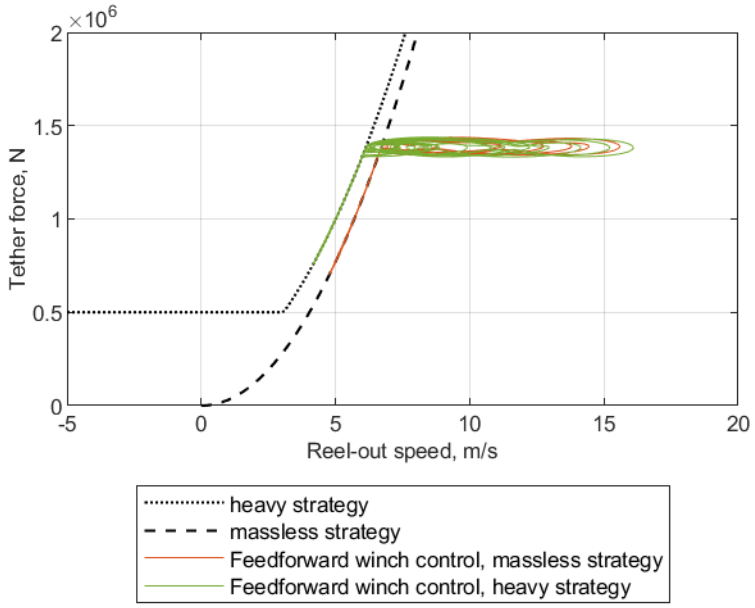

Figure 10.43: Winch control curve response for the feedforward winch controller developed in this chapter and a feedforward winch controller using the massless curve.

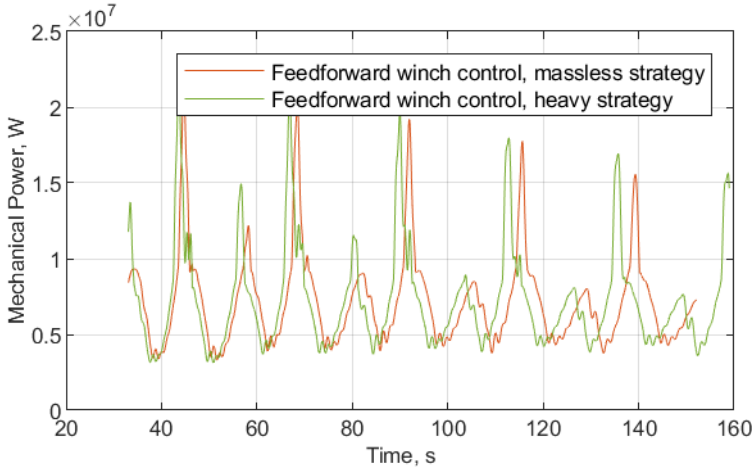

Figure 10.44: Power output for the feedforward winch control curve developed in this chapter and a massless winch control curve

Scenario 3: Winch parameters
Again, to verify the effect of inappropriately sized winch parameters, the inertia of the winch is increased by a factor 100. The response on the winch control curve is shown in Figure 10.45. When using the higher inertia, the response is much worse. The system doesn't move nicely along the prescribed curve anymore but oscillates heavily around it. As a consequence the peak tether force is higher and the 2-phase strategy would be difficult to implement because the power limit is not cleanly reached in a single point.

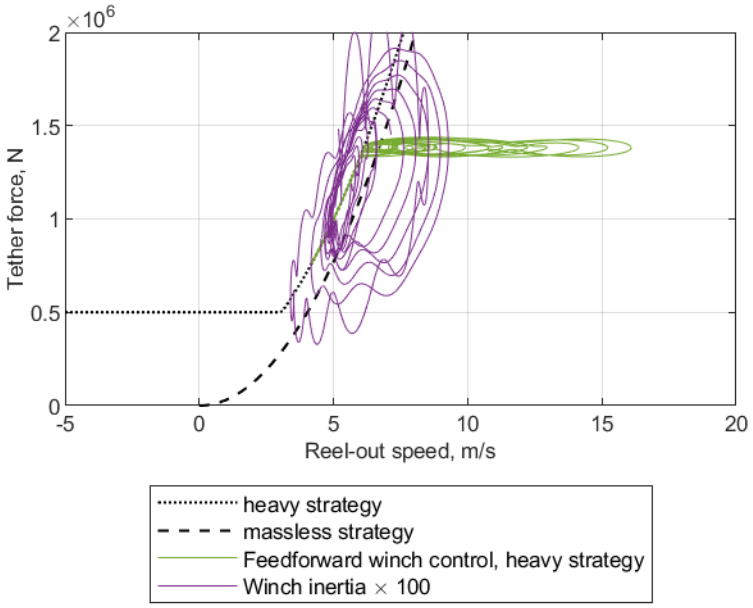

Figure 10.45: Winch control curve response for the feedforward winch controller developed in this chapter and the same controller when using a winch inertia that is 100× higher.

10.5. Conclusion and discussion

The current winch control strategy of MegAWES is to keep the tether force constant as a function of a wind speed measurement. However, it has been shown that for optimal instantaneous power extraction the tether force must be varied as elevation, tether length and the course angle change for kite's with mass (only azimuth does not have an effect). In addition, a power limit to MegAWES was added which led to several potential research directions. For this work the 2-phase strategy was chosen that assumed an average operating point and a minimum tether force to keep the kite airborne, even when flying up at low wind speeds.

The tether force reference has two distinct parts: a flat minimum tether force, and a curved part which prescribes the optimal state given an average operating condition. For the first part a PI controller needs to be used while for the second part a feedforward controller is better. To combine these two controllers, they run parallel with the same tether force reference. Since the winch parameters were designed appropriately, the feedforward controller has enough bandwidth in the curved part so that the PI controller does not need to be very active there.

This control architecture was first verified using the quasi-steady model in a Simulink simulation. Under input variations at the tether force frequency of MegAWES, the system tracks the reference tether force very well. However, the power output was not greater than when using the optimal winch controller derived for massless kites. Even though the reel-out factor is slightly sub-optimal when using the massless strategy, the effect on power output is small. This highlights two things: First, to really make use of the mass effect of kite's, more sophisticated control strategies must likely be designed. Second, it highlights the importance of optimising over the complete pumping cycle since these two strategies can obtain very similar instantaneous power output by reeling out at different speeds.

In verification scenario 3 the effect of a larger winch was investigated. In conjunction with chapter 9, an additional conclusion about winch parameters can be made. When the winch inertia is too big,

or the radius too small, the winch dynamics are too slow for the feedforward control law to keep the system at its optimal operating condition. When not compensating with a PI controller (as in chapter 9), the reel-out factor is no longer optimal over time and can even become greater than one which could lead to the kite stalling and crashing. When compensating with a PI controller the mean power output is optimal again but at the expense of the quality of the power output. To keep the system at the ideal reel-out factor, the winch power has to oscillate greatly to compensate the lag of the winch. This strengthens the conclusion of chapter 9 that winch (and generator) inertia and radius must be within strict design requirements.

However, from verification scenario 1C it is also clear that the winch parameters were too conservative and that a higher inertia and/or lower radius could still work. The tether force tracking, in the curved part of the (v_r, F_t)-curve should be tracked mostly by the feedforward signal and even at a frequency 50 times higher than the MegAWES tether force frequency it is able to do this. In chapter 9 a safety factor of 10 on the MegAWES frequency was chosen and an allowable power loss of 1% at a reel-out speed of 1 m/s. Relaxing the safety margin, power loss requirement and minimum reel-out speed for that power loss would result in a larger allowable inertia and/or lower allowable radius which in turn would make the system actually lag behind more at these high tether force frequencies.

This interplay between the feedforward and PI controller, and the winch parameters is an important new research area for large scale airborne wind energy systems. If requirements on maximum inertia and minimum radius cannot be relaxed enough, it could be that no existing components exist that would allow operating a MegAWES system with the presented control architecture.

A second verification was done using the 3DOF dynamic simulation of MegAWES. The conclusions from the quasi-steady simulation were strengthened using this more realistic model. Since the 3DOF dynamics were only available at a wind speed of 22 m/s, the minimum tether force was not reached so there was no use for a PI controller parallel to the feedforward controller. However, it was possible now to compare the results to the current megAWES control architecture. The most important result was that using the feedforward winch controller ensured that the winch did not have to put energy into the system to keep the tether force constant when the kite was flying upwards. By allowing a lower tether force during this portion of flight, the minimum power during the traction phase was increased from −4.7 MW to 3.1 MW. This thus reduces the requirements on ground systems such as the generator and battery systems.

The peak power and peak winch acceleration were still high. This will be solved using kite tether force control in the next chapter.

11

Kite control design

The sixth research question is:

Research question 6

What is the performance of the kite tether force controller?

When the system is using a feedforward winch control law it stays on a winch control curve, under the condition that the winch parameters were appropriately sized, as discussed in chapter 9. In chapter 10, a winch control curve was designed around an average operating point for the MegAWES system including a minimum tether force. However, its power output was not significantly higher than when using the winch control curve as derived for massless systems. So in this chapter both curves will be used going forward.

During verification of the winch control curve in section 10.4, the winch control law also included a maximum tether force. It was clear that this led to an increase in reel-out speed, which led to undesired power peaks. In this chapter, a novel idea, first developed in chapter 4, called 'kite tether force controlled' will be developed and verified in the 3DOF dynamics simulation of MegAWES.

The controller will be designed in section 11.1. The results will be shown in section 11.2. This chapter is concluded in section 11.3.

11.1. Controller design

The optimal winch control curve designed in the previous chapter is shown again in Figure 11.1, next to the optimal winch control curve for massless kites. For the 2-phase strategy it is assumed that the tether force limit and power limit coincide. So once the system reaches that point on the winch control curve, it should stay at that point if the wind speed increases, by lowering the angle of attack of the kite. When using the 2-phase strategy, the kite knows when the power limit is reached by only measuring the tether force. So when the kite ensures that the maximum tether force is not exceeded, the system stays at the power limit.

The objectives of a kite angle of attack controller are twofold. First, when operating below the tether force limit, the kite must fly at the highest allowable angle of attack, resulting in an optimal lift-to-drag ratio, resulting in maximum power extraction from the wind. Secondly, when operating above the tether force limit, the kite must lower its angle of attack such that the system stays at the tether force limit. To achieve this, a novel kite tether force controller was designed that uses a PI controller with back-calculation and nonlinear dynamic inversion to calculate the angle of attack reference. The block diagram for this architecture is shown in Fig. 11.2.

The PI controller, enclosed in mint, outputs a reference lift force for the kite. While for massless kites in quasi-steady flight, the lift force is always in equilibrium with the tether force, heavy systems such as MegAWES must also use their lift force to compensate gravity. To compensate for this and other model uncertainties, an integrator is used. The reference angle of attack is then calculated using a nonlinear model for the lift, shown in Eq. (11.1).

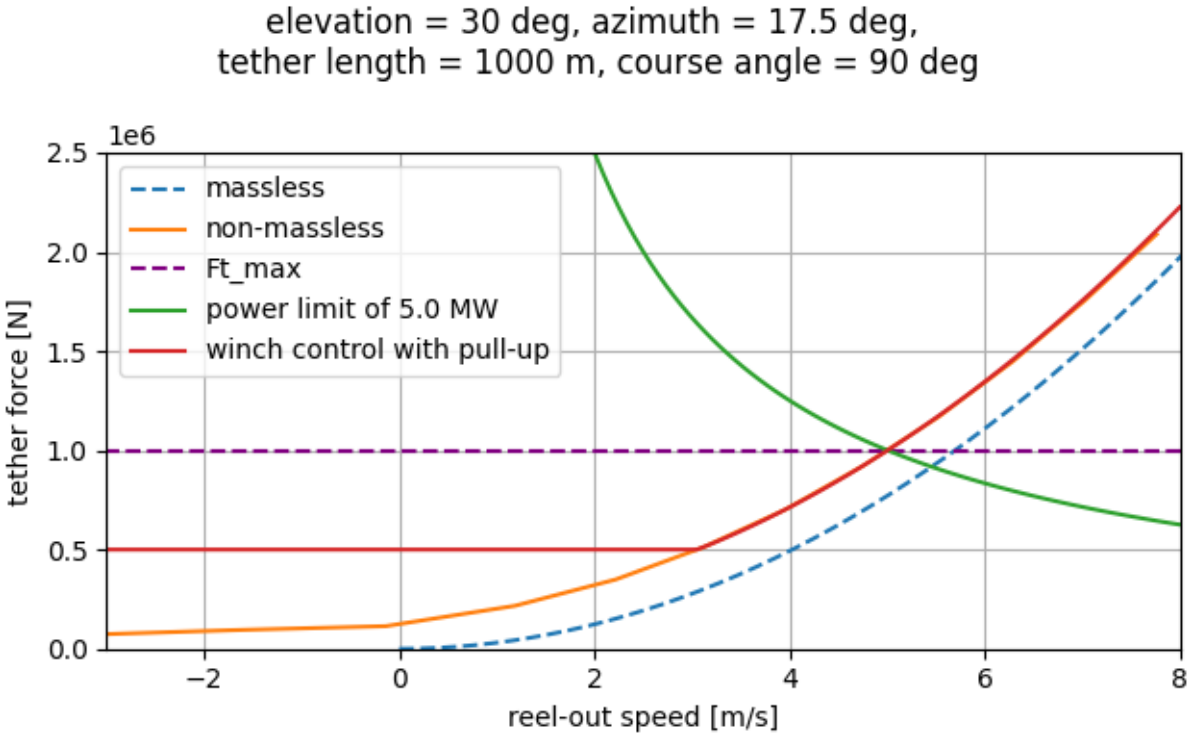

Figure 11.1: Winch control curve designed in the previous chapter (red) and for massless kites (blue dotted).

The PI controller uses a constant tether force reference, which is at the tether force limit. When the system is above this reference, the PI controller will output a lower lift force reference, lowering the angle of attack reference.

But when the system is operating below the tether force limit, the PI controller will increase the lift force reference to drive the angle of attack reference up to its maximum value, as desired. To avoid integrator wind-up and unsafe angle of attack references, back-calculation is used with $K_b = 1$. The dynamic saturation comes from the minimum and maximum possible lift force that the system can provide, based on minimum and maximum allowable angle of attack and the current airspeed.

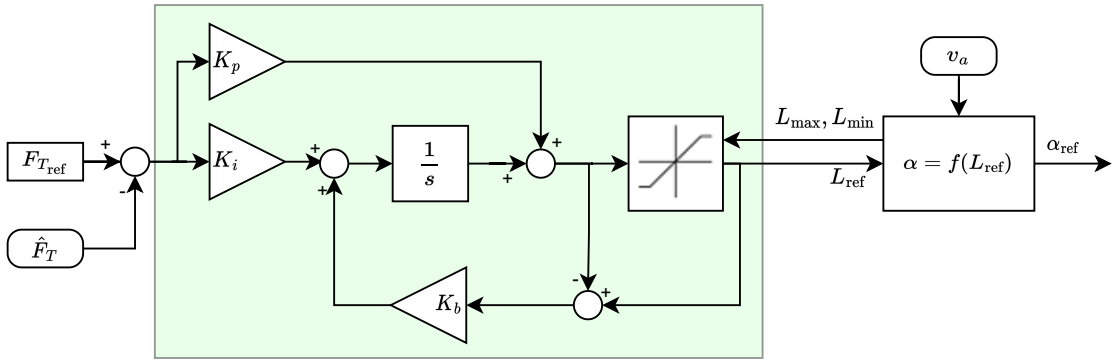

Figure 11.2: Block diagram of the kite tether force controller. The part that represents a PI controller with back-calculation is enclosed in mint.

$$\alpha_{\text{ref}} = \frac{\frac{L_{\text{ref}}}{\frac{1}{2}\rho v_a^2 S} - C_{L_0}}{C_{L_\alpha}} \tag{11.1}$$

11.1.1. Integration in the MegAWES simulation

In the current implementation, the bank angle and angle of attack are calculated in a single block and are thus coupled. This is done using the inverse point mass dynamics of the path and its desired trajectory, based on Rapp, Schmehl, Oland, and Haas (2019). The bank angle reference from this block is preserved but a new separate, decoupled block to calculate the angle of attack reference was added. In this block, the control architecture previously shown in Figure 11.2 was implemented.

The bank angle and angle of attack reference are filtered by a second order filter that imposes dynamic limits and acceleration and rate saturation on the change in angles. This ensures that the 3DOF dynamics don't have a much higher bandwidth in angle of attack and bank angle than the 6DOF dynamics and thus makes the 3DOF case more realistic.

The MegAWES simulation framework saturates the winch velocity and acceleration. As shown in chapter 9, the winch inertia is too small leading to a high bandwidth for the winch dynamics, which could lead to excessive acceleration. So the controller limits its torque output such that the system stays within acceleration limits. As discussed in chapter 6, this happens 99% of the time. In this work, the saturation on the winch dynamics has been removed. The feedforward controller is designed with this assumption. In section 11.2, it will be shown that the winch acceleration is much lower and smoother than in the baseline.

Since the winch saturation is removed the retraction phase is no longer successful. The winch controller (also in the baseline) is not able to prevent the kite from overshooting the ground station as the kite and winch are not able to work together in harmony for a transition back into the traction phase. The focus of this work is on the traction phase, in the results, only the (first) traction phase is shown.

11.1.2. Tuning the PI controller

The two gains of the PI controller are tuned by sweeping through a grid of possible values and evaluating the three control objectives for different values in the 3DOF simulation. Both gains are swept from 0 to 2.5 with a stepsize of 0.25 and the resulting tether force overshoot, maximum power output, and mean power are analyzed. These results are shown in Figure 11.3 for the massless strategy and in Figure 11.4 for the heavy strategy.

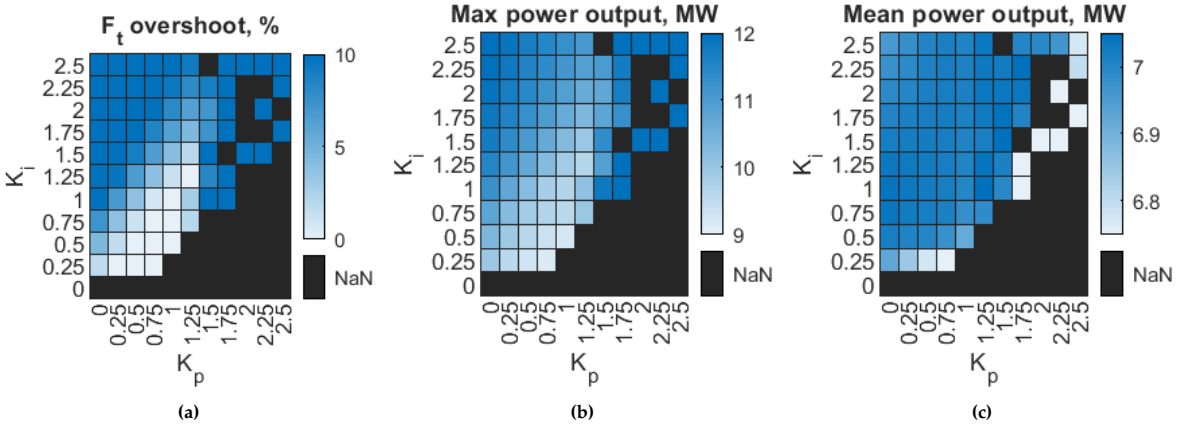

Figure 11.3: Tether force overshoot (a), maximum power (b), and mean power (c) during the traction phase for different values of K_p and K_i when using the massless strategy.

Both graphs show a similar pattern, that was previously discussed in Part II. Though, as expected, using the heavy strategy has a lower mean power because its power limit is lower. For both the heavy and massless strategy gains of 0.75 and 1.0 were selected for K_p and K_i respectively. This combination is not close to a combination that leads to failure, has a lower tether force overshoot, low maximum power, and high mean power, and thus fulfils all control objectives.

It's a good sign that the gains are not very sensitive to the choice of winch control strategy because this means that the controller is robust to changes in winch behaviour.

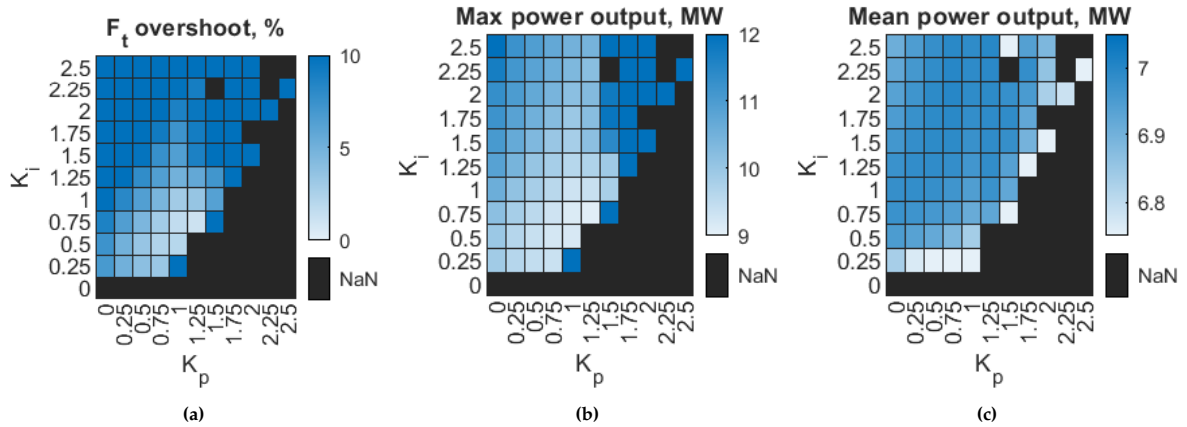

Figure 11.4: Tether force overshoot (a), maximum power (b), and mean power (c) during the traction phase for different values of K_p and K_i when using the heavy strategy.

11.1.3. Selecting the tether force reference

In Figure 11.1, a maximum tether force of 1.0×10^6 N was used, since a similar maximum operational tether force was used in the 6DOF dynamics of MegAWES. However, in the 3DOF simulation, the maximum tether force currently reached at a wind speed of 22 m/s (the only available wind speed for the 3DOF simulation) is 1.437×10^6 N. Since there will likely be a bit of tether force overshoot of the kite tether force controller, the reference tether force was selected such that the peak tether force experienced during the traction phase did not exceed the peak tether force of the baseline.

The kite tether force controllers will be used in two scenario's. One where the winch is using the heavy strategy as developed in the previous chapter and one where the winch uses the massless winch control curve. Since the strategies have different points where they reach the power limit, the tether force limits are also different and shown in Table 11.1.

Table 11.1: Tether force reference for kite tether force control, both when using the heavy or massless winch control curve.

	$F_{t_{\text{ref}}}$ N
heavy strategy	1.251×10^6
massless strategy	1.380×10^6

The power limits for these two strategies are different because they reach the peak tether force at different points on the winch control curve. When assuming that the systems will perfectly stay on the prescribed winch control curve, the heavy strategy will hit a peak tether force (1.437×10^6 N) at a reel-out speed of 6.3 m/s, while when using a massless strategy will reach that peak tether force at a reel-out speed of 6.8 m/s. The resulting peak power will thus be 9.0 MW and 9.8 MW respectively.

11.2. Results

This section is split into three subsections. First, the kite tether force controller will be combined with the heavy strategy for the winch control curve, developed in the previous chapter. Performance will be compared to the baseline, the current implementation in MegAWES. Second, the heavy strategy will be compared with the massless strategy. Finally, these three strategies will be compared directly by comparing some statistics about the power distribution.

11.2.1. Using the heavy strategy

In chapter chapter 10, it was shown that using the feedforward winch controller improved the minimum power during the traction phase from −4.7 MW to 3.5 MW. The kite tether force controller works together with this feedforward controller, but is used to reduce the peak power. In Figure 11.5, the power output is compared. The minimum power is 3.8 MW, comparable to the case with only the feedforward strategy. In addition however, the peak power has now been reduced from 20.0 MW to 9.0 MW. The peak power is as expected when multiplying the highest expected tether force (1.437×10^6 N) with the

corresponding reel-out speed from the winch control curve (6.3 m/s).

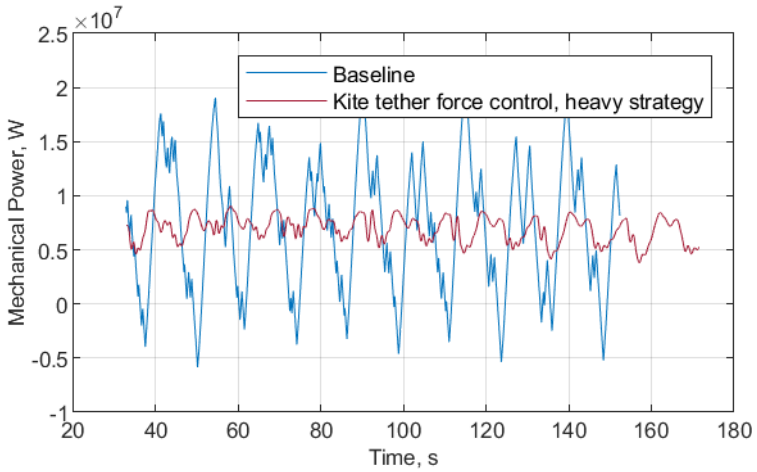

Figure 11.5: Comparison of the power output between baseline and kite tether force control combined with the feedforward winch control using the heavy strategy.

The response on the winch control curve is shown in Figure 11.6. The kite tether force controller is able to perfectly keep the system on the curve related to the heavy strategy and has the same peak tether force as the baseline. In chapter 10, the winch had to reel out faster to keep below the tether force limit but now the tether force is reduced by the kite and the system can simply always stay on this curve.

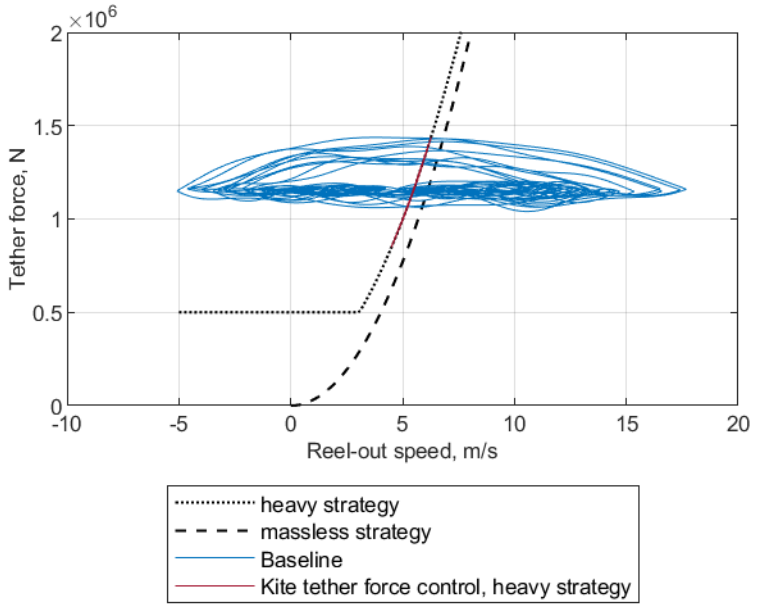

Figure 11.6: Comparison of the winch control curve response between baseline and kite tether force control combined with the feedforward winch control using the heavy strategy.

In Figure 11.7, the angle of attack is shown. Twice per figure-of-eight, so everytime the kite is flying downwards, the angle of attack is lowered. It is lowered quite smoothly without any high frequency content. This is partly due to the second order filter between commanded and actual angle of attack. Furthermore there are two more interesting observations: there is an asymmetry in the angle of attack when its flying down in the figure of eight from the right or the left, it is unknown what causes this behaviour. Furthermore, the minimum value of the angle of attack goes up over time. This is explained by the fact that the tether drag increases as the kite is reeled out so that a similar tether force is achieved at a higher angle of attack due to the decrease in airspeed. This shows that the kite tether force controller is able to compensate for these changes that would be difficult to precisely model.

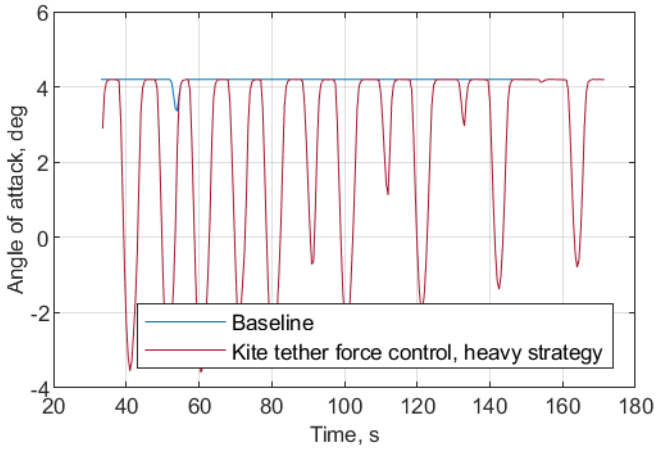

Figure 11.7: Comparison of the angle of attack between baseline and kite tether force control combined with the feedforward winch control using the heavy strategy.

The winch dynamics are much better. As first observed in chapter 6, the winch acceleration in the baseline clips at the maximum acceleration 99% of the time. Using the larger winch inertia and this kite tether force control algorithm, the acceleration is much smoother as shown in Figure 11.8. This also results in a much more constant reel-out speed.

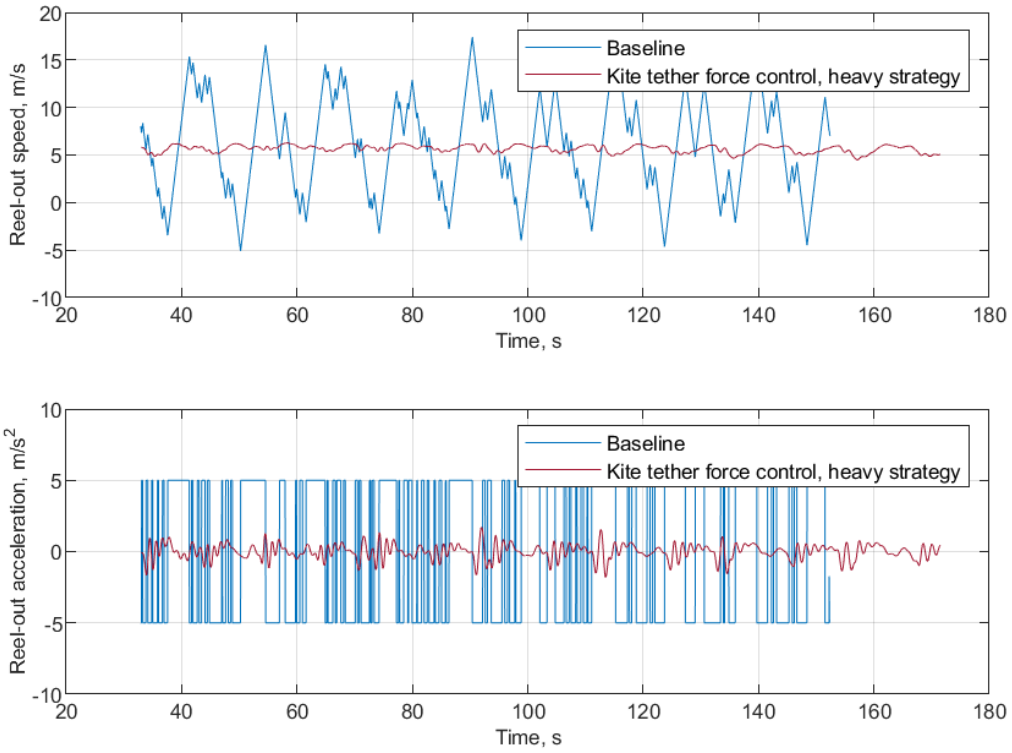

Figure 11.8: Comparison of the winch reel-out speed and acceleration between baseline and kite tether force control combined with the feedforward winch control using the heavy strategy.

11.2.2. Using the massless strategy

Instead of using the winch control curve derived in the previous chapter (the 'heavy strategy'). It is compared to the winch control curve as prescribed by Equation 9.4. Still, the same kite tether force controller at the kite is used.

In Figure 11.9 the winch control curve response for these two strategies is shown. In this figure the difference is clearly visible. Due to tuning of the reference tether force for the tether force controller, discussed in subsection 11.1.2, the peak tether force of both strategies is identical.

The power output is shown in Figure 11.10. The minimum power output is usually better when using the heavy strategy as it drives the system to a higher tether force for a given reel-out speed. It was found that this is beneficial for heavy kites in the previous chapter. It is furthermore clear that the peak power for the heavy strategy is lower. This is not because of the kite tether force controller working differently but purely because the point on the winch control curve where the tether force limit (1.437×10^6 N) is reached is at a lower reel-out speed (6.3 m/s instead of 6.8 m/s), and thus at a lower power.

Since the massless strategy allows a higher power output, the angle of attack is also at its maximum value for longer. Here the advantage of kite tether force control is clear: As long as it can, it will stay at the maximum allowable angle of attack and only decrease it when needed without the need for additional knowledge. The winch controller has changed its control curve and the kite controller simply adapts by only changing its reference maximum tether force because the overshoot changed slightly.

11.2.3. Mean power

In this subsection, the baseline strategy will be compared to kite tether force control using the massless and heavy strategy based on the power distribution, electrical power, and mean cycle power.

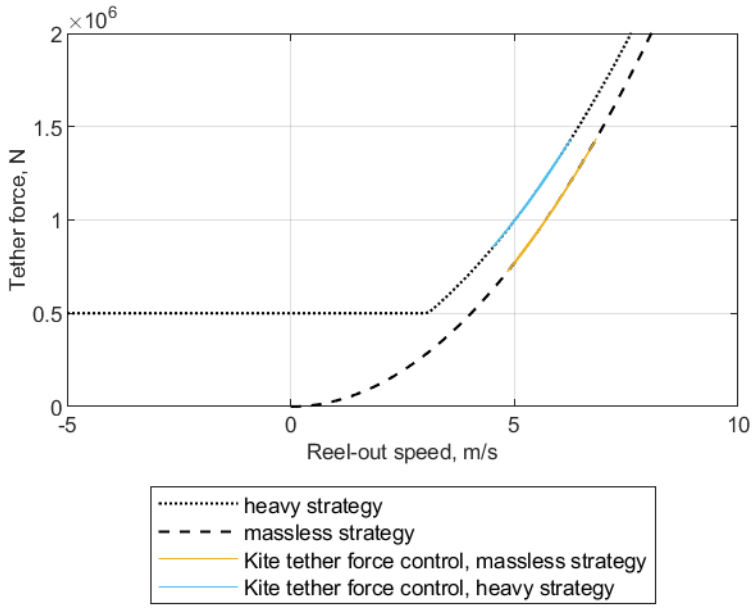

Figure 11.9: Comparison of the winch control curve response between the kite tether force controller combined with the feedforward winch control using either the heavy strategy or the massless strategy.

Power distribution

The power distribution during the traction phase for the three strategies is shown in Figure 11.12. The kite tether force control architectures have a higher minimum power, going from negative (−4.7 MW) to positive (3.5 MW and 3.8 MW for the massless and heavy strategy respectively), due to the feedforward winch controller. Furthermore, the peak power has been greatly reduced, from 20.0 MW to 9.8 MW and 9.0 MW, due to the kite tether force controller.

The mean power output is between 3 and 5% smaller as shown in Table 11.2. However, this is a small cost compared to the desired power smoothing effects.

Table 11.2: Mean mechanical power for all strategies during the traction phase. With percentages comparing the archtectures using kite tether force control to the baseline.

	$P_{m_{\text{mean}}}$ MW
baseline	7.23
heavy strategy	6.89 (95.3%)
massless strategy	7.02 (97.1%)

Electrical power

When power is used during the traction phase, using the baseline strategy, this must come from an on-site energy storage system. Not only does this raise the requirements and thus costs of such a system, it also comes with electrical efficiency losses (Joshi et al., 2022).

The electrical power is given in Equation 11.2 (Eijkelhof & Schmehl, 2022; Fechner & Schmehl, 2013), where η_g denotes the generator efficiency, η_m the motor efficiency, and η_b the battery storage efficiency. It is clear that there are losses from mechanical power to electrical power. Furthermore, electrical losses are greater when power must be consumed by the winch.

$$P_e = \begin{cases} P_m > 0: & P_m \eta_g \\ P_m < 0: & \frac{P_m}{\eta_m \eta_b} \end{cases} \tag{11.2}$$

When taking this into account, the mean electrical power is given in Table 11.3. As expected, the difference between baseline and kite tether force control becomes smaller at between 2 and 4%.

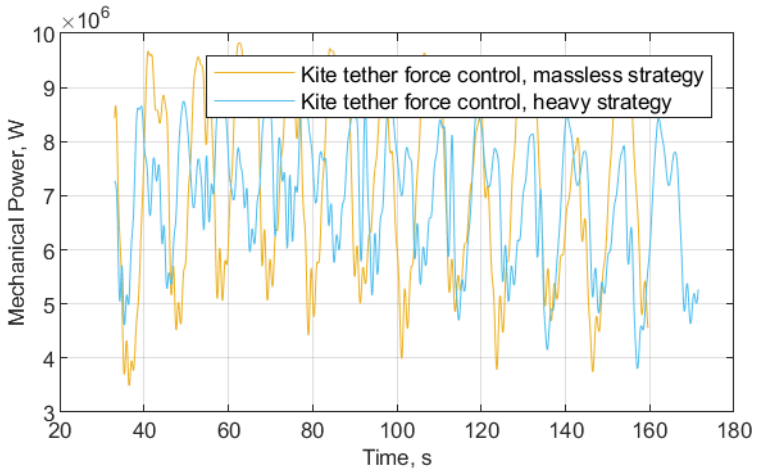

Figure 11.10: Comparison of the power output between the kite tether force controller combined with the feedforward winch control using either the heavy strategy or the massless strategy.

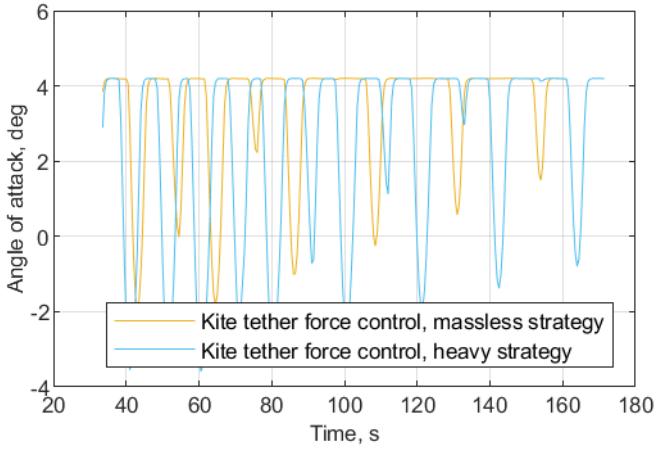

Figure 11.11: Comparison of the angle of attack between the kite tether force controller combined with the feedforward winch control using either the heavy strategy or the massless strategy.

Mean cycle power

The electrical energy of the traction phase can be calculated by multiplying the mean electrical power by the duration of the traction phase. By subtracting the required energy for the retraction phase, the cycle energy can be calculated. This is assumed to be 93 MJ and is derived by integrating the power used by the baseline during retraction. By dividing the cycle energy by the cycle time, the mean cycle electrical energy can be calculated. This is shown in Table 11.4. Whereas the mean mechanical power during the traction phase was about 5% lower than the baseline, the mean electrical cycle power is less than 1% lower than the baseline when using one of the kite tether force control architectures. This is because the kite tether force controllers don't use power anymore during the traction phase. Furthermore, the traction phase was longer, especially using the heavy strategy, resulting in a higher mean cycle power.

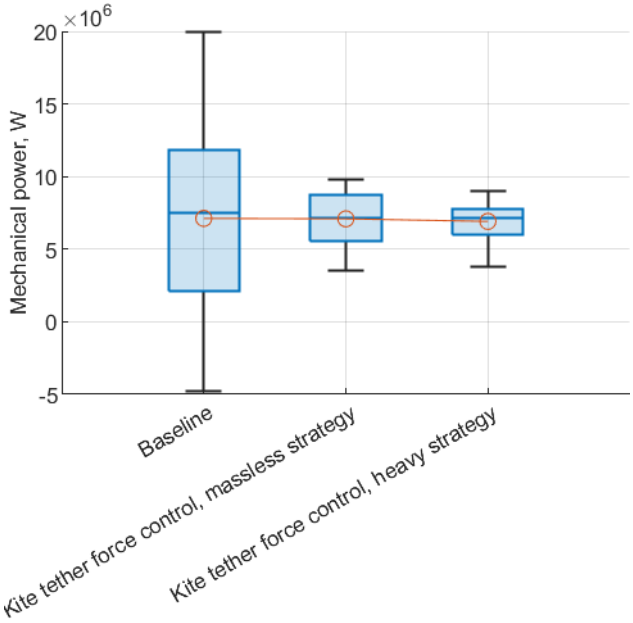

Figure 11.12: Power distribution during the traction phase of baseline and kite tether force control combined with the feedforward winch control using either the heavy strategy or the massless strategy. The red dots denote the mean power.

Table 11.3: Mean electrical power for all strategies during the traction phase.

	$P_{m_{\text{mean}}}$ MW
baseline	6.45
heavy strategy	6.19 (96.0%)
massless strategy	6.30 (97.8%)

Table 11.4: Mean electrical cycle power for all strategies.

	$P_{m_{\text{mean}}}$ MW
baseline	4.42
heavy strategy	4.39 (99.5%)
massless strategy	4.38 (99.1%)

11.3. Conclusion and Discussion

The current winch control strategy of MegAWES is to keep the tether force constant as a function of a wind speed measurement. However, this leads to high tether force peaks. Using the angle of attack of the kite, the amount of energy extracted from the wind can be lowered so that these peaks disappear. In this chapter a novel architecture to control the angle of attack has been presented called 'kite tether force control. It is used in conjunction with the 2-phase strategy where the power limit is reached at the same point on the winch control curve as the tether force limit. This means that by controlling the tether force overshoot, the kite effectively controls the power overshoot as well. The winch thus doesn't have to change its control law at all and keeps doing the same feedforward winch control curve.

Using a PI controller with back-calculation and nonlinear dynamic inversion, the kite tether force controller always aims at the maximum safe angle of attack that does not exceed the reference tether force. So it is using only a measurement of the tether force and airspeed, and a model of the lift curve to calculate an angle of attack reference. Furthermore, it has three tunable parameters, the constant tether force reference, which should be slightly below the desired peak tether force and two gains for the PI controller.

This architecture has been combined with two different feedforward winch control laws: one using the winch control curve developed in chapter 10 and one using the winch control curve derived for massless kites (Equation 9.4). Both control architectures lowered the peak power from 20 MW to 9.0 MW and 9.8 MW respectively, thus successfully lowering the peak power by more than 50%.

In addition, it was able to adjust to disturbances that are difficult to model. The tether drag increases during the traction phase. The PI controller simply accounted for this by requesting more lift, leading to higher angle of attack references, but never above the desired maximum angle of attack.

Kite tether force control is always combined with a feedforward control strategy which shows the full potential of this new control architecture. Besides lower peak power the minimum power has been increased from -4.7 MW to 3.8 MW and 3.5 MW respectively.

Besides power smoothing, the winch acceleration was much smoother with peaks of about $1.8\,\mathrm{m/s^2}$ instead of clipping at the bounds of $5\,\mathrm{m/s^2}$ 99% of the time. The change in acceleration was also much smoother. This resulted in a more more constant reel-out speed.

The difference between using a the heavy and the massless winch control curve was small, but some hints towards further optimisation were found: First, the heavy strategy had a better minimum power and was thus likely closer to the optimal reel-out factor for MegAWES, as discussed in the previous chapter. However, due to the use of the 2-phase strategy, the peak power it could produce was lower than when using a massless strategy. Future research should focus on non-quadratic, but smooth winch control curves that allow a minimum tether force and optimal reel-out speed as discussed in chapter 10 but are also compatible with a chosen power limit, rather than a power limit derived from the maximum tether force.

Furthermore, even though there was a second order reference model that followed the commanded angle of attack, this strategy should be verified in a 6DOF simulation. The kite likely needs good control authority on the angle of attack to follow the reference. Alternatively, direct lift surfaces, like flaps, could be used to increase the control authority and bandwidth of the controller that follows the lift reference, like in Lombaerts and Looye, 2013 and discussed in chapter 4.

In this analysis no uncertainties in the lift curve were considered. Furthermore, no disturbances such as gusts were injected. The PI controller could compensate for uncertainties but it needs to be investigated whether the bandwidth of the kite tether force controller is high enough to compensate for gusts. The winch will help, but only using the feedforward controller.

In this kite tether force control architecture, the angle of attack is decoupled from the bank angle. Better lateral control could be achieved by coupling these two controllers because they are dependent on each other.

Part V

Conclusion and Discussion

12

Conclusion and Discussion

The objective of this work was twofold. First, the literature study aimed to find ways to improve the reliability of fixed-wing, ground-gen airborne wind energy systems in a turbulent and gusty wind field by investigating the nominal and robust performance of INDI controllers on the MegAWES simulation framework. The conclusion of this part of the work can be found in chapter 8.

The main idea that emerged from this literature study was to implement a power limit in the 3DOF MegAWES simulation framework using a feedforward winch controller and kite tether force control to reduce the power fluctuations of utility-scale airborne wind energy systems. The power fluctuations of MegAWES were between $-4.7\,\mathrm{MW}$ and $20.0\,\mathrm{MW}$ during the traction phase, which puts high requirements on the ground station infrastructure such as the generator and battery. This problem was deemed more important than just robust inner loop flight control and thus the focus was shifted away from INDI and towards control architectures to reduce power fluctuations.

It was found that a feedforward winch controller could reduce the minimum power and that kite tether force control could lower the peak power of the system. Before a feedforward winch controller could be implemented however, the winch inertia and radius had to be resized as they were found to be too small in the preliminary experiment in chapter 6.

The changes to the MegAWES framework for this work have been published on Eijkelhof et al. (2021) on the branch `DevTetherForceControl`[1]. Furthermore, the design tools used to arrive at a new winch sizing and winch control curve can be found in Eijkelhof (2023) on the branch `WinchControl_QuasiSteady`[2].

The conclusion and discussion of each of the research questions for the experimental part of this thesis will be summarised.

Research question 4

What is the effect of the radius and inertia of the winch on the system dynamics?

The equations of motion of the winch are derived by assuming that the winch acts as a single rotating body on which the tether force, generator torque, and friction moment act. By assuming a feedforward winch controller for the generator torque and a quasi-steady model for the tether force, the closed loop response based on wind input is derived.

The pole location is always in the left-hand plane, thus confirming that using this feedforward winch control law always results in asymptotically stable dynamics. The pole location moves further to the left (higher bandwidth) for a lower inertia and higher radius of the winch. It is concluded that the winch radius and inertia have a substantial effect on the dynamics of the system and should thus be carefully selected.

For small systems the bandwidth requirement is very soft because they only need to adapt their reel-out speed to a change in wind. For heavier systems, the mass effect becomes significant, which changes the apparent wind speed during the patterns flown. This increases the bandwidth requirement

[1] https://github.com/awegroup/MegAWES/tree/DevTetherForceControl
[2] https://github.com/awegroup/MegAWES-Design/tree/WinchControl_QuasiSteady

which has not been previously mentioned in the literature. For MegAWES a radius of 1.5 m with an inertia of 1.0×10^4 kgm^2 leads to a bandwidth that can accommodate the change in airspeed at a frequency 10-times the airspeed when the system is operating at a low reel-out speed (and the behaviour is the slowest).

If the inertia of the generator is too large or radius too small, the power production is severely reduced due to lag between reel-out speed and tether force. Furthermore, leads to higher tether force peaks, potentially resulting in tether rupture. One could try to reduce the lag by adding an additional controller, however, this would come at the expense of additional control effort which increases the power fluctuations.

While the selected inertia is three orders of magnitudes higher than the current value, a reference wind turbine with a rated power of 5.0 MW has a generator inertia around the low speed axis of roughly 1×10^7 kgm^2 Elkodama et al., 2022. If the same generator is to be used on the MegAWES system, it would require a radius of 47 m to have the same bandwidth as the winch designed in this paper. This makes it unlikely that MegAWES could use the same generators as used for wind turbines. However, the requirements of this paper could likely be relaxed as a power fraction of 99 % at 10 times the tether force frequency of the system is quite stringent.

A recommendation for future work is to include a tether model in the equations of motion and investigate if a more sophisticated kite model changes the conclusions of this analysis. In this work, the tether is assumed to be rigid, thus instantaneously transferring the lift generated by the kite to a tether force felt by the ground station. In reality, a tether would act like a spring-damper system, thus the lift would first move the kite in the lateral direction after which tether force would be built up. This would add a roll-off at high frequencies on the tether force dynamics that were neglected in this work.

Research question 5

How to adapt the existing feedforward winch controllers that are derived for massless kites for kites with mass?

A quasi-steady model with mass is used to analyse the optimal reel-out factor for kites with mass. It is found that the optimal reel-out factor changes as a function of elevation, tether length and course angle. The effect of mass is most severe at low wind speeds: when the kite is flying downwards the optimal reeling factor is higher while it is lower when the kite is flying upwards. This makes sense because the gravity force is either helping or working against the kite.

The quasi-steady model with mass converged to a certain minimum tether force when flying downwards at different low wind speeds. This indicated that that tether force could be used as a suitable minimum tether force for the winch control strategy for kites with mass.

By selecting an average operating condition (elevation, azimuth, tether length, course angle), a single curve in the (v_r, F_t) space is found. Compares to the optimal winch strategy for massless kites, this curve is moved slightly to the left which leads to higher tether forces for a given reel-out speed. This makes sense because the kite with mass requires some of its lift to be used to compensated gravity rather than be used to generate a higher tether force. This winch control strategy enabled using the 2-phase strategy so that kite tether force control can limit the peak power for the next research question.

However, the new winch control curve does not lead to an improved power output, both when verifying it with a quasi-steady model simulation and the point mass simulation of MegAWES. The power output was not higher than the power output when using the curve for massless kites (provided that the curve for massless kites was augmented with a minimum tether force to avoid stall). However, it was confirmed that the winch parameters previously selected, resulted in a good response on the winch control curve.

An empirical study towards the optimal feedforward winch control curve with a minimum tether force for fixed-wing systems, like Berra and Fagiano, 2021 did for soft-wing kites, could be an interesting research opportunity. There are many parameters to optimise: mean cycle power, peak power, minimum power, and minimum airspeed for safety. One could make non-quadratic curves in the (v_r, F_t) space that optimise these quantities. Besides winch control, the kite pattern can also be changes. The figures-of-eight flown by the MegAWES kite are outside-up, meaning that the system has to fight gravity when it is also experiencing cosine losses due to the increased azimuth Diehl, 2013. It is recommended to investigate the effect of an inside-up figure of eight on the performance.

Research question 6

What is the performance of the kite tether force controller?

The kite tether force controller designed in this work uses a PI controller on the tether force error which outputs a reference lift force. A dynamic inversion block then calculates the required angle of attack. To ensure that the kite is always tending towards high angles of attack, which are best for power production, the reference tether force is simply set close to the tether force operational limit. To avoid angle of attack references that are unsafe, the dynamic inversion block also calculates the minimum and maximum lift force reference which are used by a back-calculation algorithm to saturate the integrator of the PI controller.

This reduces the peak power by about 50 % in the 3DOF simulation of MegAWES. The angle of attack reference is frequently clipped at its maximum value, but when needed, lowers smoothly to achieve a reduction of power.

While the mechanical power during the traction phase is reduced by about 3 %, the mean electrical power over the entire cycle is reduced by less than 1 %. This is because the traction phase is slightly longer when using tether force control because the winch does not have to reel-out faster when the power peaks occur.

The kite tether force controller thus reduces the requirements on the drivetrain without substantially affecting the mean cycle power. Compared to optimal control based approaches that dynamically change the angle of attack, this controller uses a measurement of the tether force, airspeed, and angle of attack and an estimate of the lift curve.

In a future study, it is recommended to include model and sensor uncertainties and disturbances to investigate how robust this control strategy is to that. Furthermore, even though there was a second order reference model that followed the commanded angle of attack, this strategy should be verified in a 6DOF simulation. The kite likely needs good control authority on the angle of attack to follow the reference. Alternatively, direct lift surfaces, like flaps, could be used to increase the control authority and bandwidth of the controller that follows the lift reference, like in Lombaerts and Looye, 2013. In this work the kite tether force controller was used in conjunction with the 2-phase strategy but could also be employed with the 3-phase strategy Fechner and Schmehl, 2013 in the future.

This work aimed to reduce the power fluctuations of utility-scale airborne wind energy systems. By implementing a feedforward winch controller the minimum power during the traction phase was increased from negative to positive and the kite tether force controller reduced the peak power while minimally affecting the mean cycle power. This overall resulted in a reduction between the minimum and maximum power during the traction phase of about 75 %.

This shows that the feedforward winch control that adapts the tether force is better suited to utility-scale systems compared to an approach that keeps the tether force constant. Furthermore, the kite tether force controller can be a requirement to shave off unwanted peak loads for the generator.

Reducing the range between minimum and maximum power output reduces the requirements on the generator and energy storage systems (such as batteries) at the ground station. This reduces both cost and the environmental impact of airborne wind energy systems. Reducing the cost of utility-scale airborne wind energy brings it step closer to becoming reality. While reducing the environmental impact ensures that it can provide with even cleaner energy. Together, these two steps bring us closer to a sustainable future.

References

Acquatella, P., Van Kampen, E.-J., & Chu, Q. P. (2022, January 3). A Sampled-Data Form of Incremental Nonlinear Dynamic Inversion for Spacecraft Attitude Control. AIAA SCITECH 2022 Forum. doi:10.2514/6.2022-0761

Aguiar, A., Hespanha, J., & Kokotovic, P. (2005). Path-following for nonminimum phase systems removes performance limitations. *IEEE Transactions on Automatic Control*, *50*(2), 234–239. doi:10.1109/TAC.2004.841924

Ampyx Power. (n.d.). Our technology explained. Retrieved November 17, 2022, from https://www.ampyxpower.com/our-technology-explained/

Antsaklis, P. J., Passino, K. M., & Wang, S. (1991). An introduction to autonomous control systems. *IEEE Control Systems*, *11*(4), 5–13. doi:10.1109/37.88585

Archer, C., & Caldeira, K. (2009). Global Assessment of High-Altitude Wind Power. *Energies*, *2*(2), 307–319. doi:10.3390/en20200307

Archer, C. L. (2013). An Introduction to Meteorology for Airborne Wind Energy. In U. Ahrens, M. Diehl, & R. Schmehl (Eds.), *Airborne Wind Energy* (pp. 81–94). doi:10.1007/978-3-642-39965-7

Au, S.-K., & Beck, J. L. (2001). Estimation of small failure probabilities in high dimensions by subset simulation. *Probabilistic Engineering Mechanics*, *16*(4), 263–277. doi:10.1016/S0266-8920(01)00019-4

Bacon, B., & Ostroff, A. (2000, August 14). Reconfigurable flight control using nonlinear dynamic inversion with a special accelerometer implementation. In *AIAA Guidance, Navigation, and Control Conference and Exhibit*. AIAA Guidance, Navigation, and Control Conference and Exhibit. doi:10.2514/6.2000-4565

Bartyś, M., & Hryniewicki, B. (2019). The Trade-Off between the Controller Effort and Control Quality on Example of an Electro-Pneumatic Final Control Element. *Actuators*, *8*(1), 23. doi:10.3390/act8010023

Bauer, F., Kennel, R. M., Hackl, C. M., Campagnolo, F., Patt, M., & Schmehl, R. (2018). Drag power kite with very high lift coefficient. *Renewable Energy*, *118*, 290–305. doi:10.1016/j.renene.2017.10.073

Bauer, F., Petzold, D., Kennel, R. M., Campagnolo, F., & Schmehl, R. (2019). Control of a drag power kite over the entire wind speed range. *Journal of Guidance, Control, and Dynamics*, *42*(10), 2167–2182. doi:10.2514/1.G004207

Beal, T. R. (1993). Digital simulation of atmospheric turbulence for Dryden and von Karman models. *Journal of Guidance, Control, and Dynamics*, *16*(1), 132–138. doi:10.2514/3.11437

Bechtle, P., Schelbergen, M., Schmehl, R., Zillmann, U., & Watson, S. (2019). Airborne wind energy resource analysis. *Renewable Energy*, *141*, 1103–1116. doi:10.1016/j.renene.2019.03.118

Berra, A., & Fagiano, L. (2021, June 29). An optimal reeling control strategy for pumping airborne wind energy systems without wind speed feedback. (pp. 1199–1204). 2021 European Control Conference (ECC). doi:10.23919/ECC54610.2021.9655018

Betz, A., & Randall, D. G. (1966). *Introduction to the theory of flow machines* (1st. English edition). London, England: Pergamon Press.

Burton, T., Jenkins, N., Sharpe, D., & Bossanyi, E. (2011). *Wind Energy Handbook* (Second Edition). John Wiley & Sons, Ltd.

Cakiroglu, C., Van Kampen, E.-J., & Chu, Q. P. (2018, January 8). Robust Incremental Nonlinear Dynamic Inversion Control Using Angular Accelerometer Feedback. In *2018 AIAA Guidance, Navigation, and Control Conference*. 2018 AIAA Guidance, Navigation, and Control Conference. doi:10.2514/6.2018-1128

Canale, M., Fagiano, L., Ippolito, M., & Milanese, M. (2006). Control of tethered airfoils for a new class of wind energy generator. (pp. 4020–4026). Proceedings of the 45th IEEE Conference on Decision and Control. doi:10.1109/CDC.2006.376775

Canale, M., Fagiano, L., & Milanese, M. (2010). High Altitude Wind Energy Generation Using Controlled Power Kites. *IEEE Transactions on Control Systems Technology*, *18*(2), 279–293. doi:10.1109/TCST.2009.2017933

Candade, A., Ranneberg, M., & Schmehl, R. (2020). Structural analysis and optimization of a tethered swept wing for airborne wind energy generation. *Wind Energy*, *23*(4), 1006–1025. doi:10.1002/we.2469

Chai, R., Tsourdos, A., Savvaris, A., Chai, S., Xia, Y., & Philip Chen, C. (2021). Review of advanced guidance and control algorithms for space/aerospace vehicles. *Progress in Aerospace Sciences*, *122*, 100696. doi:10.1016/j.paerosci.2021.100696

Chang, J., De Breuker, R., & Wang, X. (2022, January 3). Discrete-time Design and Stability Analysis for Nonlinear Incremental Fault-tolerant Flight Control. In *AIAA SCITECH 2022 Forum*. AIAA SCITECH 2022 Forum. doi:10.2514/6.2022-2034

Chang, J., Guo, Z., De Breuker, R., & Wang, X. (2022). Predictor-based Adaptive Incremental Nonlinear Dynamic Inversion for Fault-Tolerant Flight Control*. *IFAC-PapersOnLine*, *55*(6), 730–736. doi:10.1016/j.ifacol.2022.07.214

Cobb, M., Barton, K., Fathy, H., & Vermillion, C. (2019, July). An Iterative Learning Approach for Online Flight Path Optimization for Tethered Energy Systems Undergoing Cyclic Spooling Motion. In *2019 American Control Conference (ACC)* (pp. 2164–2170). 2019 American Control Conference (ACC). doi:10.23919/ACC.2019.8814773

Cobb, M. K., Barton, K., Fathy, H., & Vermillion, C. (2020). Iterative Learning-Based Path Optimization for Repetitive Path Planning, With Application to 3-D Crosswind Flight of Airborne Wind Energy Systems. *IEEE Transactions on Control Systems Technology*, *28*(4), 1447–1459. doi:10.1109/TCST.2019.2912345

De Lellis, M., Mendonça, A., Saraiva, R., Trofino, A., & Lezana, Á. (2016). Electric power generation in wind farms with pumping kites: An economical analysis. *Renewable Energy*, *86*, 163–172. doi:10.1016/j.renene.2015.08.002

De Schutter, J., Leuthold, R., Bronnenmeyer, T., Paelinck, R., & Diehl, M. (2019, December). Optimal control of stacked multi-kite systems for utility-scale airborne wind energy. In *2019 IEEE 58th Conference on Decision and Control (CDC)* (pp. 4865–4870). 2019 IEEE 58th Conference on Decision and Control (CDC). doi:10.1109/CDC40024.2019.9030026

Department of Defence. (1997, December 19). *MIL-HDBK-1797: Flying Qualities of Piloted Aircraft*.

Diederich, F., Drischler, J., & Aeronautics, U. S. N. A. C. for. (1957). *Effect of spanwise variations in gust intensity on the lift due to atmospheric turbulence*. National Advisory Committee for Aeronautics. Retrieved from https://books.google.nl/books?id=OsjLSgAACAAJ

Diehl, M. (2013). Airborne Wind Energy: Basic Concepts and Physical Foundations. In U. Ahrens, M. Diehl, & R. Schmehl (Eds.), *Airborne Wind Energy* (pp. 3–22). doi:10.1007/978-3-642-39965-7

Echeverri, P., Fricke, T., Homsy, G., & Tucker, N. (2020, September). *The Energy Kite: Selected Results From the Design, Development and Testing of Makani's Airborne Wind Turbines, Part I*. Makani. Retrieved June 12, 2023, from https://x.company/projects/makani/

Eijkelhof, D. (2023). MegAWES-Design. Retrieved from github.com/awegroup/MegAWES-Design

Eijkelhof, D., Fasel, U., & Rapp, S. (2021). MegAWES (3DoF & 6DoF kite dynamics). Retrieved November 29, 2022, from https://github.com/awegroup/MegAWES

Eijkelhof, D., Rapp, S., Fasel, U., Gaunaa, M., & Schmehl, R. (2020). Reference Design and Simulation Framework of a Multi-Megawatt Airborne Wind Energy System. *Journal of Physics: Conference Series*, *1618*(3). doi:10.1088/1742-6596/1618/3/032020

Eijkelhof, D., & Schmehl, R. (2022). Six-degrees-of-freedom simulation model for future multi-megawatt airborne wind energy systems. *Renewable Energy*, *196*, 137–150. doi:10.1016/j.renene.2022.06.094

Elkodama, A., Ismaiel, A., Abdellatif, A., & Shaaban, S. (2022). Modelling and Simulation of an Asynchronous Generator for a 5 MW Wind Turbine. *International Review of Automatic Control (IREACO)*, *15*(5), 233. doi:10.15866/ireaco.v15i5.22922

Erhard, M., & Strauch, H. (2015). Flight control of tethered kites in autonomous pumping cycles for airborne wind energy. *Control Engineering Practice*, *40*, 13–26. doi:10.1016/j.conengprac.2015.03.001

Erhard, M., & Strauch, H. (2018). Automatic control of pumping cycles for the SkySails prototype in airborne wind energy. In R. Schmehl (Ed.), *Airborne wind energy: Advances in technology development and research* (pp. 189–213). doi:10.1007/978-981-10-1947-0_9

Etkin, B. (2012). *Dynamics of Atmospheric Flight*. Dover Publications.

Fagiano, L., Huynh, K., Bamieh, B., & Khammash, M. (2013, July 12). On sensor fusion for airborne wind energy systems. doi:10.1109/TCST.2013.2269865

Fagiano, L., Nguyen-Van, E., Rager, F., Schnez, S., & Ohler, C. (2018). Autonomous Take-Off and Flight of a Tethered Aircraft for Airborne Wind Energy. *IEEE Transactions on Control Systems Technology*, *26*(1), 151–166. doi:10.1109/TCST.2017.2661825

Fagiano, L., Quack, M., Bauer, F., Carnel, L., & Oland, E. (2022). Autonomous Airborne Wind Energy Systems: Accomplishments and Challenges. *Annual Review of Control, Robotics, and Autonomous Systems*, *5*(1), 603–631. doi:10.1146/annurev-control-042820-124658

Fagiano, L., Zgraggen, A., Morari, M., & Khammash, M. (2014). Automatic Crosswind Flight of Tethered Wings for Airborne Wind Energy: Modeling, Control Design, and Experimental Results. *IEEE Transactions on Control Systems Technology*, *22*(4), 1433–1447. doi:10.1109/TCST.2013.2279592

Fechner, U., & Schmehl, R. (2013). Model-Based Efficiency Analysis of Wind Power Conversion by a Pumping Kite Power System. In U. Ahrens, M. Diehl, & R. Schmehl (Eds.), *Airborne Wind Energy* (pp. 249–269). doi:10.1007/978-3-642-39965-7_14

Fechner, U., & Schmehl, R. (2018). Flight Path Planning in a Turbulent Wind Environment. In R. Schmehl (Ed.), *Airborne Wind Energy: Advances in Technology Development and Research*. doi:10.1007/978-981-10-1947-0

Fechner, U., van der Vlugt, R., Schreuder, E., & Schmehl, R. (2015). Dynamic model of a pumping kite power system. *Renewable Energy*, *83*, 705–716. doi:10.1016/j.renene.2015.04.028

Fernandes, M. C. R. M., Vinha, S., Paiva, L. T., & Fontes, F. A. C. C. (2022). L0 and L1 Guidance and Path-Following Control for Airborne Wind Energy Systems. *Energies*, *15*(4), 1390. doi:10.3390/en15041390

Fernandes, M. C., Silva, G. B., Paiva, L. T., & Fontes, F. A. (2018). A Trajectory Controller for Kite Power Systems with Wind Gust Handling Capabilities, 543–550. doi:10.5220/0006914205430550

Grondman, F., Looye, G., Kuchar, R. O., Chu, Q. P., & Van Kampen, E.-J. (2018, January 8). Design and Flight Testing of Incremental Nonlinear Dynamic Inversion-based Control Laws for a Passenger Aircraft. In *2018 AIAA Guidance, Navigation, and Control Conference*. 2018 AIAA Guidance, Navigation, and Control Conference. doi:10.2514/6.2018-0385

Gros, S., Zanon, M., & Diehl, M. (2012, June). Orbit control for a power generating airfoil based on nonlinear MPC. In *2012 American Control Conference (ACC)* (pp. 137–142). 2012 American Control Conference - ACC 2012. doi:10.1109/ACC.2012.6315367

Hagen, L. V., Petrick, K., Wilhelm, S., & Schmehl, R. (2023). Life-Cycle Assessment of a Multi-Megawatt Airborne Wind Energy System. *Energies*, *16*(4), 1750. doi:10.3390/en16041750

Han, Z., & Chen, Y. (2022). Energy Optimization of Airborne Wind Energy System via Deep Reinforcement Learning. In Y. Jia, W. Zhang, Y. Fu, & S. Zhao (Eds.), *Proceedings of 2022 Chinese Intelligent Systems Conference* (Vol. 950, pp. 706–714). doi:10.1007/978-981-19-6203-5_70

Hussen, K. van, Dietrich, E., Smeltink, J., Berentsen, K., Sleen, M. van der, Haffner, R., & Fagiano, L. (2018). Study on challenges in the commercialisation of airborne wind energy systems. *European Commission*. doi:10.2777/87591

Ilzhöfer, A., Houska, B., & Diehl, M. (2007). Nonlinear MPC of kites under varying wind conditions for a new class of large-scale wind power generators. *International Journal of Robust and Nonlinear Control*, *17*(17), 1590–1599. doi:10.1002/rnc.1210

International Electrotechnical Commission. (2005). Wind turbines - Part 1: Design requirements. International Electrotechnical Commission.

IRENA. (2022). *Renewable Energy Statistics 2022*. Abu Dhabi: International Renewable Energy Agency. Retrieved from www.irena.org/Publications

Johnson, E. N., & Calise, A. J. (2001, September). Pseudo-Control Hedging: A New Method For Adaptive Control. (p. 24). Advances in Navigation Guidance and Control Technology Workshop. Alabama, USA.

Jørgensen, B. H., Holttinen, H., IEA Wind Operating Agents, & Charlotte Hede Lindev. (2021, August). *Annual Report 2020*. IEA Wind TCP. Retrieved from https://%20iea-wind.org/

Joshi, R., von Terzi, D., Kruijff, M., & Schmehl, R. (2022). Techno-economic analysis of power smoothing solutions for pumping airborne wind energy systems. *Journal of Physics: Conference Series*, *2265*(4), 042069. doi:10.1088/1742-6596/2265/4/042069

Karg, B., & Lucia, S. (2019, June). Learning-based approximation of robust nonlinear predictive control with state estimation applied to a towing kite. In *2019 18th European Control Conference (ECC)* (pp. 16–22). 2019 18th European Control Conference (ECC). doi:10.23919/ECC.2019.8796201

Kawaguchi, J., Ninomiya, T., & Miyazawa, Y. (2011). Stochastic Approach to Robust Flight Control Design Using Hierarchy-Structured Dynamic Inversion. *Journal of Guidance, Control, and Dynamics*, *34*(5), 1573–1576. doi:10.2514/1.53257

Kier, T. M., Müller, R., & Looye, G. (2020, January 6). Analysis of Automatic Control Function Effects on Vertical Tail Plane Critical Load Conditions. In *AIAA Scitech 2020 Forum*. AIAA Scitech 2020 Forum. doi:10.2514/6.2020-1621

Kumtepe, Y., Pollack, T., & Van Kampen, E.-J. (2022, January 3). Flight Control Law Design using Hybrid Incremental Nonlinear Dynamic Inversion. In *AIAA SCITECH 2022 Forum*. AIAA SCITECH 2022 Forum. doi:10.2514/6.2022-1597

Li, H., Olinger, D. J., & Demetriou, M. A. (2015a, July). Attitude tracking control of an Airborne Wind Energy system. In *2015 European Control Conference (ECC)* (pp. 1510–1515). 2015 European Control Conference (ECC). doi:10.1109/ECC.2015.7330752

Li, H., Olinger, D. J., & Demetriou, M. A. (2015b, July). Control of an airborne wind energy system using an aircraft dynamics model. In *2015 American Control Conference (ACC)* (pp. 2389–2394). 2015 American Control Conference (ACC). doi:10.1109/ACC.2015.7171090

Li, H., Olinger, D. J., & Demetriou, M. A. (2016, July). Attitude tracking control of a GroundGen airborne wind energy system. In *2016 American Control Conference (ACC)* (pp. 4095–4100). 2016 American Control Conference (ACC). doi:10.1109/ACC.2016.7525565

Li, H., Olinger, D. J., & Demetriou, M. A. (2018). Attitude Tracking Control of an Airborne Wind Energy System. In R. Schmehl (Ed.), *Airborne Wind Energy: Advances in Technology Development and Research* (pp. 215–239). doi:10.1007/978-981-10-1947-0

Licitra, G., Koenemann, J., Bürger, A., Williams, P., Ruiterkamp, R., & Diehl, M. (2019). Performance assessment of a rigid wing Airborne Wind Energy pumping system. *Energy*, *173*, 569–585. doi:10.1016/j.energy.2019.02.064

Liepmann, H. W. (1952). On the Application of Statistical Concepts to the Buffeting Problem. *Journal of the Aeronautical Sciences*, *19*(12), 793–800. doi:10.2514/8.2491

Lombaerts, T., & Looye, G. (2013). Design and Flight Testing of Nonlinear Autoflight Control Laws Incorporating Direct Lift Control. In Q. Chu, B. Mulder, D. Choukroun, E.-J. van Kampen, C. de Visser, & G. Looye (Eds.), *Advances in Aerospace Guidance, Navigation and Control*. doi:10.1007/978-3-642-38253-6

Loyd, M. L. (1980). Crosswind kite power (for large-scale wind power production). *Journal of Energy*, *4*(3), 106–111. doi:10.2514/3.48021

Luchsinger, R. H. (2013). Pumping Cycle Kite Power. In U. Ahrens, M. Diehl, & R. Schmehl (Eds.), *Airborne Wind Energy* (pp. 47–64). doi:10.1007/978-3-642-39965-7_3

Malz, E., Hedenus, F., Göransson, L., Verendel, V., & Gros, S. (2020). Drag-mode airborne wind energy vs. wind turbines: An analysis of power production, variability and geography. *Energy*, *193*, 116765. doi:10.1016/j.energy.2019.116765

Mann, J. (1998). Wind field simulation. *Probabilistic Engineering Mechanics*, *13*(4), 269–282. doi:10.1016/S0266-8920(97)00036-2

Manwell, J., McGowan, J., & Rogers, A. (2009). *Wind Energy Explained: Theory, Design and Application* (2nd ed.). West Sussex, United Kingdom: Wiley.

Matamoros, I., & de Visser, C. C. (2018, January 8). Incremental Nonlinear Control Allocation for a Tailless Aircraft with Innovative Control Effectors. In *2018 AIAA Guidance, Navigation, and Control Conference*. 2018 AIAA Guidance, Navigation, and Control Conference. doi:10.2514/6.2018-1116

Moncayo, H., Perhinschi, M., Wilburn, B., Wilburn, J., & Karas, O. (2012, August 13). UAV Adaptive Control Laws Using Non-Linear Dynamic Inversion Augmented with an Immunity-based Mechanism. In *AIAA Guidance, Navigation, and Control Conference*. AIAA Guidance, Navigation, and Control Conference. doi:10.2514/6.2012-4678

Mooij, E., & Wang, X. [Xuerui]. (2021, January 11). Incremental Sliding Mode Control for Aeroelastic Launch Vehicles with Propellant Slosh. In *AIAA Scitech 2021 Forum*. AIAA Scitech 2021 Forum. doi:10.2514/6.2021-1221

Near Zero. (2012, September 9). *Energy High in the Sky: Expert Perspectives on Airborne Wind Energy Systems*. Retrieved from http://nearzero.org

Njiri, J. G., & Söffker, D. (2016). State-of-the-art in wind turbine control: Trends and challenges. *Renewable and Sustainable Energy Reviews*, *60*, 377–393. doi:10.1016/j.rser.2016.01.110

Park, S., Deyst, J., & How, J. (2004, August 16). A New Nonlinear Guidance Logic for Trajectory Tracking. In *AIAA Guidance, Navigation, and Control Conference and Exhibit*. AIAA Guidance, Navigation, and Control Conference and Exhibit. doi:10.2514/6.2004-4900

Pollack, T. S. C., & van Kampen, E. (2022). Robust Stability and Performance Analysis of Incremental Dynamic Inversion-based Flight Control Laws. (p. 16). AIAA SCITECH 2022 Forum. doi:10.2514/6.2022-1395

Polzin, M., Wood, T. A., Hesse, H., & Smith, R. S. (2017). State Estimation for Kite Power Systems with Delayed Sensor Measurements. *IFAC-PapersOnLine*, *50*(1), 11959–11964. doi:10.1016/j.ifacol.2017.08.1176

Rapp, S. (2021). *Robust Automatic Pumping Cycle Operation of Airborne Wind Energy Systems* (Doctoral dissertation, Delft University of Technology). doi:10.4233/UUID:AB2ADF33-EF5D-413C-B403-2CFB4F9B6BAE

Rapp, S., & Schmehl, R. (2021). Enhancing Resilience of Airborne Wind Energy Systems Through Upset Condition Avoidance. *Journal of Guidance, Control, and Dynamics*, *44*(2), 251–265. doi:10.2514/1.G005189

Rapp, S., Schmehl, R., Oland, E., & Haas, T. (2019). Cascaded Pumping Cycle Control for Rigid Wing Airborne Wind Energy Systems. *Journal of Guidance, Control, and Dynamics*, *42*(11), 2456–2473. doi:10.2514/1.G004246

Rapp, S., Schmehl, R., Oland, E., Smidt, S., Haas, T., & Meyers, J. (2019, January 7). A Modular Control Architecture for Airborne Wind Energy Systems. In *AIAA Scitech 2019 Forum*. AIAA Scitech 2019 Forum. doi:10.2514/6.2019-1419

Ruiterkamp, R., & Sieberling, S. [Sören]. (2013). Description and Preliminary Test Results of a Six Degrees of Freedom Rigid Wing Pumping System. In U. Ahrens, M. Diehl, & R. Schmehl (Eds.), *Airborne Wind Energy* (pp. 443–458). doi:10.1007/978-3-642-39965-7_26

Salma, V., Friedl, F., & Schmehl, R. (2020). Improving reliability and safety of airborne wind energy systems. *Wind Energy*, *23*(2), 340–356. doi:10.1002/we.2433

Schelbergen, M., & Schmehl, R. (n.d.). TU Delft AWE Workshop. Retrieved from https://github.com/awecourse/workshop

Schmehl, R. (Ed.). (2018). *Airborne Wind Energy: Advances in Technology Development and Research*. doi:10.1007/978-981-10-1947-0

Schmidt, H., de Vries, G., Renes, R. J., & Schmehl, R. (2022a, July). Social Acceptance of Airborne Wind Energy. (p. 1). Airborne Wind Energy Conference (AWEC). Milano, Italy.

Schmidt, H., de Vries, G., Renes, R. J., & Schmehl, R. (2022b). The Social Acceptance of Airborne Wind Energy: A Literature Review. *Energies*, *15*(4), 1384. doi:10.3390/en15041384

Shukla, P., Skea, J., Slade, R., Al Khourdajie, A., Diemen, R. van, McCollum, D., … Luz, S. (2022). IPCC, 2022: Climate Change 2022: Mitigation of Climate Change. Contribution of Working Group III to the Sixth Assessment Report of the Intergovernmental Panel on Climate Change. *Cambridge University Press*. doi:10.1017/9781009157926

Shukla, P., Skea, J., Slade, R., Khourdajie, A. A., Diemen, R. van, McCollum, D., … Luz, S. (2022). IPCC, 2022: Summary for Policymakers. doi:10.1017/9781009157926.001

Sieberling, S. [S.], Chu, Q. P., & Mulder, J. A. (2010). Robust Flight Control Using Incremental Nonlinear Dynamic Inversion and Angular Acceleration Prediction. *Journal of Guidance, Control, and Dynamics*, *33*(6), 1732–1742. doi:10.2514/1.49978

Sieberling, S. [Sören]. (2013). Flight Guidance and Control of a Tethered Glider in an Airborne Wind Energy Application. In Q. Chu, B. Mulder, D. Choukroun, E.-J. van Kampen, C. de Visser, & G. Looye (Eds.), *Advances in Aerospace Guidance, Navigation and Control* (pp. 337–351). doi:10.1007/978-3-642-38253-6

Simplício, P., Pavel, M., van Kampen, E., & Chu, Q. (2013). An acceleration measurements-based approach for helicopter nonlinear flight control using incremental nonlinear dynamic inversion. *Control Engineering Practice*, *21*(8), 1065–1077. doi:10.1016/j.conengprac.2013.03.009

Smeur, E., Chu, Q., & de Croon, G. (2016). Adaptive incremental nonlinear dynamic inversion for attitude control of micro aerial vehicles. In *Guidance Navigation Control Conference*. doi:10.2514/6.2016-1390

Smeur, E., De Croon, G., & Chu, Q. (2016). Gust disturbance alleviation with incremental nonlinear dynamic inversion. In *IEEE International Conference on Intelligent Robots and Systems (IROS)* (pp. 5626–5631). doi:10.1109/IROS.2016.7759827

Smit, B., Pollack, T., & Kampen, E. (2022). Adaptive Incremental Nonlinear Dynamic Inversion Flight Control for Consistent Handling Qualities. In *AIAA SCITECH Forum*. doi:10.2514/6.2022-1394

Smith, P. (1998, August 10). A simplified approach to nonlinear dynamic inversion based flight control. In *23rd Atmospheric Flight Mechanics Conference*. 23rd Atmospheric Flight Mechanics Conference. doi:10.2514/6.1998-4461

Todeschini, D., Fagiano, L., Micheli, C., & Cattano, A. (2019, July). Control of vertical take off, dynamic flight and landing of hybrid drones for airborne wind energy systems. In *2019 American Control Conference (ACC)* (pp. 2177–2182). 2019 American Control Conference (ACC). doi:10.23919/ACC.2019.8815202

Todeschini, D., Fagiano, L., Micheli, C., & Cattano, A. (2021). Control of a Rigid Wing Pumping Airborne Wind Energy System in all Operational Phases. *Control Engineering Practice*, *111*. doi:10.1016/j.conengprac.2021.104794

Trevisi, F., Castro-Fernández, I., Pasquinelli, G., Riboldi, C. E. D., & Croce, A. (2022). Flight trajectory optimization of Fly-Gen airborne wind energy systems through a harmonic balance method. *Wind Energy Science*, *7*(5), 2039–2058. doi:10.5194/wes-7-2039-2022

United Nations. (2021, December). Emerging Climate Technologies in the Energy Supply Sector. United Nations Framework Convention on Climate Change. Retrieved from https://unfccc.int/ttclear/tec/energysupplysector.html

United States Department of Energy. (2021, November). Challenges and Opportunities for Airborne Wind Energy in the United States.

van 't Veld, R., Van Kampen, E.-J., & Chu, Q. P. (2018, January 8). Stability and Robustness Analysis and Improvements for Incremental Nonlinear Dynamic Inversion Control. In *2018 AIAA Guidance, Navigation, and Control Conference*. 2018 AIAA Guidance, Navigation, and Control Conference. doi:10.2514/6.2018-1127

van der Vlugt, R., Bley, A., Noom, M., & Schmehl, R. (2019). Quasi-steady model of a pumping kite power system. *Renewable Energy*, *131*, 83–99. doi:10.1016/j.renene.2018.07.023

Van Hagen, L. (2021). *Life Cycle Assessment of Multi-Megawatt Airborne Wind Energy* (Unpublished). Retrieved March 28, 2022, from 10.13140/RG.2.2.11307.77604

Van Rooij, R. (1996, September). *Modification of the boundary layer calculation in RFOIL for improved airfoil stall prediction* (No. IW-96087R). Delft University of Technology. Netherlands. Retrieved from https://www.osti.gov/etdeweb/biblio/20102159

Vermillion, C., Cobb, M., Fagiano, L., Leuthold, R., Diehl, M., Smith, R. S., ... Demetriou, M. (2021). Electricity in the air: Insights from two decades of advanced control research and experimental flight testing of airborne wind energy systems. *Annual Reviews in Control*, *52*, 330–357. doi:10.1016/j.arcontrol.2021.03.002

Vertovec, N., Ober-Blöbaum, S., & Margellos, K. (2022, June). Safety-Aware Hybrid Control of Airborne Wind Energy Systems. Retrieved from https://www.vertovec.info/publication/safety-aware-hybrid-control-of-airborne-wind-energy-systems/

Wang, X. [X.], Van Kampen, E., Chu, Q., & De Breuker, R. (2019). Flexible aircraft gust load alleviation with incremental nonlinear dynamic inversion. *Journal of Guidance, Control, and Dynamics*, *42*(7), 1519–1536. doi:10.2514/1.G003980

Wang, X. [X.], Van Kampen, E.-J., Chu, Q., & Lu, P. (2019). Incremental sliding-mode fault-tolerant flight control. *Journal of Guidance, Control, and Dynamics*, *42*(2), 244–259. doi:10.2514/1.G003497

Wang, X. [X.], van Kampen, E., & Chu, Q. (2017). Gust load alleviation and ride quality improvement with incremental nonlinear dynamic inversion. In *Atmos. Flight Mech. Conf.* doi:10.2514/6.2017-1400

Wang, X. [Xuerui]. (2019). *Incremental Sliding Mode Flight Control* (Doctoral dissertation, Delft University of Technology). Retrieved from https://doi.org/10.4233/uuid:c8259a08-bbee-4af0-b570-1350a2dd8d89

Wang, X. [Xuerui], Mkhoyan, T., & De Breuker, R. (2022). Nonlinear Incremental Control for Flexible Aircraft Trajectory Tracking and Load Alleviation. *Journal of Guidance, Control, and Dynamics*, *45*(1), 39–57. doi:10.2514/1.G005921

Wang, X. [Xuerui], Mkhoyan, T., Mkhoyan, I., & De Breuker, R. (2021). Seamless Active Morphing Wing Simultaneous Gust and Maneuver Load Alleviation. *Journal of Guidance, Control, and Dynamics*, *44*(9), 1649–1662. doi:10.2514/1.G005870

Wang, X. [Xuerui], Sun, S., van Kampen, E.-J., & Chu, Q. (2019). Quadrotor Fault Tolerant Incremental Sliding Mode Control driven by Sliding Mode Disturbance Observers. *Aerospace Science and Technology*, *87*, 417–430. doi:10.1016/j.ast.2019.03.001

Wang, X. [Xuerui], van Kampen, E.-J., Chu, Q., & Lu, P. (2019). Stability Analysis for Incremental Nonlinear Dynamic Inversion Control. *Journal of Guidance, Control, and Dynamics*, *42*(5), 1116–1129. doi:10.2514/1.G003791

Weber, J., Marquis, M., Cooperman, A., Draxl, C., Hammond, R., Jonkman, J., ... Shields, M. (2021). *Airborne Wind Energy*. National Renewable Energy Laboratory (NREL). Retrieved from nrel.gov/publications

Wrage, S. (2022). Making AWE a Reality. Airborne Wind Energy Conference, Milano, Italy: SkySails Power GmbH. Retrieved from http://resolver.tudelft.nl/uuid:5e7ba020-de8d-4ed1-ac04-5466f8750a55

Zanon, M., Gros, S., & Diehl, M. (2013). Model Predictive Control of Rigid-Airfoil Airborne Wind Energy Systems. In U. Ahrens, M. Diehl, & R. Schmehl (Eds.), *Airborne Wind Energy* (pp. 219–234). doi:10.1007/978-3-642-39965-7

Zgraggen, A. U., Fagiano, L., & Morari, M. (2016). Automatic Retraction and Full-Cycle Operation for a Class of Airborne Wind Energy Generators. *IEEE Transactions on Control Systems Technology*, *24*(2), 594–608. doi:10.1109/TCST.2015.2452230

Zillmann, U., & Bechtle, P. (2018). Emergence and Economic Dimension of Airborne Wind Energy. In R. Schmehl (Ed.), *Airborne Wind Energy: Advances in Technology Development and Research*. doi:10.1007/978-981-10-1947-0